

Submitted to the Astrophysical Journal Supplement

PROPERTIES OF QSO METAL LINE ABSORPTION SYSTEMS AT HIGH REDSHIFTS: NATURE AND EVOLUTION OF THE ABSORBERS AND THE IONIZING RADIATION BACKGROUND¹

Alec Boksenberg

University of Cambridge, Institute of Astronomy, Madingley Road, Cambridge, CB3 0HA, UK

boksy@ast.cam.ac.uk

Wallace L. W. Sargent

Palomar Observatory, 105-24 California Institute of Technology, Pasadena, CA 91125

wws@astro.caltech.edu

and

Michael Rauch

The Observatories of the Carnegie Institution of Washington, 813 Santa Barbara St., Pasadena, CA 91101

mr@ociw.edu

ABSTRACT

A sample of 908 C IV absorber components clumped in 188 systems outside the Lyman forest in the redshift range $1.6 \lesssim z \lesssim 4.4$ have been identified in Keck HIRES spectra of nine QSOs. These and corresponding lines of Si IV, C II, Si II and N V have been fitted with Voigt profiles to obtain column densities and C IV Doppler parameters. The properties of the C IV absorbers are almost constant although their system velocity spreads tend to increase with decreasing redshift. We find a mild increase in C IV comoving mass density with decreasing redshift with a mean $\langle \Omega_{\text{C IV}} \rangle = (3.8 \pm 0.7) \times 10^{-8}$ (1σ uncertainty limits; spatially flat Λ CDM cosmology with $\Omega_{\Lambda} = 0.7$, $\Omega_{\text{M}} = 0.3$ and $h = 0.71$), in broad agreement with earlier work. Corresponding values of C/H in

¹The data presented herein were obtained at the W.M. Keck Observatory, which is operated as a scientific partnership among the California Institute of Technology, the University of California and the National Aeronautics and Space Administration. The Observatory was made possible by the generous financial support of the W.M. Keck Foundation.

the Lyman forest based on Ω_b from the CMB and ionization fractions from our data are $[\text{C}/\text{H}]_{\langle z \rangle=4.0} \geq -3.11^{+0.14}_{-0.19}$ and $[\text{C}/\text{H}]_{\langle z \rangle=2.1} \geq -2.64^{+0.15}_{-0.22}$, suggesting a rise by a factor ~ 3 . Relating the hydrogen mass density more directly to regions containing the C IV absorbers our values for $[\text{C}/\text{H}]$ become $\gtrsim -2.2$ at $\langle z \rangle = 4.0$ and $\gtrsim -2.0$ at $\langle z \rangle = 2.1$. C IV absorber components exhibit strong clustering out to $\Delta_v \lesssim 300 \text{ km s}^{-1}$ but there is no clustering on any scale between *systems*. We argue that for our sample the C IV clustering is entirely due to the peculiar velocities of gas present in the outer extensions of galaxies. We find no change in the median column density ratio Si IV/C IV with redshift, particularly no large change near $z = 3$, contrary to previous observations; other ionic ratios vary continuously with redshift. We show that these are only partial indicators of ionization state and remedy this by use of specific pairs of ionic ratios. We demonstrate that the majority of absorbers are photoionized and find that at $z \lesssim 2.65$ QSOs dominate the ionization of the absorption systems whereas at $z \gtrsim 3.4$ an additional, dominant contribution from galaxies with specific spectral characteristics and high radiative escape fraction in the energy range 1–4 Ryd is required. These results also indicate that $[\text{Si}/\text{C}] = 0.0\text{--}0.4$ fits the data well. Between $z = 2.65$ and $z = 3.4$ there is evident transition in the ionization properties of the absorbers, with large scatter. The UV spectral properties required for the galaxies are not reproduced by standard stellar population synthesis models. We conclude that the heavy element absorbers at $z \gtrsim 3.4$ are located close to galaxies and irradiated dominantly by them, consistent with our independent conclusion from clustering properties.

Subject headings: intergalactic medium — cosmology: observations — galaxies: formation — quasars: absorption lines — quasars: individual

1. INTRODUCTION

The spectra of exceptional quality delivered by the Keck I High Resolution Spectrograph (HIRES; Vogt et al. 1994) have revealed individual metal absorption features related to the high redshift Lyman forest for a large fraction of the stronger lines (Cowie et al. 1995; Tytler et al. 1995; Songaila & Cowie 1996; Womble, Sargent, & Lyons 1996). By redshift $z \sim 3$ such absorbers are found to have a median carbon abundance approximately 10^{-2} of solar (with substantial scatter) and Si/C similar to Galactic halo stars, although these values are based on rather uncertain ionization corrections (Songaila & Cowie 1996; Rauch, Haehnelt, & Steinmetz 1997a). There is evidence for some metal enrichment also at considerably lower H I column densities (Ellison et al. 2000; Schaye et al. 2000a). While it is still unclear how the pollution of the forest material has come about, the observed metal absorbers provide a powerful probe of early stages in the growth of structure and the formation of galaxies and give an observational approach to determining the spectral character of the cosmological ionizing background at those times.

In recent years, detailed hydrodynamical simulations of cosmological structure formation in the presence of a photoionizing background which yield direct quantities for comparison with observations have been performed by several groups (Cen et al. 1994; Zhang, Anninos, & Norman 1995; Hernquist et al. 1996; Davé & Tripp 2001; Viel et al. 2002). In these simulations it is straightforward to compute the neutral hydrogen absorption that would be produced in the light of a background QSO along an arbitrary line of sight through the simulation volume. It is impressive that such results can reproduce the evolving spectral appearance and statistical properties of cosmologically distributed H I absorbers in considerable detail, spanning the range from the weakest detected to those showing damped Lyman α profiles.

An important insight gained from the simulations is that galaxies and H I absorbers develop naturally together in the hierarchical formation of structure. High column density lines ($N(\text{H I}) \gtrsim 10^{17} \text{ cm}^{-2}$) arise from radiatively cooled gas associated with forming galaxies in collapsed, high density, compact regions. Lower column density absorption ($N(\text{H I}) \lesssim 10^{15} \text{ cm}^{-2}$) occurs in the shallower dark matter potential wells, containing gas in various stages of gravitational infall and collapse; typically these are in the form of flattened or filamentary structures of moderate overdensity with Doppler parameters that are often set by peculiar motions or Hubble flow in addition to thermal broadening. Gravitational, pressure and ram-pressure confinement all play significant roles. Such a scenario in which metal absorption arises in gas assumed to be homogeneously enriched has been discussed by Rauch et al. (1997a). In their simulation the large velocity widths of some metal absorbers arise from interactions between associated protogalactic clumps or from alignments of groups of such objects along chance filaments in the line of sight. This simple model does not include stellar “feedback” of energy and momentum from galaxies which could strongly modify the local gas distribution and kinematic state by producing outflows opposing the general infalling motion as well as contributing to the enrichment of the gas and fundamentally influencing the local ionizing conditions. However, increasing attention is now being given to accounting for stellar processes in galaxy formation simulations (Marri & White 2002; Theuns et al. 2002; Croft et al. 2002; Springel & Hernquist 2002; Nagamine, Springel, & Hernquist 2003). Evidence for stellar feedback in the intergalactic medium has recently been reported, for example, by Rauch, Sargent, & Barlow (1999; 2001), Bond et al. (2001), and Adelberger et al. (2003).

The strength and spectrum of the metagalactic ionizing radiation background at high redshift and the nature of the sources which ionized the intergalactic medium are outstanding issues in cosmology. Although QSOs have long been accepted as the main contributors to the metagalactic ionizing radiation, there has been speculation on whether they dominate at the highest redshifts (Bechtold et al. 1987; Donahue & Shull 1987; Shapiro & Giroux 1987; Bajtlik, Duncan, & Ostriker 1988; Meiksin & Madau 1993; Haardt & Madau 1996). Most of recent studies suggest that QSOs fall short of producing enough flux to satisfy measurements of the “proximity effect” at redshifts significantly beyond $z \sim 3$ where the space density of bright QSOs is sharply decreasing (Cooke, Espey, & Carswell 1997; Rauch et al. 1997b; Madau, Haardt, & Rees 1999; Scott et al. 2000; Bianchi, Cristiani, & Kim 2001). The presence of a strong population of high redshift Lyman-

break galaxies (Steidel et al. 1996, 1999) and the detection of significant flux beyond the Lyman limit escaping from such galaxies (Steidel, Pettini, & Adelberger 2001) lend support to the idea that star-forming regions dominated the ionizing background at early times (Haehnelt et al. 2001). The spectral shape of the ultraviolet background radiation should be reflected in the ionization pattern of QSO metal system absorbers (Chaffee et al. 1986; Bergeron & Stasińska 1986; Steidel & Sargent 1989; Vogel & Reimers 1993; Giroux & Shull 1997; Boksenberg, Sargent, & Rauch 2001) and this can be used to identify the character of the ionizing sources if the spectral modifications due to propagation of the radiation through the intergalactic material are properly accounted for (Haardt & Madau 1996). In turn, this can lead to robust determinations of heavy element abundances in galaxy halos and in denser regions of the intergalactic medium.

In this paper we study the ionization state and kinematic properties of a large sample of metal absorbers and trace their evolution in redshift, greatly extending our earlier work (Boksenberg 1997; Boksenberg et al. 2001). In §2 we describe the observations and initial data reduction and in §3 outline our analysis of the absorbers, represented as multi-phase-ionization systems containing individual single-phase component regions. In §4 we give full tables of results with supporting information, comments and displays. In §5 we define the samples which we use in §6 to derive statistical properties and the redshift evolution of absorber quantities, in §7 for clustering studies from which we deduce the nature of the absorbers, and in §8 for redshift distributions of ionic ratios and redshift-selected samples of ionic ratio combinations. In §8 we also verify that collisional ionization is not an important ionizing mechanism for the observed species and show the influence of changes in column density and metallicity. In §9 we study the properties of absorbers near the observed background QSOs. In §10, from comparison of the characteristics of the observed ionic ratio combinations with results of photoionization modelling using the Cloudy code (Ferland 1996), we draw specific conclusions about the sources contributing to the ionizing radiation environment and how the effective balance of these changes with redshift. We summarize our results in §11. In a further paper (in preparation) we determine in greater detail the parameters of the best observed absorbers.

2. OBSERVATIONS AND DATA REDUCTION

The work presented in this paper is based on our HIRES observations of a set of nine QSOs with redshifts $2.32 < z_{\text{em}} < 4.56$, listed with associated information in Table 1. Most of the spectra were obtained using a slitwidth of $0''.86$ yielding a resolution $\sim 6.6 \text{ km s}^{-1}$ FWHM covered by roughly three pixels. The exception is for the gravitationally-lensed object Q1422+2309 (Patnaik et al. 1992) of which we take the data from image component C using a narrower slitwidth, $0''.574$, yielding $\sim 4.4 \text{ km s}^{-1}$ FWHM, and obtained in excellent seeing ($\lesssim 0''.6$) with position angle set to minimize contamination from the closely-spaced neighbouring components A and B (Rauch et al. 1999).

Two partially overlapping configurations for each wavelength region were used to give complete

coverage of the free spectral range for the HIRES echelle format. The data were reduced as described in Barlow & Sargent (1996), with the individual exposures for each QSO wavelength-shifted to heliocentric, vacuum values and added together with weights according to their signal-to-noise ratio (S/N). Continuum levels were delineated by means of polynomial fits to regions apparently free of absorption features and these were used to produce continuum-normalized spectra in preparation for the analysis of the absorption systems.

Due to the spectral variations in instrument efficiency and the sharply uneven exposures over the range resulting from the overlapped setups, in combination with the intrinsic spectral variation of signal intensity from the QSOs themselves, the spectra show complex and quite large variations in S/N along their lengths. To account for these individual patterns of S/N, matching statistical 1σ error arrays are built up during the reduction stages and associated with each completed spectrum file. A rough indication of minimum signal quality is given in Table 1 by S/N values sampled at a few rest-wavelength positions (avoiding emission lines) in common to each spectrum.

3. DETERMINATION OF ABSORPTION-LINE PARAMETERS

3.1. Selection Strategy

The metal absorbers typically appear as well-defined clumps with velocity structure ranging up to a few hundred km s^{-1} in width. In general there are wide expanses of apparently clear redshift space between such clumps. We classify these absorbing entities as *systems* and identify them by the presence of C IV. Within each system we define a population of physical “clouds”, termed *components*, each having a Gaussian velocity distribution of arbitrary width which collectively produce the velocity structure in detail.

Because of blending with H I absorption for metal lines in the Lyman forest, which becomes increasingly severe to higher redshifts, our data sample is built primarily on measurements made outside the forest; only in some exceptionally favourable cases (indicated in the tables) are metal lines in the forest included. Outside the forest C IV absorption is prevalent and is the only ion detected in the weakest systems. Stronger systems also contain lines of some, or occasionally most, of the species Si IV, C II, Si II, N V, O I, Al II, Al III, Fe II or Ni II, if available in the observed spectral range.

For the work presented in this paper we concentrate on the lines C IV $\lambda\lambda 1548.195, 1550.770$, Si IV $\lambda\lambda 1393.755, 1402.770$, C II $\lambda 1334.5323$, Si II $\lambda 1260.4221$ and N V $\lambda\lambda 1238.821, 1242.804$.² If a line is not detected at the wavelength expected from the presence of other species in the same system, an upper limit is determined, except for lines falling in the Lyman forest. In systems

²All rest-frame vacuum wavelengths and related atomic data used here are from Morton (1991) except for those which have revised f -values as given in the compilation of Tripp, Lu, & Savage (1995).

with Si II $\lambda 1260$ in the forest, we substitute $\lambda 1526.7066$ and include $\lambda 1304.3702$ if available, but these lines are relatively much weaker than $\lambda 1260$ and detected only when Si II is strong; when not detected, upper limits obtained from these alternative lines are generally too high to be useful.

3.2. Profile-Fitting Analysis

For the analysis of our spectra we applied the Voigt profile-fitting package VPFIT developed by R. F. Carswell and collaborators (Carswell et al. 1987, 2002) and kindly made available to us. VPFIT is a χ^2 -minimization program capable of making detailed fits to the absorption profiles of several different transitions simultaneously. It estimates redshift, z , Doppler parameter, b and column density, N , with their associated errors, for the individual components of the systems in the defined fitting regions. For the instrumental resolution included in this procedure we took $b_{instr} = 2.83 \text{ km s}^{-1}$ for Q1422+239C and $b_{instr} = 3.96 \text{ km s}^{-1}$ for the rest. Since the χ^2 -minimization technique operates on the reduced spectra there is a degree of correlation between neighbouring pixels arising from the rebinning of the data in the reduction process. To compensate for this smoothing we derived an error-correction file for each spectrum obtained by comparison of values at many wavelengths in the accumulated error array with directly measured values of the root-mean-square fluctuation in the final continuum. The error-correction factor is relatively small, typically in the range 1.1–1.3, and is applied automatically within VPFIT.

While the lower ionization species often are dominated by narrower components and the higher ionization ones by broader, we found, consistent with the S/N, that a range of component widths invariably are present in both sets. We conclude that the different ionic species in a system trace the same physical cloud regions; depending on the ionization states of these regions, each species shows its individual balance of component absorption strengths. We infer that the individual components identified in the metal systems represent *single-phase-ionization absorbing regions* co-existing in multi-phase system complexes. We demonstrate with a simple example case that the absorbing regions indeed conform quite closely with this idealized model.

Using a system at $z = 2.285$ in Q1626+6433, we show in Figure 1 how the derived components distribute themselves among the low to high ionic species. While different components dominate in C II and N V, both sets of components co-exist as blended, strong constituents of the C IV overall profile well-separable in our analysis. Thus the components of this system straightforwardly represent individual regions having quite different degrees of ionization unambiguously traceable through the species. We deal with this point more quantitatively later in the paper. A considerably more complex example similarly demonstrating such separation into physically simple component entities is discussed in §4.

The unifying assumptions we therefore adopted in our analysis are (a) that the component redshift structure seen in one ion corresponds exactly to that in any other ion of the same system, while allowing that in general the relative strengths of the components be different, and (b) that the

Doppler parameters of corresponding components in different ionic species (in general containing thermal broadening and turbulent motion terms) are physically related.

For each QSO the first step in our procedure was to identify all C IV absorption doublets evident outside the forest. In VPFIT, doublet or other members of the same ion automatically are fitted with the same parameters when the wavelength regions where they occur are specified. We began our analysis by deriving the parameters of all necessary components that could be identified in the fitting of the profiles of the C IV doublets. In the relatively few cases where components of one doublet member were excessively confused by blending with interloping species at other redshifts, or were otherwise severely contaminated, we used the remaining member.

Next, all other members of our defined set of ionic species potentially present in the available wavelength range, *whether apparent or not*, were assigned the same initial set of component redshifts and linked to track together with C IV in the subsequent fitting stages. The component b -values for all ionic species of the same atom (C IV with C II and Si IV with Si II) also were linked to track together. To enable VPFIT to derive mutually consistent b -values among atoms (*i.e.* each containing appropriate contributions of individual thermal broadening and common turbulence broadening for each cloud region) it was necessary both to assign realistic component temperatures (see below) and to relate the b -values of all species present. (Because of the relative atomic weights, changes in temperature have only a slight effect on the relative b -values for C and N but can produce quite marked changes in those for Si.) VPFIT then was allowed to attempt simultaneous fits to the line profiles in a first complete pass. Potential components not detected “dropped out” of the analysis and subsequently were assigned upper limits in the manner described below.³

Generally our procedure resulted in a set of profiles which corresponded well to the data for all of the components detected in each species. We found it beneficial to iterate the process by making two or three VPFIT runs while refining the nominal component temperatures between the runs. In the few cases when a component in C IV was weak while C II was strong, C II was substituted as the prime species in the analysis. For some strong, well-separated, components, reliable b -values sometimes could be obtained independently for Si as well as C, although these cases were relatively rare.

To obtain nominal component temperatures we used results given by Rauch et al. (1996) from a formal decomposition into thermal and Gaussian non-thermal motions in a sample of related C IV and Si IV absorption components, shown in their Figure 3 as a plot of C IV thermal against total b -values. They derive a mean temperature of 3.8×10^4 K but note that their analysis is dominated by narrower components which have smaller measurement errors than the more uncertain broader features. They also suggest that a tail in the b -value distribution towards large values apparently indicating temperatures beyond 10^5 K and increased non-thermal contributions may well represent

³In some instances a minor velocity shift relative to C IV, typically a small fraction of 1 km s^{-1} , was made to one or other of the profiles of widely separated species in the same system to correct for slight departures from the nominal global fit to the wavelength scale (Barlow & Sargent 1996).

blends of components. Our analysis supports this view. Since C IV is more common and generally stronger than the other species, a blend of components representing a typical mix of relatively high ionization regions tends to appear significantly broader in C IV than Si IV. If interpreted as a single feature this indeed is likely to indicate an erroneously high temperature. We also show in §8 that collisional ionization at temperatures near 10^5 K cannot be significant for the absorbing regions we observe. Consequently we use the plot given by Rauch et al. as an aid to set temperatures only for the numerous narrower components in our sample ($b \lesssim 10 \text{ km s}^{-1}$).

For the more rarely-occurring broader components we found our fits to the observed profiles to be consistent with there being relatively little difference in the b -values among the species, consequently leading to large turbulent contributions. We set the temperature of these nominally at the mean 3.8×10^4 K given by Rauch et al. To explore the validity of this approximation we made VPFIT trials using a complex system at $z = 2.291$ in Q1626+6433 (described in §4.2) to indicate the effect on the achieved column density values resulting from successive changes in assigned component temperatures. This system contains several broad components which overlap with numerous narrow ones. It is an appropriate example because in the profile-fitting process components are not treated in isolation but adjusted relative to one another to achieve the fit to the data; the degree to which a given component is influenced by others in this process then depends on their relative strength over its range of overlap. We compared the column density results for all components in the complex for two widely-spaced trial temperatures, 1×10^4 K and 1×10^5 K, assigned to the three broadest components, numbered 2, 4 and 14 in Figure 5 (where we have used the nominal temperature 3.8×10^4 K). These temperatures exceed the range expected for clouds of low metallicity and density photoionized by the intergalactic ultraviolet background radiation and so is a stringent test. The initial temperature assignments of the remainder of the components were treated equally in the two cases, following the procedure already described. In Figure 2 we show the resultant column densities for C IV, Si IV, C II and Si II obtained for the two cases. The two sets of values are not significantly different, nor from our results using the adopted nominal temperature. It is apparent that the derived column densities for the individual components do not depend strongly on the thermal properties of the *broad* components in an absorption complex and gives us confidence that our necessarily approximate approach is a sound procedure for obtaining reliable column densities.

On the same basis, the more constrained temperature bounds set by the widths of the narrower components make the derived column densities for these less sensitive still to changes in assigned temperature. The relative insensitivity to profile width applies equally for the instrumental profile, which varies by $\sim \pm 3.8\%$ in velocity width over the spectral range (Barlow & Sargent 1996), and allowed us to use a single, averaged, figure for each spectrum, given above.

Most system members are well isolated from lines at other redshifts and the analysis using the described procedure is generally straightforward. When blending does occur, if some lines belong to doublets whose other members are uncontaminated, or if they are linked with accessible lines of related transitions, we found reliable values usually could be obtained for blended lines by a

simultaneous analysis of all the systems present. Component parameter values judged to be too uncertain due to blending were excluded from the subsequent scientific analysis.

Component parameter errors as given by VPFIT are nominally 1σ values, but confusion between too-closely overlapping components with comparable parameters can give very large apparent errors.⁴ Consequently, in making our profile fits we avoided “overfitting” and adopted the general rule to end with the minimum number of components that gave a reasonable fit after achieving a reduced χ^2 close to 1 per degree of freedom globally for the set of spectral regions linked in the analysis.

At the conclusion of the fitting process for each system we obtained the associated errors on the component column densities alone by fixing the corresponding values of z and b in a final iteration. In this operation we also derived upper limits for all potential components within the different species which had been too weak to survive the first pass of the analysis. We did this by re-introducing them with the appropriate fixed values for z and b and a small assigned column density well below the threshold of significance. The associated error values which are obtained become the adopted 1σ upper limits.

The ability of the Voigt profile-fitting technique to separate different absorbing regions, even though it is sometimes arbitrary, gives it significant advantage over the apparently more direct technique of computing optical depths throughout an absorption complex (Savage & Sembach 1991; Songaila 1998) because the latter cannot account for overlapping blends of adjacent components, interlopers from other systems or differential temperature broadening between species of the same physical component. It is also clear that the wide range of ionization conditions generally found within a system means that reliable determinations of ionic *ratios* cannot be obtained simply from ratios of *total* system quantities as used by Songaila & Cowie (1996) and Songaila (1998); to be physically meaningful they must be determined individually from the components of the multi-phase systems as we do later in this paper.

4. PRESENTATION OF RESULTS

4.1. The Data

Following the prescription outlined in the previous section, for each system we obtained excellent simultaneous fits over all species with a single pattern of component redshifts and appropriately linked b -values. As a full example of this we show in Figure 3 our VPFIT results superimposed on the observations for all the detected systems in Q1626+6433 having more than just C IV accessible. In Tables 2–10 we list the derived values for all available components of our target transitions in

⁴Nevertheless, the combined column densities in such cases remains accurate and VPFIT has a procedure which can be used to give the correct error for the *total* column density of a set of adjacent components in a complex.

the spectra of the nine QSOs. Column 1 gives the absorption redshift z ; column 2 gives b -values for C and column 3, imposed b -values for Si as described in §3.2 shown bracketted and independent values when left as a free parameter, unbracketted⁵ (b -values used for N are not given but are close to those of C when representing the same physical component); columns 4 to 8 give column densities; and column 9 identifies components by number within a system. Each system is headed in the tables with the mean redshift of its constituent components. Where there is severe contamination, strong saturation or too much confusion from blending by lines at other redshifts to give useful quantities, no entry is given as explained in a footnote. In the few marginal cases of weak lines when VPFIT yielded a column density lower than the associated error (instead of making a rejection) these two quantities are added in quadrature and included in the table as an upper limit. Redshifts are vacuum, heliocentric values and are based on the C IV components, but apply consistently to all species, as described in §3. The listed b -values for C almost always are the result of fits to C IV which usually dominates in strength over C II. In rare cases, when component regions have low ionization and C IV is very weak, independent b -values are derived solely from C II (and Si II when left as a free parameter). For the well separated, stronger components the formal 1σ error in z is typically $\lesssim 0.000005$ and in b (for C, and Si when independently derived), $\lesssim 0.5 \text{ km s}^{-1}$.

Very few indeed of the absorption features in our spectra remain unidentified and of these most are very weak and some may be spurious. No dense forest of weak metal lines is seen even in the spectra having the highest S/N in our sample. To allow ready comparison among the QSOs, in Figure 4 we show “spike diagrams” displaying the column densities of all detected components identified in Tables 2–10; note that the vertical scales for Si IV, Si II and N V are lower by 1 dex than the others. The missing indeterminate values indicated in the tables are relatively few and have only a minor effect on the appearance of the spike diagrams. The coverage in redshift outside the forest for the main species of our sample occurs between the two dotted vertical lines shown in each frame. For Si II this applies for $\lambda 1260$ only but we also show values where usefully obtained from strong $\lambda 1527$ and these, of course, appear at redshifts which would be in the forest for $\lambda 1260$; such cases are clarified in the footnotes to Tables 2–10. For all species except C IV the relatively few values reliably obtained from metal lines in the Lyman forest also are shown in the diagrams.

4.2. Broad Absorption Features

A substantial number of systems contain one or more broad (up to a few $\times 10 \text{ km s}^{-1}$), generally high ionization, components self-consistently present in both members of the C IV doublet, that overlap in velocity space with many of the more numerous narrower components. Often a broad feature protrudes (in velocity) at the edge of a system boundary and can be seen directly as having a structureless appearance. In some cases the presence of a significant broad feature immersed among the body of narrow components in a system is required to “depress” the profile of one or

⁵We show only the more reliable values for these; values with large uncertainties are left bracketted.

more of the observed species to account for differences in the characteristics of the corresponding profiles. While we could contrive to construct the broad features from a solid blend of numerous narrow components we do not believe that this recourse is justified by the data, and good fits using single broad components were obtained in general. Nevertheless, it must be remembered that the implicit model envisaged in the VPFIT profile constructions characterizes each assumed cloud in a system only by temperature and Gaussian turbulence broadening, while significant velocity gradients could also feature in the true overall absorption profile. The broad, high ionization components thus might represent spatially associated but physically distinct regions of low volume density dominated by bulk motions (Rauch et al. 1996). Limitations to the detection of broad components are discussed in §6.2.

A simple example with partially exposed high ionization broad components is the $z = 2.056$ system in Q1626+6433, for which the constituents of the C IV $\lambda 1548$ profile are shown in the upper panels of Figure 5. Here, component 1, with $b \sim 21 \text{ km s}^{-1}$, is well enough separated from the others for its smooth outline to be clearly seen and component 4, with $b \sim 55 \text{ km s}^{-1}$, although more immersed (and partially overlapping with component 1) reveals an extended shallow wing. The two panels on the right separately show combinations of the broad and narrow components.

In the lower panels of the same figure details of the $z = 2.291$ system in Q1626+6433 are shown as a more complex as well as more comprehensive example, with broad features which are more immersed in the system. We go first to the panels on the left. The narrower components, $b(\text{C IV}) \lesssim 10 \text{ km s}^{-1}$ (see Table 2), here mostly have quite low ionization, with C II relatively strong; components 11 and 17 are the exceptions. Of the broader components, 2 and 4 unusually also have significant strength in C II, while the remainder have relatively high ionization with C IV strong and C II very weak or undetected.

The associated three sets of panels on the right of Figure 5 highlight different subsets of these components. While the contributions of the combined high ionization components dominate the overall profile of C IV (middle set), it is particularly striking that the embedded combined subset of narrow, lower ionization components (top set) closely resembles the Si IV overall profile and indeed the C II profile. As before, this emphasises the successful segregation of differently ionized regions. The broadest high ionization component (14, with $b \sim 32 \text{ km s}^{-1}$) is the strongest by far in C IV and is the only significant component identified in the weak N V profile shown in Figure 3.

5. DEFINITION OF SAMPLES

From the data in Tables 2–10 we define two samples *sa* and *sb*. We use sample *sa* for the statistical and clustering investigations in §6 and §7 and *sb* for the ionization balance presentations in §8. Sample *sa* is statistically complete. Sample *sb* is used to probe the ionization state of the gas from individual ionic *ratios* which, as will become clear in later sections, does not require a statistically homogeneous population of absorbers.

To avoid significant proximity ionization effects both samples are selected to have system velocities $\gtrsim 3000 \text{ km s}^{-1}$ from the nominal redshifts of the background QSOs (Pascarelle et al. 2001). We find no significant differences in our results or conclusions based on these samples if we extend the limit to 5000 km s^{-1} .

It would be useful to determine individual H I column densities for each of the components we detect in C IV in order to set thresholds for $N(\text{H I})$ in our samples. Although this is possible in some cases it cannot be done reliably in general. The large thermal broadening experienced by H I relative to the metal species studied here causes severe confusion among adjacent components in a great many of the systems; this is compounded by the strongly saturated nature of most of the Lyman α system profiles, as can be seen from the examples in Figure 3. Higher members of the Lyman series are not uniformly available in the redshift range of our data. Consequently we did not attempt to set formal $N(\text{H I})$ thresholds, except in the particular cases of components showing discernible Lyman α damping wings as described in the sample definitions below. However, we found from many VPFIT trials using selected higher redshift systems having several available Lyman series members (for which we assume the H I profiles contain the component population identified in the metals) that the absorbers in our chosen samples generally are optically thin in the Lyman continuum. Later we show through Cloudy modelling how the optical thickness, as well as increasing metallicity, influences the derived quantities.

The samples are further defined as follows:

sample *sa*—contains all C IV, Si IV, C II, Si II and N V lines which fall outside the Lyman forest, while limiting Si II only to the strong transition $\lambda 1260$; includes the apparent partial Lyman limit system at $z = 3.381$ in Q1422+2309C;⁶ excludes all components in a system showing significant Lyman α damping wings for any of its components;⁷

sample *sb*—includes all components in sample *sa* with the exception of the few having ionic members which are saturated (shown in square brackets in the tables); adds lines of Si II $\lambda\lambda 1304, 1527$ if outside the forest (but upper limits are obtained only from $\lambda 1260$ when it is accessible outside the forest); adds strong, unambiguous lines in relatively clear regions of the forest for any species except C IV; includes some components from systems showing relatively mild damping wings in Lyman α ($z = 2.761$ in Q1107+4847, $z = 2.904$ in Q0636+6801 and $z = 2.770$ in Q1425+6039: see the footnotes to the tables) but, in order to limit self-shielding effects, uses only components well-separated in velocity from those having high $N(\text{H I})$.

Sample *sa* contains 867 C IV components in 185 systems and sample *sb*, 908 C IV components in 188 systems. When using these samples, in most cases we also set appropriate column density

⁶For this relatively simple system there is no evidence in the line ratios for the presence of a low ionization region (see footnote to Table 7).

⁷The high H I column density may have been a reason for obtaining the spectra for these systems, which then do not represent a statistically homogeneous contribution to our data set.

thresholds on C IV and sometimes additionally on other species (specified in §§6–8) to avoid bias due to variations in S/N across the redshift range.

6. EVOLVING STATISTICAL PROPERTIES

6.1. Redshift Sampling of C IV, Si IV, C II, Si II and N V

The distribution in redshift of the C IV component column densities, $N(\text{C IV})$, for sample *sa* is shown in the top panel of Figure 6. For each system the values appear as vertical distributions of data points. To avoid confusion in the crowded figures, errors, listed in Tables 2–10, are not indicated in this and subsequent similar figures; mostly these are relatively small. The histogram at the bottom of each panel shows the number of sightlines covered at each bin in redshift from the nine sightlines of this sample. The second and third panels compare component subsets from the simpler and the more complex systems contained in the C IV sample, arbitrarily taken as systems respectively having number $n \leq 6$ and $n \geq 7$ identified components. The column densities *summed* over each system are displayed in the bottom panel.

The panels in Figure 7 give displays for the Si IV, C II, Si II ($\lambda 1260$) and N V component column densities, in this case corresponding to the top panel of Figure 6 only (note the vertical scale shifts for Si IV, Si II and N V relative to C IV). The coverage in redshift outside the Lyman forest as indicated in the histograms is different for each ion (see Figure 4). Within the permitted redshift ranges all system components detected in C IV are represented in the other species either as determined values or upper limits; in both cases Si IV and N V are accepted even if only one member of a doublet is outside the Lyman forest. Only Si IV and C II adequately cover the complete redshift range, while Si II and N V are rather poorly sampled. By comparing with C IV in Figure 6 it is evident that proportionally fewer of the simpler systems contain detected Si IV components, and fewer still C II. Si II mimics C II quite closely within the redshift intervals in common. Despite the meagre coverage, it is interesting to note that at the lower redshifts N V is detected in most of the few narrow windows available, suggesting that *in this range the ion is quite prevalent*.

6.2. C IV Component Doppler Parameter–Column Density Relationship

The top panel in Figure 8 shows values presented in the $b\text{--}\log N$ plane for all C IV components in sample *sa*, extending over the range $1.6 < z < 4.4$. The large majority of components are well resolved. The lower bound in b -value seen in the diagram for these data comes both at about the minimum value resolvable and near the level of thermal broadening for gas at $\sim 10^4$ K. In the lower two panels the plot is given separately for $z < 3.1$ and $z > 3.1$ where the data divide into roughly equal numbers of components (and, it so happens, systems). We see that there is no marked difference between the lower and higher redshift plots except perhaps for a mild extension

to higher column densities at the lower redshifts.

We note that observational biases are present or potentially present in these data (Rauch et al. 1992). Foremost, the unfilled triangular zone tending to the top left of the diagrams arises because at lower column densities the broader, and therefore shallower, components become relatively more difficult to detect above the noise. Thus, the broadest components are detected only at the higher column densities. In addition, there is a tendency for weak, broad components to be masked by more numerous, narrower components which, in general, overlap with them. Broad, shallow systems can also be confused with small residual undulations in the continuum level. Indeed, trial simulations indicated the magnitude of these effects is greater than expected simply from the limitation of S/N in the data.

A second possible bias is for the intrinsic narrowness of some lines to be hidden when approaching line saturation. This would affect the b -values for the narrower, higher column density components at the bottom right of the diagrams. However, trials showed this is not a significant effect within the range of column densities in our data set.

A potential third effect can be expected from unseparated blends of closely overlapping components which would then appear as single components with larger b -values and higher column densities. While recognising that defining components as entities is an approximate process, and that we have aimed to introduce the minimum number of components to fit the spectral profiles, we believe that beyond our resolution limit such blending occurs relatively rarely in our high quality data.

There is some evidence for a small rise in the b -values at the lower boundary of the plots with increasing $N(\text{C IV})$, amounting to $\sim 1 \text{ km s}^{-1}$ over a factor of more than 100 in column density, possibly reflecting the latter two bias effects at some level. This is somewhat less than the effect noted by Rauch et al. (1996) using a smaller data set.

In following sections we keep in mind particularly the first of these bias effects.

6.3. C IV Component Column Density and Doppler Parameter Distributions

Figure 9 shows the distributions of $N(\text{C IV})$ and $b(\text{C IV})$ for all components of sample *sa*. Again we compare values for the ranges $1.6 < z < 3.1$ and $3.1 < z < 4.4$ (having means $\langle z \rangle = 2.51$ and 3.58) and also separately show plots for the *simple* and *complex* systems as defined in §6.1.

For $N(\text{C IV})$ there is a mildly significant difference between the component distributions of the *simple* and *complex* systems, with the latter peaking at a value about three times higher than the former. In contrast, the distributions of b -values are quite similar. It is clear, however, that the apparent shapes of these distributions are strongly influenced by the incomplete sampling in the “exclusion” zone explained in the last section, which severely distorts the true shapes of the distributions. This effect is manifested in $N(\text{C IV})$ by the sharp fall towards smaller column densities

beyond the peak at $\log N(\text{C IV}) \sim 12.5$. In $b(\text{C IV})$ the presence of a peak and the fall to small values beyond it are probably real, while the sampling deficiency brings about a too-rapid fall in the tail of the distribution extending to larger b -values.

Confining attention to the well sampled regions, here we see more quantitatively than in Figure 8 that there is little significant bulk change for either $b(\text{C IV})$ or $N(\text{C IV})$ from higher to lower redshifts. In particular, there is no discernible change in the behaviour of the components of simpler and more complex systems with redshift.

6.4. C IV System Column Density and Velocity Spread Distributions

In Figure 10 we give histograms similar to those in Figure 9 but now for the total system C IV column density, $N_{\text{sys}}(\text{C IV})$, and the total spread in velocity between system components, $\Delta v_{\text{sys}}(\text{C IV})$. Because of the way they are defined both parameters show a marked difference between the distributions for *simple* and *complex* systems.

The effect of incomplete sampling of low column density components is more complicated in these cases than for the *component* distributions just described. For *systems* the sampling deficiency is diluted because the weak components are not in general concentrated near low $N_{\text{sys}}(\text{C IV})$ but are spread among the systems, most of which contain several stronger components. Only the single-component systems directly mirror the sampling effect; the presence or absence of weak components embedded in systems with relatively high aggregate column densities cannot significantly influence the detection of these systems. It is possible that a proportion of the fall to small values of total column density is real. Similarly, for $\Delta v_{\text{sys}}(\text{C IV})$ there would be only a mild effect due to incomplete sampling, dependent on how the broad and narrow components are distributed within a multi-component system.

There is no large change with redshift in the distributions for $N_{\text{sys}}(\text{C IV})$ but there is a hint that in the higher redshift data set there is a bias towards relatively smaller values. For $\Delta v_{\text{sys}}(\text{C IV})$ there is a clearer change, with *systems at the higher redshifts covering a smaller velocity range*.

6.5. Relations between C IV System Column Density, Velocity Spread and Number of Components

Some significant relationships between $N_{\text{sys}}(\text{C IV})$, $\Delta v_{\text{sys}}(\text{C IV})$, and the number of components detected in a system, $n_{\text{sys}}(\text{C IV})$, are shown in Figure 11, again comparing values for $1.6 < z < 3.1$ and $3.1 < z < 4.4$. $N_{\text{sys}}(\text{C IV})$ is strongly dependent both on $n_{\text{sys}}(\text{C IV})$ and $\Delta v_{\text{sys}}(\text{C IV})$ and, in turn, there is a strong proportionality between the latter two. Note that in these logarithmic plots, systems with only one detected component (*i.e.* nominally of zero velocity extent) are excluded. Petitjean & Bergeron (1994) found similar relationships involving total

equivalent width rather than column density. We find no marked systematic changes with redshift in any of the relationships.

6.6. C IV Component and System Differential Column Density Distributions

Figure 12 gives the C IV differential column density distribution function $f(N, X)$ for both the individual components of sample *sa* and for these summed as systems, each in the same two redshift subsets as before. The data are summed over the bin size $10^{0.3}N$ as shown and the vertical error bars are $\pm 1\sigma$ values derived from the number of absorbers in each bin. The function $f(N, X)$ is defined as the number of absorbers per unit column density per unit absorption pathlength, $d^2\mathcal{N}/dNdX$ (this accounts for the multiple redshift coverage from the different sightlines), where for a given redshift interval dz , the Λ CDM cosmology-corrected absorption pathlength interval dX is given by

$$dX = \frac{(1+z)}{\sqrt{\Omega_M(1+z) + \Omega_\Lambda/(1+z)^2}} dz \quad (\Omega = 1) \quad (1)$$

where $\Omega = \Omega_M + \Omega_\Lambda$ and we use $\Omega_M = 0.3$, $\Omega_\Lambda = 0.7$.

First, for the *components*, there is remarkably little difference between the two redshift subsets. The incompleteness at low column densities seen in Figure 8 causes the turnover below $N \sim 10^{12.5}$ but, otherwise, the observed distribution can be approximated as a power-law $f(N, X) \propto N^{-\beta}$ up to $N \sim 10^{13.5}$ when the observations again fall away because very few components have higher column density. There is a hint that this fall-off is greater at high redshift. The power law slope is closely similar for both redshift subsets; we obtain $\beta = 1.84$ for these combined and show this in the figure. For a lower resolution sample with $\langle z \rangle = 2.65$ Petitjean & Bergeron (1994) obtain $\beta = 1.64$.

For the *systems*, there is similarly little difference between the two redshift subsets. The drop below $N \sim 10^{12.5}$, evidently proportionally greater than for the components, again contains the incomplete sampling effect explained in §6.4. A power-law fit over the range $N = 10^{13.0}$ – $10^{14.3}$ with $\beta = 1.6$, as shown, is a good representation. With sparser data Ellison et al. (2000) obtained $\beta = 1.44$ for systems near $z = 3.2$ while Songaila (2001) from more extensive data found $\beta = 1.8$ for her sample over the range $1.5 \lesssim z \lesssim 4.5$. We notice Songaila’s results extend to somewhat higher column densities than we find in our system data set. Including the seven complex systems with mildly damped Lyman α profiles (and separated from the emission redshift by $\gtrsim 3000$ km s $^{-1}$) makes very little difference to our results, either in the system or component cases.

6.7. Redshift Evolution of System Ionic Number Densities and Population Total Column Densities

In Figure 13 we display redshift evolution plots for all the observed species in the systems of sample *sa*. As a baseline we select systems having total column density $N_{\text{sys}}(\text{C IV}) > 1 \times 10^{12} \text{ cm}^{-2}$, yielding 179 systems, and additionally apply the individual thresholds indicated in the figure for Si IV, C II, Si II and N V. Imposing these thresholds gives close to homogeneous sampling for each ion over the observed redshift range.

Looking first at C IV, the six panels give the total number of systems per unit redshift interval $d\mathcal{N}_{\text{sys}}/dz$ and the aggregated column density per unit redshift interval dN_{tot}/dz as a function of redshift for the sets of *all*, *simple* and *complex* systems in sample *sa* as defined previously. The data are corrected for multiple redshift coverage and summed over the arbitrarily adopted bins indicated by the horizontal bars. The indicated $\pm 1\sigma$ uncertainties for dN_{tot}/dz are based on the number of systems present in each bin weighted by system total column density, and are dominated by the few systems with highest column densities. For $d\mathcal{N}_{\text{sys}}/dz$ the number alone of systems detected above the column density threshold defines the indicated uncertainties. The resultant distributions in redshift are remarkably constant, although some mild trends are apparent.

To examine the evolution of the number density of systems with redshift, $\mathcal{N}(z) (\equiv d\mathcal{N}_{\text{sys}}/dz)$, in the comoving volume we use (Misawa et al. 2002)

$$\mathcal{N}(z) = \mathcal{N}_0 \frac{(1+z)^{2+\epsilon}}{\sqrt{\Omega_M(1+z)^3 + \Omega_\Lambda}} \quad (\Omega = 1), \quad (2)$$

where \mathcal{N}_0 is the local value of $\mathcal{N}(z)$ and we take $\Omega_M = 0.3$, $\Omega_\Lambda = 0.7$ as before. If the absorbers have constant comoving volume density and constant proper size then $\epsilon = 0$. The same form can be used for the comoving total column density of the absorber population by substituting $N(z) (\equiv dN_{\text{tot}}/dz)$ and N_0 , and we put κ in place of ϵ to identify the evolution in this case.

In the left panels ($d\mathcal{N}_{\text{sys}}/dz$) we show in dotted lines fits to the three data sets for unevolving populations. In dashed lines we give actual fits to the data, with $\epsilon = 0.35$ (*all*), $\epsilon = 0.5$ (*simple*) and $\epsilon = -0.25$ (*complex*). The latter fits give only a small improvement over the unevolving cases and within the uncertainties the data are consistent with *no evolution in number density*. Misawa et al. (2002) using their combined sample EM15 including data from Sargent, Boksenberg, & Steidel (1988a) and Steidel (1990) obtain $\epsilon = -1.18$, quite strongly evolving in the sense of increasing number density with cosmic time as the two earlier studies had found (largely with the same data). However the two samples are very different. Ours is a very sensitive survey of relatively few QSOs and contains a large number of weak systems; the other surveys have much lower resolution and yield only strong systems, with rest-frame equivalent width $W_0 > 0.15 \text{ \AA}$ (implying $N_{\text{sys}}(\text{C IV}) \gtrsim 5 \times 10^{13} \text{ cm}^{-2}$), from nearly an order of magnitude more QSOs yet with fewer (136) redshifts in the combined sample. Systems in our sample with column density greater than this high threshold

show, within rather large errors, C IV evolutionary behaviour consistent with the earlier studies, although we agree with Misawa et al. that the number density is about twice that found by Steidel (1990).

In the right panels (dN_{tot}/dz) we show dotted line fits to unevolving populations as before. This describes the *simple* subset well but there appears to be a departure for *complex* systems which show an excess below $z = 3$, reflected also in the full sample. The dashed line actual fits to the data have $\kappa = -1.2$ (*all*), $\kappa = -0.56$ (*simple*) and $\kappa = -1.4$ (*complex*).

For the *complex* systems the derived positive evolution in total C IV column density with cosmic time yet with constant number density indicates an increasing mean column density per system. In contrast, the *simple* systems (these make up the bulk of the systems for C IV) are consistent with being a *fully unevolving* population. A difference in evolution between weaker and stronger systems was noticed by Steidel (1990) in his high column density sample.

We note that changes in the threshold column density produce little, if any, significant effect on the total column density values because the stronger systems dominate in the totals. For the subset of *complex* systems changes in the threshold also have little effect on number density because they are detected well above the threshold imposed for the full sample. For the *simple* subset the column densities range down to low values so the number density here is sensitive to the adopted threshold; nevertheless, doubling the threshold to $N_{syst}(\text{C IV}) > 2 \times 10^{12} \text{ cm}^{-2}$, for example, makes relatively little change to the total number of systems detected in the full sample (164 from 179) and does not change our conclusions.

Like C IV, Si IV shows little evidence for evolution in number density (dotted line) for the full sample. There is a hint that this is the result of countervailing trends in the *simple* and *complex* subsets (for all species these are defined by the parent number of C IV components) but the data are also consistent with unevolving contributions from these subsets. In total column density Si IV appears to evolve in similar fashion to C IV. However, in the *complex* subset the unusually strong (for Si IV) system at $z = 1.927$ in Q1626+6433 (Figure 3) has a large effect on the observed trend. To illustrate this the lowest redshift bin is plotted in two forms, one containing the $z = 1.927$ system and one beginning at $z = 2.0$ which excludes it. The resulting, unevolving, trend in the latter case may be more typical of the redshift evolution of Si IV total column density. This alternative binning is also shown in the full data set, with the same conclusion. (In C IV, however, we find the observed rise at low redshift is not significantly influenced by the $z = 1.927$ system.)

Changes with redshift appear greater in C II, although here the data are rather limited and the errors are large. *Complex* systems now strongly dominate the population (note the large scale change in dN_{tot}/dz for the subset of *simple* systems); consequently, these and the full sample follow closely similar behaviour. They indicate strong positive evolution with cosmic time both in number density and total column density, although not with high significance. (In C II the strong $z = 1.927$ system is in the Lyman forest, so not included.)

The data are even more limited for Si II and accidental sampling of strong systems (see Figure 7)

enhances the lower bin in z . It is interesting that N v, sampled even more poorly in redshift, indicates a steep rise in total column density per mean system with cosmic time. This trend implies increasing levels of ionization and seems to conflict with C II which indicates the reverse.

The lack of evolution in C IV total column density in terms of the *simple* systems and the mild evolution of the *complex* systems is surprising because it depends not only on the evolution of overall abundance of carbon, but also on the shape and normalization of the ionizing radiation background and the density of the absorbing regions. Over the extensive redshift range observed, large changes would be expected *a priori* in response to the evolving baryon density and character of the ionizing sources and the development of structure, even for constant metallicity. Si IV, insofar as the data allow, presents a broadly similar picture to the behaviour of C IV. Nevertheless, C II and N v do indicate evolutionary changes, although these appear to be contradictory. However, we need to be cautious in interpreting all the observations in Figure 13 in this way because we are not here identifying the detailed ionization balance in isolated absorbing regions but taking a more global view of the individual properties of the ionic species. We return to this issue in our analysis of ionization conditions in the system *components* in §8.

6.8. Evolution of C IV Mass Density

The comoving C IV mass density is given by

$$\Omega_{\text{C IV}}(z) = \frac{H_0}{c} \frac{m_{\text{C IV}}}{\rho_{\text{crit}}} \frac{\sum N_{\text{tot}}(\text{C IV}, z)}{\Delta X(z)}, \quad (3)$$

where $\rho_{\text{crit}} = 1.89 \times 10^{-29} h^2 \text{ g cm}^{-3}$ is the cosmological closure density, $m_{\text{C IV}}$ is the mass of the ion and $H_0 = 100h \text{ km s}^{-1} \text{ Mpc}^{-1}$. We calculate $\Delta X(z)$ from equation (1) and $\sum N_{\text{tot}}(\text{C IV}, z)$ from the data in Figure 13. The four bins we show for C IV in the figure have mean redshifts $\langle z \rangle = 2.1, 2.7, 3.2, 4.0$. For the full sample (top panel) and using $h = 0.71$ (Spergel et al. 2003) we obtain respective values $\Omega_{\text{C IV}} = (5.7 \pm 2.3, 3.6 \pm 1.3, 3.2 \pm 0.8, 2.9 \pm 1.0) \times 10^{-8}$ (1σ uncertainties). These values are formally consistent with being invariant over the range $1.6 < z < 4.4$ but also suggest a mild evolutionary increase in $\Omega_{\text{C IV}}$ with decreasing redshift, in contrast to system number density. Songaila (2001, 2002) also found a more or less constant trend in the same redshift range; she assumed a $q_0 = 0.5$, $\Lambda = 0$ cosmology and when this is adjusted to the cosmology used above our values of $\Omega_{\text{C IV}}$ agree with Songaila’s within the errors.

The mean of our values over the redshift range is $\langle \Omega_{\text{C IV}} \rangle = (3.8 \pm 0.7) \times 10^{-8}$ at $\langle z \rangle = 3.1$. If we compare the lowest redshift bin with the mean of the other three (over which the values are very similar) we get formally $\Omega_{\text{C IV}} = (5.7 \pm 2.3) \times 10^{-8}$ at $\langle z \rangle = 2.1$ and $\langle \Omega_{\text{C IV}} \rangle = (3.2 \pm 0.6) \times 10^{-8}$ at $\langle z \rangle = 3.3$.

The subset of *simple* systems, showing no evidence for evolution over the full redshift range,

yields $\langle \Omega_{\text{C IV}_{spl}} \rangle = (1.5 \pm 0.4) \times 10^{-8}$ at $\langle z \rangle = 3.1$. For the *complex* systems over the same redshift range $\langle \Omega_{\text{C IV}_{cplx}} \rangle = (2.5 \pm 0.6) \times 10^{-8}$; however, given the positive evolution in C IV mass density, we again compare the lowest redshift bin with the mean of the other three and get formally $\Omega_{\text{C IV}_{cplx}} = (4.1 \pm 2.2) \times 10^{-8}$ at $\langle z \rangle = 2.1$, and $\langle \Omega_{\text{C IV}_{cplx}} \rangle = (1.8 \pm 0.5) \times 10^{-8}$ at $\langle z \rangle = 3.3$.

To estimate the total carbon mass density, Ω_{C} , we need to know the C IV ionization fraction $f_{\text{C IV}} = n_{\text{C IV}}/n_{\text{C}}$. In §10 we find that the metagalactic ionizing radiation field at $z \lesssim 2.7$ is dominated by QSOs, from which we determine that $f_{\text{C IV}}$ peaks at 0.25 for optically thin, low metallicity absorbers (Songaila (2001) takes 0.5 for the ionization fraction). Using our value as an upper limit gives $\Omega_{\text{C}} \geq (2.3 \pm 0.9) \times 10^{-7}$ for the full sample in the $\langle z \rangle = 2.1$ bin. At higher redshifts we deduce in §10 that the absorbing clouds are ionized by a galaxy-dominated radiation field and in this case find $f_{\text{C IV}}$ peaks at 0.38, giving $\Omega_{\text{C}} \geq (7.7 \pm 2.7) \times 10^{-8}$ for the full sample in the $\langle z \rangle = 4.0$ bin.

We now estimate the average metallicity of the gas in all C IV systems, making the assumption that our C IV absorbers represent the cool phase of intergalactic matter which also produces strong H I absorption (as distinct from the “warm-hot” phase, characterized by the strong presence of O VI). We take the baryon density in the Lyman forest, Ω_{Ly} , relative to the total baryon density obtained from measurements of the cosmic microwave background, $\Omega_{\text{b}} = 0.0224h^{-2}$ with $h = 0.71$ (Spergel et al. 2003), as $\Omega_{\text{Ly}}/\Omega_{\text{b}} \geq 0.9$ (Rauch et al. 1997b; Weinberg et al. 1997) and obtain (using the He mass fraction $Y = 0.238$ (Olive, Steigman, & Walker 2000)) $\Omega_{\text{C}}/\Omega_{\text{H}} \geq (7.5 \pm 3.0) \times 10^{-6}$ at $\langle z \rangle = 2.1$ and $\geq (2.6 \pm 0.9) \times 10^{-6}$ at $\langle z \rangle = 4.0$. Taking the solar value $(\text{C}/\text{H})_{\odot} = 2.72 \times 10^{-4}$ by number from Holweger (2001) and Allende Prieto, Lambert, & Asplund (2002), we obtain⁸ $[\text{C}/\text{H}]_{\langle z \rangle=2.1} \geq -2.64^{+0.15}_{-0.22}$ and $[\text{C}/\text{H}]_{\langle z \rangle=4.0} \geq -3.11^{+0.14}_{-0.19}$.

Thus our data suggest a distinct, although not highly significant, rise by a factor ~ 3 in the average metallicity of carbon with cosmic time over our observed redshift range $z = 4.4\text{--}1.6$. As we show in the next section, most if not all of the metal systems we detect are closely associated with galaxies so we do not in general probe the metal content of the more widespread intergalactic medium. Consequently, our values derived by comparison with the total intergalactic hydrogen mass density are underestimates of the metal/hydrogen ratios of the average absorber in our C IV sample.

Pursuing this, most of our C IV systems relate to Lyman α absorbers with relatively high column density, as can be inferred from Figure 3. Cen & Simcoe (1997) find from hydrodynamical simulations that the fraction of mass in Lyman α clouds with $N(\text{HI}) \geq 3 \times 10^{14} \text{ cm}^{-2}$ is approximately 0.25 at $z = 2$ and 0.13 at $z = 4$. Using these estimates our values for $[\text{C}/\text{H}]$ become $\gtrsim -2.0$ at $\langle z \rangle = 2.1$ and $\gtrsim -2.2$ at $\langle z \rangle = 4.0$, now suggesting a constant metallicity of carbon. The comparison with simulations is quite uncertain, however, because the physical state of the Lyman α

⁸In the usual fashion we express the logarithmic abundance of element X relative to element Y compared with the solar values as $[\text{X}/\text{Y}] = \log(\text{X}/\text{Y}) - \log(\text{X}/\text{Y})_{\odot}$.

clouds in the vicinity of galaxies is not typical of the general intergalactic medium (Adelberger et al. 2003). Nevertheless, these results are not very different from the value $[C/H] \sim -2.5$ at $z \sim 3$ (with scatter of about 1 dex) obtained from more direct estimates (Songaila & Cowie 1996; Rauch et al. 1997a).

7. C IV COMPONENT AND SYSTEM CLUSTERING

Previous studies of the two-point correlation function have shown that C IV components cluster strongly on velocity scales $\lesssim 200 \text{ km s}^{-1}$, with significant clustering out to a few 100 km s^{-1} more, and in some cases extending to larger scales of order $1000\text{--}10000 \text{ km s}^{-1}$ (Sargent et al. 1980; Young, Sargent, & Boksenberg 1982; Sargent et al. 1988a; Steidel 1990; Petitjean & Bergeron 1994; Rauch et al. 1996; Womble et al. 1996). The extension to larger velocities is not a general property and can be traced to a few unusually complex groups of systems (Sargent & Steidel 1987; Heisler, Hogan, & White 1989; Dinshaw & Impey 1996; Quashnock, Vanden Berk, & York 1996). Clustering similar to that observed in C IV has been measured in Mg II (Sargent, Steidel, & Boksenberg 1988b; Petitjean & Bergeron 1990; Steidel & Sargent 1992; Churchill, Vogt, & Charlton 2003). It has been suggested that the clustering signal reflects galaxy clustering, clustering of clouds within the same galactic halo, or a combination of the two. The issue is complicated by the wide disparity in velocity resolution, data quality, and sample size among the different observations. The clustering seen in metals seems to contrast with that observed in H I which in general shows no significant clustering signal (Sargent et al. 1980), or comparatively weak clustering (McDonald et al. 2000) at larger column densities (Cristiani et al. 1997). However, in H I much of the small-scale structure is obscured by unresolved blending of overlapping velocity components due to the greater thermal broadening (Fernández-Soto et al. 1996) and the often saturated absorption profiles (see Figure 3; the H I profiles shown there are selected by detection of associated C IV absorption and generally are stronger than the majority of the forest lines). We shall return to this point in the discussion below.

7.1. Two-Point Velocity Correlation Function

In Figure 14 we give velocity two-point correlation functions (TPCF) for the C IV absorbers. In the standard manner these are normalized to the expected number of pairs per bin computed for a set of random distributions in redshift space matching the individual wavelength ranges and number of C IV absorbers observed for each of the nine QSOs in the sample. The simulated randomly distributed absorbers were collated by pairwise velocity separation in 1000 realizations and compared with the distribution of velocity separations in the data to derive the correlation $\xi(\Delta v) = \{N_{\text{data}}(\Delta v)/N_{\text{random}}(\Delta v)\} - 1$, where Δv is the velocity in km s^{-1} of one cloud as measured by an observer in the rest frame of the other.

In the top panel of the figure we show the result for the 867 individual *components* of sample *sa* (without a column density threshold limit) spanning the total range $1.6 < z < 4.4$ with velocity resolution 15 km s^{-1} for $\Delta v \leq 370 \text{ km s}^{-1}$ and 20 km s^{-1} for $\Delta v \geq 370$. The data points indicate the middle of the bins, with the first bin excluded because its width is comparable to the width of the C IV components. The $\pm 1\sigma$ errors in the simulated random distribution are smaller than the data points shown. The mean redshift is $\langle z \rangle = 3.04$. Following the usual pattern, the clustering signal in our data is strong at small velocity separations while declining steeply with increasing separation. The velocity correlation length, defined as the pair separation for which $\xi(\Delta v_0) = 1$, is $v_0 = 230 \text{ km s}^{-1}$, with significant signal extending only to $\sim 300 \text{ km s}^{-1}$.

The second panel includes the same data and also adds individual results for the two subsets with $z < 3.1$ and $z > 3.1$ and respective means $\langle z \rangle = 2.51$ and 3.58 . There is a clear difference between these subsets, with stronger correlation at the lower redshifts. We need to treat this result with some caution because the data sets belonging to the individual QSOs show substantial variance in the overall *shape* of the TPCF. However, on recomputing the TPCF after removing the data from one or more of the QSOs in several different trial combinations we found that a substantial redshift variation in the sense shown is always present.

The third panel gives the result when all components of the systems exhibiting significant Lyman α absorption damping wings (see the footnotes to Tables 2–10 for approximate H I column densities) are added to sample *sa*, which we then call sample *ds+sa*. As before, we include only systems separated from the emission redshift by $\gtrsim 3000 \text{ km s}^{-1}$. This larger sample of 1020 components may be statistically less homogeneous than the original (see below). The profile is somewhat lumpier than for sample *sa*, now with $v_0 = 330 \text{ km s}^{-1}$ and significant signal extending to $\sim 400 \text{ km s}^{-1}$. The increase in Δv relative to sample *sa* is consistent with the generally large velocity widths and richness of the added highly complex systems (see Tables 2–10).

Structure similar to that for sample *ds+sa* has been found for C IV mixed samples at intermediate and high redshifts in earlier studies (Petitjean & Bergeron 1994; Songaila & Cowie 1996; Womble et al. 1996; Rauch et al. 1996). Petitjean & Bergeron fitted the shape of the TPCF by using two Gaussians, obtaining a best fit with velocity dispersions $\sigma = 109$ and 525 km s^{-1} for their full sample and $\sigma = 95$ and 450 km s^{-1} for a selected subset. With a higher resolution sample Rauch et al. found need for a three-component Gaussian fit with $\sigma = 22, 136$ and 300 km s^{-1} . Following the same procedure for our samples *sa* and *ds+sa*, we parameterized the TPCF as a multi-component Gaussian

$$\xi(\Delta v) = A_1 \exp\left(-\frac{\Delta v^2}{2\sigma_1^2}\right) + A_2 \exp\left(-\frac{\Delta v^2}{2\sigma_2^2}\right) \dots, \quad (4)$$

where A_n is the amplitude of the n^{th} component; the results are shown in Figure 14. First, for *sa*, we achieve a very good two-component fit with $\sigma_1 = 47.5 \text{ km s}^{-1}$, $A_1 = 8.2$, $\sigma_2 = 112 \text{ km s}^{-1}$, $A_2 = 10.2$. A one-component fit is ruled out and more than two components is unnecessary.

For the separate contributions in the two redshift ranges $z < 3.1$ and $z > 3.1$ we obtain fits each with a narrow component identical to that in the full sample and one broader one with $\sigma_2 = 100 \text{ km s}^{-1}$, $A_2 = 14.5$ and $\sigma_2 = 124 \text{ km s}^{-1}$, $A_2 = 6.7$, respectively. For *ds+sa* we obtain a good two-component fit with $\sigma_1 = 47.5 \text{ km s}^{-1}$, $A_1 = 10.3$, $\sigma_2 = 150 \text{ km s}^{-1}$, $A_2 = 10.5$; here the narrow component has the same width as before but a slightly larger amplitude. A three-component fit, shown in the figure, does slightly better overall, with a narrow component again identical to that in *sa* and others with $\sigma_2 = 85 \text{ km s}^{-1}$, $A_2 = 5.0$, $\sigma_3 = 170 \text{ km s}^{-1}$, $A_3 = 7.5$, although there is a slight excess in the tail of the function which is better matched by the two-component fit.

The bottom set of panels in the figure gives results for the data treated as *systems*; here the $\pm 1\sigma$ errors in the random distributions (significantly larger than for the components because of the smaller numbers) are shown by bounding thin lines. In the first panel, the result obtained using the 192 system redshifts for sample *ds+sa* with velocity resolution 500 km s^{-1} and extending to $\Delta v = 12000 \text{ km s}^{-1}$ is shown on an expanded vertical scale. The TPCF is notably flat over the whole range of separations, demonstrating clearly that the *systems* of C IV absorption lines are randomly distributed. Using the purer sample *sa* gives an almost identical result because the seven complex, mildly damped systems in sample *ds+sa* contribute to the total with equal weight to the rest of the systems (we have given the *ds+sa* case to demonstrate that this result is not specific to sample *sa*). We find the same pattern for velocity resolutions below 500 km s^{-1} as well as up to several 1000 km s^{-1} and Δv beyond 50000 km s^{-1} ; a large-scale example is in the second panel of the set.

Typically a system spans a few 100 km s^{-1} . Almost all the systems extend over less than 300 km s^{-1} and most extend less than 150 km s^{-1} (see Figure 10). Searching more finely on the smaller scale, in the third panel of the bottom set we show the TPCF for a subset of the sample in which we include only the 146 systems having velocity spread $\Delta v_{\text{sys}}(\text{C IV}) < 150 \text{ km s}^{-1}$, and use velocity resolution 150 km s^{-1} . Here again the result is indistinguishable from a random distribution.

Summarising the above results, for *components*, we observe, as others have already noted, that the detailed shape of the TPCF depends on the specific contents of the samples used, although broadly the results are similar. Our larger sample both gives better statistical definition than before and excludes QSO spectra containing known, highly untypical, complex groups of strong systems, such as for PKS 0237–233, which can dominate the correlation signal particularly at larger Δv (Heisler et al. 1989). Furthermore, by also excluding the few unusual systems containing significant Lyman α damping wings, we regard our sample *sa* as representing the “normal” great majority of C IV absorption systems. With this sample of components we obtain a more compact TPCF than in most other work and find no evidence of clustering at large Δv . Specifically, the shape of our observed TPCF does not require Gaussian components as broad as those found by Petitjean & Bergeron (1994) or Rauch et al. (1996). Churchill et al. (2003) came to a similar conclusion for Mg II absorbing clouds. Most importantly, we do not see evidence of *system* clustering in our sample *on any scale* from Δv as small as 150 km s^{-1} , where the general *components* clustering signal is still strong, out to very large separation values. We now use these results to investigate

the origin of the correlation signal.

7.2. Comparison with Galaxy Clustering

It seems that for all our component samples in the top three panels of Figure 14 the TPCF has a common narrow core component, with broader components whose characteristics depend on the precise definition of the sample. While this gives a clue to the dynamical makeup of the absorber population we should bear in mind that this is a contrived description of the TPCF (we found an exponential fit is almost as good in all cases).

For galaxies, the TPCF is a simple, fundamental statistic of the galaxy distribution. Estimations of *real-space* galaxy clustering yield a TPCF very close to power-law form over a broad range of scales (Loveday et al. 1995; Zehavi et al. 2002; Hawkins et al. 2003), although on detailed examination this is seen to be largely fortuitous (Zehavi et al. 2003). The parameters of the power-law depend on the characteristics of the sample galaxies, dominantly on their luminosity (Norberg et al. 2002). Galaxy clustering in *redshift-space*, on the other hand, is strongly affected by gravitationally induced distortions. On small scales, random peculiar velocities will cause clustering to be underestimated, while on large scales coherent infalling bulk flows will lead to an overestimate of the clustering amplitude (Kaiser 1987). Consequently, the form of the redshift-space TPCF departs considerably from a simple power-law (Zehavi et al. 2002; Hawkins et al. 2003). Large scale Λ CDM simulations show good correspondence with the observed galaxy clustering (Benson et al. 2001; Weinberg et al. 2003). In particular, these simulations predict remarkably little comoving clustering evolution from high redshifts to the present epoch (although the underlying dark matter clustering evolves strongly), agreeing well with a recent estimation of the spatial TPCF from a sample of Lyman-break galaxies at $z \sim 3$ (Adelberger et al. 2003).

Figure 15 reproduces the sample *sa* component TPCF in logarithmic form; we include the two-component form of Gaussian fit as in Figure 14. The stepped horizontal lines give the system TPCF $+1\sigma$ bin errors from the bottom set of panels of Figure 14 taken as upper limits, in to 500 km s^{-1} from the first panel then to 150 km s^{-1} from the third. We convert the velocity scale for our sample at $\langle z \rangle = 3.04$ to h^{-1} comoving Mpc using $\Omega_{\Lambda} = 0.7$, $\Omega_{\text{M}} = 0.3$ and Hubble constant h in units of $100 \text{ km s}^{-1} \text{ Mpc}^{-1}$ and show this at the top of the figure for comparison with the galaxy estimations. The two differently-scaled short-long-dashed lines are results from the large 2dF Galaxy Redshift Survey (Hawkins et al. 2003) for the galaxy real-space TPCF as fitted by the power-law $(r/r_0)^{-\gamma_r}$ with $r_0 = 5.05h^{-1} \text{ Mpc}$, $\gamma_r = 1.67$ and the corresponding redshift-space TPCF as fitted piecewise by the power-law $(s/s_0)^{-\gamma_s}$ with $s_0 = 13h^{-1} \text{ Mpc}$, $\gamma_s = 0.75$ at small scales, and $s_0 = 6.82h^{-1} \text{ Mpc}$, $\gamma_s = 1.57$ around s_0 . The dotted line is the spatial TPCF for Lyman-break galaxies from Adelberger et al. (2003); in redshift-space this should show distortion of similar character to the nearby samples.

Figure 15 shows clearly that above $\Delta v \sim 150 \text{ km s}^{-1}$ the (one-dimensional) TPCF for the C IV

components dips significantly below the TPCF found for galaxy clustering. This effect is more pronounced for the galaxy redshift-space TPCF which is the more appropriate for comparison. In addition, the lack of significant absorber *system* clustering observed above $\Delta v = 150 \text{ km s}^{-1}$ gives a very substantial deficit in clustering amplitude relative to galaxies out to at least $\Delta v \sim 1000 \text{ km s}^{-1}$.

7.3. Absorbers and Galaxies

To complete the picture we now consider observations associating absorbers with galaxies. Attempts to establish directly how metal absorption systems and galaxies are connected have focussed on searches for galaxies near the line of sight to QSOs with the same redshifts as the absorbers (Boksenberg & Sargent 1978; Bergeron & Boissé 1991; Steidel, Dickinson, & Persson 1994; Le Brun et al. 1997; Steidel et al. 2002). Most work of this kind has been done at $z \lesssim 1$ for relatively strong systems selected by the presence of Mg II and associated with gas having $N(\text{H I}) \gtrsim 10^{17} \text{ cm}^{-2}$ (*i.e.* Lyman limit systems). Steidel et al. (2002) investigated the kinematical properties of several such cases with projected impact parameter $20 \lesssim d \lesssim 100 \text{ kpc}$. The identified galaxies appear to be relatively normal spirals, with circular velocities $100 \leq v_c \leq 260 \text{ km s}^{-1}$. While the absorber characteristics are consistent with rotation being dominant also for the absorbing gas, the total range of velocities, typically 200–300 km s^{-1} , and their placing to one side of the galaxy systemic redshift, is not consistent with simple disc rotation viewed along a single sightline. (The expectation that a sightline through a galaxy at large radius would show only a small differential rotational velocity, contrary to the observed velocity spread of the absorption systems, earlier had counted against the idea that the velocity structure in the systems is due to motions associated with single galaxies (Sargent et al. 1988a).) Steidel et al. suggest that models to explain their observations require either extremely thick rotating gas layers, rotation velocities that vary with height above the extrapolated galactic plane, or a combination of both, with rotational motion dominating over radial infall or outflow even for gas well out of the galactic plane. At higher redshifts, the velocity structure of some of the strongest Mg II absorbers is suggestive of superwinds arising in actively star-forming galaxies (Bond et al. 2001) and more generally there is mounting evidence for the importance of large-scale galactic winds (Pettini et al. 2001; Adelberger et al. 2003). C IV absorption is kinematically strongly correlated with Mg II and usually extends more widely in velocity (Churchill et al. 2001; Churchill & Steidel 2002).⁹ More substantially, from a large observational sample Adelberger et al. (2003) demonstrate a close association between C IV absorption systems and Lyman-break galaxies.

⁹The kinematics of the absorbing gas observed in strongly-damped Lyman α systems (rare, metal systems for which $N(\text{H I}) \geq 2 \times 10^{20} \text{ cm}^{-2}$) similarly appears consistent with rotating thick disc geometries (Prochaska & Wolfe 1998), although not uniquely (Haehnelt, Steinmetz, & Rauch 1998; McDonald & Miralda-Escudé 1999), but there is difficulty reconciling the high ionization species with the low in the same model (Wolfe & Prochaska 2000).

7.4. Conclusions on the Identity of Metal Absorbers

In the light of observations linking Mg II and C IV absorption systems with specific galaxies close to the line of sight to the background QSO, and the fact that these galaxies have extended kinematic structure of a few 100 km^{-1} similar to the C IV systems in our samples, it seems inescapable that our velocity correlation results for the absorption *components* in sample *sa*, contrasting with the lack of *system* clustering, are entirely due to the peculiar velocities of the gas present in the outer extensions of galaxies, *not to general galaxy-galaxy clustering*. This conclusion is not changed when we substitute the component sample *ds+sa* with its bias to highly complex systems. The different broader components we find in the Gaussian fits to the shape of the TPCF in the various cases we described earlier may reflect the distribution of the more disturbed cases of outflow into the extended regions probed, while the ubiquitous narrow component may indicate underlying, more quiescent, disc-like motion.

The lack of clustering for the C IV systems means *there is no obvious observational distinction between the metal systems and strong H I systems*. Because any complex component structure in H I is largely hidden, the H I absorption lines effectively are counted as systems like the C IV systems. However, the H I lines are detected in far greater number and probe to much lower densities in the intergalactic medium, so in general do not represent the same population as the observed metal systems which are more directly associated with galaxies.

The explanation for the lack of system clustering in our C IV sample, while the systems are known to be correlated with galaxies, must simply be geometrical: the single sightline available to each background QSO, although highly extended in redshift, samples the smaller-scale galaxy population so sparsely that it is a rare occurrence for the gaseous extent of more than one galaxy to be probed in a given cluster or group. The situation for measurements of galaxy redshifts in clustering studies is quite different: here, all galaxies in the plane of the sky are included, with defined sample specifications, and the spatial variance is completely sampled three-dimensionally on all scales.

It is intriguing that in the range $\Delta v \sim 30\text{--}150 \text{ km s}^{-1}$ the C IV absorption component correlation function closely coincides with the galaxy redshift-space correlation function where this is heavily distorted by peculiar velocities (Figure 15). On our interpretation this correspondence must be fortuitous. Indeed, we find no clustering between *systems* at $\Delta v = 150 \text{ km s}^{-1}$ in the same sample.

We do not, of course, rule out the possibility of more extended correlated structures appearing when a sightline fortuitously passes along a large-scale filamentary or sheetlike structure of galaxies in a supercluster, bringing about a rich complex of absorber systems well extended in redshift, but the incidence of such occurrences must be low (Sargent & Steidel 1987; Dinshaw & Impey 1996; Qhashnock et al. 1996). Rauch et al. (1996) considered a less extreme version of such a model to explain the tail of the TPCF found in their smaller C IV sample by Hubble flow velocity extension. On the other hand, Simcoe, Sargent, & Rauch (2002) find that for the components of a limited

sample (12) of O VI-selected systems tracing the warm-hot intergalactic medium the velocity TPCF is similar to the spatial power-law form seen for galaxies, with a comoving correlation length $\sim 7h^{-1}$ Mpc. They conclude that for this population the signal is dominated by large-scale structure. C IV is also present in most of the sample of O VI absorption systems. We stress again, however, that in the present work we seek to characterize the “normal” situation obtaining for the large bulk of weak metal absorption systems in the cooler phase identified by C IV. In this respect our work is very different from large-scale studies using sparse samples of strong C IV systems. Quashnock et al. (1996) used 373 QSO sightlines having a total of 360 strong C IV absorption systems covering the redshift range 1.2–4.5 (in contrast, our sample has an average of about 20 systems per sightline). With a velocity resolution of about 600 km s^{-1} they found weak clustering, $\xi \sim 0.4$, on scales of superclusters, with significant signal contributed by groups of absorbers in only 7 of the sightlines. Quashnock & Vanden Berk (1998) extended this study to smaller scales using velocity resolution 180 km s^{-1} and a restricted sample of 260 strong C IV systems drawn from 202 sightlines, finding significant clustering of power-law form on scales of clusters and superclusters. Our sample of numerous relatively weak C IV systems in few sightlines clearly does not probe such large-scale structure. Nor, as we have seen, do our systems strongly sample galaxies within clusters. Our high velocity resolution data perform a complimentary role of finely probing the environment in the vicinity of *single* galaxies, through the properties of the components of the systems. The smooth distribution in the TPCF (Figure 15) shown by the components of the full population of systems ranging from the weakest (very simple) to the strongest (very complex), and the lack of distinction in clustering between such systems, suggest that spatially all systems are similar objects.

Finally, we consider the apparent evolution in redshift shown in the second panel in Figure 14. Although, as we have found, the comoving number density of C IV systems does not change with redshift, we shall demonstrate later in this paper that the radiation environment to which the absorbers are exposed changes markedly with redshift and is very different for the two redshift subsets used. At the lower redshifts the ionizing radiation from the background QSOs dominates, while at higher redshifts galaxies close to the absorbing clouds dominate the ionizing flux. The more diffuse metagalactic illumination of the absorbers on the one hand and the more locally confined exposure on the other, could influence the observable geometrical spread of the systems. We see in Figure 10, for example, that the distribution in system velocity spread changes with redshift. Although velocities do not simply translate to spatial distribution, the apparent evolutionary change in component clustering presumably reflects such differences.

8. EVOLVING IONIZATION BALANCE

8.1. Redshift Evolution of Ionic Ratios

In Figure 16 we show the distribution in redshift of the column density ratio Si IV/C IV for absorbers in which Si IV is accessible. As before, the obvious vertical associations are members of

the same system. In all cases we take $N(\text{C IV}) > 1 \times 10^{12} \text{ cm}^{-2}$ as an acceptance threshold.

The top left panel displays the component values for the full sample *sb*. The related panel on the right gives median values obtained over the redshift spans defined by the horizontal bars; the indicated uncertainties are 1σ bootstrap values. Unlike the single-species redshift distributions presented in §6, here we do not need to correct for multiple redshift coverage because each ionic ratio value represents an independent measure of absorber ionization *balance* (although incomplete, as we explain later). The upper limits shown in the left panel are included in the median values; the occasional high upper limit coming above the derived median does not significantly influence the accuracy of the results. It is striking that within the small uncertainties the median value of Si IV/C IV is consistent with being constant over the whole observed range $1.9 < z < 4.4$.

In the second and third sets of panels we show the component data for the subsets of *simple* and *complex* systems defined as before. For the *simple* subset there is a significant continuous fall in the median with cosmic time, by about 0.4 dex over the observed range, while the *complex* subset, again, is consistent with being constant over the range.

In the bottom panels we use sample *sb* to show total *system* ionic ratios, obtained after first separately summing the individual Si IV and C IV component values. Once again, there is no detectable change in the median over $1.9 < z < 4.4$. Although we have earlier explained the shortcomings of using total system values for ionic ratio determinations we give these in the figure for comparison with earlier work by Songaila & Cowie (1996) and Songaila (1998). These authors have argued that their observed evolution of Si IV/C IV, which shows a jump at $z \sim 3$ by at least 0.5 dex in the median, requires a sudden hardening of the ionizing background that is consistent with an abrupt reduction at that redshift in the opacity of the evolving intergalactic medium to He II ionizing photons as He II completely ionizes to He III. We have earlier reported that we have not found such a jump (Boksenberg 1997; Boksenberg et al. 2001), a result also found by Kim, Cristiani, & D’Odorico (2002), and we confirm this with the more extensive investigations here. The reason for the difference between our findings and the previous work is not clear.

Nevertheless, use simply of the ratio Si IV/C IV to measure the influence of He II ionizing radiation on the absorbers has significant limitations and we do not make any claims concerning the evolution of the ambient ionizing spectrum based on Figure 16. While the components in a given system might be expected to receive the same exposure to the metagalactic radiation, their extensive vertical distributions within systems show directly that Si IV/C IV cannot be a unique indicator of the ionizing flux. Most likely this is because of differences in density among the individual absorbers within a system. We also note that the totalled values plotted in the bottom panel have a scatter of more than an order of magnitude.

Several workers have found support more directly for high He II opacity in the intergalactic medium at $z \gtrsim 3$ (Reimers et al. 1997; Heap et al. 2000; Kriss et al. 2001; Smette et al. 2002). Schaye et al. (2000b) and Theuns et al. (2002) showed that He II reionization at $z \sim 3.5$ results in an increase by a factor 2 in the temperature of the intergalactic medium at the mean density

and found evidence for such a jump from observations of Lyman α forest lines. Bernardi et al. (2003) have claimed a sudden depression in the Lyman forest effective optical depth at $z \sim 3.2$ by $\sim 10\%$ which is consistent with He II reionization. However, analyses by McDonald et al. (2001) and Zaldarriaga, Hui, & Tegmark (2001) do not show a significant temperature change at these redshifts, although the temperatures they found are higher than expected for photoionized gas in ionization equilibrium with a cosmic background, as can be explained by gradual additional heating due to ongoing He II reionization.

Displays corresponding to the top panels in Figure 16 are given in Figure 17 for the column density ratios C II/C IV, Si II/Si IV, Si II/C II and N V/C IV, although for all but the first there is more uncertainty arising from upper limits. The median C II/C IV values show rather more variation with redshift than Si IV/C IV, with a progressive rise by ~ 0.4 dex over $z \sim 3.7$ –1.9. Si II/Si IV values show a yet steeper trend, rising by ~ 0.7 dex over this range, while the trend of Si II/C II appears quite flat, although in both cases the data are sparse. N V/C IV values indicate a rising trend from $z \sim 3.5$ to lower redshifts but there are too few data within the few narrow windows for which N V can be studied to indicate the behaviour at the higher redshifts.

Although some collective inferences might be made about the radiation environment from the data in Figures 16 and 17, the fact remains that individual ionic ratios give only partial evidence of ionization state. In following sections we use combinations of these ratios as more complete indicators with which to derive information on the evolution of the ionizing spectral energy distribution and the physical properties of the absorbers.

8.2. Redshift Evolution of Ionic Ratio Combinations

In Figure 18 we give two-dimensional column density ratio displays of Si IV/C IV : C II/C IV derived for the individual components in sample *sb* for which we can either measure or obtain an upper limit for Si IV and C II, again taking $N(\text{C IV}) > 1 \times 10^{12} \text{ cm}^{-2}$ as an acceptance threshold. In the left panels we compare our full data set for these ratios in three redshift ranges with model predictions of the Cloudy code (Ferland 1996; version 90.04) computed for one-sided illumination of a plane-parallel slab of low metallicity gas ($Z = 0.003 \times \text{solar}$) optically thin in the H I Lyman continuum ($N(\text{H I}) = 10^{15} \text{ cm}^{-2}$).¹⁰ We use a recent version of the Haardt & Madau (1996) photoionizing background kindly provided to us (Haardt 1998; see §10.1) to represent the evolving contribution of QSOs alone at redshifts $z_{HM} = 2.3, 3.0, 3.9$, appropriate for the redshift ranges of the data, and give the mean intensity at the H I Lyman limit, J_{ν_0} , for these cases in the caption to the figure. We introduce the cosmic microwave background at these redshifts to include Compton

¹⁰We use these as nominal values convenient for illustration and do not imply that they are specifically demanded by the observations. The effects of varying the properties of the absorbers are considered in §8.4.

cooling of the absorbers.¹¹ In this modelling we include solar relative metal abundances as listed in Cloudy (Grevesse & Anders 1989; Grevesse & Noels 1993), but for Si additionally use a higher value to conform with observations relating to early, low-metallicity environments. Galactic metal-poor stars show $[\text{Si}/\text{Fe}]$ extending to $\sim 0.3\text{--}0.4$ fairly uniformly over the range $-3.5 \lesssim [\text{Fe}/\text{H}] \lesssim -1$, in a common pattern with other α -elements (McWilliam et al. 1995; Ryan, Norris, & Beers 1996) and is thought to reflect the yield from Type II supernovae. Depending on the interpretation of corrections for the presence of dust there is a similar excess in damped Lyman α absorption systems (Lu et al. 1996; Vladilo 1998; Pettini et al. 2000). On the other hand, C/Fe measurements in metal-poor stars generally give approximately solar values although with considerable scatter (McWilliam et al. 1995; McWilliam 1997; Israelian, García López, & Rebolo 2000). Based on these data we take $[\text{Si}/\text{C}] = 0.4$ as a representative upper level. The recent revisions of photospheric abundance values by Holweger (2001) and Allende Prieto et al. (2002) combine to increase the Si/C solar value by 0.19 dex while uncertainties in dielectronic recombination rate coefficients for Si IV and C IV (Savin 2000; Schippers et al. 2003) could translate to a significant systematic lowering or raising of the inferred ratio as derived with Cloudy for the conditions in our photoionized absorbers. In view of the existing uncertainties we retain the nominal values in the version of the Cloudy code we have used.

Unlike the presentation in Figure 16, it is particularly striking that the data now take on a coherent appearance. Values from components in a given system now string out along a track with relatively little scatter, accomodating the different ionization states present. For the lowest range of redshifts ($z = 1.9\text{--}2.65$) the model achieves a good match to the data within the adopted Si/C bounds (interestingly, in view of the uncertainties mentioned in the previous paragraph), while towards higher redshifts there is first an upward scatter in the data ($z = 2.65\text{--}3.4$) then a substantial overall rise, by a factor ~ 3 ($z = 3.4\text{--}4.4$). We note that at the highest redshifts there are relatively more components having strong C IV ($N(\text{C IV}) > 1 \times 10^{13} \text{ cm}^{-2}$) and detected Si IV but only upper limits in C II (the open symbols with left-pointing arrows out to the low C II/C IV, or higher ionization, part of the diagram¹²), as is already indicated from the data in Figures 16 and 17. Most of the components having both Si IV and C II with only upper limits have $N(\text{C IV}) < 5 \times 10^{12} \text{ cm}^{-2}$. We illustrate separately the corresponding behaviour of the *simple* and *complex* subsets of the sample. These figures demonstrate that the components in the *simple* systems tend to populate the higher ionization regions of the diagrams while the *complex* systems have a wider range of ionization. Both subsets follow the same paths in the diagrams and the same general evolutionary behaviour with redshift, again suggesting they represent similar objects.

¹¹Compton cooling becomes significant at low densities and high redshifts but the effect is relatively small in the range of our data (see §10); the cooling timescale may be longer than the age of the Universe at the redshift of interest (Meiksin 1994). The cosmic microwave background is not included in the Haardt & Madau radiative transfer computations, which assume a fixed temperature in the ionization modelling (Haardt & Madau 1996).

¹²The significance of C II/C IV as an indicator of the ionization state (or in a more restricted sense, the density) of the absorbers in the context of our observations is explained in §8.4.

For the undifferentiated sample *sb* we show in Figure 19 corresponding displays of two other combinations of the ionic ratios. For Si II/Si IV : C II/C IV a single model fit is applicable because there is no relative abundance dependence. Indeed, the data points tend to cluster more closely together in the lowest and highest redshift panels than they do in Figure 18. At the lowest redshifts the model fits the data well. In the highest redshift interval the data generally fall below the model, while in the middle range there is increased scatter with a trend in the same sense. Again there is distinct progressive evolution in redshift in the displayed quantities. For Si II/C II : C II/C IV the model prediction gives good fits to the data points, with no obvious evolution in redshift.

Finally, in Figure 20 we show displays of N V/C IV : C II/C IV. For the model curves we again use both the solar relative abundance of N/C (upper curve) and an upper bounding value appropriate for low metallicity absorbers, reflecting the early production of nitrogen. Henry, Edmunds, & Köppen (2000) give data for C/O and N/O in H II regions and stars from which we obtain $[N/C] \sim -0.2$ at low metallicities, used as the second value in the figure. However, it should be borne in mind that for both values there is considerable uncertainty in such data. Around the solar value (where metal-sensitive secondary production of N contributes significantly) there is scatter of several tenths dex in the observations, while at low metallicity (where primary N production dominates over secondary) additional departure to considerably lower values of N/C is expected as a consequence of the relatively long time delay for the release of primary N because of its origin in lower mass stars. Indications of the latter, with downward dispersion of N relative abundance by up to 1 dex, are seen in damped Lyman α absorption systems (Pettini, Lipman, & Hunstead 1995; Lu Sargent & Barlow 1998; Centurión et al. 1998; Pilyugin 1999; Pettini et al. 2002; Centurión et al. 2003). We represent this downward dispersion by the shaded region in the figure. At the lowest redshifts, the match between the data and the QSO ionization model is not as good as in Figures 18 and 19. Nevertheless, while our data for N V are more limited than for the other species and the relationship between the data and the model is not as clear, an evolutionary trend is again evident over the whole observed redshift range. At the highest redshifts N V/C IV extends down to relatively low values indicated by upper limits only, as we have shown earlier.

It is clear from Figures 18–20 that two-dimensional analyses like those presented are necessary to make useful interpretations of the ionization properties of the absorbers. We deal with this in more detail in §10 and explore the effect of varying the spectrum of the photoionizing radiation on the various ionic ratios we have measured.

8.3. Photoionization Equilibrium or Collisional Ionization?

From the data in Figures 18–20 we see that our assumption that the absorbers are *photoionized* is well borne out by the general concordance of the observations with the shapes of the model curves, albeit with the additional evolutionary effects. It is particularly important to note that there is *no significant distinction between the broader and narrower components* in the sample, which fit equally well. This result confirms that the broader components represent highly turbulent or bulk

velocity-extended structures rather than regions at high temperature and dominantly thermally broadened.

We demonstrate this by modelling the additional effect of significant collisional heating on the ionization equilibrium. We use the lowest redshift case, $z_{HM} = 2.3$, for which the pure QSO form of metagalactic ionizing radiation background is dominant. In photoionization equilibrium, Cloudy modelling at this redshift gives mean temperatures $\lesssim 5 \times 10^4$ K in the C II/C IV range of our data; some specific examples are given later in Figure 23. In pure collisional ionization equilibrium the C IV ionization fraction strongly peaks at 10^5 K (Sutherland & Dopita 1993) and there is a peak at the same temperature in a more complicated case of a nonequilibrium radiatively cooling gas (Shapiro & Moore 1976) as discussed by Tripp et al. (2002). Such a temperature corresponds to $b \simeq 10$ km s $^{-1}$ and is already ruled out for our narrower components (see the b -value distribution given in Figure 9). In the same circumstances Si IV peaks at a slightly lower temperature: 0.8×10^5 K.

To identify the observable effects of collisional ionization, in Figure 21 we show in plots of Si IV/C IV : C II/C IV and Si II/Si IV : C II/C IV (corresponding to the top panels in Figures 18 and 19 but with extended axes) idealized models run in Cloudy at three fixed temperatures 0.8, 1.0 and 1.2×10^5 K in the presence of the same metagalactic ionizing radiation background at $z_{HM} = 2.3$ and for the same absorber parameters as defined in Figure 18. The pure photoionization equilibrium model as shown before is included for comparison. The assumed Si/C relative abundance values are adopted as in the previous figures. The collisional ionization curves terminate in the diagrams where the ionic ratios become independent of total hydrogen volume density in the model (near $n(\text{H}) = 3 \times 10^{-2}$ cm $^{-3}$). In the absence of ionizing radiation the fixed temperature collisional models at all densities give single values at these termination points.

At temperatures where collisional ionization would be dominant these models bear no overall resemblance to our observations. We can conclude that the majority of the absorbers in our samples are in photoionization equilibrium.

8.4. Effects of Changes in Absorber Parameters

In Figure 22, again using Si IV/C IV : C II/C IV and Si II/Si IV : C II/C IV, we demonstrate with our $z_{HM} = 2.3$ photoionization equilibrium model as applied in the top panels of Figures 18 and 19, how these ratios are affected by changes in metallicity, $[Z]$, and H I column density, $N(\text{H I})$. For clarity we restrict the displays here to the single value of solar Si/C relative abundance. The nominal case with $Z = 0.003 \times \text{solar}$ (*i.e.* $[Z] = -2.5$) and $N(\text{H I}) = 10^{15}$ cm $^{-2}$ is shown in thin continuous lines.

For Si IV/C IV : C II/C IV (upper panels), changes in metallicity and H I column density have little effect for $\log N(\text{C II})/N(\text{C IV}) \gtrsim -1$: significant departures from the nominal case occur only at lower C II/C IV values. Comparison with the data in the top panel of Figure 18 suggests that

most of the components in our sample have $[Z] \lesssim -1.5$ and $N(\text{H I}) \lesssim 10^{16.5} \text{ cm}^{-2}$. In contrast, $\text{Si II}/\text{Si IV} : \text{C II}/\text{C IV}$ (lower panels of Figure 22) is almost invariant to changes in metallicity and H I column density.

Figure 23 shows corresponding changes in total hydrogen volume density, $n(\text{H})$, and mean temperature within the gaseous column, $\langle T_e \rangle$, over the observed $\text{C II}/\text{C IV}$ range of our data plots at $z_{\text{HM}} = 2.3$. Increasing the metallicity leads to a reduction in temperature due to increased cooling; increasing the column density to about $N(\text{H I}) = 10^{16.5}$ raises the temperature, while above that column density $\langle T_e \rangle$ decreases. At the same time there is comparatively little change in the near-linear relationship between $n(\text{H})$ and $\text{C II}/\text{C IV}$. For a given radiation field $\text{C II}/\text{C IV}$ is thus a good indicator of the gas density (or ionization parameter). Using this, we see from the top panel in Figure 18 that the absorbers vary in density over the range $n(\text{H}) = 10^{-3.5} - 10^{-1.7} \text{ cm}^{-3}$.

For the components with Si and C b -values listed independently in Tables 2–10 (*i.e.* with $b(\text{Si})$ shown *unbracketted*: see §§3 and 4) we obtain (following Rauch et al. (1996)) an average absorber temperature of $(2.0 \pm 0.2) \times 10^4 \text{ K}$, broadly consistent with Figure 23 for intermediate to low $\text{C II}/\text{C IV}$ over which Si IV or Si II are (necessarily) relatively strong. At $z < 3.1$ and $z > 3.1$ the values are $(1.9 \pm 0.3) \times 10^4 \text{ K}$ and $(2.1 \pm 0.4) \times 10^4 \text{ K}$ respectively, showing no significant change with redshift. These values are lower than Rauch et al.’s mean of $3.8 \times 10^4 \text{ K}$, but as we have explained in §3, on the one hand we strictly include only the narrower components ($b \lesssim 10 \text{ km s}^{-1}$), and on the other, in Rauch et al.’s analysis differential blending effects in broader components may give a tendency to estimate apparently higher temperatures. We explore the temperature properties and other physical parameters of the absorbers more fully in a further paper (in preparation).

An important conclusion from the results in Figure 22 is that the systematic evolutionary effects exhibited in the ionic ratios are not caused by *changes in absorber properties*. For example, the observed trends in the ionic ratios are the opposite of those to be expected if the mean metallicity and H I column density of the absorbers increase with cosmic time. We must therefore look to evolution in the *ionizing radiation environment* to explain the observations.

9. ABSORBERS CLOSE IN REDSHIFT TO THE QSOS

For comparison with the results given in §§6 and 7, all of which use data selected to avoid the local influence of the observed background QSOs, we show in Figure 24, in similar displays, the properties of those absorbers in our sample which are in the near-vicinity of the QSOs. The data consistently conform with expectations for gas in photoionization equilibrium illuminated by a hard radiation source: C IV is substantially stronger than Si IV ; C II and Si II are relatively weak or undetected; and N V is strong and observed over the full available redshift range. For the comparisons with model ionic ratio combinations shown in the bottom set of panels, we replace the metagalactic ionizing flux with a simple power-law spectral energy distribution of the form $f_\nu \propto \nu^{-1.8}$ (Zheng et al. 1997; Laor et al. 1997; Telfer et al. 2002) with 10 times the mean background

intensity at $z_{HM} = 2.3$ to represent the dominating radiation of a local QSO, not modified by transfer processes in the intergalactic medium. Very slight differences between the two redshift intervals, barely apparent even at low C II/C IV (*i.e.* at low density), is the consequence of different Compton cooling by the microwave background.

10. EVOLVING SPECTRAL CHARACTERISTICS OF THE IONIZING RADIATION ENVIRONMENT FROM IONIC RATIO COMBINATIONS

In §8.2 we compared our observations with predictions of photoionization models of low metallicity absorbers optically thin in the H I Lyman continuum exposed to an evolving metagalactic ionizing radiation background obtained from radiative transfer computations. There we used a simple fiducial case including only QSOs as the source of the ionizing background, as in Haardt & Madau (1996) but updated (Haardt 1998). While we concluded in §8.3 that there is clear indication from these comparisons that our observations are consistent with expectations of photoionization equilibrium, there is evidently also a strong evolutionary effect not reproduced by the assumed ionizing radiation model. Below, we explore the implications of our observations for the spectral characteristics of the ionizing radiation and move to a more general form of metagalactic radiation field containing contributions from both QSOs and galaxies, each with their own evolutionary behaviour. In addition to using a standard galaxy synthesis model we also investigate the effects of a contrived galaxy spectral energy distribution.¹³

We stress that in computing the mean intensity of the metagalactic radiation all cosmically distributed sources must be included from the outset. The results for different sources cannot be added since the background radiation intensity determines the ionization balance of the clumpy intergalactic medium which in turn determines the background radiation intensity. In specific examples we also include the effects of stars in the local environments of the absorbers. To first order such contributions *can* be added incrementally if the flux in aggregate is insufficient to modify the ionization state of the general intergalactic medium significantly. However, in our application we do not imply any *addition* of sources: in effect we are simply defining *the location of the absorbers* relative to existing distributed galaxies. Thus, an isolated absorber will be exposed only to the general metagalactic radiation while an absorber located close to a galaxy will also experience a direct, possibly dominant, “proximity effect”.

¹³We acknowledge the generosity of Haardt & Madau in setting up and processing several specific cosmological radiative transfer models for us (Haardt 1998).

10.1. New Haardt & Madau Models for the Cosmic Ionizing Radiation Background Including Template Galaxies

A brief account of their revised radiative transfer computations is given in Haardt & Madau (2001). We include here a short description of the assumed QSO and galaxy source contributions. Haardt & Madau now adopt a spatially flat Λ CDM cosmology with $\Omega_\Lambda = 0.7$, $\Omega_M = 0.3$ and use $H_0 = 65 \text{ km s}^{-1} \text{ Mpc}^{-1}$.

The QSO contribution to the radiation background is based on Boyle et al.’s (2000) two-power-law blue luminosity function, with the redshift evolution of the break luminosity L_B^* following the analytical fit described in Madau et al. (1999). The assumed optical–ultraviolet spectral energy distribution is similar to that given in Haardt & Madau (1996) except in the region shortward of 1050 \AA where the form becomes $f_\nu \propto \nu^{-1.8}$, steeper than the original exponent. The extension into the X-ray region has also been revised, consistent with the X-ray data from recent spaceborne missions.

The galaxy contribution is based on the rest-frame luminosity at 1500 \AA , and is assumed to arise from a young stellar population described by a star-forming galaxy template spectral energy distribution computed from Bruzual & Charlot’s (1993) isochrone synthesis evolutionary code libraries with metallicity $0.2 \times \text{solar}$, Salpeter IMF with $M_*/M_\odot < 125$, constant star formation rate and age 0.5 Gyrs. Evolution of the star formation rate as computed in Madau et al. (1996) but with the addition of recent high redshift observations (*e.g.* Steidel et al. 1999) is used to normalize the 1500 \AA rest-frame flux of stellar radiation. The emergent ionizing flux at 912 \AA is estimated from the 1500 \AA flux through the escape fraction, f_{esc} , for Lyman limit photons, defined as the fraction of emitted 912 \AA photons that escapes the galaxy without absorption by interstellar material divided by the fraction of 1500 \AA photons that escapes (Steidel et al. 2001).

In Figure 25 we compare the rest spectral energy distributions of the new models for $f_{\text{esc}} = 0.05$ and 0.5 at the two redshifts $z_{HM} = 2.3$ and 3.9 with the simple case of QSOs alone as used in Figures 18–20. We identify these models by QG_{0.05}, QG_{0.5} and Q, respectively.

10.2. Predictions of Ionic Ratio Combinations using the New Haardt & Madau Models

We now test the revised model radiation fields against the observed evolution in our ionic ratio combinations. As before, in our Cloudy modelling we include the cosmic microwave background.¹⁴

In Figure 26 we show our Cloudy-generated results for Si IV/C IV : C II/C IV at redshifts $z_{HM} = 2.3$ and 3.9 with our low and high redshift data sets respectively covering $1.9 < z < 2.65$

¹⁴However, the change in ionization balance due to Compton cooling losses from scattering off the cosmic microwave background, which increases to higher redshifts, turns out not to be significant in the range of our data.

and $3.4 < z < 4.4$, given in Figure 18. For comparison, at each redshift we plot the results computed with both radiation models, $\text{QG}_{0.05}$ and $\text{QG}_{0.5}$. The small value of f_{esc} in the former case may be typical at our lower redshifts as indicated by observations of local and intermediate redshift star-forming galaxies (Leitherer, Ferguson, & Heckman et al. 1995; Hurwitz, Jelinski, & Dixon 1997; Deharving et al. 2001; Heckman et al. 2001) and we take the latter as representative at higher redshifts following the large value of f_{esc} obtained for Lyman-break galaxies at $z \sim 3.4$ (Steidel et al 2001). In the corresponding right panels we show the forms of these metagalactic background spectra in the frequency range effective for photoionization of the absorbers relevant to our species of interest, and identify the positions of significant ionization thresholds. Compared with model Q, the intensities are raised at energies below the He II ionization edge, over which the relatively soft galactic radiation makes its contribution, and have depressions at higher energies due to increased He II continuum opacity from resultant changes in the ionization balance of the intergalactic medium. At the higher redshifts the magnitude of these effects is proportionally greater because galaxies make up a much larger fraction of the model ionizing source population.

For our low redshift case in Figure 26 we note that for model $\text{QG}_{0.05}$ the curve traced is quite close to that for model Q and still fits the data well, but for model $\text{QG}_{0.5}$ there is a substantial rise in the curve as it progresses into the higher ionization (lower C II/C IV) region resulting in a somewhat poorer fit to the data. Thus, our data are broadly consistent with a low value for f_{esc} and a dominant QSO population. Conversely, for our high redshift data set we see that a high value for f_{esc} gives a better fit in the higher ionization region of Figure 26. Nevertheless, the overall fit remains extremely poor because the model is unable to match the data in the intermediate-to-low ionization part of the diagram.

In Figure 27 we show our corresponding model $\text{QG}_{0.05}$ and $\text{QG}_{0.5}$ results at $z_{\text{HM}} = 3.9$ for the three combinations Si II/Si IV : C II/C IV, Si II/C II : C II/C IV and N V/C IV : C II/C IV with the high redshift data sets given in Figures 19 and 20. The Si II/Si IV case shows very little change from model Q for either value of f_{esc} and again the data are poorly matched by the models. For Si II/C II both models give broadly consistent fits although, unlike the other ratios, the fit for $\text{QG}_{0.05}$ remains closer to the data, similar to model Q. The data in the N V/C IV case, being all upper limits, can be marginally accommodated by varying N/C within the permitted range for both models $\text{QG}_{0.05}$ and $\text{QG}_{0.5}$. However, $\text{QG}_{0.5}$ is favoured due to the greater reduction of the He II continuum, wherein lie the ionization edges of N IV, N V and C IV, with resultant greater suppression of N V and reduced loss of C IV.

In summary, we have found that we cannot achieve good fits to the observed ionic ratios as a function of redshift with “standard” metagalactic spectral energy distributions. It is necessary to modify these. In following sections we investigate specific spectral variations in the ionizing flux.

10.3. Effect of a Large Reduction in the He II Continuum

First, we ask whether substantial suppression of the metagalactic radiation intensity in the He II continuum as proposed by Songaila & Cowie (1996) and Songaila (1998) can improve the fit to our high redshift data for Si IV/C IV : C II/C IV (the relevant ionization potentials of the Si and C species related to the appearance and loss of Si IV and C IV straddle the He II ionization edge). As we have already shown in §8.1 this is not indicated by the behaviour of Si IV/C IV median values as a function of redshift. We now test this hypothesis by arbitrarily modifying the metagalactic radiation output spectrum, and in the left panel of Figure 28 show two shapes, a horizontal cut and a deep depression, both beginning with a drop of 4 dex at the He II edge. Although these are not self-consistently modelled constructions they serve to give a gross indication of any resultant effects. We discuss model Q but models QG_{0.05} or QG_{0.5} give similar results.

The outcomes in the right panel of Figure 28 for the two shapes differ little and show a large rise in Si IV/C IV in the high ionization region similar in form to that found in Figure 26 but more extreme, and evidently go no closer to achieving a fit in the intermediate-low ionization range of the data. It is clear that this two-dimensional display of ionic ratios has only limited value as an indicator of He II continuum opacity. Moreover, from the disposition of the data and upper limits in Figure 28 it can be seen why simply using the Si IV/C IV ratio, as in Figure 16, is not a useful tool for this purpose.

In Figure 29 we show corresponding results for the other high redshift ionic ratio combinations as before. Si II/Si IV : C II/C IV shows very little change from the unmodified model Q for either of the cases and clearly is not sensitive to He II continuum suppression. Si II/C II : C II/C IV does change markedly relative to the model Q result and also to those for the QG models in Figure 27, rising higher to give an almost horizontal curve, inconsistent with the trend of the data. For N V/C IV : C II/C IV, because of the great reduction of the He II continuum, the model results in Figure 29 are significantly lowered and consequently are consistent with the data upper limits.

The results, particularly for Si IV/C IV : C II/C IV and Si II/Si IV : C II/C IV, show that modifications in the He II opacity alone do not explain our high redshift data, although the rise in Si IV/C IV in the higher ionization region of the diagram is helpful in accounting for the points with C II upper limits, noted in §8.2. As we have shown in §8.4, increasing the absorber metallicity or H I column density can have a similar effect.

10.4. Template Galaxies Local to the Absorbers

Next, in view of our conclusion in §7 that the absorbers in our sample are regions located in the outer extensions of galaxies, we attempted to account for our high redshift observations by augmenting the metagalactic background radiation with radiation from local stellar sources. As we have explained, in effect this is a redefinition of the location of the absorber, not addition of

more sources; thus, a large flux at the absorbers from such localized sources will not violate limits on the metagalactic radiation intensity defined by the H I proximity effect (Scott et al. 2000). For a local component we applied the intrinsic galaxy template spectral energy distribution used for the dispersed galaxies in the new Haardt & Madau QG models, but now not modified by passage through the intergalactic medium. For ease of reference we use the mean intensity at the Lyman limit for model Q at $z_{HM} = 3.9$ ($J_{\nu_0} = 1.6 \times 10^{-22}$ erg s $^{-1}$ cm $^{-2}$ Hz $^{-1}$ sr $^{-1}$) as the “unit” of mean intensity at the H I ionization edge and scale by factor f_{loc} in defining the relative contribution at the absorber of the radiation that has *escaped* from the assumed local galaxy. For the actual metagalactic contribution we used the model Q and QG cases in different trials with $f_{loc} = 1q$ – $100q$ (we add “ q ” to indicate that this is a multiplier of the pure QSO background case). For Si IV/C IV : C II/C IV we again obtained no better than different degrees of progressive rise into the higher ionization region similar in form to those shown in Figure 26.

In passing, we note that simply changing the *intensity* of the ionizing spectral energy distribution at the boundary of an optically thin absorber in photoionization equilibrium makes no substantial difference to the character of our ionic ratio combination diagrams: it requires suitable alterations in *spectral shape*, by means of a contribution that spectrally overwhelms the QSO contribution to the background over 1–4 Ryd, to bring about the relative changes in the ratios of the form that we are seeking.

We conclude that in both the cosmologically distributed and the locally confined situations, the assumed form of the synthesized galaxy spectrum adopted in the new models is not able to account for the observed behaviour of our metal line ratios at high redshifts.

10.5. Contrived Stellar Sources Local to the Absorbers

The general lack of concordance of the models with much of our data at high redshift is not surprising. The synthesized galaxy model that is assumed in the above discussion must be a gross approximation in its description of the emergent ionizing flux below 912 Å, our region of interest. There are indeed large uncertainties in modelling the properties of the hot star population, both in the definition of evolutionary tracks and in treating the atmospheres (Stasińska & Schaerer 1997; Crowther 2000; Kewley et al. 2001; Pauldrach, Hoffmann, & Lennon 2001; Smith, Norris, & Crowther 2002). The Bruzual & Charlot libraries use the Kurucz atmospheres given in the compilation of Lejeune, Cuisinier, & Buser (1997) (to $T_{\text{eff}} = 50,000$ K) which ignore non-LTE effects such as metallicity-dependent wind outflows or departures from plane-parallel geometry. While other synthesis models are available which give somewhat more emphasis to the treatment of the hot star population (Fioc & Rocca-Volmerange 1997; Leitherer et al. 1999; Smith et al. 2002) the scarcity of corroborating observations at short wavelengths and in metal-poor hot, massive stars compounds the uncertainty. The escape fraction, itself an uncertain quantity, gives an overly-simplistic representation of the form of self-absorption (grey, in a region where it is likely to be strongly dependent on wavelength). Moreover, the star formation rate is likely to be varying

(Bruzual & Charlot 1993; Leitherer et al. 1999; Kolatt et al. 1999). Because of the short lives of massive stars such variation is greatly amplified in the far ultraviolet and, to maintain a high average luminosity, the duty cycle must be high; accordingly, while a constant star formation rate may be a good approximation at longer wavelengths this may be too simplistic at the short wavelengths of interest here.

To investigate what combination of stellar spectral features can achieve a closer match to the observations we sought examples from available hot stellar atmosphere calculations which could serve as local sources. Good fits to the data were obtained with selected models from the range of Kurucz (1979) line-blanketed, LTE, plane-parallel, static atmospheres of solar metallicity readily available within the Cloudy code. In Figure 30 we show for Si IV/C IV : C II/C IV the predictions of a model star of effective temperature 45,000 K and $\log g = 4.5$ (we identify this contrived “galaxy” by the letter A) taken in combination with the model Q background (and the cosmic microwave background), for which we achieve a good match to the observed data points with $f_{\text{loc}} = 25q$. This combination model is identified by Q[A₂₅], with the local component indicated bracketted and the metagalactic, unbracketted. As can be seen in the figure, relative to the model Q background, the locally-enhanced spectrum has a hump just beyond the Si III ionization edge¹⁵ and a substantial dip at the C III edge, which together serve to increase the Si IV/C IV ratio.¹⁶

Figure 31 contains corresponding results for the other ionic ratio cases. For Si II/Si IV : C II/C IV use of the model Q[A₂₅] radiation environment now begins to approach a match to the data. On the other hand, for Si II/C II : C II/C IV there is a slight departure relative to the well-fitting model Q but the result remains consistent with most of the data. The upper limit values for N V/C IV : C II/C IV again can be formally accomodated within the wide permissable range in N/C.

Corresponding stellar models of 40,000 K and 50,000 K are less effective. We do not claim that the specific 45,000 K stellar model is physically correct or uniquely valid, as our remarks above imply, but merely that the character of its ionizing spectrum has features of the required form. A variety of models from other libraries, including stars of lower metallicity, also approach a match to the data. While we cannot precisely define stellar populations, it is evident that at high redshifts the observed rise in Si IV/C IV in the range of intermediate-low ionization and the lowering of Si II/Si IV can be explained by a radiative contribution with *stellar* characteristics which dominate in the ionizing range between the H I and He II ionization edges.

¹⁵Levshakov et al. (2003) arbitrarily enhanced the intergalactic He II $\lambda 304$ recombination emission feature present in the Haardt & Madau (1996) metagalactic background spectrum by a factor ~ 4 as a device to fit their observed ionic column densities in an absorption system near $z = 3$. To explain such enhancement they suggest the existence of strong intrinsic $\lambda 304$ line emission in the distributed QSOs. This universal component would be incompatible with our data at $z = 1.9$ – 3.4 .

¹⁶Quantitatively this is not as straightforward as it appears because the photoionization cross sections are effective over quite extensive energy ranges (Verner et al. 1996). The spectral changes also influence the C II/C IV ratio.

Although it is usefully indicative, $Q[A_{25}]$ strictly is not a self-consistent model because the totality of “local galaxies” should equate to distributed galaxies as sources contributing to the metagalactic radiation background, which is not the case in this approximation. At the least, there should be a depression in the He II continuum relative to model Q similar to those shown by the QG models used in Figure 26. We improve on this in the next section.

10.6. Contrived Galaxy Model for Metagalactic Sources

We now investigate a model in which the distributed population of Bruzual & Charlot template galaxies contributing to the metagalactic ionizing radiation background contained in the Haardt & Madau QG models shown in Figure 25 is replaced by a population of “galaxies” contrived from the single Kurucz 45,000 K stellar model that was used in the previous section, with a *source* flux scaling at the H I ionization edge relative to the QSOs by factor f_{met} where as before this quantifies the total ionizing radiation that has *escaped* from the galaxies (Haardt 1998). A model with $f_{\text{met}} = 10Q$ (“Q” indicates this is a multiplier of the QSO *source* flux), QA_{10} , which provides a reasonable match to the data in the case of Si IV/C IV : C II/C IV is shown in the top panels of Figure 32. However, for this model $J_{\nu_0} = 1.8 \times 10^{-21} \text{ erg s}^{-1} \text{ cm}^{-2} \text{ Hz}^{-1} \text{ sr}^{-1}$ which probably exceeds the mean intensity of the metagalactic background averaged over the range $3.4 < z < 4.4$ of our data (Scott et al. 2000).

Accordingly, in the middle panels we show a match for an arbitrary parallel case with $f_{\text{met}} = 3Q$, having $J_{\nu_0} = 6.6 \times 10^{-22} \text{ erg s}^{-1} \text{ cm}^{-2} \text{ Hz}^{-1} \text{ sr}^{-1}$, consistent with H I proximity effect measurements (Scott et al. 2000) (the spectral energy distribution for this metagalactic component is shown by the faint line in the figure), now augmented by local radiation again represented by the same hot star “galaxy” model, with $f_{\text{loc}} = 15q$. We call this model $QA_3[A_{15}]$. The combined mean intensity at the absorbers is $J_{\nu_0} = 3.0 \times 10^{-21} \text{ erg s}^{-1} \text{ cm}^{-2} \text{ Hz}^{-1} \text{ sr}^{-1}$. This model gives a somewhat better fit to the observed data points than does QA_{10} but tends not to accomodate the points with upper limits in C II quite so well because, as we have seen before, the lower suppression of the metagalactic radiation in the He II continuum produces less rise in the theoretical curve.

However, it is expected that there would be significant variation in the local ionizing environments from absorber to absorber which in aggregate will broaden the range of model parameters and generally lead to better overall fits to the data. In recognition of this likely cosmic variance, in the bottom panels we extend this model by showing bounds for the range of local source contributions of mean intensity $f_{\text{loc}} = 3q\text{--}25q$, identified as models $QA_3[A_3]$ and $QA_3[A_{25}]$, while respectively using $[\text{Si}/\text{C}] = 0$ and 0.4 for the absorbers, which better encompass the data. We recall that the relatively high ultraviolet opacity of the intergalactic medium at high redshifts means that the metagalactic background becomes more dominated by the closer sources of the distributed population (Haardt & Madau 1996) and this gives further cause for variance in the radiation environment

of the absorbers.¹⁷

Figure 33 shows results for the other ionic ratios corresponding to the bottom panel of Figure 32. Si II/Si IV : C II/C IV follows a similar trend to that noted for model Q[A₂₅] in Figure 31; further improvement still is needed. Si II/C II : C II/C IV is marginally consistent with the data. We note as before that the depression in the He II continuum tends to reduce N V/C IV.

10.7. Addition of a Stellar He I Ionization Edge

Here we aim to improve the fits for Si II/Si IV : C II/C IV and Si II/C II : C II/C IV by appropriately modifying the spectral shape of the radiation incident on the absorbers to enhance the ionization of Si II relative to C II, C IV and Si IV, thus preferentially reducing Si II/Si IV and Si II/C II. We note that the ionization potentials of C II and He I, 24.376 eV and 24.581 eV respectively, nearly coincide. Main sequence stars cooler than $\sim 35,000$ K show an intrinsic large He I edge and rapidly falling energy to shorter wavelengths relative to hotter stars; these are appropriate characteristics with which to produce the desired ionization effects. In the upper panels of Figure 34 we use as a baseline the same model containing distributed and local contrived hot star galaxies with $f_{\text{met}} = 3Q$, $f_{\text{loc}} = 15q$ as shown in the lower two panels of Figure 32 and add a cooler local stellar component, B, in the form of a synthetic galaxy spectrum obtained with the Starburst99 facility (Leitherer et al. 1999) using a Salpeter IMF, metallicity $0.2 \times \text{solar}$, $M_*/M_\odot < 20$, and constant star formation rate, with scaling $f_{\text{loc}} = 50q$. We identify this model by QA₃[A₁₅B₅₀]. The local (bracketted) A and B components together represent the combined spectral characteristics of a *single* synthetic galaxy. The total mean intensity at the absorbers is $J_{\nu_0} = 1.1 \times 10^{-20} \text{ erg s}^{-1} \text{ cm}^{-2} \text{ Hz}^{-1} \text{ sr}^{-1}$. Comparison with Figure 32 shows that the addition of component B leaves the Si IV/C IV : C II/C IV fit almost unaffected. In the lower panels of Figure 34 is the same case, but as before representing bounds in cosmic variance, with the two local stellar source components A and B scaled respectively by $f_{\text{loc}} = 5q$, $20q$ and $f_{\text{loc}} = 25q$, $200q$, giving models QA₃[A₅B₂₀] and QA₃[A₂₅B₂₀₀]. The respective total mean intensities at the absorbers are $J_{\nu_0} = 5.3 \times 10^{-21}$ and $3.5 \times 10^{-20} \text{ erg s}^{-1} \text{ cm}^{-2} \text{ Hz}^{-1} \text{ sr}^{-1}$. Again, for the absorbers in these bounding cases we have separately used $[\text{Si}/\text{C}] = 0.0$ with QA₃[A₅B₂₀] and $[\text{Si}/\text{C}] = 0.4$ with QA₃[A₂₅B₂₀₀]. The points with C II upper limits are better accommodated here than in the equivalent case shown in Figure 32. The results using this case for the other ionic ratios are given in Figure 35. The fits for Si II/Si IV : C II/C IV and Si II/C II : C II/C IV show considerable improvement over those in Figure 33 and N V/C IV : C II/C IV remains a good fit to the data.

The heavy dotted line in the lower right panel of Figure 34 is the result of using model QA₃[A₂₅B₂₀₀] with absorbers of metallicity $[Z] = -1.5$ coupled with the solar value $[\text{Si}/\text{C}] = 0.0$.

¹⁷This horizon effect can be seen in Figure 21 from the width of the redshift-smeared intergalactic He II $\lambda 304$ emission spike which becomes narrower with increasing redshift.

This does not increase the ionic model boundaries for Si IV/C IV : C II/C IV but indicates considerable further improvement for Si II/Si IV : C II/C IV and Si II/C II : C II/C IV, as shown in Figure 35, which now give excellent fits to the data for this radiative model.

Once again, we do not claim that the combination radiative model used in Figures 34 and 35 is physically correct, only that the ionizing spectra can give a good collective fit to all our ionic ratio diagrams. Similar synthesis results producing a significant He I edge can be obtained for episodic starburst galaxies with more conventional upper M_*/M_\odot . Like model Q[A₂₅] (Figure 30), the model used here is not fully self-consistent because of the incomplete match between the metagalactic and local radiative contributions. However, the approximation is far closer here and the local contribution, with the key spectral characteristics, is more dominant.

An important conclusion can be drawn from the broad similarity between the model QA₃ metagalactic background spectrum with He II continuum depression, as shown in Figures 32 and 34, and the corresponding model QG_{0.5} in Figure 26. This indicates that the contrived metagalactic background we consider in our models requires a *high escape fraction* for the ionizing radiation from the “galaxies” which is comparable with the value $f_{\text{esc}} = 0.5$ used for the template galaxies. This is true because the specific spectral details required to explain the observed *ionic ratios* we aim to match are not significant for deducing the gross ionization state of the intergalactic medium.

We go no further in attempting to model the radiative environment or absorber properties. We can conclude that the observed high redshift ionic ratios collectively can be well explained by a metagalactic ionizing radiation background from distributed QSOs and galaxies of specific ionizing spectral energy distribution, with the absorbers placed in the close vicinity of these galaxies such that the local galactic radiation received strongly dominates over the metagalactic radiation.

Finally, in Figure 36 we demonstrate that our low redshift data *cannot* be fitted with the dominant stellar contributions deduced at high redshift. In this figure we substitute the QSO source flux at $z_{HM} = 2.3$ but otherwise use the same stellar source quantities as in the lower panel of Figure 34. While galactic objects must be present at low redshift, the indication is that the radiative escape fraction in the Lyman continuum is small, less than a tenth of that we demand at high redshift, and possibly that star formation is considerably less active.

Our demonstration of the need for a significant efflux of ionizing radiation from galaxies at high redshifts supports the detection of emergent Lyman continuum radiation in Lyman-break galaxies at $z \sim 3.4$ reported by Steidel et al. (2001).¹⁸ Clarke & Oey (2002) and Fujita et al. (2002) discuss specific effects of repeated supernova explosions giving enhanced escape of ionizing radiation from galaxies, effective at high redshifts. This may well be the case for the galaxies related to the high redshift C IV absorbers. Adelberger et al. (2003) stress the role of supernovae-driven superwinds

¹⁸Giallongo et al. (2002) using a much smaller data set and Fernández-Soto, Lanzetta, & Chen (2003) employing a method based on imaging photometry of galaxies find average limits several times lower than Steidel et al.’s detection (although the large uncertainty at $z > 2.85$ in Fernández-Soto et al.’s estimate permits a large escape fraction).

in their extensive study of the local gaseous environment of Lyman-break galaxies.

10.8. Distance of the Absorbers from the Galaxies

We now enquire whether the required mean intensities give realistic separations of the absorbers from plausible local sources. We do this by assuming an L^* galaxy with $f_{\text{esc}} = 0.5$ and move it to proper distances d from an absorber such that it radiatively matches the J_{ν_0} values deduced for the *local* component of the ionizing radiation field. These local values range from $J_{\nu_0} = 4.7 \times 10^{-21}$ to $3.4 \times 10^{-20} \text{ erg s}^{-1} \text{ cm}^{-2} \text{ Hz}^{-1} \text{ sr}^{-1}$ in the model shown in the lower panels of Figure 34. We take $0.5 \times 10^{29} \text{ erg s}^{-1} \text{ Hz}^{-1}$ at the H I Lyman limit as a working value for the flux of escaped galactic radiation (Steidel et al. 1999) and find $d = 31\text{--}85 \text{ kpc}$ as the implied distance range for the absorbers. It is encouraging that the result is consistent with the observed separations of such absorbers and nearby galaxies (Churchill et al. 2001; Steidel et al. 2002; Churchill & Steidel 2002; Adelberger et al. 2003) and with our conclusions in §7. For galaxies fainter than L^* these distances accordingly reduce. In consequence, there is little room also to reduce significantly the adopted escape fraction.

11. SUMMARY

From high resolution spectral observations of nine QSOs we have compiled a large sample of metal-line systems identified as C IV absorbers outside the Lyman forest in the redshift range $1.6 \lesssim z \lesssim 4.4$ and include Si IV, C II, Si II and N V in these where available. By Voigt profile-fitting procedures we find we can closely represent these multi-phase systems as complexes of co-existing “single-phase-ionization” component regions. We obtain column densities or upper limits for individual components of each species, with Doppler parameters for C. With these we study number distributions, number densities, total ion column densities, kinematic properties and the ionization state of the absorbers and trace their evolution in redshift. We arrive at the following principal conclusions:

1. With decreasing redshift, C IV *component* column density and Doppler parameter number distributions, *system* column density number distribution, and differential column density distributions of *components and systems*, remain almost constant while *system* velocity spreads tend to increase.

2. The C IV system number density shows no cosmological evolution but there is mild evolution in the total population column density (which, however, obtains only in the more complex systems), indicating increasing column density per average system with cosmic time. We find a mean C IV comoving mass density $\langle \Omega_{\text{C IV}} \rangle = (3.8 \pm 0.7) \times 10^{-8}$ (1σ uncertainty limits; spatially flat Λ CDM cosmology with $\Omega_{\Lambda} = 0.7$, $\Omega_{\text{M}} = 0.3$ and $h = 0.71$), in broad agreement with Songaila (2001; 2002). Si IV presents a somewhat similar picture, while the other ions change more substantially with

redshift, heralding changes in ionization state.

3. Estimations at high and low redshift of the carbon cosmological mass density using ionization fractions from our data, relative to the hydrogen mass density in the Lyman forest based on Ω_b from the CMB, yield $[C/H]_{\langle z \rangle=4.0} \geq -3.11^{+0.14}_{-0.19}$ and $[C/H]_{\langle z \rangle=2.1} \geq -2.64^{+0.15}_{-0.22}$, suggesting a rise by a factor ~ 3 . Relating the hydrogen mass density more directly to regions containing the C IV absorbers our values for $[C/H]$ become $\gtrsim -2.2$ at $\langle z \rangle = 4.0$ and $\gtrsim -2.0$ at $\langle z \rangle = 2.1$, now suggesting a constant metallicity of carbon.

4. The C IV components exhibit strong clustering out to velocity separations $\lesssim 300 \text{ km s}^{-1}$ for our prime statistical sample but there is no clustering signal for *systems* on any scale from 150 km s^{-1} out to 50000 km s^{-1} . Neither of these (one-dimensional) distributions shows similarities with (three-dimensional) galaxy clustering. Contrary to some previous claims we argue that the results are entirely due to the peculiar velocities of gas present in the outer extensions of galaxies for which we adduce other evidence.

5. We find no change in the component or system median column density ratio Si IV/C IV with redshift and particularly no large change near $z = 3$, contrary to previous observations coupled with claims that this can indicate the onset of complete reionization of He II. Other ionic ratios do vary (continuously) with redshift but we show that these all are only partial indicators of ionization state.

6. Using combinations of ionic ratios we demonstrate that the vast majority of absorbers are in photoionization equilibrium, not collisionally ionized.

7. Our data support the presence in the absorbers of a range in relative abundance $[Si/C] \sim 0.0\text{--}0.4$, consistent with α -element enhancement in galactic metal-poor stars.

8. We observe substantial evolution in redshift in specific combinations of ionic ratios, as follows:

9. At $z \lesssim 2.65$ we find that QSOs dominate the metagalactic ionizing radiation background and that contributions from galaxies have minimal effect. This requires a low escape fraction for ionizing radiation from galaxies, $f_{\text{esc}} \lesssim 0.05$, consistent with other observations.

10. At $z \gtrsim 3.4$ we find that neither QSOs as dominant contributors to the metagalactic background, nor a high opacity in the He II continuum, can explain the observed ionic ratios. Between $z = 2.65$ and $z = 3.4$ there is evident transition in the ionization properties of the absorbers, with large scatter.

11. In the presence of the QSO population, we can match our highest redshift observations well by the addition of a dominant contribution from galaxies with specific spectral characteristics in the energy range 1–4 Ryd, although not by standard stellar population synthesis models.

12. With the specific spectral features required to explain the observations the mean intensity at the absorbers substantially exceeds the limit imposed by the proximity effect (Scott et al. 2000)

if all the flux were contributed by distributed galaxies and QSOs. Accordingly, we conclude that the absorbers must be in the locality of the galaxies such that the local galactic radiation received strongly dominates over the metagalactic radiation, consistent with our independent conclusion from clustering properties.

13. At these high redshifts such sources require a much higher escape fraction than at our lowest redshift interval, supporting the detection of emergent Lyman continuum radiation in Lyman-break galaxies at $z \sim 3.4$ reported by Steidel et al. (2001).

14. Although the ionic ratio combinations basically are sensitive only to the *shape* of the spectral energy distribution we find from comparison with the adopted QSO contribution to the ionizing background that the resultant mean intensity of the radiation received from the dominant local galaxy contribution is consistent with observed separations from galaxies if $f_{\text{esc}} \gtrsim 0.5$.

We are greatly indebted to Tom Barlow for the initial data reduction, Bob Carswell for providing VPFIT and being so unstinting with his time for schooling, advice and assistance, Francesco Haardt with Piero Madau for their generosity in providing many new computations of radiative transfer models for the metagalactic background radiation and for help and discussions, Gary Ferland for providing Cloudy and related advice, David Valls-Gabaud and Roderick Johnstone for their considerable help with the use of Cloudy, Robert Lupton for advice and provision of a new facility within SM, Bob Abraham and Rob Simcoe for kindly providing analysis software, and Max Pettini, Samantha Rix, Paul Crowther, Martin Haehnelt, Stephen Smartt, Christopher Tout, Michael Irwin, George Efstathiou and Michael Murphy for assistance and helpful discussions. We also thank the Keck Observatory staff for their assistance with the observations. Finally, we extend special thanks to those of Hawaiian ancestry on whose sacred mountain we are privileged to be guests. Without their generous hospitality, the observations presented herein would not have been possible. A.B. gratefully acknowledges support from The Leverhulme Trust and from PPARC. W.L.W.S has been supported by NSF grants AST-9900733 and AST-0206067. M.R. is grateful for support from the NSF through grant AST-0098492 and from NASA through grant AR-90213.01-A.

REFERENCES

- Adelberger, K., L., Steidel, C., C., Shapley, A., E., & Pettini, M. 2003, ApJ, 584, 45
- Allende Prieto, C., Lambert, D. L., & Asplund, M. 2002, ApJ, 573, L137
- Bajtlik, S., Duncan, R. C., & Ostriker, J. P. 1988, ApJ, 327, 570
- Barlow, T. A., & Sargent, W. L. W. 1997, AJ, 113, 136
- Bechtold, J., Weymann, R. J., Lin, Z., & Malkan, M. A. 1987, ApJ, 315, 180
- Benson, A. J., Frenk, C. S., Baugh, C. M., Cole, S., & Lacey, C. G. 2001, MNRAS, 327, 1041

- Bergeron, J., & Boissé, P. 1991, *A&A*, 243, 344
- Bergeron, J., & Stasińska, G. 1986, *A&A*, 169, 1
- Bernardi, M., et al. 2003, *AJ*, 125, 32
- Bianchi, S., Cristiani, S., & Kim, T.-S. 2001, *A&A*, 376, 1
- Boksenberg, A. 1997, *Structure and Evolution of the Intergalactic Medium from QSO Absorption Line Systems*, P. Petitjean, & S. Charlot, Edition Frontieres, 85
- Boksenberg, A., & Sargent, W. L. W. 1978, *ApJ*, 220, 42
- Boksenberg, A., Sargent, W. L. W., & Rauch, M. 2000, *The Birth of Galaxies*, Proceedings of the Xth Rencontres de Blois, June 28–July 4 1998, B. Guiderdoni, F. R. Bouchet, T. X. Thuân, J. T. T. Vân, The Gioi Publishers, Vietnam, 429
- Bond, N. A., Churchill, C. W., Charlton, J. C., & Vogt, S. S. 2001, *ApJ*, 562, 641
- Boyle, B. J., Griffiths, R. E., Shanks, T., Stewart G. C., & Georgantopoulos, I. 1993, *MNRAS*, 260, 49
- Bruzual, A. G., & Charlot, S. 1993, *ApJ*, 405, 538
- Carswell, R. F., Webb, J. K., Baldwin, J. A., & Attwood, B. 1987, *ApJ*, 319, 709
- Carswell, R. F., Webb, J. K., Cooke, A.J., & Irwin, M.J. 2002, Institute of Astronomy, University of Cambridge, <http://www.ast.cam.ac.uk/~rfc/vpfit.html>
- Cen, R., & Simcoe, R. A. 1997, *ApJ*, 483, 8
- Cen, R., Miralda-Escudé, J., Ostriker J. P., & Rauch, M. 1994, *ApJ*, 437, L9
- Centurión, M., Bonifacio, P., Molaro, P., Vladilo, G. 1998, *ApJ*, 509, 620
- Centurión, M., Molaro, P., Vladilo, G., Pèroux, C., Levshakov, S. A., D’Odorico, V. 2003, *astro-ph/0209256*, *A&A*, submitted
- Chaffee, F. H., Foltz, C. B., Bechtold, J., & Weymann, R. J. 1986, *ApJ*, 301, 116
- Churchill, C. W., & Steidel, C. C. 2002, *astro-ph/0209256*, *The IGM/Galaxy Connection*, conference held in Boulder, Colorado, August 8–10 2002, in press
- Churchill, C. W., Vogt, S. S., & Charlton, J. C. 2003, *AJ*, 125, 98
- Churchill, C. W., Mellon, R. R., Charlton, J. C., Jannuzi, B. T., Kirhakos, S., Steidel, C. C., & Schneider, D. P., 2001, *ApJ*, 562, 641
- Clarke, C. & Oey, M. S. 2002, *MNRAS*, 337, 1299

- Cooke, A. J., Espey, B., & Carswell, R. F. 1997, MNRAS, 284, 552
- Cowie, L. L., Songaila, A., Kim, T. -S., & Hu, E. M. 1995, AJ, 109, 1522
- Cristiani, S., D’Odorico, S., D’Odorico, V., Fontana, A., Giallongo, E., & Savaglio, S. 1997, MNRAS, 285, 209
- Croft, R. A. C., Hernquist, L., Springel, V., Westover, M., & White, M. 2002, astro-ph/0204460, MNRAS, submitted
- Crowther, P. A. 2000, A&A, 356, 191
- Davé, R., & Tripp, T. M. 2001, ApJ, 553, 528
- Deharving, J. -M., Buat, V., Brun, V. L., Milliard, B., Kunth, D., Shull, J. M., & Gry, C. 2001, A&A, 375, 805
- Dinshaw, N., & Impey, C. D. 1996, ApJ, 458, 73
- Donahue, M., & Shull, J. M. 1987, ApJ, 323, L13
- Ellison, S. L., Songaila, A., Schaye, J., & Pettini, M. 2000, AJ, 120, 1175
- Ferland, C. J. 1996, *Hazy I, Brief Introduction to Cloudy 90*, University of Kentucky, Department of Physics and Astronomy Internal Report
- Fernández-Soto, A., Lanzetta, K. M., & Chen, H.-W. 2003, astro-ph/0303286, MNRAS, submitted
- Fernández-Soto, A., Lanzetta, K. M., Barcons, X., Carswell, R. F., Webb, J. K., & Yahil, A. 1996, ApJ, 460, L85
- Fioc, M., & Rocca-Volmerange, B. 1997, A&A, 326, 950
- Fujita, A., Martin C., Low, M. -M. M., & Abel, T. 2002, astro-ph/0208278, ApJ, submitted
- Giallongo, E., Cristiani, S., D’Odorico, S., & Fontana, A. 2002, ApJ, 568, L9
- Giroux, M. L. & Shull, J. M. 1997, AJ, 113, 1505
- Grevesse, N., & Anders, E. 1989, *Cosmic Abundances of Matter*, AIP Conference Proceedings 183, C. J. Waddington, New York:AIP, 1
- Grevesse, N., & Noels, A. 1993, *Origin & Evolution of the Elements*, N. Prantzos, E. Vangioni-Flam, & M. Casse, Cambridge University Press, 15
- Haardt, F. 1998, private communications from 1998 to 2000
- Haardt, F., & Madau, P. 1996, ApJ, 461, 20

- Haardt, F., & Madau, P. 2001, astro-ph/0106018, XXXVI Rencontres de Moriond, 2001, to be e-published
- Haehnelt, M. G., Steinmetz, M., & Rauch, M., 1998, ApJ, 495, 647
- Haehnelt, M. G., Madau, P., Kudritzki, R., & Haardt, F. 2001, ApJ, 549, L151
- Hawkins, E. et al. 2003, astro-ph/0212375, MNRAS, submitted
- Heap, S. R., Williger, G. M., Smette, A., Hubeny, I., Sahu, M. S., Jenkins, E. B., Tripp, T. M., & Winkler, J. N. 2000, ApJ, 534, 69
- Heckman, T. M., Sembach, K. R., Meurer, G. R., Leitherer, C., Calzetti, D., & Martin, C. L. 2001, ApJ, 558, 56
- Heisler, J., Hogan, C. J., & White, S. D. M. 1989, ApJ, 347, 52
- Henry, R. B. C., Edmunds, M. G., & Köppen, J. 2000, ApJ, 541, 660
- Hernquist, L., Katz, N., Weinberg, D.II., & Miralda-Escudé, J. 1996, ApJ, 457, L51
- Holweger, H. 2001, *Solar and Galactic Composition: A Joint SOHO/ACE Workshop*, AIP Conference Proceedings 598, R. F. Wimmer-Schweingruber, New York:AIP, 23
- Hurwitz, M., Jelinski, P., & Dixon, W. v. D. 1997, ApJ, 481, L31
- Israelian, G., García López, R. J., & Rebolo, R. 2000, *The Chemical Evolution of The Milky Way: Stars versus Clusters*, F. Matteucci, & F. Giovannelli, Vulcano, Italy, September 20-24 1999, 35
- Kaiser, N. 1987, MNRAS, 227, 1
- Kewley, L. J., Dopita, M. A., Sutherland, R. S., Heisler, C. A., & Trevena, J. 2001, ApJ, 556, 121
- Kim, T., Cristiani, S., & D’Odorico, S. 2002, A&A, 383, 747
- Kolatt, T. S., Bullock, J. S., Somerville, R. S., Sigad, Y., Jonsson, P., Kravtsov, A. V., Klypin, A. A., Primack, J. R., Faber, S. M., Dekel, A. 1999, ApJ, 523, L109
- Kriss, G. A., et al. 2001, Science, 293, 1112
- Kurucz, R. L., 1979, ApJS, 40, 1
- Laor, A., Fiore, F., Elvis, M., Wilkes, B. J., & McDowell, J. C. 1997, ApJ, 477, 93
- Le Brun, V., Bergeron, J., & Boissé, P., & Deharving, J. M. 1997, A&A, 321, 733
- Leitherer, C., Ferguson, H. C., & Heckman, T. M. 1995, ApJ, 454, L19

- Leitherer, C., Schaerer, D., Goldader, J. D., González Delgado, R. M., Robert, C., Kune, D. F., de Mello, D. F., Devost, D., & Heckman, T. M. 1999, *ApJS*, 123, 3
- Lejeune, T., Cuisinier, F., & Buser, R. 1997, *A&A*, 125, 229
- Levshakov, S. A., Agafonova, I. I., Centurión, M., & Molaro, P. 2003, *A&A*, 397, 851
- Loveday, J., Maddox, S. J., Efstathiou, G., & Peterson, B. A. 1995, *ApJ*, 442, 457
- Lu, L., Sargent, W. L. W., & Barlow, T. A. 1998, *AJ*, 115, 55
- Lu, L., Sargent, W. L. W., Barlow, T. A., Churchill, C. W., & Vogt, S. S. 1996, *ApJS*, 107, 475
- Madau, P., Haardt, F., & Rees, M. J. 1999, *ApJ*, 514, 648
- Madau, P., Ferguson, H. C., Dickinson, M. E., Giavalisco, M., Steidel, C. C., & Fruchter, A. 1996, *MNRAS*, 283, 1388
- Marri S., & White, S. D. M. 2002, *astro-ph/0207448*, *MNRAS*, submitted
- McDonald, P., & Miralda-Escudé, J. 1999, *ApJ*, 519, 486
- McDonald, P., Miralda-Escudé, J., Rauch, M., Sargent, W. L. W., Barlow, T. A., & Cen, R. 2001, *ApJ*, 562, 52
- McDonald, P., Miralda-Escudé, J., Rauch, M., Sargent, W. L. W., Barlow, T. A., Cen, R., & Ostriker, J. P. 2000, *ApJ*, 543, 1
- McWilliam, A. 1997, *ARA&A*, 35, 503
- McWilliam, A., Preston, G. W., Sneden, C., & Searle, L. 1995, *AJ*, 109, 2757
- Meiksin, A. 1994, *ApJ*, 431, 109
- Meiksin, A., & Madau, P. 1993, *ApJ*, 412, 34
- Misawa, T., Tytler, D., Iye, M., Storrie-Lombardi, L., Suzuki, N., & Wolfe, A. M. 2002, *AJ*, 123, 1847
- Morton, D. 1991, *ApJS*, 77, 119
- Nagamine, K., Springel, V., & Hernquist, L. 2003, *astro-ph/0302187*, *MNRAS*, submitted
- Norberg, P., et al. 2002, *MNRAS*, 332, 827
- Olive, K. A., Steigman, G. & Walker, T. P. 2000, *Phys. Rep.*, 333, 389
- Pascarelle, S., M., Lanzetta, K. M., Chen, H.-W., Webb, J., K. 2001, *ApJ*, 560, 101
- Patnaik, A. R., Browne, I. W., Walsh, D., Chaffee, F. H., & Foltz, C. B. 1992, *MNRAS*, 259, 1P

- Pauldrach, A. W. A., Hoffmann, T. L., & Lennon, M. 2001, *A&A*, 375, 161
- Petitjean, P., & Bergeron, J. 1990, *A&A*, 231, 309
- Petitjean, P., & Bergeron, J. 1994, *A&A*, 283, 759
- Pettini, M., Lipman, K., & Hunstead, R. W. 1995, *ApJ*, 451, 100
- Pettini, M., Ellison, S. L., Bergeron, J., & Petitjean, J. 2002, *A&A*, 391, 21
- Pettini, M., Ellison, S. L., Steidel, C. C., Shapley, A. E., & Bowen, D. V. 2000, *ApJ*, 532, 65
- Pettini, M., Shapley, A. E., Steidel, C. C., Cuby, J., Dickinson, M., Moorwood, A. F. M., Adelberger, K. L., & Giavalisco, M. 2001, *ApJ*, 554, 981
- Pilyugin, L. S. 1999, *A&A*, 346, 428
- Prochaska, J. X., & Wolfe, A. M. 2000, *ApJ*, 507, 113
- Quashnock, J. M. & Vanden Berk, D. E. 1998, *ApJ*, 500, 28
- Quashnock, J. M., Vanden Berk, D. E., & York, D. G. 1996, *ApJ*, 472, L69
- Rauch, M., Haehnelt, M. G., & Steinmetz, M. 1997a, *ApJ*, 481, 601
- Rauch, M., Sargent, W. L. W., & Barlow, T. A. 1999, *ApJ*, 515, 500
- Rauch, M., Sargent, W. L. W., & Barlow, T. A. 2001, *ApJ*, 554, 823
- Rauch, M., Sargent, W. L. W., Womble, D. S., & Barlow, T. A. 1996, *ApJ*, 467, L5
- Rauch, M., Carswell, R. F., Chaffee, F.H., Foltz, C. B., Webb, J. K., Weymann, R. J., Bechtold, J., & Green, R. F. 1992, *ApJ*, 390, 387
- Rauch, M., Miralda-Escudé, J., Sargent, W. L. W., Barlow, T. A., Weinberg, D. H., Hernquist, L., Katz, N., Cen, R., & Ostriker, J. P. 1997b, *ApJ*, 489, 7
- Reimers, D., Kohler, S., Wisotzki, L., Groote, D., Rodriguez-Pascual, P., & Wamsteker, W. 1997, *A&A*, 327, 890
- Ryan, S. G., Norris, J. E., & Beers, T. C. 1996, *ApJ*, 471, 254
- Sargent, W. L. W., & Steidel, C. C. 1987, *ApJ*, 322, 142
- Sargent, W. L. W., Boksenberg, A., & Steidel, C. C. 1988a, *ApJS*, 68, 539
- Sargent, W. L. W., Steidel, C. C., & Boksenberg, A. 1988b, *ApJ*, 334, 22
- Sargent, W. L. W., Young, P. J., Boksenberg, A., & Tytler, D. 1980, *ApJS*, 42, 41

- Savage, B. D., & Sembach, K. R. 1991, *ApJ*, 379, 245
- Savin, D. W. 2000, *ApJ*, 533, 106
- Schaye, J., Rauch, M., Sargent, W. L. W., & Kim, T.-S. 2000a, *ApJ*, 541, L1
- Schaye, J., Theuns, T., Rauch, M., Efstathiou, G., & Sargent, W. L. W. 2000b, *MNRAS*, 318, 817
- Schippers et al. 2003, astro-ph/0301170, *Stellar Coronae in the Chandra and XMM-Newton Era*, F. Favat & J Drake, ASP Conference Series, in press
- Scott, J., Bechtold, J., Dobrzycki, A., & Kulkarni, V. P. 2000, *ApJS*, 130, 67
- Shapiro, P. R., & Giroux, M. L. 1987, *ApJ*, 321, L107
- Shapiro, P. R., & Moore, R. T. 1976, *ApJ*, 207, 460
- Simcoe, R. A., Sargent, W. L. W., & Rauch, M. 2002, *ApJ*, 578, 737
- Smette, A., Heap, S. R., Williger, G. M., Tripp, T. M., Jenkins, E. B., & Songaila, A. 2002, *ApJ*, 564, 542
- Smith, L.J., Norris, R. P. F., & Crowther, P. A. 2002, *MNRAS*, 337, 1309
- Songaila, A. 1998, *AJ*, 115, 2184
- Songaila, A. 2001, *ApJ*, 561, L153
- Songaila, A. 2002, *ApJ*, 568, L139 [erratum]
- Songaila, A., & Cowie, L. L. 1996, *AJ*, 112, 335
- Spergel, D. N., et al. 2003, astro-ph/0302209, *ApJ*, submitted
- Springel, V., & Hernquist, L. 2002, astro-ph/0206393, *MNRAS*, submitted
- Stasińska, G., & Schaerer, D. 1997, *A&A*, 322, 615
- Steidel, C. C. 1990, *ApJS*, 72, 1
- Steidel, C. C., & Sargent, W. L. W. 1989, *ApJ*, 343, L33
- Steidel, C. C., & Sargent, W. L. W. 1992, *ApJS*, 80, 1
- Steidel, C. C., Dickinson, M., & Persson, E. 1994, *ApJ*, 437, L75
- Steidel, C. C., Pettini, M., & Adelberger, K. L. 2001, *ApJ*, 546, 665
- Steidel, C. C., Adelberger, K. L., Giavalisco, M., Dickinson, M., & Pettini, M. 1999, *ApJ*, 519, 1

- Steidel, C., Giavalisco, M., Pettini, M., Dickinson, M., & Adelberger, K. L. 1996, *ApJ*, 462, L17
- Steidel, C. C., Kollmeier, J. A., Shapley, A. E., Churchill, C. W., Dickinson, M., & Pettini, M. 2002, *ApJ*, 570, 526
- Sutherland, R. S., & Dopita, M. A. 1993, *ApJS*, 88, 253
- Telfer, R. C., Zheng, W., Kriss, G. A., & Davidsen, A. F. 2002, *ApJ*, 565, 773
- Theuns, T., Schaye, J., Zaroubi, S., Kim, T., Tzanavaris, P., & Carswell, B. 2002, *ApJ*, 567, L103
- Tripp, T. M., Lu, L., & Savage, B. D. 1995, *ApJS*, 102, 239
- Tripp, T. M., et al. 2002, *ApJ*, 575, 697
- Tytler, D., Fan, X. -M., Burles, S., Cottrell, L., Davis, C., Kirkman, D., & Zuo, L. 1995, *QSO Absorption Lines*, G. Meylan, Berlin: Springer-Verlag, 289
- Verner D. A., Ferland, G. J., Korista, K. T., & Yakovlev, D. G. 1996, *ApJ*, 465, 487
- Viel, M., Matarrese, S., Mo, H. J., Theuns, T., & Haehnelt, M. G. 2002, *MNRAS*, 336, 685
- Vladilo, G. 1998, *ApJ*, 493, 583
- Vogel, S., & Reimers, D. 1993, *A&A*, 274, L5
- Vogt, S. S., et al. 1994, *S.P.I.E.E.* 2198, 362
- Weinberg, D. H., Davé, R., Katz, N., Hernquist, L. 2003, astro-ph/0212356, *ApJ*, submitted
- Weinberg, D. H., Miralda-Escudé, J., Hernquist, L., & Katz, N. 1997, *ApJ*, 490, 564
- Wolfe, A. M., & Prochaska, J. X. 2000, *ApJ*, 545, 603
- Womble, D. S., Sargent, W. L. W., & Lyons, R. S. 1996, *Cold Gas at High Redshift*, M. Bremer, H. Rottgering, C. Carilli, & P. van de Werf, Dordrecht: Kluwer, 249
- Young, P., Sargent, W. L. W., & Boksenberg, A. 1982, *ApJS*, 48, 455
- Zaldarriaga, M., Hui, L., & Tegmark, M. 2001, *ApJ*, 557, 519
- Zehavi, I., et al. 2002, *ApJ*, 571, 172
- Zehavi, I., et al. 2003, astro-ph/0301280, *ApJ*, submitted
- Zhang, Y., Anninos, P., & Norman, M. L. 1995, *ApJ*, 453, L57
- Zheng, W., Kriss, G. A., Telfer, R. C., Grimes, J. P., & Davidsen, A. F. 1997, *ApJ*, 475, 469

Table 1. Log of Observations

Object	z_{em} ^a	V(R) mag	Dates ^b	λ -Range ^c Å	Exposure ^d s	FWHM ^e km s ⁻¹	S/N ^f
Q1626+6433	2.320	15.8	1995 May 19 — 1996 Jul 22	3580 — 6179 ^g	24063	6.6	88 — 128 — 137
Q1442+2931	2.661	16.2	1994 Jun 12 — 1995 Jun 21	3624 — 6150 ^g	22500	6.6	113 — 107 — 121
Q1107+4847	2.966	16.7	1994 Dec 26 — 1995 Feb 22	3643 — 6663	26000	6.6	90 — 94 — 81
Q0636+6801	3.175	16.5	1993 Nov 13 — 1995 Feb 22	3643 — 6663	36200	6.6	112 — 107 — 100
Q1425+6039	3.199	16.5	1995 May 18 — 1995 May 19	3736 — 6540	37200	6.6	168 — 140 — 113
Q1422+2309C	3.628	17.3	1998 Feb 01 — 1999 Apr 14	3569 — 7347	51200	4.4	92 — 90 — 61
Q1645+5520	4.059	(18.1)	1997 May 09 — 1997 May 30	4557 — 8123	72200	6.6	102 — 119 — 81
Q1055+4611	4.131	(17.7)	1995 Apr 07 — 1996 May 24	4587 — 8009	27037	6.6	71 — 47 — 31
Q2237–0607	4.559	(18.3)	1994 Oct 10 — 1995 Aug 21	4933 — 8800	54000	6.6	62 — 42 — 28

^aRedshift determined from the peak of the Lyman α emission line in the HIRES spectrum.

^bTotal period over which observations were made.

^cTotal available wavelength range, extending from within the Lyman forest to beyond the C IV emission line.

^dTotal time spent on the separate exposures.

^eThese are approximate values. Along the echelle orders the velocity resolution differs from the mean by $\sim \pm 3.8\%$.

^fS/N over three pixels (roughly equal to a resolution element for all but Q1422+2309C) outside the Lyman forest sampled near the three wavelengths $\lambda\lambda 1270, 1380, 1500$ in the rest frame of the QSO: by avoiding the main emission lines these tend to conservative estimates.

^gIn subsequent observations coverage of the Lyman forest is extended to ~ 3200 Å.

Table 2. Heavy Element Absorption Lines: Q1626+6433 $z_{em} = 2.320$

z	$b(\text{C})$ km s^{-1}	$b(\text{Si})$ km s^{-1}	$N(\text{C IV})$ 10^{12}cm^{-2}	$N(\text{Si IV})$ 10^{11}cm^{-2}	$N(\text{C II})$ 10^{12}cm^{-2}	$N(\text{Si II})$ 10^{11}cm^{-2}	$N(\text{N V})$ 10^{12}cm^{-2}	n
1	2	3	4	5	6	7	8	9
1.779								
1.778627	11.5	...	1.91 ± 0.18	1
1.778827	4.4	...	0.55 ± 0.13	2
1.779004	9.9	...	3.33 ± 0.20	3
1.779140	7.0	...	7.40 ± 0.20	4
1.779332	10.8	...	17.8 ± 0.3	5
1.779552	10.5	...	4.99 ± 0.20	6
1.779787	4.7	...	0.42 ± 0.13	7
1.780057	6.5	...	0.68 ± 0.14	8
1.780347	9.3	...	7.07 ± 0.19	9
1.817								
1.816507	16.2	...	13.4 ± 0.5	1
1.816544	7.0	...	23.7 ± 0.5	2
1.816732	6.2	...	10.7 ± 0.2	3
1.816840	7.5	...	23.9 ± 0.3	4
1.816994	11.2	...	1.34 ± 0.20	5
1.843								
1.842852	11.6	...	2.52 ± 0.23	1
1.842988	20.4	...	2.44 ± 0.29	2
1.847								
1.846898	12.4	...	0.72 ± 0.18	1
1.847057	4.3	...	1.39 ± 0.13	2
1.847176	8.9	...	1.97 ± 0.16	3
1.880 ^a								
1.879931	5.6	...	1.39 ± 0.16	1
1.880008	4.5	...	2.70 ± 0.16	2
1.880148	5.4	...	1.58 ± 0.14	3
1.880304	7.4	...	1.22 ± 0.17	4
1.927 ^b								
1.925748	13.9	(12.8)	13.3 ± 0.5	35.8 ± 3.6	3.10 ± 1.77	1
1.925760	4.7	(4.1)	7.28 ± 0.35	31.8 ± 2.3	4.39 ± 1.14	2
1.925891	7.4	(5.9)	13.1 ± 0.3	51.9 ± 1.7	8.53 ± 0.89	3
1.926023	9.8	(6.9)	17.9 ± 0.3	31.5 ± 1.4	4
1.926202	8.7	(7.1)	18.5 ± 0.3	53.2 ± 1.5	5
1.926366	9.2	(6.6)	38.7 ± 0.9	52.0 ± 1.8	...	3.79 ± 2.88	...	6
1.926495	10.6	(9.1)	16.0 ± 0.6	58.4 ± 2.1	...	17.2 ± 5.2	...	7
1.926649	6.2	(4.8)	4.13 ± 0.61	24.6 ± 2.9	...	162 ± 9	...	8
1.926720	21.2	(20.5)	28.2 ± 1.9	175 ± 8	...	73.8 ± 23.3	...	9
1.926750	6.4	(5.1)	12.7 ± 0.6	41.4 ± 2.7	...	43.3 ± 6.6	...	10
1.926808	6.3	(4.9)	2.85 ± 0.62	7.03 ± 2.63	145 ± 67	212 ± 9	...	11
1.927033	10.9	(9.5)	28.2 ± 0.5	153 ± 2	188 ± 21	470 ± 36	...	12
1.927220	9.1	(6.7)	52.6 ± 1.6	163 ± 3	91.9 ± 10.3	101 ± 4	...	13
1.927316	7.5	(5.8)	34.8 ± 1.8	167 ± 4	43.6 ± 5.1	71.4 ± 3.9	...	14
1.927515	17.0	(16.1)	74.7 ± 1.7	248 ± 5	20.8 ± 7.1	61.1 ± 8.4	...	15
1.927569	7.2	(6.0)	2.30 ± 0.78	76.8 ± 4.3	$[264 \pm 40]$	329 ± 8	...	16
1.927676	8.6	(7.6)	2.22 ± 0.34	13.2 ± 1.6	21.6 ± 2.0	43.8 ± 3.8	...	17
1.927869	14.5	(13.4)	23.6 ± 0.4	39.0 ± 1.2	8.16 ± 1.16	18
1.928121	18.1	(17.3)	8.92 ± 0.24	13.0 ± 1.3	19

Table 2—Continued

z	$b(\text{C})$ km s^{-1}	$b(\text{Si})$ km s^{-1}	$N(\text{C IV})$ 10^{12}cm^{-2}	$N(\text{Si IV})$ 10^{11}cm^{-2}	$N(\text{C II})$ 10^{12}cm^{-2}	$N(\text{Si II})$ 10^{11}cm^{-2}	$N(\text{N V})$ 10^{12}cm^{-2}	n
1	2	3	4	5	6	7	8	9
2.048								
2.047888	13.4	(12.2)	10.7 ± 0.2	< 0.90	< 0.43	1
2.048114	6.9	(5.8)	2.36 ± 0.16	< 0.68	< 0.33	2
2.048295	3.1	(2.1)	0.60 ± 0.12	< 0.57	< 0.26	3
2.056 ^c								
2.054822	20.6	(19.8)	8.29 ± 0.25	< 2.08	1
2.055124	8.2	7.4	17.1 ± 0.3	19.8 ± 1.1	2.10 ± 0.42	2
2.055374	10.0	8.8	57.5 ± 0.6	51.1 ± 1.4	4.15 ± 1.22	3
2.055457	54.6	(54.3)	19.3 ± 0.5	9.00 ± 1.16	4
2.055510	9.4	(7.6)	11.9 ± 0.8	< 4.43	5
2.056254	4.1	(2.9)	0.45 ± 0.11	< 0.89	6
2.069								
2.069290	11.4	(10.0)	1.86 ± 0.13	1.71 ± 0.83	< 0.42	1
2.099 ^d								
2.097649	8.3	(6.7)	2.38 ± 0.15	< 0.74	< 0.37	1
2.097893	5.9	(5.2)	10.7 ± 0.2	5.01 ± 1.15	0.64 ± 0.36	2
2.097995	3.7	(2.4)	1.14 ± 0.17	3.02 ± 0.93	< 0.35	3
2.098061	21.9	(21.2)	15.4 ± 0.3	3.30 ± 2.44	< 0.78	4
2.098451	3.7	(2.4)	0.42 ± 0.11	< 0.46	< 0.27	5
2.098758	7.6	(6.5)	2.33 ± 0.14	4.02 ± 0.70	< 0.35	6
2.098963	4.3	(3.6)	9.93 ± 0.20	3.16 ± 0.54	< 0.34	7
2.099068	9.2	(7.3)	13.6 ± 0.2	1.81 ± 0.67	< 0.42	8
2.099335	3.7	(2.4)	1.03 ± 0.14	< 1.07	< 0.36	9
2.099424	19.0	(18.1)	7.65 ± 0.27	< 1.13	< 0.66	10
2.099921	17.2	(16.4)	0.54 ± 0.19	< 0.92	< 0.61	11
2.110 ^e								
2.108121	17.3	(16.3)	0.55 ± 0.16	< 0.89	1
2.109167	5.6	4.4	17.4 ± 0.3	81.5 ± 1.6	21.1 ± 1.0	19.1 ± 3.1	...	2
2.109186	26.4	(25.4)	3.89 ± 0.35	< 1.86	3
2.109396	4.7	4.4	3.59 ± 0.13	16.9 ± 0.7	4
2.109512	5.1	3.4	1.37 ± 0.12	9.28 ± 0.60	7.84 ± 0.46	15.9 ± 2.2	...	5
2.109622	9.1	(4.5)	1.95 ± 0.15	4.29 ± 0.57	2.61 ± 0.48	6
2.109767	6.8	(5.4)	1.34 ± 0.13	7.31 ± 0.64	2.58 ± 0.38	5.31 ± 2.39	...	7
2.109956	18.2	(17.4)	3.67 ± 0.21	2.89 ± 1.06	< 0.64	8
2.110138	5.8	(4.2)	5.43 ± 0.15	20.9 ± 0.8	22.5 ± 0.8	22.6 ± 1.4	...	9
2.110231	4.6	(2.9)	4.63 ± 0.16	15.8 ± 0.7	98.2 ± 6.5	328 ± 8	...	10
2.110307	3.6	(2.8)	2.45 ± 0.13	7.22 ± 0.58	2.39 ± 0.64	2.78 ± 1.02	...	11
2.110416	6.1	(4.5)	4.23 ± 0.14	9.20 ± 0.60	3.80 ± 0.39	12
2.110524	6.1	(4.2)	0.97 ± 0.12	< 0.78	4.34 ± 0.36	9.11 ± 1.01	...	13
2.110706	6.7	(5.1)	1.12 ± 0.18	3.58 ± 0.67	6.16 ± 0.56	6.71 ± 1.01	...	14
2.110752	3.1	(2.0)	0.75 ± 0.15	7.07 ± 0.76	< 0.45	15
2.110902	...	2.5	< 0.18	< 0.89	< 0.56	2.47 ± 1.14	...	16
2.110925	11.1	(9.7)	2.15 ± 0.26	< 2.08	< 1.04	17
2.111460	7.4	(5.8)	1.20 ± 0.11	< 0.63	< 0.34	18
2.208								
2.208279	9.1	(7.3)	0.62 ± 0.12	< 0.68	< 0.41	1
2.208481	8.6	(6.7)	4.84 ± 0.13	< 0.67	< 0.40	2

Table 2—Continued

z	$b(\text{C})$ km s^{-1}	$b(\text{Si})$ km s^{-1}	$N(\text{C IV})$ 10^{12}cm^{-2}	$N(\text{Si IV})$ 10^{11}cm^{-2}	$N(\text{C II})$ 10^{12}cm^{-2}	$N(\text{Si II})$ 10^{11}cm^{-2}	$N(\text{N V})$ 10^{12}cm^{-2}	n
1	2	3	4	5	6	7	8	9
2.244 ^f								
2.242572	4.0	3.0	5.76 ± 0.12	5.74 ± 0.46	2.99 ± 0.29	2.18 ± 0.40	...	1
2.242732	13.7	(12.6)	15.6 ± 0.2	2.57 ± 0.69	0.60 ± 0.42	< 0.69	1.28 ± 0.38	2
2.243104	5.3	(4.0)	0.60 ± 0.17	2.24 ± 0.74	1.20 ± 0.45	0.87 ± 0.64	...	3
2.243116	15.8	(14.8)	8.30 ± 0.26	< 1.21	< 0.73	< 1.04	1.12 ± 0.64	4
2.243618	15.7	(14.7)	0.93 ± 0.14	< 1.52	< 0.42	< 1.53	...	5
2.243853	5.0	(3.9)	0.95 ± 0.09	< 0.73	...	< 0.45	...	6
2.244120	7.8	7.5	13.5 ± 0.2	7.76 ± 0.58	2.36 ± 0.33	1.85 ± 0.53	1.07 ± 0.42	7
2.244502	8.4	(6.5)	27.6 ± 0.4	3.46 ± 0.97	< 0.61	...	6.57 ± 0.75	8
2.244628	32.7	(32.2)	14.8 ± 0.9	< 3.66	< 1.76	...	24.3 ± 2.4	9
2.244701	7.9	(5.7)	96.2 ± 1.2	21.6 ± 1.0	0.69 ± 0.56	...	8.71 ± 0.80	10
2.244805	...	3.3	< 2.18	5.76 ± 0.62	< 0.38	...	2.16 ± 0.38	11
2.244962	15.0	(14.0)	$[282 \pm 7]$	40.5 ± 1.3	0.81 ± 0.66	...	24.0 ± 0.8	12
2.245070	3.3	(2.7)	14.1 ± 2.9	6.52 ± 0.62	2.54 ± 0.34	< 0.59	...	13
2.245192	...	1.8	< 0.63	10.30 ± 0.66	< 0.39	< 0.39	...	14
2.245272	8.3	5.1	70.4 ± 0.6	11.40 ± 0.76	< 1.87	< 0.61	9.16 ± 0.45	15
2.245432	19.9	(19.5)	0.89 ± 0.20	< 1.01	< 6.24	16
2.285 ^g								
2.284676	11.2	(9.8)	0.62 ± 0.14	< 0.51	< 0.34	< 0.51	0.58 ± 0.32	1
2.285099	4.5	3.2	17.8 ± 0.7	36.4 ± 1.3	5.62 ± 0.70	3.11 ± 0.82	< 0.62	2
2.285106	9.9	(8.7)	20.5 ± 0.5	12.9 ± 1.2	< 0.87	< 1.11	4.80 ± 0.83	3
2.285366	6.1	(5.0)	14.7 ± 0.2	1.08 ± 0.46	0.39 ± 0.32	< 0.42	3.82 ± 0.31	4
2.285459	5.3	2.9	11.2 ± 0.2	7.54 ± 0.47	3.22 ± 0.33	2.13 ± 0.39	< 0.27	5
2.285611	7.8	(6.4)	1.39 ± 0.12	< 0.48	< 0.31	< 0.43	1.64 ± 0.29	6
2.291 ^h								
2.289859	3.9	(3.3)	< 0.10	1.34 ± 0.46	10.8 ± 0.4	14.7 ± 0.7	< 0.31	1
2.290042	21.4	(20.7)	6.94 ± 0.24	29.9 ± 1.1	25.8 ± 0.8	23.3 ± 1.1	< 0.69	2
2.290200	5.1	(5.2)	2.11 ± 0.16	12.1 ± 0.8	12.9 ± 0.6	16.7 ± 0.8	< 0.40	3
2.290275	16.8	(15.9)	7.73 ± 0.28	23.7 ± 1.3	6.03 ± 0.82	< 1.48	< 0.81	4
2.290527	11.6	(10.3)	3.17 ± 0.28	< 1.01	< 0.66	< 0.85	< 0.83	5
2.290602	6.8	(5.9)	1.80 ± 0.21	7.69 ± 0.77	2.05 ± 0.49	0.93 ± 0.65	< 0.52	6
2.290765	3.1	(2.0)	0.15 ± 0.14	1.16 ± 0.54	3.86 ± 0.40	3.81 ± 0.56	...	7
2.290885	15.3	(14.3)	2.69 ± 0.46	< 1.53	< 1.11	< 1.37	...	8
2.290946	6.3	5.4	0.46 ± 0.27	4.99 ± 0.93	16.7 ± 0.7	20.8 ± 1.0	...	9
2.291440	3.6	2.3	5.80 ± 0.13	13.0 ± 0.5	4.60 ± 0.28	6.45 ± 0.47	...	10
2.291592	10.0	(8.4)	19.4 ± 0.3	5.32 ± 0.69	0.68 ± 0.43	< 0.71	< 0.92	11
2.291743	5.5	(4.9)	22.3 ± 0.4	43.2 ± 0.9	12.9 ± 0.5	9.26 ± 0.75	< 0.61	12
2.291855	3.5	(3.1)	15.2 ± 0.5	31.2 ± 0.9	27.3 ± 0.9	29.8 ± 1.4	< 0.54	13
2.291885	32.1	(31.6)	68.8 ± 0.9	17.4 ± 2.7	< 1.99	...	13.6 ± 2.3	14
2.291925	7.4	(6.4)	16.7 ± 0.5	23.7 ± 1.2	10.1 ± 0.7	7.79 ± 1.36	< 0.91	15
2.292226	5.0	3.4	1.67 ± 0.14	5.75 ± 0.50	9.38 ± 0.36	12.5 ± 1.4	< 0.47	16
2.292389	6.8	(5.6)	1.46 ± 0.12	< 0.46	< 0.27	...	< 0.60	17
2.321 ⁱ								
2.320332	5.8	(5.1)	4.78 ± 0.14	8.39 ± 0.50	< 0.34	< 0.51	0.45 ± 0.26	1
2.320418	6.2	(5.4)	5.37 ± 0.16	3.01 ± 0.51	< 0.36	< 0.46	< 0.26	2
2.320611	16.8	(15.9)	10.2 ± 0.2	1.73 ± 0.67	...	< 0.61	< 0.37	3
2.321037	19.4	(18.7)	1.18 ± 0.16	< 0.70	...	< 0.62	< 0.72	4

Table 2—Continued

z	$b(\text{C})$ km s^{-1}	$b(\text{Si})$ km s^{-1}	$N(\text{C IV})$ 10^{12}cm^{-2}	$N(\text{Si IV})$ 10^{11}cm^{-2}	$N(\text{C II})$ 10^{12}cm^{-2}	$N(\text{Si II})$ 10^{11}cm^{-2}	$N(\text{N V})$ 10^{12}cm^{-2}	n
1	2	3	4	5	6	7	8	9
2.323 ^j								
2.322463	15.0	(14.0)	5.12 ± 0.15	0.99 ± 0.59	...	< 0.62	0.86 ± 0.31	1
2.322685	7.9	(6.5)	4.43 ± 0.12	< 0.63	...	< 0.44	< 0.23	2
2.322916	6.9	(6.3)	0.55 ± 0.10	< 0.42	...	< 0.59	< 0.22	3
2.323258	19.0	(18.2)	6.49 ± 0.21	< 1.93	...	< 0.76	< 0.40	4
2.323364	5.4	(4.7)	3.34 ± 0.14	1.92 ± 0.39	< 0.50	< 0.43	< 0.30	5
2.323631	18.2	(17.4)	8.13 ± 0.17	1.12 ± 0.64	< 0.86	< 0.66	0.67 ± 0.34	6
2.324049	9.9	(8.2)	2.78 ± 0.12	< 0.46	< 0.31	< 0.50	< 0.32	7

^aComponent 4 of C IV $\lambda 1551$ coincides with Si II $\lambda 1527$ at $z = 1.927$ and is not used.

^bSi IV $\lambda 1394$ contains weak N V $\lambda 1239$ at $z = 2.291$ and C II at $z = 2.056$. Although C II is in the forest, useful values are obtained for all components except 4–10, for which comparison with Si II $\lambda\lambda 1260, 1304, 1527$ suggests have some underlying H I (see Figure 3), and component 19 which is weak and additionally may be contaminated. Component 16 is mildly saturated in C II (value in square brackets) and weak in C IV: the Lyman α profile indicates $\log N(\text{H I}) \lesssim 18.7$. Si II values come predominantly from $\lambda 1527$, although mild contamination of component 12 is identified and determined from use of $\lambda 1304$ which is in a clear region of the forest; $\lambda 1260$ also seems uncontaminated over most of its profile and the same parameters give a consistent fit to the data for this line. An anomalous, weak, narrow feature appearing at $z = 1.927969$ in C II and another at $z = 1.926123$ in Si II, not detected in the other species, are indicated in Figure 3 but not included here.

^cSi IV $\lambda 1394$ is blended with very weak Ni II $\lambda 1455$ at $z = 1.927$. C II is largely blended with Si IV $\lambda 1394$ at $z = 1.927$ and N V $\lambda 1239$ at $z = 2.291$ but components 2 and 3 have good values; component 6, which seems to separate out in the VPFIT analysis (see Figure 3), is too uncertain to use.

^dSi IV $\lambda 1394$ is blended with strong Al III $\lambda 1855$ at $z = 1.328$ and values come mostly from $\lambda 1403$.

^eSi IV $\lambda 1394$ is partially blended with Al III $\lambda 1863$ at $z = 1.328$; C IV $\lambda 1548$ in the $z = 1.817$ system encroaches slightly on $\lambda 1403$. C II contains Si II $\lambda 1260$ at $z = 2.291$ but, in the main, separation of these is straightforward (see Figure 3). Component 10 is very strong in C II and relatively weak in C IV: mild damping wings centred on this position appear to be present in the Lyman α profile and indicate $\log N(\text{H I}) \sim 18.3$. Si II $\lambda 1260$ is in the forest where it is partially clear (although here blended with very weak Si II $\lambda 1193$ at $z = 2.285$) and $\lambda 1527$ is quite strong; together they yield self-consistent values for the stronger components; in component 16 the narrow Si II feature is not detected in the other listed species but seems to be present in Si III $\lambda 1207$.

^fC IV $\lambda 1548$ contains weak Si II $\lambda 1527$ at $z = 2.291$; components 10 and 12 are saturated in $\lambda 1548$ and 10 (value in square brackets) is close to this in $\lambda 1551$, and the values listed should be regarded as approximate. In component 13 C II shows a strongly significant feature but Si II $\lambda 1260$ is not detected; Si II is generally weak and partially mixed with N V $\lambda 1243$ at $z = 2.291$, making some component values too uncertain to use. N V is in the forest but useful values are obtained using both members of the doublet.

^gC IV $\lambda 1551$ is blended with weaker C IV $\lambda 1548$ at $z = 2.291$. N V is outside the forest.

^hC IV $\lambda 1548$ includes very weak Ni II $\lambda 1742$ at $z = 1.927$ and strong C IV $\lambda 1551$ at $z = 2.285$. Si II $\lambda 1260$ is overlapped by C II at $z = 2.110$, making upper limits for components 14 and 17 indeterminate; component 6 seems contaminated and should be treated as uncertain. Although component 1 is strong in C II and Si II, while undetected in C IV, the Lyman α profile gives $\log N(\text{H I}) \lesssim 15.8$. Component 13 is the strongest in C II and Si II; although C IV is also quite strong, mild Lyman α damping wings centred on this component indicate $\log N(\text{H I}) \sim 17.7$. N V $\lambda 1239$ is blended with C II at $z = 2.056$ and strong Si IV $\lambda 1394$ at $z = 1.927$, and $\lambda 1243$ is somewhat contaminated with weak Si II $\lambda 1260$ at $z = 2.244$: only the more certain values are listed. Many of the smaller values for $b(\text{C})$ are from C II.

ⁱThis may be associated with the $z = 2.323$ system. In components 3 and 4 C II seems contaminated, possibly with weak absorption related to nearby Al III $\lambda 1855$ at $z = 1.390$, and these are not used.

^jThis is close to z_{em} . C II is heavily blended with Mg II $\lambda 2796$ at $z = 0.586$, masking components 1–4.

Table 3. Heavy Element Absorption Lines: Q1442+2931 $z_{em} = 2.67$

z	$b(\text{C})$ km s^{-1}	$b(\text{Si})$ km s^{-1}	$N(\text{C IV})$ 10^{12}cm^{-2}	$N(\text{Si IV})$ 10^{11}cm^{-2}	$N(\text{C II})$ 10^{12}cm^{-2}	$N(\text{Si II})$ 10^{11}cm^{-2}	$N(\text{N V})$ 10^{12}cm^{-2}	n
1	2	3	4	5	6	7	8	9
1.910								
1.910424	7.9	...	2.12 ± 0.12	1
1.910599	3.6	...	0.53 ± 0.09	2
1.974								
1.973317	17.2	...	1.81 ± 0.27	1
1.973565	17.6	...	2.53 ± 0.28	2
1.974424	28.6	...	1.82 ± 0.29	3
1.974861	11.5	...	10.9 ± 0.2	4
1.975146	11.0	...	3.11 ± 0.17	5
2.090 ^a								
2.089580	15.4	...	2.90 ± 0.28	1
2.089774	4.7	...	0.88 ± 0.18	2
2.090303	5.4	...	0.63 ± 0.18	3
2.090874	7.6	...	1.26 ± 0.21	4
2.091066	8.6	...	11.0 ± 0.3	5
2.157								
2.156836	11.4	...	5.43 ± 0.23	1
2.156930	7.3	...	2.44 ± 0.18	2
2.330								
2.328990	39.3	(39.0)	5.42 ± 0.42	5.68 ± 1.76	1
2.329069	9.2	(7.6)	1.60 ± 0.21	< 0.82	2
2.329410	3.8	(3.0)	0.69 ± 0.12	0.71 ± 0.50	3
2.329688	15.4	(14.4)	1.15 ± 0.20	3.46 ± 0.84	4
2.329961	10.0	(8.3)	13.4 ± 0.2	4.47 ± 0.72	5
2.330120	8.9	(7.2)	11.4 ± 0.3	3.13 ± 0.68	6
2.330268	7.3	5.7	10.1 ± 0.3	13.5 ± 0.8	7
2.330440	25.8	(25.2)	24.5 ± 0.6	9.78 ± 1.83	8
2.330553	6.6	5.2	14.3 ± 0.3	4.14 ± 0.81	9
2.410 ^b								
2.409461	9.7	(8.0)	5.37 ± 0.26	< 0.67	< 0.23	1
2.410576	27.7	(27.2)	4.99 ± 0.39	< 1.38	< 0.45	2
2.411017	11.1	(9.6)	3.21 ± 0.26	< 1.04	< 0.31	3
2.438 ^c								
2.436427	...	10.0	< 0.45	4.97 ± 1.96	< 1.14	4.71 ± 1.68	...	1
2.436507	10.0	(8.3)	< 0.69	4.72 ± 2.30	33.1 ± 1.9	64.0 ± 3.3	...	2
2.436590	5.8	(4.7)	< 0.29	5.53 ± 1.31	50.2 ± 2.1	114 ± 4	...	3
2.436698	6.4	(5.2)	0.31 ± 0.19	3.75 ± 0.94	21.7 ± 0.9	51.7 ± 2.0	...	4
2.436878	14.0	(12.9)	0.62 ± 0.26	6.47 ± 1.34	6.78 ± 0.57	14.0 ± 2.1	...	5
2.437046	7.5	(6.1)	< 0.28	< 1.30	20.3 ± 0.6	37.4 ± 1.5	...	6
2.437198	14.3	(13.2)	0.55 ± 0.28	< 1.91	3.25 ± 0.57	7
2.437377	5.7	(4.5)	0.34 ± 0.17	1.23 ± 0.75	10.5 ± 0.4	18.6 ± 1.2	...	8
2.437608	7.4	(6.4)	1.52 ± 0.24	12.8 ± 1.2	13.5 ± 0.5	21.2 ± 1.5	...	9
2.437736	9.9	(8.3)	16.9 ± 0.4	94.6 ± 2.8	16.0 ± 0.6	15.4 ± 2.1	...	10
2.437942	10.7	(9.2)	38.6 ± 0.5	136 ± 4	27.4 ± 0.7	22.3 ± 2.7	...	11
2.438079	5.2	(4.1)	3.45 ± 0.50	40.7 ± 2.7	12.2 ± 1.2	12
2.438130	5.1	(4.1)	8.94 ± 0.47	31.2 ± 2.0	30.2 ± 1.7	71.9 ± 3.7	...	13
2.438241	4.6	(3.6)	5.51 ± 0.28	48.0 ± 1.8	67.4 ± 3.0	137 ± 4	...	14

Table 3—Continued

z	$b(\text{C})$ km s^{-1}	$b(\text{Si})$ km s^{-1}	$N(\text{C iv})$ 10^{12}cm^{-2}	$N(\text{Si iv})$ 10^{11}cm^{-2}	$N(\text{C ii})$ 10^{12}cm^{-2}	$N(\text{Si ii})$ 10^{11}cm^{-2}	$N(\text{N v})$ 10^{12}cm^{-2}	n
1	2	3	4	5	6	7	8	9
2.438393	11.7	(10.4)	20.5 ± 0.5	36.9 ± 1.4	12.9 ± 0.6	15.9 ± 3.2	...	15
2.438555	4.8	(3.9)	4.03 ± 0.64	61.9 ± 2.8	6.26 ± 0.62	11.9 ± 1.2	...	16
2.438695	19.8	(19.1)	84.9 ± 2.8	64.0 ± 3.6	18.1 ± 1.6	20.3 ± 2.7	...	17
2.438748	3.3	(2.2)	1.16 ± 0.85	5.68 ± 1.38	6.03 ± 0.68	11.5 ± 1.3	...	18
2.438853	4.6	(3.6)	...	151 ± 14	25.5 ± 1.0	50.7 ± 2.3	...	19
2.438926	7.2	(5.6)	...	100 ± 7	7.43 ± 1.05	9.08 ± 1.29	...	20
2.439099	13.6	(12.5)	...	215 ± 8	2.25 ± 1.45	21
2.439118	3.3	(2.2)	...	< 3.24	5.09 ± 0.69	9.88 ± 1.24	...	22
2.439193	4.3	(3.2)	...	29.4 ± 2.9	2.68 ± 0.48	23
2.439303	4.3	(3.2)	74.3 ± 19.5	134 ± 13	10.0 ± 1.5	26.5 ± 2.6	...	24
2.439392	11.3	(9.9)	< 18.00	< 23.90	12.5 ± 5.6	12.3 ± 6.1	...	25
2.439440	9.7	(8.0)	92.1 ± 14.2	201 ± 16	14.5 ± 4.9	14.0 ± 7.2	...	26
2.439502	16.5	(15.6)	49.3 ± 3.6	16.0 ± 5.7	17.4 ± 2.5	18.7 ± 9.4	...	27
2.439570	5.0	(4.0)	8.64 ± 1.36	17.3 ± 2.4	17.3 ± 1.1	44.2 ± 3.6	...	28
2.439843	9.7	(8.1)	37.8 ± 0.8	32.9 ± 1.3	< 0.29	29
2.440018	12.8	(11.5)	44.0 ± 1.0	13.5 ± 1.6	1.09 ± 0.47	30
2.440106	5.2	(4.1)	10.5 ± 0.6	15.4 ± 1.2	< 0.34	31
2.440272	14.1	(13.0)	4.91 ± 0.39	< 1.47	< 0.40	32
2.468 ^d								
2.465539	9.8	(8.2)	0.82 ± 0.21	< 0.94	< 0.30	1
2.466100	13.7	(12.5)	2.64 ± 0.27	1.58 ± 0.87	< 0.34	2
2.467054	8.1	(6.8)	3.27 ± 0.28	11.8 ± 0.8	3
2.467202	10.4	(8.9)	3.78 ± 0.37	6.30 ± 0.85	4
2.467431	13.1	(10.4)	12.8 ± 0.4	36.8 ± 1.0	5.37 ± 0.36	5
2.467787	14.4	(13.4)	7.59 ± 0.40	6.55 ± 0.92	0.78 ± 0.36	6
2.468138	16.2	(15.3)	3.37 ± 0.40	< 1.84	< 0.37	7
2.468781	10.0	(8.4)	1.03 ± 0.31	1.64 ± 0.74	0.47 ± 0.30	8
2.469790	13.8	(12.7)	0.59 ± 0.27	< 1.14	< 0.45	9
2.474 ^e								
2.473053	6.3	(5.1)	0.85 ± 0.18	2.35 ± 0.55	< 0.28	1
2.473672	11.6	(8.4)	39.6 ± 0.5	15.5 ± 0.7	1.06 ± 0.38	...	5.39 ± 0.39	2
2.473854	8.6	(8.0)	23.2 ± 0.4	15.6 ± 0.7	0.88 ± 0.35	...	0.86 ± 0.32	3
2.474214	5.3	3.8	36.6 ± 0.6	59.0 ± 1.1	11.7 ± 0.3	7.92 ± 2.09	1.17 ± 0.26	4
2.474581	6.3	(5.1)	4.30 ± 0.30	1.32 ± 0.84	< 0.48	5
2.474618	20.0	(19.2)	11.8 ± 0.4	8.59 ± 1.46	< 1.17	6
2.484 ^f								
2.483662	5.3	(4.8)	5.58 ± 0.16	2.18 ± 1.07	< 0.26	1
2.502 ^g								
2.501596	3.8	(3.0)	0.58 ± 0.14	< 0.74	1
2.501706	59.3	(59.1)	4.15 ± 0.46	< 1.92	2
2.502287	10.7	(9.2)	8.62 ± 0.22	< 0.69	3
2.502480	4.4	(3.7)	0.74 ± 0.14	< 0.49	< 0.30	4
2.555 ^h								
2.554845	8.9	(7.1)	2.24 ± 0.14	< 2.53	1
2.555491	24.8	(24.2)	4.31 ± 0.22	< 1.60	2
2.616 ⁱ								
2.614827	5.7	(4.8)	1.30 ± 0.12	< 0.49	...	< 0.30	< 0.37	1
2.615327	6.8	4.8	16.4 ± 0.3	15.0 ± 0.6	...	< 0.30	< 0.42	2
2.615620	10.4	(10.1)	1.12 ± 0.15	< 0.66	...	< 0.39	< 0.34	3

Table 3—Continued

z	$b(\text{C})$ km s^{-1}	$b(\text{Si})$ km s^{-1}	$N(\text{C IV})$ 10^{12}cm^{-2}	$N(\text{Si IV})$ 10^{11}cm^{-2}	$N(\text{C II})$ 10^{12}cm^{-2}	$N(\text{Si II})$ 10^{11}cm^{-2}	$N(\text{N V})$ 10^{12}cm^{-2}	n
1	2	3	4	5	6	7	8	9
2.615880	10.1	(8.5)	3.16 ± 0.16	< 0.69	...	< 0.37	0.47 ± 0.18	4
2.616086	6.9	(5.8)	7.44 ± 0.18	< 0.71	...	< 0.38	< 0.24	5
2.616313	9.9	(8.3)	4.23 ± 0.16	< 0.63	...	< 0.39	< 0.20	6
2.616537	8.4	(6.9)	2.74 ± 0.15	1.35 ± 0.57	< 0.49	< 0.37	< 0.18	7
2.616833	3.7	(2.4)	0.42 ± 0.10	< 0.43	< 0.25	< 0.34	< 0.13	8
2.617074	8.8	(7.3)	9.57 ± 0.20	< 0.58	< 0.70	< 0.34	0.87 ± 0.17	9
2.617366	7.5	(6.5)	0.45 ± 0.13	< 0.59	< 0.86	< 0.33	< 0.21	10
2.617593	4.9	(4.1)	5.28 ± 0.18	< 0.50	< 0.28	< 0.29	1.08 ± 0.19	11
2.617723	4.2	(3.2)	1.43 ± 0.20	< 0.57	< 0.32	< 0.33	0.76 ± 0.22	12
2.617824	19.0	(18.2)	23.0 ± 0.4	...	< 0.62	< 0.70	1.85 ± 0.41	13
2.618157	4.2	3.1	7.83 ± 0.20	7.96 ± 0.53	0.80 ± 0.26	0.95 ± 0.27	< 0.41	14
2.623 ^j								
2.622695	3.7	(2.4)	0.57 ± 0.12	< 0.47	...	< 0.52	< 0.17	1
2.623229	11.9	(10.6)	4.99 ± 0.20	< 0.79	< 0.51	< 0.39	< 0.35	2
2.623507	11.5	(10.1)	4.15 ± 0.21	3.23 ± 0.78	0.91 ± 0.38	0.86 ± 0.38	0.39 ± 0.22	3

^aC IV $\lambda 1551$ is immersed in Si IV $\lambda 1393$ at $z = 2.438$ and is not used.

^bIn component 1 C IV $\lambda 1551$ is contaminated and is not used. Si IV $\lambda 1403$ is masked by C IV $\lambda 1548$ at $z = 2.090$.

^cThis is a damped Lyman α system with components 3 and 14 particularly strong in C II, Si II and O I, and weak in C IV: respective values $\log N(\text{H I}) \sim 19.7$ and ~ 19.5 give a good fit to the damping wings. In components 19–23 C IV $\lambda\lambda 1548, 1551$ is too saturated to be useful; here C II provides the values for $b(\text{C})$. Si IV $\lambda 1393$ contains C IV $\lambda 1551$ at $z = 2.090$. Si II $\lambda 1260$, in the forest but only mildly contaminated, is used to supplement strong $\lambda\lambda 1304, 1527$ and all are collectively self-consistent; errors are from $\lambda\lambda 1304, 1527$ alone.

^dApparent contamination of components 3 and 4 in C II makes the values too uncertain to include.

^eThe Si II value is from $\lambda 1527$. N V is in the forest but for components 2–4 useful values come from $\lambda 1239$, in a relatively clear region, which show corresponding velocity structure to the components in C IV.

^fSi IV $\lambda 1394$ is contaminated and is not used.

^gIn components 1–3 C II is masked by Mg II $\lambda 2804$ at $z = 0.667$.

^hC II is very weak and too noisy to give useful upper limits. Si II $\lambda 1260$ is outside the forest but masked by N V $\lambda 1239$ at $z = 2.616$.

ⁱC IV $\lambda 1551$ is blended with weaker C IV $\lambda 1548$ at $z = 2.623$. In components 1–6 C II is masked by Si IV $\lambda 1403$ at $z = 2.438$. N V is outside the forest; in components 1–3 $\lambda 1239$ is blended with O I $\lambda 1302$ at $z = 2.438$, and in component 14 with Si II $\lambda 1304$ in the same system, and these are not used.

^jC IV $\lambda 1548$ is blended with C IV $\lambda 1551$ at $z = 2.616$. The close proximity to Si IV $\lambda 1393$ at $z = 2.468$ makes component 1 of C II too uncertain to use.

Table 4. Heavy Element Absorption Lines: Q1107+4847 $z_{em} = 2.966$

z	$b(\text{C})$ km s^{-1}	$b(\text{Si})$ km s^{-1}	$N(\text{C IV})$ 10^{12}cm^{-2}	$N(\text{Si IV})$ 10^{11}cm^{-2}	$N(\text{C II})$ 10^{12}cm^{-2}	$N(\text{Si II})$ 10^{11}cm^{-2}	$N(\text{N V})$ 10^{12}cm^{-2}	n
1	2	3	4	5	6	7	8	9
2.117								
2.117266	17.1	...	2.24 ± 0.11	1
2.142								
2.141509	6.4	...	0.54 ± 0.10	1
2.143								
2.143112	4.6	...	2.23 ± 0.12	1
2.143203	6.3	...	14.2 ± 0.2	2
2.143354	7.8	...	2.33 ± 0.12	3
2.153								
2.153354	4.5	...	0.80 ± 0.08	1
2.153512	9.5	...	2.78 ± 0.11	2
2.662 ^a								
2.661857	9.2	(7.4)	3.36 ± 0.15	1.04 ± 0.72	< 0.23	1
2.662490	7.4	(5.9)	1.43 ± 0.17	< 0.62	< 0.17	2
2.685								
2.684145	3.7	(2.4)	0.53 ± 0.19	1.46 ± 0.71	< 0.22	1
2.684571	5.5	(4.5)	2.78 ± 0.80	9.10 ± 1.54	< 0.35	2
2.684737	10.9	(9.4)	1.42 ± 0.87	< 2.32	< 0.63	3
2.696								
2.695978	43.6	(43.2)	5.04 ± 0.57	< 2.00	< 0.71	1
2.696339	23.6	(23.0)	2.71 ± 0.43	< 1.52	< 0.54	2
2.696666	7.8	(6.3)	5.02 ± 0.20	1.95 ± 0.67	< 0.76	3
2.696923	4.9	(4.2)	0.92 ± 0.14	1.26 ± 0.58	< 0.21	4
2.724 ^b								
2.722208	6.0	(4.9)	9.77 ± 0.19	1.53 ± 0.64	< 0.24	1
2.723588	9.8	(8.2)	0.88 ± 0.17	0.91 ± 0.70	2
2.723883	8.2	(6.8)	4.15 ± 0.17	11.3 ± 0.7	0.44 ± 0.27	3
2.724112	5.2	(4.3)	3.06 ± 0.27	29.4 ± 1.5	1.01 ± 0.37	0.85 ± 0.47	...	4
2.724211	14.9	(13.9)	14.2 ± 0.5	55.2 ± 2.2	4.30 ± 0.68	4.80 ± 0.83	...	5
2.724488	16.6	(15.6)	9.61 ± 0.54	11.2 ± 2.3	< 0.87	6
2.724564	6.1	(5.0)	4.34 ± 0.33	8.01 ± 1.34	< 0.58	7
2.724874	13.2	(12.0)	1.33 ± 0.21	7.72 ± 1.04	1.76 ± 0.36	8
2.725077	6.0	(4.9)	0.50 ± 0.15	6.75 ± 0.77	1.01 ± 0.26	9
2.761 ^c								
2.758824	12.2	(10.9)	1.05 ± 0.22	< 0.89	< 0.52	1
2.759098	7.3	(6.0)	52.9 ± 1.2	23.2 ± 1.0	0.88 ± 0.27	...	4.64 ± 0.44	2
2.759319	9.8	(8.1)	425 ± 32	193 ± 4	10.7 ± 0.4	6.90 ± 2.66	11.9 ± 0.6	3
2.759466	3.6	(2.7)	7.36 ± 3.53	83.1 ± 4.6	7.55 ± 0.34	12.3 ± 2.1	...	4
2.759609	19.6	(18.8)	6.30 ± 0.39	< 1.38	< 0.39	5
2.759996	4.8	(4.0)	3.95 ± 0.18	< 0.63	< 0.22	6
2.760219	10.4	(8.9)	3.87 ± 0.29	< 1.48	< 0.39	7
2.760309	4.4	(3.7)	14.4 ± 0.4	< 0.78	< 0.29	...	5.54 ± 0.51	8
2.760514	10.3	(8.8)	7.97 ± 0.26	< 1.18	< 0.48	9
2.760665	4.5	(3.9)	7.41 ± 0.27	9.75 ± 0.77	< 0.23	10
2.760807	7.9	(6.3)	20.1 ± 0.3	13.2 ± 0.8	0.93 ± 0.28	11
2.761007	6.8	(5.7)	18.5 ± 0.5	13.0 ± 0.8	0.57 ± 0.27	12
2.761161	8.4	(6.6)	64.2 ± 1.2	27.5 ± 1.0	2.29 ± 0.33	13

Table 4—Continued

z	$b(\text{C})$ km s^{-1}	$b(\text{Si})$ km s^{-1}	$N(\text{C IV})$ 10^{12}cm^{-2}	$N(\text{Si IV})$ 10^{11}cm^{-2}	$N(\text{C II})$ 10^{12}cm^{-2}	$N(\text{Si II})$ 10^{11}cm^{-2}	$N(\text{N V})$ 10^{12}cm^{-2}	n
1	2	3	4	5	6	7	8	9
2.761329	7.8	(6.6)	10.1 ± 0.6	16.2 ± 1.1	0.82 ± 0.36	14
2.761452	7.2	5.4	43.6 ± 0.9	69.5 ± 1.7	9.65 ± 0.39	10.8 ± 2.4	...	15
2.761613	10.6	(9.0)	7.66 ± 0.29	14.3 ± 1.0	< 0.37	16
2.761853	7.5	(6.2)	3.68 ± 0.20	17.8 ± 0.9	7.40 ± 0.31	7.91 ± 2.30	...	17
2.762018	7.0	(5.7)	5.53 ± 0.23	20.7 ± 0.9	4.51 ± 0.32	3.82 ± 2.23	...	18
2.762164	6.7	(5.4)	5.66 ± 0.31	14.1 ± 0.9	5.57 ± 0.44	11.3 ± 2.7	...	19
2.762337	9.7	(8.1)	20.8 ± 1.0	46.0 ± 2.1	70.4 ± 1.4	122 ± 5	...	20
2.762414	4.9	(4.1)	224 ± 17	234 ± 15	< 1.17	< 4.32	< 1.39	21
2.762538	3.3	(2.5)	6.97 ± 0.45	9.51 ± 1.03	7.57 ± 0.39	22
2.762646	15.0	(14.0)	7.58 ± 0.33	17.8 ± 1.3	7.92 ± 0.49	23
2.762923	4.8	(4.4)	3.56 ± 0.24	18.9 ± 1.2	2.69 ± 0.32	5.33 ± 3.24	...	24
2.763017	4.6	(3.8)	3.26 ± 0.28	20.6 ± 1.3	12.6 ± 0.5	33.1 ± 3.7	...	25
2.763098	4.8	(4.0)	9.34 ± 0.31	21.3 ± 1.1	< 0.35	26
2.763268	11.4	(10.0)	3.67 ± 0.31	7.32 ± 1.20	3.72 ± 0.48	27
2.763356	3.3	(2.4)	1.04 ± 0.20	8.65 ± 0.91	8.02 ± 0.39	21.9 ± 3.3	...	28
2.763500	6.5	(5.2)	1.91 ± 0.18	6.64 ± 0.74	9.11 ± 0.32	10.6 ± 2.9	...	29
2.763681	10.6	(10.4)	0.70 ± 0.20	3.22 ± 0.90	3.97 ± 0.33	30
2.763998	8.2	(6.7)	< 0.27	1.80 ± 0.72	9.51 ± 0.31	17.2 ± 2.8	...	31
2.870 ^d								
2.869980	11.3	(9.9)	3.37 ± 0.26	< 2.25	...	< 0.56	...	1
2.870310	10.9	(9.4)	12.4 ± 0.3	31.7 ± 2.3	< 0.38	< 0.71	...	2
2.870585	13.2	(12.0)	5.29 ± 0.31	< 2.54	< 0.41	< 0.33	...	3
2.909 ^e								
2.908791	10.1	...	2.17 ± 0.16	< 0.18	1
2.956 ^f								
2.956177	11.4	(10.0)	1.14 ± 0.15	< 0.72	...	< 0.62	< 0.28	1

^aIn component 1 Si IV $\lambda 1403$ is contaminated and is not used.

^bIn components 1–4 Si IV $\lambda 1403$ is blended with Mg II $\lambda 2804$ at $z = 0.863$. In component 2 C II is too noisy to be useful. Si II $\lambda 1260$ is in the forest but is used to supplement weak $\lambda 1527$: convincing values are obtained for components 4 and 5, consistent with $\lambda 1527$.

^cThis is a mildly-damped Lyman α system with the low ionization region centred on component 20 as indicated by strong C II, Si II and O I and relatively weak C IV: for this, $\log N(\text{H I}) \sim 19.1$ gives a good fit to the outer parts of the damping wings. Despite its close proximity in velocity to the optically thick region, component 21 is very strong in C IV and undetectable in the low ionization species. Si II $\lambda 1260$ is in the forest but this and $\lambda 1193$ are used to supplement $\lambda 1527$ and available portions of $\lambda 1304$: the values obtained for the stronger components are listed with errors from $\lambda \lambda 1304, 1527$ alone. N V is in the forest but good values for components 2, 3 and 8 come from both members of the doublet and component 21 has a useful upper limit from $\lambda 1243$.

^dSi IV $\lambda 1394$ is not used because it is too strong relative to $\lambda 1403$.

^eSi IV $\lambda 1393$ coincides with Al III $\lambda 1855$ at $z = 1.938$ and $\lambda 1403$ is too noisy to give a reliable value. C II and Si II both are too contaminated to be useful. N V is outside the forest.

^fC II is masked by Si IV $\lambda 1403$ at $z = 2.761$.

Table 5. Heavy Element Absorption Lines: Q0636+6801 $z_{em} = 3.175$

z	$b(\text{C})$ km s^{-1}	$b(\text{Si})$ km s^{-1}	$N(\text{C IV})$ 10^{12}cm^{-2}	$N(\text{Si IV})$ 10^{11}cm^{-2}	$N(\text{C II})$ 10^{12}cm^{-2}	$N(\text{Si II})$ 10^{11}cm^{-2}	$N(\text{N V})$ 10^{12}cm^{-2}	n
1	2	3	4	5	6	7	8	9
2.311								
2.310164	9.4	...	2.65 ± 0.16	1
2.310456	8.4	...	3.10 ± 0.16	2
2.310679	8.3	...	3.24 ± 0.16	3
2.311054	16.4	...	20.1 ± 0.3	4
2.311286	12.1	...	15.3 ± 0.2	5
2.311721	22.4	...	9.06 ± 0.27	6
2.312144	9.6	...	0.83 ± 0.16	7
2.312500	25.7	...	3.94 ± 0.29	8
2.325								
2.324395	4.4	...	0.25 ± 0.08	1
2.324753	9.3	...	2.13 ± 0.12	2
2.324890	7.1	...	4.49 ± 0.12	3
2.325103	11.0	...	3.37 ± 0.13	4
2.325270	6.8	...	0.26 ± 0.10	5
2.436								
2.435508	3.2	...	0.69 ± 0.09	1
2.474 ^a								
2.472749	4.8	...	11.1 ± 0.3	1
2.472778	13.4	...	5.75 ± 0.38	2
2.473178	8.0	...	5.84 ± 0.17	3
2.473427	5.8	...	3.64 ± 0.15	4
2.473591	9.8	...	5.79 ± 0.18	5
2.473870	19.4	...	5.74 ± 0.25	6
2.474504	7.0	...	13.0 ± 0.2	7
2.474628	10.7	...	8.13 ± 0.22	8
2.474966	15.2	...	11.0 ± 0.2	9
2.475250	6.8	(5.7)	53.4 ± 0.7	77.6 ± 4.4	2.69 ± 0.47	3.52 ± 0.90	...	10
2.475374	5.6	3.8	56.1 ± 1.1	113 ± 7	11.0 ± 0.6	12.4 ± 1.0	...	11
2.475483	9.1	...	17.2 ± 0.3	12
2.475874	28.9	...	5.96 ± 0.40	13
2.475973	7.0	...	3.29 ± 0.18	14
2.595								
2.594509	8.2	...	1.86 ± 0.12	1
2.594744	4.6	...	0.79 ± 0.11	2
2.594834	5.8	...	1.46 ± 0.12	3
2.621								
2.621012	12.6	...	1.69 ± 0.23	1
2.621429	17.2	...	4.90 ± 0.27	2
2.681 ^b								
2.680228	8.7	(6.9)	1.49 ± 0.19	< 0.94	1
2.681582	16.8	(15.9)	0.94 ± 0.31	< 1.62	2
2.681729	8.0	(6.3)	0.49 ± 0.22	1.43 ± 1.11	3
2.682134	16.9	(15.9)	6.59 ± 0.26	< 1.33	4
2.690								
2.690484	7.6	(6.3)	1.67 ± 0.21	1.38 ± 0.44	1

Table 5—Continued

z	$b(\text{C})$ km s^{-1}	$b(\text{Si})$ km s^{-1}	$N(\text{C IV})$ 10^{12}cm^{-2}	$N(\text{Si IV})$ 10^{11}cm^{-2}	$N(\text{C II})$ 10^{12}cm^{-2}	$N(\text{Si II})$ 10^{11}cm^{-2}	$N(\text{N V})$ 10^{12}cm^{-2}	n
1	2	3	4	5	6	7	8	9
2.868 ^c								
2.867186	9.3	(7.5)	0.35 ± 0.20	< 1.14	< 0.32	1
2.867448	6.5	(5.3)	0.97 ± 0.18	< 1.02	< 0.19	2
2.867921	9.4	(7.6)	3.48 ± 0.22	< 0.86	< 0.26	3
2.868426	8.6	(6.8)	0.83 ± 0.18	< 0.57	< 0.21	4
2.868799	9.1	(7.3)	5.30 ± 0.21	3.08 ± 0.55	< 0.21	5
2.892								
2.890422	6.4	(5.2)	0.81 ± 0.12	1.05 ± 0.46	< 0.24	1
2.890751	14.6	(13.5)	1.18 ± 0.19	< 1.00	< 0.35	2
2.890979	3.7	(2.4)	0.43 ± 0.11	< 0.49	< 0.33	3
2.891193	3.7	(2.4)	0.79 ± 0.11	< 0.38	< 0.20	4
2.891348	7.3	(6.0)	3.44 ± 0.14	< 0.52	< 0.26	5
2.891574	11.1	(9.6)	1.18 ± 0.16	2.05 ± 0.61	0.71 ± 0.30	6
2.891873	6.5	(5.7)	7.40 ± 0.21	1.29 ± 0.61	< 0.50	7
2.891972	22.7	(22.0)	11.0 ± 0.4	< 1.22	< 0.62	8
2.893152	11.2	(9.8)	2.38 ± 0.16	< 0.67	< 0.40	9
2.893931	3.7	(2.4)	0.44 ± 0.10	< 0.43	< 0.32	10
2.904 ^d								
2.902448	20.3	...	7.52 ± 0.31	1
2.902615	8.2	(6.8)	4.42 ± 0.28	16.7 ± 1.0	< 0.58	2
2.902811	16.0	(15.1)	21.8 ± 0.7	61.2 ± 2.3	< 0.90	3
2.902970	25.5	(24.9)	28.5 ± 0.9	20.2 ± 2.9	4.14 ± 1.21	4
2.903256	4.3	(3.3)	1.46 ± 0.24	7.27 ± 0.84	< 0.43	5
2.903348	20.2	(19.5)	28.7 ± 0.5	52.0 ± 1.8	2.20 ± 0.77	6
2.903645	7.1	(5.8)	1.91 ± 0.18	< 0.67	< 0.56	7
2.903904	7.3	(6.3)	2.05 ± 0.41	28.1 ± 1.4	1.81 ± 1.20	8
2.903992	15.8	(14.8)	18.8 ± 0.7	12.3 ± 2.1	< 2.37	9
2.904141	3.8	(2.9)	5.56 ± 0.32	34.9 ± 1.5	[486 \pm 57]	481 \pm 11	...	10
2.904277	7.0	(5.8)	31.5 ± 0.6	330 ± 8	79.1 \pm 13.5	153 \pm 4	...	11
2.904403	7.7	(6.3)	4.38 ± 1.30	160 ± 8	[213 \pm 31]	452 \pm 7	...	12
2.904569	18.4	(17.5)	94.6 ± 3.5	432 ± 14	35.2 \pm 17.6	16.0 \pm 6.8	...	13
2.904679	9.2	(7.4)	24.4 ± 3.5	182 ± 17	< 16.10	34.2 \pm 6.6	...	14
2.904727	5.6	(4.6)	< 1.79	40.5 ± 8.9	117 \pm 8	167 \pm 5	...	15
2.904947	5.7	(4.7)	3.31 ± 0.55	7.83 ± 1.90	2.35 \pm 1.13	4.72 \pm 1.16	...	16
2.904951	25.6	(25.0)	16.3 ± 1.6	65.2 ± 5.8	< 3.54	17
2.905153	6.4	4.6	9.26 ± 0.44	75.9 ± 2.0	12.8 \pm 1.0	14.4 \pm 1.0	...	18
2.905313	9.3	(7.6)	3.27 ± 0.25	20.8 ± 1.1	4.14 \pm 0.55	7.87 \pm 0.78	...	19
2.905486	4.7	2.7	< 0.26	1.77 ± 0.77	5.71 \pm 0.47	12.7 \pm 0.9	...	20
2.905509	19.3	(18.5)	3.27 ± 0.40	16.1 ± 1.8	2.03 \pm 0.92	21
3.009 ^e								
3.007413	8.7	(6.8)	1.02 ± 0.25	< 0.57	< 0.39	1
3.010096	13.3	(12.1)	4.65 ± 0.31	< 0.67	< 0.49	2
3.013								
3.012890	17.5	(16.6)	0.83 ± 0.34	< 0.77	< 0.49	1
3.013251	18.5	(17.6)	2.33 ± 0.43	< 0.91	< 0.61	2
3.013468	12.7	(11.5)	9.83 ± 0.38	5.91 ± 0.73	< 0.53	3
3.013730	3.2	(2.5)	0.82 ± 0.17	< 0.36	< 0.26	4
3.013933	9.3	(7.5)	1.95 ± 0.24	< 0.49	< 0.34	5

Table 5—Continued

z	$b(\text{C})$ km s^{-1}	$b(\text{Si})$ km s^{-1}	$N(\text{C IV})$ 10^{12}cm^{-2}	$N(\text{Si IV})$ 10^{11}cm^{-2}	$N(\text{C II})$ 10^{12}cm^{-2}	$N(\text{Si II})$ 10^{11}cm^{-2}	$N(\text{N V})$ 10^{12}cm^{-2}	n
1	2	3	4	5	6	7	8	9
3.018								
3.017230	6.2	(5.4)	22.1 ± 0.4	5.71 ± 0.58	0.40 ± 0.31	1
3.017391	6.4	(5.2)	18.0 ± 0.4	2.96 ± 0.57	< 0.37	2
3.017537	7.5	(5.1)	3.51 ± 0.26	< 0.62	< 0.34	3
3.017875	2.6	(1.7)	0.79 ± 0.23	< 0.44	< 0.24	4
3.111 ^f								
3.111315	10.3	(8.7)	2.34 ± 0.15	< 0.52	< 0.76	< 0.26	< 0.54	1

^aOnly C IV is outside the forest but the strong, narrow components 10 and 11 are clearly distinguished in Si IV $\lambda 1394$ and C II, where they are relatively free of contamination. In these components Si II $\lambda 1260$ is also well-measured in the forest and is used to supplement $\lambda 1527$.

^bSi IV $\lambda 1394$ is blended with C IV $\lambda 1548$ at $z = 2.311$ and overall rather noisy, and is not used.

^cIn components 1 and 2 Si IV $\lambda 1394$ is blended with stronger C IV $\lambda 1551$ at $z = 2.474$ and the values come from $\lambda 1403$ alone.

^dThis is a complex system with strong C II, Si II and O I and relatively weak C IV; although H I is not obviously damped, from the extent of Lyman α wings associated with components 10 and 12, the strongest in the low-ionization species, the combined limit is $\log N(\text{H I}) \lesssim 18.7$. In the broad component 1 Si IV and C II are weak and too uncertain to include. In components 10 and 12 C II is saturated and the values (in square brackets) are indicative only. Si II $\lambda 1260$ is in the forest but onward from component 10 is relatively clear of contamination and is used to supplement $\lambda 1304$, which is outside and relatively strong although components 1–9 are undetected; $\lambda 1527$ seems somewhat contaminated and is not used. For component 20 $b(\text{C})$ comes from C II.

^eSi IV $\lambda 1394$ is contaminated and is not used.

^fN V is outside the forest; $\lambda 1239$ is blended with strong Si II $\lambda 1304$ at $z = 2.904$ and the upper limit is from $\lambda 1243$ alone.

Table 6. Heavy Element Absorption Lines: Q1425+6039 $z_{em} = 3.199$

z	$b(\text{C})$ km s^{-1}	$b(\text{Si})$ km s^{-1}	$N(\text{C IV})$ 10^{12}cm^{-2}	$N(\text{Si IV})$ 10^{11}cm^{-2}	$N(\text{C II})$ 10^{12}cm^{-2}	$N(\text{Si II})$ 10^{11}cm^{-2}	$N(\text{N V})$ 10^{12}cm^{-2}	n
1	2	3	4	5	6	7	8	9
2.343								
2.342658	9.9	...	4.83 ± 0.07	1
2.342825	10.1	...	5.57 ± 0.07	2
2.343112	8.3	...	2.50 ± 0.06	3
2.476								
2.475446	13.2	...	2.16 ± 0.12	1
2.475735	12.9	...	4.87 ± 0.13	2
2.476010	7.4	...	8.01 ± 0.12	3
2.476190	3.9	...	0.38 ± 0.08	4
2.476558	2.1	...	0.24 ± 0.07	5
2.486								
2.485350	11.7	...	2.04 ± 0.10	1
2.485641	10.4	...	4.17 ± 0.10	2
2.486022	8.1	...	2.27 ± 0.09	3
2.486233	9.9	...	7.76 ± 0.11	4
2.486466	10.6	...	10.5 ± 0.1	5
2.486635	7.8	...	9.60 ± 0.12	6
2.486847	10.4	...	18.8 ± 0.2	7
2.487046	12.9	...	12.6 ± 0.2	8
2.487377	29.2	...	0.99 ± 0.17	9
2.513								
2.513450	8.3	...	1.29 ± 0.11	1
2.606								
2.605744	7.4	...	1.13 ± 0.08	1
2.624								
2.624447	16.3	...	1.77 ± 0.16	1
2.646 ^a								
2.645671	12.5	(11.2)	1.13 ± 0.11	< 0.58	1
2.646265	23.5	(22.8)	1.03 ± 0.16	< 1.52	2
2.646557	11.8	(10.4)	4.08 ± 0.12	< 0.61	3
2.702 ^b								
2.702178	20.9	(20.1)	0.99 ± 0.14	< 0.51	1
2.702463	8.0	(6.6)	0.69 ± 0.09	0.75 ± 0.24	2
2.726 ^b								
2.726083	24.1	(23.5)	2.98 ± 0.17	< 0.75	1
2.726279	11.1	(9.7)	3.07 ± 0.12	3.71 ± 0.37	2
2.770 ^c								
2.768786	14.6	(13.6)	0.70 ± 0.12	1.82 ± 0.40	1
2.769114	8.4	(6.9)	2.44 ± 0.10	0.89 ± 0.29	2
2.769332	7.3	(6.1)	0.66 ± 0.09	5.28 ± 0.30	...	3.16 ± 1.39	...	3
2.769603	16.9	(15.9)	4.45 ± 0.16	2.24 ± 0.50	...	11.6 ± 2.5	...	4
2.769767	5.6	(4.7)	2.13 ± 0.11	42.4 ± 0.5	...	697 ± 11	...	5
2.769870	3.3	(2.2)	0.57 ± 0.13	8.31 ± 0.43	...	628 ± 61	...	6
2.769947	7.2	(6.0)	1.67 ± 0.19	16.8 ± 0.6	...	526 ± 11	...	7
2.770029	3.7	(2.7)	0.39 ± 0.13	8.87 ± 0.43	...	315 ± 14	...	8
2.770122	6.0	(4.9)	0.94 ± 0.12	8.21 ± 0.38	...	220 ± 3	...	9
2.770252	30.1	(29.6)	1.62 ± 0.22	< 0.74	10

Table 6—Continued

z	$b(\text{C})$ km s^{-1}	$b(\text{Si})$ km s^{-1}	$N(\text{C iv})$ 10^{12}cm^{-2}	$N(\text{Si iv})$ 10^{11}cm^{-2}	$N(\text{C II})$ 10^{12}cm^{-2}	$N(\text{Si II})$ 10^{11}cm^{-2}	$N(\text{N v})$ 10^{12}cm^{-2}	n
1	2	3	4	5	6	7	8	9
2.771054	6.9	(5.6)	0.91 ± 0.08	7.66 ± 0.30	...	3.68 ± 1.29	...	11
2.773 ^d								
2.772536	11.5	(10.1)	3.31 ± 0.25	< 0.31	1
2.772726	6.8	(3.9)	$[494 \pm 9]$	5.72 ± 0.27	0.88 ± 0.14	...	121 ± 2	2
2.772863	4.0	(2.7)	56.8 ± 1.6	3.53 ± 0.47	0.57 ± 0.15	...	11.1 ± 0.8	3
2.772893	9.6	(7.9)	2.72 ± 0.47	< 0.68	4
2.773427	24.0	(23.3)	2.86 ± 0.24	< 0.45	5
2.774082	15.6	(14.6)	1.14 ± 0.19	< 0.36	6
2.796								
2.795972	5.6	(4.7)	2.22 ± 0.12	< 0.39	1
2.796182	10.2	(8.6)	1.72 ± 0.14	< 0.44	2
2.827 ^e								
2.825084	9.0	(7.1)	1.00 ± 0.12	1.29 ± 0.45	2.15 ± 0.14	2.34 ± 1.36	...	1
2.825332	7.6	(6.1)	2.12 ± 0.14	< 0.45	9.82 ± 0.20	14.8 ± 2.4	...	2
2.825449	4.2	(3.2)	25.2 ± 0.4	4.32 ± 0.59	20.1 ± 0.4	38.8 ± 5.1	...	3
2.825534	3.6	(2.5)	27.7 ± 0.7	16.5 ± 0.9	27.8 ± 0.8	10.0 ± 2.8	...	4
2.825621	5.5	(4.4)	18.5 ± 0.3	15.0 ± 0.8	82.5 ± 2.1	629 ± 79	...	5
2.825763	7.0	(5.7)	6.88 ± 0.72	7.23 ± 1.11	104 ± 5	194 ± 16	...	6
2.825831	...	9.5	< 1.94	25.0 ± 1.6	< 7.48	< 16.2	...	7
2.825917	5.8	(4.9)	2.44 ± 0.61	< 1.59	51.4 ± 3.5	114 ± 9	...	8
2.826024	13.8	(12.6)	26.4 ± 0.6	78.5 ± 1.6	46.5 ± 3.2	26.5 ± 2.8	...	9
2.826134	5.7	(5.7)	< 0.37	< 1.98	18.0 ± 7.1	60.8 ± 3.6	...	10
2.826240	9.6	(7.8)	5.74 ± 0.55	9.33 ± 1.63	99.6 ± 29.4	48.2 ± 7.2	...	11
2.826324	9.7	(8.0)	9.87 ± 0.49	26.8 ± 1.4	...	273 ± 10	...	12
2.826467	5.2	(3.8)	3.16 ± 0.29	5.30 ± 0.77	...	399 ± 34	...	13
2.826567	7.7	(6.1)	7.23 ± 0.62	19.1 ± 1.9	14
2.826644	...	9.5	< 1.90	9.40 ± 5.82	15
2.826731	15.5	(14.5)	8.70 ± 1.98	32.7 ± 8.4	16
2.826817	22.1	(21.4)	40.0 ± 3.0	67.3 ± 9.5	17
2.826867	...	12.0	< 2.12	41.4 ± 6.2	18
2.827209	4.6	(3.7)	0.65 ± 0.35	< 1.03	183 ± 40	342 ± 13	...	19
2.827274	16.9	(16.0)	23.6 ± 1.1	41.3 ± 3.3	< 26.8	43.0 ± 16.8	...	20
2.827395	7.3	(6.0)	3.49 ± 0.48	12.8 ± 1.4	125 ± 8	230 ± 7	...	21
2.827571	14.2	(13.1)	3.26 ± 0.46	< 1.83	4.31 ± 2.94	27.4 ± 6.8	...	22
2.827646	8.1	(6.5)	< 0.38	3.94 ± 1.02	99.5 ± 1.8	204 ± 5	...	23
2.827820	9.3	(7.6)	1.71 ± 0.19	< 0.64	31.6 ± 0.5	62.5 ± 3.3	...	24
2.827976	12.9	(11.7)	5.12 ± 0.36	11.8 ± 1.3	0.78 ± 0.48	25
2.828086	16.4	(15.5)	2.67 ± 0.34	< 1.32	1.17 ± 0.40	26
2.830 ^f								
2.828551	13.7	(12.6)	2.44 ± 0.14	2.93 ± 0.49	0.29 ± 0.14	1
2.828831	11.0	(9.5)	2.45 ± 0.16	3.02 ± 0.55	1.99 ± 0.14	2
2.829053	3.3	(2.2)	< 0.13	0.57 ± 0.40	0.92 ± 0.11	3
2.829371	15.2	(14.2)	4.94 ± 1.14	32.8 ± 2.8	18.3 ± 0.8	30.9 ± 5.6	...	4
2.829382	3.3	(2.2)	1.42 ± 0.17	7.41 ± 0.64	5.28 ± 0.19	8.83 ± 1.79	...	5
2.829527	37.2	(36.8)	35.8 ± 2.4	< 5.73	< 1.62	6
2.829571	5.9	(4.8)	25.9 ± 0.6	51.8 ± 1.6	0.39 ± 0.20	7
2.829671	7.2	(5.8)	75.9 ± 3.8	168 ± 3	20.4 ± 0.4	26.0 ± 2.3	...	8
2.829772	5.2	(4.2)	12.7 ± 1.4	93.7 ± 3.6	18.0 ± 0.4	32.0 ± 2.4	...	9
2.829830	8.1	(6.7)	44.7 ± 1.1	66.9 ± 2.3	3.24 ± 0.47	10
2.829921	14.3	(13.2)	1.34 ± 0.61	11.9 ± 1.5	4.76 ± 0.45	14.4 ± 3.8	...	11
2.830156	10.2	(8.7)	5.02 ± 0.44	14.3 ± 1.0	6.05 ± 0.37	9.00 ± 2.75	...	12
2.830335	31.3	(30.8)	55.6 ± 1.1	27.6 ± 2.6	4.61 ± 0.98	13
2.830421	4.1	(3.3)	21.5 ± 0.8	60.8 ± 1.9	44.8 ± 1.0	84.8 ± 2.2	...	14

Table 6—Continued

z	$b(\text{C})$ km s^{-1}	$b(\text{Si})$ km s^{-1}	$N(\text{C iv})$ 10^{12}cm^{-2}	$N(\text{Si iv})$ 10^{11}cm^{-2}	$N(\text{C ii})$ 10^{12}cm^{-2}	$N(\text{Si ii})$ 10^{11}cm^{-2}	$N(\text{N v})$ 10^{12}cm^{-2}	n
1	2	3	4	5	6	7	8	9
2.830583	4.7	(3.5)	19.0 ± 1.7	82.1 ± 6.1	43.4 ± 2.5	321 ± 8	...	15
2.830610	12.6	(11.3)	41.8 ± 2.6	185 ± 7	20.6 ± 6.0	16
2.830678	4.5	(3.5)	1.60 ± 0.49	11.1 ± 1.6	26.3 ± 1.1	42.1 ± 3.5	...	17
2.830733	5.9	(5.0)	3.29 ± 0.62	3.95 ± 1.46	1.64 ± 1.12	18
2.830857	14.9	(13.8)	2.10 ± 0.23	11.0 ± 0.8	4.61 ± 0.30	19.0 ± 3.2	...	19
2.950								
2.947838	11.9	(10.6)	4.35 ± 0.16	< 0.43	< 0.20	1
2.948156	13.6	(12.4)	4.56 ± 0.17	0.78 ± 0.46	< 0.21	2
2.949959	10.8	(9.3)	2.18 ± 0.12	< 0.58	< 0.23	3
2.950342	14.5	(13.4)	7.64 ± 0.21	1.92 ± 0.70	< 0.48	4
2.950455	6.8	5.0	4.94 ± 0.17	5.36 ± 0.61	< 0.27	5
2.950678	11.1	(9.6)	16.2 ± 0.2	5.53 ± 0.42	< 0.24	6
2.951200	19.1	(18.3)	0.74 ± 0.14	< 0.59	< 0.28	7
2.964 ^e								
2.963297	14.4	(13.3)	2.66 ± 0.15	< 0.75	< 0.25	1
2.963438	8.9	(7.1)	1.98 ± 0.12	0.88 ± 0.53	< 0.21	2
2.963631	7.6	(6.1)	1.14 ± 0.09	< 0.39	< 0.15	3
2.963969	13.0	(11.8)	3.89 ± 0.15	1.68 ± 0.65	4
2.964099	8.8	(7.0)	7.26 ± 0.14	7.89 ± 0.54	0.36 ± 0.21	5
3.025 ^h								
3.024624	7.2	(6.0)	0.66 ± 0.13	< 0.54	1
3.024790	4.1	(2.7)	0.62 ± 0.11	< 0.35	2
3.056 ⁱ								
3.055479	23.9	(23.2)	1.87 ± 0.23	< 0.56	< 0.31	1
3.055883	16.4	(15.4)	1.79 ± 0.20	< 0.51	2
3.056135	6.0	...	0.74 ± 0.12	...	< 0.20	3
3.067 ^j								
3.066627	10.5	(8.9)	0.97 ± 0.20	< 0.34	< 0.19	< 0.18	...	1
3.066970	10.4	(8.9)	6.69 ± 0.26	8.61 ± 0.39	< 0.23	< 0.24	...	2
3.067122	6.0	4.9	3.33 ± 0.22	15.1 ± 0.4	< 0.31	< 0.24	...	3
3.074 ^j								
3.073988	7.1	(5.8)	2.60 ± 0.17	< 0.55	< 0.24	< 0.27	...	1
3.096 ^k								
3.095190	10.9	(9.5)	2.33 ± 0.14	< 0.39	< 0.17	< 0.13	0.57 ± 0.17	1
3.095418	6.3	(3.7)	7.53 ± 0.13	10.3 ± 0.4	< 0.15	< 0.10	0.43 ± 0.14	2
3.095753	10.6	(9.1)	1.31 ± 0.13	0.60 ± 0.42	< 0.35	< 0.14	0.28 ± 0.17	3
3.095938	5.3	(4.4)	1.46 ± 0.11	0.87 ± 0.32	< 0.14	< 0.11	< 0.22	4
3.135 ^l								
3.133470	4.8	(3.8)	3.18 ± 0.34	4.58 ± 0.26	< 0.23	< 0.27	0.26 ± 0.09	1
3.133645	9.9	(8.2)	9.22 ± 0.49	11.7 ± 0.4	< 0.48	0.55 ± 0.20	< 0.13	2
3.133929	19.4	(18.6)	6.50 ± 0.62	4.93 ± 0.50	< 0.42	< 0.31	< 0.36	3
3.134197	4.1	(3.0)	1.08 ± 0.31	< 0.25	< 0.27	< 0.14	< 0.09	4
3.134458	20.1	(19.4)	3.35 ± 0.29	< 0.48	< 0.38	< 0.29	< 0.18	5
3.135247	8.2	(6.7)	0.89 ± 0.16	0.75 ± 0.29	< 0.25	< 0.31	< 0.09	6
3.135512	7.8	(7.1)	2.06 ± 0.18	7.12 ± 0.33	< 0.37	< 0.21	< 0.10	7
3.135682	8.4	(6.9)	3.96 ± 0.22	3.26 ± 0.36	< 0.29	< 0.26	< 0.22	8
3.135841	5.7	(4.5)	0.85 ± 0.26	5.88 ± 0.44	< 0.35	< 0.30	< 0.15	9
3.135884	16.2	(15.3)	7.18 ± 0.41	< 0.74	< 0.57	< 0.54	< 0.23	10

Table 6—Continued

z	$b(\text{C})$ km s^{-1}	$b(\text{Si})$ km s^{-1}	$N(\text{C IV})$ 10^{12}cm^{-2}	$N(\text{Si IV})$ 10^{11}cm^{-2}	$N(\text{C II})$ 10^{12}cm^{-2}	$N(\text{Si II})$ 10^{11}cm^{-2}	$N(\text{N V})$ 10^{12}cm^{-2}	n
1	2	3	4	5	6	7	8	9
3.155 ^m								
3.152981	14.6	(13.5)	3.37 ± 0.22	< 0.86	< 0.29	< 0.23	< 0.15	1
3.153348	11.7	(10.3)	2.45 ± 0.19	< 0.47	< 0.25	< 0.20	0.25 ± 0.09	2
3.153683	4.1	(3.1)	0.58 ± 0.13	< 0.29	< 0.15	< 0.14	< 0.06	3
3.154125	14.9	(13.8)	4.14 ± 0.21	0.85 ± 0.49	< 0.27	< 0.23	< 0.10	4
3.154566	12.2	(10.9)	1.11 ± 0.19	0.74 ± 0.44	< 0.23	< 0.20	< 0.09	5
3.155016	13.6	(12.4)	0.63 ± 0.19	< 0.46	< 0.25	0.44 ± 0.22	< 0.09	6
3.156047	27.4	(26.8)	2.63 ± 0.31	< 0.97	< 0.32	< 0.31	0.39 ± 0.15	7
3.174 ⁿ								
3.172790	7.0	(5.6)	0.34 ± 0.09	< 0.40	< 0.13	< 0.14	< 0.07	1
3.173329	7.0	(5.7)	0.59 ± 0.09	< 0.43	< 0.18	< 0.14	< 0.07	2
3.174383	7.5	(6.1)	0.40 ± 0.10	< 0.28	< 0.13	< 0.15	< 0.07	3
3.174750	7.9	(6.3)	1.18 ± 0.10	0.78 ± 0.28	< 0.14	< 0.15	< 0.12	4
3.175030	8.8	6.1	3.17 ± 0.11	3.05 ± 0.49	0.49 ± 0.15	< 0.15	< 0.09	5
3.175362	14.1	(13.0)	14.3 ± 0.3	10.7 ± 0.7	< 0.33	< 0.34	0.57 ± 0.17	6
3.175432	6.5	5.3	11.9 ± 0.2	29.1 ± 0.5	1.08 ± 0.23	0.90 ± 0.24	< 0.12	7
3.175603	7.6	6.6	6.02 ± 0.13	14.9 ± 0.3	0.62 ± 0.15	0.49 ± 0.16	< 0.08	8
3.175806	3.7	(2.4)	0.49 ± 0.08	0.68 ± 0.23	< 0.12	< 0.12	< 0.06	9

^aSi IV values are from $\lambda 1403$ only, as $\lambda 1394$ is in the forest.

^bSi IV $\lambda 1403$ is blended with Si IV $\lambda 1394$ at $z = 2.726$.

^cThis is a mildly-damped Lyman α system with very strong Si II $\lambda 1527$ spanning components 5–9; for these collectively a good fit to the damping wings is given by $\log N(\text{H I}) \sim 19.4$. C IV $\lambda 1551$ is blended with strong Si II $\lambda 1527$ at $z = 2.830$ and is not used. Si II values are from $\lambda 1527$.

^dC IV $\lambda 1548$ is blended with strong Si II $\lambda 1527$ at $z = 2.827$; in component 2 both members of the doublet are saturated and the value (in square brackets) is highly approximate. C II is in the forest; the values for components 2 and 3 are extracted from a complex blend with Si III $\lambda 1207$ at $z = 3.174$ and H I, and are indicative only. N V is in the forest but gives good values for the two strong components; these appear to be slightly broader than is consistent with C IV although the partial saturation makes this uncertain.

^eThis is a damped Lyman α system with very strong C II and Si II centred on components 5 and 13–18; for these collectively a reasonable fit to the damping wings is given by $\log N(\text{H I}) \sim 20.3$. Si II is obtained from appropriate sections of $\lambda 1527$, which is partially blended with C IV $\lambda 1548$ at $z = 2.773$, and of $\lambda 1260$ and $\lambda 1190$, which are in the forest but useful in parts. C II is heavily saturated in components 12–18, and Si II $\lambda 1527$ in 14–18: these regions are not included.

^fC II requires a strong, narrow component apparently with $N(\text{C II}) = (1.28 \pm 0.09) \times 10^{13}$ at $z = 2.830513$, but this is inconsistent with the pattern in the other species so probably the feature is spurious and is not included. Si II is from $\lambda 1527$; blending with C IV $\lambda 1551$ at $z = 2.770$ masks the first few components.

^gIn component 4 C II is obscured by the outlying component 11 of Si II $\lambda 1527$ in the $z = 2.770$ system.

^hSi IV $\lambda 1403$ is masked by C IV $\lambda 1548$ at $z = 2.646$. C II is contaminated by Si IV $\lambda 1403$ between the systems at $z = 2.827$ and $z = 2.830$ and is too uncertain to use.

ⁱIn component 3 C IV $\lambda 1551$ at $z = 2.646$ encroaches on Si IV $\lambda 1394$ and $\lambda 1403$ is too noisy to be useful. In component 2 C II seems contaminated and is not included.

^jC IV $\lambda 1551$ contains C IV $\lambda 1548$ at $z = 3.074$.

^kN V values are from $\lambda 1243$, which is outside the forest.

^lIn components 1–5 C IV $\lambda 1548$ is blended with strong Al II $\lambda 1671$ at $z = 2.830$ and is not used. N V is out of the forest; in components 1–5 $\lambda 1243$ is contaminated with Mg II $\lambda 2796$ at $z = 0.837$ and is not used.

^mComponent 7 of C IV $\lambda 1551$ is blended with Ni II $\lambda 1710$ at $z = 2.770$. N V $\lambda 1243$ is obscured by Ni II $\lambda 1370$ at $z = 2.770$.

ⁿThis is close to z_{em} . In component 5 Si IV $\lambda 1394$ contains an unknown interloper and is not used.

Table 7. Heavy Element Absorption Lines: Q1422+2309C $z_{em} = 3.628$

z	$b(\text{C})$ km s^{-1}	$b(\text{Si})$ km s^{-1}	$N(\text{C IV})$ 10^{12}cm^{-2}	$N(\text{Si IV})$ 10^{11}cm^{-2}	$N(\text{C II})$ 10^{12}cm^{-2}	$N(\text{Si II})$ 10^{11}cm^{-2}	$N(\text{N V})$ 10^{12}cm^{-2}	n
1	2	3	4	5	6	7	8	9
2.666								
2.664781	12.2	...	0.51 ± 0.08	1
2.665222	11.0	...	2.32 ± 0.08	2
2.665472	11.0	...	1.95 ± 0.10	3
2.665677	19.0	...	0.99 ± 0.12	4
2.666934	23.8	...	1.75 ± 0.11	5
2.683								
2.682774	12.3	...	5.55 ± 0.45	1
2.682926	5.9	...	0.98 ± 0.20	2
2.683053	5.5	...	1.18 ± 0.17	3
2.698								
2.696877	4.4	...	0.39 ± 0.09	1
2.697222	16.3	...	3.73 ± 0.17	2
2.697658	11.6	...	9.58 ± 0.16	3
2.698099	9.1	...	1.11 ± 0.12	4
2.698400	9.6	...	9.62 ± 0.17	5
2.698586	15.3	...	7.62 ± 0.19	6
2.698882	13.9	...	5.46 ± 0.15	7
2.720								
2.719820	12.1	...	1.26 ± 0.13	1
2.720073	7.9	...	1.74 ± 0.12	2
2.720227	6.9	...	4.84 ± 0.14	3
2.720556	6.4	...	0.29 ± 0.10	4
2.720706	3.8	...	0.29 ± 0.08	5
2.720877	6.5	...	0.40 ± 0.10	6
2.749 ^a								
2.748395	7.4	...	0.78 ± 0.20	1
2.748609	6.0	...	0.92 ± 0.18	2
2.748772	6.6	...	1.64 ± 0.20	3
2.748898	5.1	(3.6)	11.8 ± 0.3	76.8 ± 3.3	4
2.748988	7.9	(6.5)	9.43 ± 0.32	27.5 ± 1.7	5
2.749192	6.5	...	8.29 ± 0.22	6
2.749424	8.4	...	1.65 ± 0.26	7
2.749682	29.1	...	5.23 ± 0.89	8
2.749869	6.6	...	3.36 ± 0.27	9
2.772								
2.771677	8.2	...	1.36 ± 0.10	1
2.797								
2.796547	3.9	...	0.61 ± 0.16	1
2.796770	15.6	...	2.29 ± 0.33	2
2.810								
2.809782	8.4	...	1.82 ± 0.19	1
2.895								
2.895100	16.6	...	2.04 ± 0.19	1
2.895453	13.4	...	7.51 ± 0.27	2
2.895619	24.7	...	5.03 ± 0.34	3

Table 7—Continued

z	$b(\text{C})$ km s^{-1}	$b(\text{Si})$ km s^{-1}	$N(\text{C IV})$ 10^{12}cm^{-2}	$N(\text{Si IV})$ 10^{11}cm^{-2}	$N(\text{C II})$ 10^{12}cm^{-2}	$N(\text{Si II})$ 10^{11}cm^{-2}	$N(\text{N V})$ 10^{12}cm^{-2}	n
1	2	3	4	5	6	7	8	9
2.908								
2.907689	7.1	...	0.35 ± 0.10	1
2.908058	15.6	...	0.62 ± 0.15	2
2.910								
2.909696	11.1	...	2.54 ± 0.23	1
2.946 ^b								
2.945154	4.1	...	0.67 ± 0.21	1
2.945482	11.7	...	1.41 ± 0.37	2
2.947520	8.3	...	3.11 ± 0.26	3
2.962								
2.960740	21.5	...	2.15 ± 0.26	1
2.961036	11.0	...	2.22 ± 0.19	2
2.961527	8.3	...	3.03 ± 0.16	3
2.961866	10.2	...	14.7 ± 0.2	4
2.962084	7.4	...	6.12 ± 0.18	5
2.962367	10.1	...	6.82 ± 0.19	6
2.971 ^c								
2.971006	17.0	...	0.58 ± 0.50	1
2.971447	14.3	...	2.05 ± 0.46	2
2.971637	3.5	...	0.43 ± 0.12	3
2.976								
2.975823	23.4	...	2.55 ± 0.24	1
2.976224	10.6	...	6.54 ± 0.18	2
2.999								
2.999214	9.4	...	1.19 ± 0.40	1
2.999228	25.1	...	5.03 ± 0.63	2
3.036								
3.035061	4.7	...	0.95 ± 0.13	1
3.036510	12.7	...	1.40 ± 0.20	2
3.064 ^d								
3.063229	6.6	(5.4)	1.52 ± 0.26	< 0.20	1
3.063442	5.8	(4.8)	2.57 ± 0.38	< 0.27	2
3.063491	17.5	(16.6)	3.98 ± 0.63	< 0.48	3
3.063997	18.8	(18.0)	2.49 ± 0.43	< 0.32	4
3.064458	9.2	(7.4)	1.71 ± 0.49	< 0.22	5
3.071								
3.071100	7.2	(5.7)	4.40 ± 0.25	< 0.36	1
3.086 ^e								
3.086064	5.6	(4.4)	1.06 ± 0.28	< 0.39	1
3.086338	2.7	(2.2)	0.52 ± 0.15	< 0.28	2
3.086675	7.1	(5.9)	5.97 ± 0.31	< 0.39	3
3.086839	8.6	(6.8)	2.10 ± 0.31	< 0.45	4
3.090 ^f								
3.089900	13.0	(11.8)	10.0 ± 0.4	2.27 ± 0.99	1
3.089958	4.7	(3.6)	0.47 ± 0.28	2.65 ± 0.63	2
3.090280	14.1	(13.0)	14.1 ± 0.3	12.3 ± 0.7	3
3.090533	6.9	(5.5)	4.22 ± 0.23	4.00 ± 0.45	4

Table 7—Continued

z	$b(\text{C})$ km s^{-1}	$b(\text{Si})$ km s^{-1}	$N(\text{C IV})$ 10^{12}cm^{-2}	$N(\text{Si IV})$ 10^{11}cm^{-2}	$N(\text{C II})$ 10^{12}cm^{-2}	$N(\text{Si II})$ 10^{11}cm^{-2}	$N(\text{N V})$ 10^{12}cm^{-2}	n
1	2	3	4	5	6	7	8	9
3.090793	7.0	(5.6)	2.94 ± 0.23	3.12 ± 0.80	5
3.091068	8.7	(6.9)	10.6 ± 0.2	9.16 ± 0.84	6
3.095								
3.094889	34.0	(33.6)	2.07 ± 0.79	< 4.90	1
3.135 ^g								
3.132520	25.5	(24.9)	2.79 ± 0.36	< 1.16	1
3.133873	23.5	(22.9)	7.95 ± 0.40	8.95 ± 0.79	2
3.134141	4.1	(2.7)	0.92 ± 0.18	0.77 ± 0.33	3
3.134477	13.9	(12.8)	8.83 ± 0.30	5.13 ± 0.81	4
3.136905	8.2	(6.8)	1.17 ± 0.24	5.17 ± 0.50	5
3.137113	7.2	(5.3)	0.84 ± 0.37	4.79 ± 0.66	6
3.137169	18.0	(17.1)	5.35 ± 0.59	6.26 ± 1.17	7
3.191								
3.191375	3.2	(2.2)	0.44 ± 0.12	0.91 ± 0.47	1
3.191465	8.9	(7.1)	1.09 ± 0.20	< 0.74	2
3.240								
3.240194	19.6	(18.9)	2.02 ± 0.31	< 1.12	< 0.17	1
3.240683	6.0	(3.9)	0.80 ± 0.17	< 0.57	< 0.21	2
3.257								
3.256900	3.7	(2.4)	0.33 ± 0.13	< 0.41	< 0.15	1
3.257301	11.1	(9.6)	0.64 ± 0.21	< 1.79	< 1.06	2
3.265								
3.264800	24.1	(23.5)	0.74 ± 0.34	3.89 ± 1.30	< 0.70	1
3.265423	3.7	(2.4)	0.69 ± 0.14	1.85 ± 0.43	< 0.18	2
3.265766	14.8	(13.7)	3.75 ± 0.26	< 0.91	< 0.30	3
3.381 ^h								
3.380070	22.5	(21.9)	6.52 ± 0.61	< 1.64	< 0.54	1
3.380491	7.0	(5.7)	0.30 ± 0.28	...	< 0.30	2
3.380702	13.1	(11.9)	2.53 ± 0.42	< 1.01	< 0.31	3
3.381418	10.9	(9.4)	4.10 ± 0.38	< 0.87	< 0.28	4
3.381678	9.4	(7.6)	14.0 ± 0.4	< 0.76	< 0.27	5
3.382043	11.5	(10.1)	6.79 ± 0.40	< 0.89	< 0.29	6
3.382311	10.0	(8.4)	8.68 ± 0.37	2.81 ± 1.06	< 0.28	7
3.382702	8.2	(6.3)	3.27 ± 0.38	< 1.19	< 0.31	8
3.382897	34.1	(33.7)	4.73 ± 0.91	< 2.29	< 0.65	9
3.411 ⁱ								
3.411015	23.7	(23.0)	1.85 ± 0.35	< 2.55	< 0.52	1
3.411549	18.1	(17.2)	7.21 ± 0.33	5.11 ± 2.17	2
3.449 ^j								
3.446226	14.8	(13.7)	2.95 ± 0.43	< 1.13	< 0.48	1
3.446600	12.6	(11.4)	1.51 ± 0.39	4.72 ± 0.89	< 0.35	2
3.446920	6.4	5.6	8.18 ± 0.34	28.2 ± 0.8	< 0.32	3
3.447182	9.4	(7.8)	7.56 ± 0.41	16.8 ± 0.8	< 0.32	4
3.447436	10.9	(9.5)	19.1 ± 0.6	36.9 ± 1.0	< 0.44	5
3.448237	12.4	(11.1)	1.15 ± 0.36	1.94 ± 0.85	< 0.84	6
3.448651	13.9	(12.7)	3.44 ± 0.46	17.7 ± 1.0	2.38 ± 0.36	7
3.449293	15.6	(14.6)	2.48 ± 0.59	6.39 ± 1.00	< 0.37	8

Table 7—Continued

z	$b(\text{C})$ km s^{-1}	$b(\text{Si})$ km s^{-1}	$N(\text{C iv})$ 10^{12}cm^{-2}	$N(\text{Si iv})$ 10^{11}cm^{-2}	$N(\text{C II})$ 10^{12}cm^{-2}	$N(\text{Si II})$ 10^{11}cm^{-2}	$N(\text{N v})$ 10^{12}cm^{-2}	n
1	2	3	4	5	6	7	8	9
3.450572	7.4	(6.0)	0.89 ± 0.31	< 0.96	< 0.59	9
3.451366	16.0	(15.0)	10.5 ± 0.7	5.83 ± 1.02	< 0.36	10
3.452104	7.9	(6.3)	0.82 ± 0.29	3.51 ± 0.70	< 0.33	11
3.480 ^k								
3.479506	15.3	(14.2)	1.75 ± 0.45	< 1.10	< 0.70	< 0.54	...	1
3.479808	3.7	(2.4)	0.95 ± 0.25	< 0.48	< 0.32	< 0.11	...	2
3.480393	8.4	(6.5)	0.88 ± 0.33	< 0.68	< 0.44	< 0.25	...	3
3.494 ^l								
3.493317	14.6	(13.5)	2.02 ± 0.37	< 1.00	< 0.78	< 0.28	...	1
3.494874	6.6	(5.8)	2.08 ± 0.25	< 0.90	< 0.38	< 0.16	...	2
3.515 ^m								
3.514535	11.3	(9.9)	0.71 ± 0.27	2.73 ± 1.60	< 0.30	< 0.44	...	1
3.514666	6.2	(5.0)	5.79 ± 0.28	5.69 ± 1.28	< 0.52	< 0.38	...	2
3.514808	11.8	(10.5)	0.85 ± 0.33	< 3.74	< 0.52	< 0.50	...	3
3.515015	10.4	(8.9)	1.65 ± 0.25	< 1.21	< 0.31	< 0.39	...	4
3.538 ⁿ								
3.534600	22.7	(22.0)	5.12 ± 0.41	< 1.26	< 0.30	< 0.70	< 0.39	1
3.534900	3.3	(2.2)	1.55 ± 0.20	< 0.51	< 0.21	< 0.29	< 0.28	2
3.535083	7.4	(5.1)	4.60 ± 0.26	< 0.63	...	< 0.35	< 0.19	3
3.535589	19.5	(18.7)	9.82 ± 0.44	< 1.82	...	< 0.67	< 0.31	4
3.535966	12.8	(11.6)	27.2 ± 0.6	38.2 ± 1.3	< 0.41	< 0.61	< 0.33	5
3.536159	5.5	(3.7)	4.67 ± 0.42	21.7 ± 0.9	1.27 ± 0.20	< 0.37	< 0.28	6
3.536394	35.7	(35.3)	32.1 ± 1.0	37.0 ± 2.7	1.27 ± 0.63	7
3.536661	9.5	(8.9)	< 0.45	6.48 ± 1.18	2.75 ± 0.27	2.48 ± 0.60	< 0.40	8
3.537267	6.6	(5.5)	5.93 ± 0.61	56.4 ± 1.9	2.60 ± 0.41	3.55 ± 0.74	< 0.30	9
3.537330	19.1	(18.3)	7.76 ± 1.21	32.5 ± 3.0	5.87 ± 0.82	2.65 ± 1.46	< 0.72	10
3.537502	7.1	4.8	4.70 ± 0.49	12.0 ± 1.1	< 0.37	0.85 ± 0.53	< 0.29	11
3.538037	20.6	(19.8)	4.50 ± 0.41	7.58 ± 1.23	< 0.28	< 0.66	< 0.34	12
3.538625	22.2	(21.5)	38.6 ± 0.8	69.3 ± 2.0	1.16 ± 0.42	...	< 0.46	13
3.538729	6.1	4.5	24.8 ± 1.0	74.3 ± 2.0	1.20 ± 0.26	0.76 ± 0.47	< 0.28	14
3.538821	5.2	(3.8)	2.64 ± 0.53	13.4 ± 1.5	0.98 ± 0.21	1.36 ± 0.38	< 0.31	15
3.539320	9.1	(7.5)	22.2 ± 0.6	21.6 ± 1.3	< 0.32	< 0.62	< 0.43	16
3.539530	6.8	(5.2)	8.83 ± 0.50	8.23 ± 1.31	< 0.32	< 0.51	< 0.32	17
3.539539	29.2	(28.7)	7.72 ± 1.19	< 3.71	< 0.84	< 1.50	< 0.66	18
3.539921	8.7	(6.8)	< 0.52	< 1.14	1.21 ± 0.32	1.38 ± 0.49	< 0.39	19
3.540053	5.7	(4.6)	0.54 ± 0.27	5.44 ± 0.73	1.08 ± 0.22	1.12 ± 0.34	...	20
3.540232	6.8	(5.9)	0.97 ± 0.32	2.27 ± 0.88	2.55 ± 0.27	3.64 ± 0.44	< 0.27	21
3.540307	32.9	(32.4)	5.22 ± 0.74	< 7.86	< 1.67	22
3.541473	8.5	(6.9)	2.60 ± 0.26	< 0.84	< 0.22	< 4.86	< 0.51	23
3.588 ^o								
3.586854	15.6	(14.6)	9.40 ± 0.23	16.1 ± 1.1	< 0.48	...	< 0.41	1
3.587173	16.0	(15.0)	7.07 ± 0.21	4.72 ± 1.09	< 0.58	...	< 0.48	2
3.588893	18.7	(17.9)	2.53 ± 0.19	< 1.09	< 0.49	< 0.65	< 0.86	3
3.589238	9.8	(8.1)	2.97 ± 0.15	< 1.19	< 0.36	< 0.47	< 0.48	4
3.589597	15.0	(14.0)	0.48 ± 0.17	< 2.13	< 0.49	< 0.94	< 0.44	5
3.624 ^p								
3.623388	7.2	(4.7)	3.02 ± 0.18	< 0.95	< 0.32	< 0.27	0.85 ± 0.20	1

Table 7—Continued

z	$b(\text{C})$ km s^{-1}	$b(\text{Si})$ km s^{-1}	$N(\text{C IV})$ 10^{12}cm^{-2}	$N(\text{Si IV})$ 10^{11}cm^{-2}	$N(\text{C II})$ 10^{12}cm^{-2}	$N(\text{Si II})$ 10^{11}cm^{-2}	$N(\text{N V})$ 10^{12}cm^{-2}	n
1	2	3	4	5	6	7	8	9
3.623546	5.7	(4.5)	12.9 ± 0.3	< 0.58	< 0.36	< 0.29	4.84 ± 0.35	2
3.623668	5.9	(4.7)	9.83 ± 0.24	< 0.57	< 0.34	< 0.29	8.21 ± 0.28	3
3.623857	7.8	(6.6)	7.45 ± 0.19	< 0.62	< 0.48	< 0.31	2.11 ± 0.23	4
3.624206	10.6	(9.1)	13.1 ± 0.3	< 0.76	< 0.58	< 0.37	5.41 ± 0.27	5
3.624360	4.4	(3.0)	5.21 ± 0.33	2.45 ± 0.62	< 0.49	< 0.51	2.09 ± 0.23	6
3.624433	5.7	(4.7)	18.3 ± 0.4	2.72 ± 0.69	< 0.42	< 0.34	1.76 ± 0.30	7
3.624659	9.8	(8.1)	3.99 ± 0.20	< 0.67	< 0.65	< 0.35	0.71 ± 0.22	8
3.624913	8.6	(6.7)	1.95 ± 0.17	< 0.61	< 0.40	< 0.30	0.52 ± 0.19	9
3.625269	12.9	(11.6)	3.48 ± 0.21	< 0.84	< 0.41	< 0.38	0.67 ± 0.27	10

^aComponents 1 and 2 of C IV $\lambda 1548$ are blended with Si IV $\lambda 1403$ at $z = 3.135$ and are not used. Although Si IV is in the forest, for $\lambda 1394$ the strong components 4 and 5 are in a relatively clear region and give reliable values.

^bComponents 1 and 2 of C IV $\lambda 1548$ are blended with Si IV $\lambda 1394$ at $z = 3.381$.

^cC IV $\lambda 1548$ is blended with Si IV $\lambda 1394$ at $z = 3.411$ and Si IV $\lambda 1403$ at $z = 3.381$.

^dIn component 5 C IV $\lambda 1548$ is blended with Si IV $\lambda 1394$ at $z = 3.515$; $\lambda 1551$ includes strong C IV $\lambda 1551$ at $z = 3.071$. Si IV $\lambda 1403$ mostly is masked by Si IV $\lambda 1394$ at $z = 3.090$ and C IV $\lambda 1548$ at $z = 2.683$.

^eC IV $\lambda 1548$ is blended with Si IV $\lambda 1394$ at $z = 3.538$.

^fC IV $\lambda 1548$ contains Si IV $\lambda 1403$ at $z = 3.515$. Si IV $\lambda 1394$ is in a blend with C IV $\lambda 1548$ at $z = 2.685$, very weak Si IV $\lambda 1403$ at $z = 3.064$ and an unidentified interloper observed at $\lambda 5701.65$, while $\lambda 1403$ is partly contaminated, but from the available complementary regions good values for Si IV are obtained.

^gComponent 1 of Si IV $\lambda 1394$ is masked by C IV $\lambda 1548$ at $z = 2.720$; components 5–7 of $\lambda 1403$ are blended with C IV $\lambda 1548$ at $z = 2.749$.

^hThis is nominally a partial Lyman limit system with total $\log N(\text{H I}) \sim 17.2$ but the metal low ionization components are relatively very weak. Si IV $\lambda 1394$ in component 2 coincides with an unidentified feature, and in components 7 and 8 is blended with C IV $\lambda 1548$ at $z = 2.946$, while $\lambda 1403$ in components 1 and 2 is blended with C IV $\lambda 1551$ at $z = 2.962$, in components 8 and 9 with C IV $\lambda 1548$ at $z = 2.971$, and in component 8 also with very weak Si IV $\lambda 1394$ at $z = 3.411$; nevertheless, acceptable Si IV values are obtained for all but component 2. In components 8 and 9 C II is blended with weak C IV $\lambda 1551$ at $z = 2.772$ but the upper limits obtained are reliable.

ⁱSi IV $\lambda 1394$ is blended with C IV $\lambda 1548$ at $z = 2.971$ and Si IV $\lambda 1403$ at $z = 3.381$. Component 2 of C II is masked by C IV $\lambda 1551$ at $z = 2.797$.

^jC IV is contaminated by numerous, very sharp absorption features in the atmospheric B band, but, by including these in the fitting process for both lines, acceptable values for C IV are obtained in all components.

^kSi IV $\lambda 1403$ is heavily contaminated and the upper limits are from $\lambda 1394$ alone.

^lSi IV $\lambda 1403$ contains C IV $\lambda 1548$ at $z = 3.071$ and C IV $\lambda 1551$ at $z = 3.064$ and is not used.

^mSi IV $\lambda 1394$ is blended with C IV $\lambda 1548$ at $z = 3.064$; $\lambda 1403$ is blended with strong C IV $\lambda 1548$ at $z = 3.090$.

ⁿComponents 14–17 of Si IV $\lambda 1394$ are blended with C IV $\lambda 1548$ at $z = 3.086$. In components 3 and 4 C II is too uncertain due to blending with C IV $\lambda 1548$ at $z = 2.910$. N V $\lambda 1243$ is outside the forest.

^oComponent 2 of C II is blended with C IV $\lambda 1551$ at $z = 2.946$ but a useful upper limit is obtained from the C IV doublet. In components 1 and 2 Si II seems too strong relative to C II and probably contains an unidentified interloper. N V is outside the forest; in components 1 and 2 $\lambda 1243$ is masked by Si IV $\lambda 1394$ at $z = 3.090$.

^pThis is close to z_{em} .

Table 8. Heavy Element Absorption Lines: Q1645+5520 $z_{em} = 4.059$

z	$b(\text{C})$ km s^{-1}	$b(\text{Si})$ km s^{-1}	$N(\text{C IV})$ 10^{12}cm^{-2}	$N(\text{Si IV})$ 10^{11}cm^{-2}	$N(\text{C II})$ 10^{12}cm^{-2}	$N(\text{Si II})$ 10^{11}cm^{-2}	$N(\text{N V})$ 10^{12}cm^{-2}	n
1	2	3	4	5	6	7	8	9
3.015 ^a								
3.015050	7.6	...	0.33 ± 0.14	1
3.077								
3.076981	9.4	...	1.87 ± 0.17	1
3.077221	7.5	...	7.76 ± 0.20	2
3.129								
3.128710	9.6	...	5.63 ± 0.18	1
3.128965	8.8	...	3.32 ± 0.17	2
3.129373	12.3	...	0.58 ± 0.17	3
3.129718	3.9	...	0.39 ± 0.12	4
3.162								
3.161225	10.7	...	1.53 ± 0.18	1
3.161492	11.1	...	2.19 ± 0.19	2
3.161902	6.9	...	0.86 ± 0.15	3
3.162173	8.2	...	3.78 ± 0.18	4
3.162467	17.0	...	4.51 ± 0.23	5
3.163007	20.4	...	2.00 ± 0.23	6
3.163694	14.8	...	1.42 ± 0.20	7
3.193								
3.191963	12.3	...	1.57 ± 0.16	1
3.192446	6.7	...	2.94 ± 0.15	2
3.192939	54.9	...	11.8 ± 0.6	3
3.193282	15.8	...	22.1 ± 0.6	4
3.193326	26.4	...	10.5 ± 0.8	5
3.197								
3.197463	21.8	...	2.38 ± 0.17	1
3.217								
3.216356	9.5	...	2.34 ± 0.17	1
3.216813	24.6	...	3.71 ± 0.26	2
3.262								
3.261994	7.3	...	1.58 ± 0.25	1
3.262161	12.3	...	0.69 ± 0.19	2
3.289								
3.287711	27.0	...	3.72 ± 0.28	1
3.287996	4.8	...	0.96 ± 0.15	2
3.288217	13.6	...	10.5 ± 0.2	3
3.288687	16.6	...	14.1 ± 0.3	4
3.288982	6.2	...	3.93 ± 0.29	5
3.289042	18.0	...	10.3 ± 0.4	6
3.290097	21.9	...	4.97 ± 0.28	7
3.322 ^b								
3.321753	21.4	...	1.74 ± 0.22	1
3.322353	10.0	...	2.34 ± 0.18	2
3.322653	11.5	...	3.72 ± 0.19	3
3.323056	19.4	...	2.38 ± 0.25	4
3.341 ^c								
3.340614	10.5	...	1.06 ± 0.18	1
3.340873	7.7	...	1.08 ± 0.19	2
3.341186	9.0	...	1.35 ± 0.23	3
3.341488	19.6	...	1.43 ± 0.35	4

Table 8—Continued

z	$b(\text{C})$ km s^{-1}	$b(\text{Si})$ km s^{-1}	$N(\text{C IV})$ 10^{12}cm^{-2}	$N(\text{Si IV})$ 10^{11}cm^{-2}	$N(\text{C II})$ 10^{12}cm^{-2}	$N(\text{Si II})$ 10^{11}cm^{-2}	$N(\text{N V})$ 10^{12}cm^{-2}	n
1	2	3	4	5	6	7	8	9
3.341989	6.0	...	0.60 ± 0.26	5
3.348								
3.347710	11.7	...	0.29 ± 0.16	1
3.348360	3.0	...	0.20 ± 0.11	2
3.348956	4.2	...	0.15 ± 0.10	3
3.349254	3.3	...	0.17 ± 0.13	4
3.355								
3.354910	38.2	...	2.04 ± 0.30	1
3.355446	4.2	...	0.57 ± 0.13	2
3.355875	13.3	...	1.75 ± 0.19	3
3.421 ^d								
3.420535	6.9	(5.7)	4.12 ± 0.24	7.72 ± 0.37	1
3.420683	5.5	(4.4)	2.20 ± 0.13	15.8 ± 0.4	2
3.420864	7.8	(6.3)	2.90 ± 0.12	6.15 ± 0.38	3
3.421238	15.4	(14.4)	1.09 ± 0.14	3.15 ± 0.77	4
3.468 ^e								
3.467167	20.2	(19.5)	7.25 ± 0.44	4.44 ± 0.74	1
3.467472	9.1	(7.3)	0.77 ± 0.26	3.40 ± 0.52	2
3.467777	12.4	(11.1)	7.70 ± 0.32	9.72 ± 0.60	3
3.467994	9.1	(7.3)	4.75 ± 0.27	6.65 ± 0.49	4
3.514 ^f								
3.513453	3.8	...	0.18 ± 0.11	1
3.513718	7.9	...	0.57 ± 0.15	2
3.514168	12.0	(10.6)	2.10 ± 0.21	2.60 ± 1.06	3
3.514432	8.0	(6.5)	6.32 ± 0.20	4.66 ± 1.50	4
3.514709	8.2	(6.8)	1.63 ± 0.17	< 1.28	5
3.544 ^g								
3.541744	23.7	(23.1)	4.70 ± 0.41	7.15 ± 1.42	1
3.542083	10.5	(8.9)	5.18 ± 0.31	12.8 ± 1.1	2
3.542454	13.6	(12.5)	26.7 ± 0.5	79.7 ± 1.6	3
3.542692	11.9	(10.6)	27.2 ± 0.7	43.5 ± 1.8	4
3.542994	17.2	(16.3)	29.7 ± 0.7	27.6 ± 1.9	5
3.543191	5.7	(4.8)	6.26 ± 0.40	< 1.26	6
3.543368	8.5	(7.0)	13.8 ± 0.4	14.4 ± 1.2	7
3.543649	9.6	(7.3)	10.2 ± 0.3	21.1 ± 1.0	8
3.544189	37.0	(36.6)	22.5 ± 0.6	10.7 ± 2.1	9
3.544496	5.9	4.0	13.2 ± 0.4	37.3 ± 0.9	10
3.544690	3.7	(2.4)	2.49 ± 0.22	3.88 ± 0.53	11
3.544864	6.5	4.3	17.1 ± 0.4	18.3 ± 0.7	12
3.545139	12.2	(10.9)	2.20 ± 0.30	3.21 ± 0.85	13
3.545413	13.5	(12.4)	0.98 ± 0.38	6.37 ± 1.06	14
3.545672	20.6	(19.9)	1.22 ± 0.44	6.95 ± 1.34	15
3.546050	9.6	(8.1)	0.84 ± 0.24	2.80 ± 0.71	16
3.567								
3.566881	18.6	(17.8)	4.43 ± 0.30	< 0.76	1
3.690 ^h								
3.689727	3.7	(2.5)	0.71 ± 0.13	< 0.80	< 0.17	1
3.689991	9.9	(8.2)	1.89 ± 0.19	< 0.98	< 0.30	2
3.690295	10.2	(8.6)	4.35 ± 0.20	1.41 ± 0.98	< 0.24	3
3.690628	9.7	(8.0)	1.57 ± 0.18	< 0.97	4

Table 8—Continued

z	$b(\text{C})$ km s^{-1}	$b(\text{Si})$ km s^{-1}	$N(\text{C IV})$ 10^{12}cm^{-2}	$N(\text{Si IV})$ 10^{11}cm^{-2}	$N(\text{C II})$ 10^{12}cm^{-2}	$N(\text{Si II})$ 10^{11}cm^{-2}	$N(\text{N V})$ 10^{12}cm^{-2}	n
1	2	3	4	5	6	7	8	9
3.752 ⁱ								
3.751265	4.8	(3.8)	2.13 ± 0.27	< 0.78	1
3.751585	30.1	(29.6)	6.29 ± 0.60	< 1.40	2
3.752008	6.0	4.4	18.1 ± 0.5	4.25 ± 0.61	< 0.32	3
3.752337	11.2	(9.8)	7.66 ± 0.43	2.12 ± 0.82	< 0.49	4
3.752502	3.3	(2.2)	3.17 ± 1.04	10.7 ± 1.2	< 0.43	5
3.752563	6.6	(5.1)	28.2 ± 1.3	23.0 ± 1.3	< 0.53	6
3.752770	5.4	(4.4)	10.6 ± 0.6	18.5 ± 1.0	7
3.752826	17.8	(17.0)	7.86 ± 0.76	4.31 ± 1.64	8
3.753340	5.9	(4.9)	2.74 ± 0.34	2.13 ± 0.59	< 0.27	9
3.753529	4.9	3.6	5.19 ± 0.64	12.3 ± 1.0	10
3.753601	11.1	(9.6)	13.6 ± 0.7	2.35 ± 1.21	11
3.759 ^j								
3.758248	13.2	(12.0)	10.2 ± 0.5	14.5 ± 0.9	1
3.758554	6.4	(4.2)	0.68 ± 0.28	< 0.60	2
3.758853	6.9	(5.8)	1.07 ± 0.28	< 0.67	< 0.35	3
3.779 ^k								
3.779260	9.3	(7.5)	2.45 ± 0.27	< 0.99	< 0.29	1
3.811								
3.810703	15.3	(14.3)	1.34 ± 0.28	< 1.40	< 0.76	1
3.811069	7.2	(6.2)	3.78 ± 0.22	< 1.39	< 0.43	2
3.863 ^l								
3.863047	8.6	(6.8)	0.80 ± 0.25	< 1.52	1
3.863418	12.8	(11.6)	2.35 ± 0.31	2.21 ± 0.84	2
3.882								
3.880075	49.7	(49.4)	12.1 ± 0.6	9.92 ± 1.49	< 0.72	1
3.880869	5.3	(4.3)	1.24 ± 0.22	< 0.50	< 0.58	2
3.976 ^m								
3.974266	34.1	(33.6)	2.60 ± 0.53	< 2.37	1
3.975273	12.9	(11.6)	1.49 ± 0.30	< 1.24	2
3.976187	32.9	...	4.62 ± 0.51	3
3.976666	7.2	...	0.75 ± 0.25	4
3.977361	21.4	...	1.59 ± 0.40	5
3.994								
3.993825	11.6	(10.3)	3.40 ± 0.25	< 0.91	< 0.44	1
3.994106	8.8	(7.1)	2.00 ± 0.22	< 0.74	< 0.43	2
4.024 ⁿ								
4.022743	18.2	...	1.78 ± 0.41	< 0.28	1
4.023270	9.4	...	3.28 ± 0.36	< 0.23	2
4.023424	4.1	(2.9)	1.57 ± 0.32	6.25 ± 0.69	< 0.19	3
4.023639	11.7	(10.4)	8.46 ± 0.42	25.7 ± 0.9	< 0.28	4
4.023960	7.5	(6.3)	3.70 ± 0.31	1.74 ± 0.66	0.41 ± 0.30	...	< 0.20	5
4.024184	4.3	(3.2)	1.20 ± 0.23	< 0.76	< 0.50	...	< 0.16	6
4.024587	10.4	(8.9)	1.62 ± 0.30	< 0.71	< 0.21	7
4.031 ^o								
4.029112	6.1	(5.1)	1.29 ± 0.35	< 0.85	< 0.30	< 0.47	< 0.19	1
4.029265	8.3	(7.1)	1.78 ± 0.42	2.29 ± 0.99	< 0.38	< 0.56	< 0.27	2
4.029479	8.2	(6.8)	7.84 ± 0.48	2.31 ± 0.95	< 0.36	< 0.53	< 0.26	3
4.029667	6.7	(5.5)	17.3 ± 0.8	10.2 ± 1.5	< 0.66	< 5.49	< 0.24	4
4.029822	7.2	(6.0)	9.66 ± 1.85	84.4 ± 4.9	< 2.77	< 11.2	< 0.60	5
4.029905	8.0	(6.6)	< 3.37	< 7.76	67.3 ± 4.1	117 ± 15	< 0.80	6

Table 8—Continued

z	$b(\text{C})$ km s^{-1}	$b(\text{Si})$ km s^{-1}	$N(\text{C IV})$ 10^{12}cm^{-2}	$N(\text{Si IV})$ 10^{11}cm^{-2}	$N(\text{C II})$ 10^{12}cm^{-2}	$N(\text{Si II})$ 10^{11}cm^{-2}	$N(\text{N V})$ 10^{12}cm^{-2}	n
1	2	3	4	5	6	7	8	9
4.030016	8.4	(6.7)	19.4 ± 1.5	17.9 ± 2.1	8.40 ± 1.98	< 14.0	< 0.43	7
4.030195	5.1	(4.1)	2.74 ± 0.49	4.03 ± 0.96	38.8 ± 1.1	109 ± 6	< 0.24	8
4.030401	9.3	(7.6)	13.3 ± 0.6	62.1 ± 1.8	33.3 ± 0.8	66.6 ± 4.3	< 0.25	9
4.030537	4.3	(3.5)	< 0.56	2.64 ± 1.54	42.8 ± 1.6	80.1 ± 4.4	< 0.23	10
4.030638	7.4	(6.1)	5.24 ± 0.64	47.4 ± 2.0	4.28 ± 0.82	8.88 ± 1.75	< 0.29	11
4.030804	11.7	(10.3)	7.53 ± 0.53	25.0 ± 1.8	0.80 ± 0.44	...	< 0.33	12
4.031558	26.0	(25.4)	5.34 ± 1.05	6.69 ± 2.96	< 0.89	...	< 0.67	13
4.031691	15.1	(14.1)	3.60 ± 0.85	< 2.90	< 0.69	...	< 0.43	14
4.032029	16.2	(15.3)	1.05 ± 0.47	< 1.08	0.66 ± 0.37	...	< 0.26	15
4.032722	6.4	(5.5)	0.46 ± 0.26	< 0.78	< 0.22	...	< 0.16	16
4.033187	18.1	(17.3)	3.04 ± 0.42	2.05 ± 1.39	< 0.38	...	< 0.36	17
4.037 ^P								
4.035756	11.3	(9.9)	4.98 ± 0.48	3.77 ± 1.14	...	< 0.40	< 0.20	1
4.036331	11.8	(10.5)	14.1 ± 0.4	20.4 ± 1.8	...	< 0.54	< 0.20	2
4.036680	6.2	(5.0)	6.61 ± 0.34	4.32 ± 0.91	...	< 0.32	< 0.25	3
4.037171	13.9	(12.8)	6.62 ± 0.41	< 0.52	...	0.89 ± 0.46	0.49 ± 0.23	4
4.037536	11.5	(10.1)	2.00 ± 0.40	2.02 ± 1.12	...	< 0.41	< 0.34	5

^aC IV $\lambda 1551$ is immersed in Si IV $\lambda 1394$ at $z = 3.468$.

^bC IV $\lambda 1551$ contains weak C II at $z = 4.024$.

^c This marks the start of a sequence of three weak C IV systems: $\lambda 1551$ blended with $\lambda 1548$ at $z = 3.348$ and $\lambda 1551$ of that system blended with $\lambda 1548$ at $z = 3.355$. Here $\lambda 1548$ contains weak C II at $z = 4.037$.

^dSi IV $\lambda 1394$ is in the forest and is not used.

^eComponent 2 of Si IV $\lambda 1394$ contains weak C IV $\lambda 1551$ at $z = 3.015$.

^fIn components 1 and 2 Si IV $\lambda 1394$ is too contaminated by atmospheric absorption to be useful, and $\lambda 1403$ is wholly masked by Si IV $\lambda 1394$ at $z = 3.544$.

^gC IV $\lambda 1551$ contains Si IV $\lambda 1403$ at $z = 4.024$. Si IV $\lambda 1394$ is partially blended with Si IV $\lambda 1403$ at $z = 3.514$ and Si II $\lambda 1260$ at $z = 4.024$, and in components 3 and 4 has interference from atmospheric emission.

^hSi IV $\lambda 1403$ and C II in component 4 are contaminated and are not used.

ⁱComponents 9–11 in C IV $\lambda 1551$ are excluded by atmospheric emission. In components 1 and 2 C II is masked by strong Si II $\lambda 1260$ at $z = 4.031$; several other components seem contaminated and are not included.

^jIn components 1 and 2 C II is too contaminated to be useful.

^kThe upper limit for Si IV is from $\lambda 1394$ alone.

^lC II is obscured by C IV $\lambda 1548$ at $z = 3.193$.

^mBoth Si IV $\lambda 1394$ and $\lambda 1403$ are largely contaminated. C II is obscured by C IV $\lambda 1548$ at $z = 3.289$.

ⁿC IV $\lambda 1551$ is blended with C IV $\lambda 1548$ at $z = 4.031$. Si IV $\lambda 1403$ is immersed in strong C IV $\lambda 1551$ at $z = 3.544$, and in components 1 and 2 $\lambda 1394$ is obscured by C IV $\lambda 1551$ at $z = 3.514$ and has interference from atmospheric absorption, but good values are obtained for components 3–7. In components 1–4 C II is dominated by C IV $\lambda 1551$ at $z = 3.322$ and in 7 is blended with Si IV $\lambda 1394$ at $z = 3.811$, making these too uncertain to include. Si II $\lambda 1260$ is completely masked by Si IV $\lambda 1394$ at $z = 3.544$. N V is outside the forest.

^oThis is a mildly-damped Lyman α system with very strong C II, Si II and O I in components 6–10: for these a good collective fit to the damping wings is given by $\log N(\text{H I}) \sim 19.7$. Onward from component 12 C IV $\lambda 1548$ is blended with C IV $\lambda 1551$ at $z = 4.024$, and in components 1 and 2 $\lambda 1551$ overlaps with C IV $\lambda 1548$ at $z = 4.037$. In the strong components Si II $\lambda 1260$ seems mildly contaminated, but together with $\lambda 1304$ and $\lambda 1527$ (itself partially contaminated by atmospheric absorption) good values are obtained for these; in components 12–17 $\lambda 1260$ is very weak and overlaps with C II at $z = 3.752$, and is excluded.

^pThis is close to z_{em} . C IV $\lambda 1548$ encroaches on C IV $\lambda 1551$ at $z = 4.031$. Si IV $\lambda 1403$ is too contaminated to be useful; $\lambda 1394$ is partly affected by atmospheric absorption but the values extracted are acceptable. C II is obscured by C IV $\lambda 1548$ at $z = 3.341$.

Table 9. Heavy Element Absorption Lines: Q1055+4611 $z_{em} = 4.131$

z	$b(\text{C})$ km s^{-1}	$b(\text{Si})$ km s^{-1}	$N(\text{C IV})$ 10^{12}cm^{-2}	$N(\text{Si IV})$ 10^{11}cm^{-2}	$N(\text{C II})$ 10^{12}cm^{-2}	$N(\text{Si II})$ 10^{11}cm^{-2}	$N(\text{N V})$ 10^{12}cm^{-2}	n
1	2	3	4	5	6	7	8	9
3.063 ^a								
3.061554	11.8	...	11.7 ± 0.5	1
3.062098	5.1	...	3.92 ± 0.33	2
3.062509	8.5	...	85.8 ± 1.5	3
3.062631	5.1	...	17.4 ± 0.8	4
3.063797	11.3	...	7.72 ± 0.49	5
3.090 ^b								
3.090400	21.3	...	1.89 ± 0.28	1
3.122								
3.121845	9.7	...	3.06 ± 0.17	1
3.122101	19.5	...	1.99 ± 0.30	2
3.122221	4.2	...	12.9 ± 0.2	3
3.122849	17.8	...	0.80 ± 0.18	4
3.154 ^c								
3.153032	17.5	...	0.64 ± 1.33	1
3.153428	14.3	...	2.97 ± 1.54	2
3.154080	21.3	...	1.00 ± 3.25	3
3.154506	16.7	...	3.23 ± 3.15	4
3.155083	16.4	...	2.26 ± 0.58	5
3.167								
3.163755	7.1	...	3.68 ± 0.22	1
3.163950	7.6	...	3.92 ± 0.23	2
3.165091	12.4	...	2.68 ± 0.25	3
3.165558	4.6	...	1.17 ± 0.17	4
3.165781	2.9	...	0.39 ± 0.15	5
3.166561	29.1	...	6.33 ± 0.41	6
3.166742	7.1	...	6.39 ± 0.24	7
3.167224	8.4	...	9.48 ± 0.22	8
3.167473	7.3	...	1.98 ± 0.18	9
3.168509	8.1	...	3.73 ± 0.21	10
3.168693	7.2	...	5.53 ± 0.23	11
3.168831	5.0	...	8.57 ± 0.24	12
3.169092	11.5	...	4.87 ± 0.22	13
3.169381	12.7	...	2.72 ± 0.22	14
3.288								
3.227592	9.8	...	11.3 ± 0.4	1
3.227819	10.2	...	5.61 ± 0.38	2
3.228245	21.5	...	2.87 ± 0.51	3
3.234								
3.233229	6.1	...	3.34 ± 0.42	1
3.233438	37.7	...	5.88 ± 1.07	2
3.233794	11.5	...	22.8 ± 0.7	3
3.235278	16.1	...	3.79 ± 0.38	4
3.238								
3.236643	13.2	...	16.7 ± 0.6	1
3.236784	4.1	...	17.1 ± 1.1	2
3.236891	6.6	...	24.0 ± 1.0	3
3.237063	11.9	...	16.8 ± 0.6	4
3.237819	9.1	...	1.34 ± 0.37	5
3.238065	9.2	...	10.1 ± 0.4	6

Table 9—Continued

z	$b(\text{C})$ km s^{-1}	$b(\text{Si})$ km s^{-1}	$N(\text{C IV})$ 10^{12}cm^{-2}	$N(\text{Si IV})$ 10^{11}cm^{-2}	$N(\text{C II})$ 10^{12}cm^{-2}	$N(\text{Si II})$ 10^{11}cm^{-2}	$N(\text{N V})$ 10^{12}cm^{-2}	n
1	2	3	4	5	6	7	8	9
3.238394	9.9	...	39.8 ± 0.8	7
3.238704	9.9	...	43.5 ± 0.9	8
3.238935	8.1	...	17.7 ± 0.6	9
3.239187	9.9	...	10.4 ± 0.4	10
3.239454	8.6	...	9.49 ± 0.44	11
3.239686	13.1	...	5.14 ± 0.48	12
3.269								
3.268635	11.6	...	4.45 ± 0.19	1
3.269058	27.5	...	2.47 ± 0.27	2
3.317 ^d								
3.314941	2.9	...	0.83 ± 0.18	1
3.315949	6.4	...	6.89 ± 0.27	2
3.316157	5.2	...	25.6 ± 0.6	3
3.316288	4.6	...	13.8 ± 0.4	4
3.316512	2.9	(1.9)	1.66 ± 0.20	4.20 ± 2.79	...	5
3.316743	3.3	...	1.20 ± 0.20	6
3.316877	7.1	(5.7)	1.28 ± 0.42	394 ± 15	...	7
3.317096	...	16.4	< 1.38	80.4 ± 29.8	...	8
3.317209	10.7	(9.1)	3.92 ± 0.76	1130 ± 53	...	9
3.317372	5.8	(4.4)	5.43 ± 0.32	300 ± 18	...	10
3.317502	6.0	(5.5)	4.96 ± 0.29	50.6 ± 5.0	...	11
3.317736	11.8	(10.4)	10.5 ± 0.4	22.7 ± 5.2	...	12
3.317904	...	5.6	< 0.34	24.1 ± 4.8	...	13
3.318032	11.1	...	8.33 ± 0.37	14
3.318580	13.4	...	3.38 ± 0.28	15
3.318987	9.4	...	1.90 ± 0.23	16
3.319472	5.7	...	1.68 ± 0.21	17
3.332 ^e								
3.331334	6.6	...	0.69 ± 0.17	1
3.331810	7.1	...	0.99 ± 0.16	2
3.332120	7.6	...	1.53 ± 0.18	3
3.332309	6.7	...	0.76 ± 0.18	4
3.332759	7.4	...	0.43 ± 0.18	5
3.359 ^f								
3.358350	10.3	...	1.25 ± 0.24	1
3.358807	15.4	...	5.23 ± 0.31	2
3.359312	18.1	...	7.89 ± 0.32	3
3.406								
3.404536	15.1	...	1.93 ± 0.39	1
3.404925	4.2	...	1.42 ± 0.25	2
3.405287	12.4	...	7.54 ± 0.40	3
3.405703	16.4	...	5.83 ± 0.42	4
3.406793	20.0	...	1.83 ± 0.36	5
3.477 ^g								
3.477280	9.6	(7.9)	8.39 ± 0.46	16.5 ± 0.6	1
3.521 ^h								
3.520890	11.6	(10.2)	5.34 ± 0.23	< 1.56	1
3.521142	7.2	(6.1)	2.28 ± 0.19	< 1.44	2

Table 9—Continued

z	$b(\text{C})$ km s^{-1}	$b(\text{Si})$ km s^{-1}	$N(\text{C IV})$ 10^{12}cm^{-2}	$N(\text{Si IV})$ 10^{11}cm^{-2}	$N(\text{C II})$ 10^{12}cm^{-2}	$N(\text{Si II})$ 10^{11}cm^{-2}	$N(\text{N V})$ 10^{12}cm^{-2}	n
1	2	3	4	5	6	7	8	9
3.533 ⁱ								
3.530549	7.3	(5.8)	3.81 ± 0.22	8.68 ± 0.78	1
3.530726	5.2	(3.6)	3.15 ± 0.34	14.4 ± 1.2	2
3.530893	15.6	(14.6)	20.8 ± 0.6	92.4 ± 1.9	3
3.531152	9.1	(6.4)	38.7 ± 1.1	78.9 ± 2.2	4
3.531349	6.3	(5.7)	19.6 ± 2.0	215 ± 11	...	49.3 ± 17.6	...	5
3.531407	7.6	(5.8)	17.4 ± 1.5	< 4.19	6
3.531621	27.8	(27.3)	35.3 ± 0.8	55.1 ± 2.3	7
3.532054	13.8	(12.7)	12.9 ± 0.5	4.31 ± 1.38	8
3.531935	5.1	(4.6)	2.18 ± 0.38	13.0 ± 1.1	9
3.532486	15.8	(14.8)	7.21 ± 0.30	21.6 ± 1.1	10
3.533012	8.7	(5.3)	2.80 ± 0.37	18.8 ± 1.2	11
3.533083	4.1	(3.8)	1.72 ± 0.30	1.41 ± 0.97	12
3.533540	20.7	(19.9)	2.07 ± 0.31	5.88 ± 1.16	13
3.534215	15.6	(14.6)	5.78 ± 0.34	1.66 ± 1.08	14
3.534449	8.5	(7.0)	15.1 ± 0.4	24.4 ± 1.0	15
3.534625	4.3	(3.8)	1.70 ± 0.22	8.72 ± 0.73	16
3.534814	...	1.3	< 0.57	4.14 ± 2.41	17
3.534819	6.0	(4.7)	6.78 ± 0.69	< 2.52	18
3.535150	11.3	(9.9)	3.26 ± 0.25	< 0.98	19
3.535521	7.4	(6.4)	67.7 ± 2.0	56.5 ± 1.4	20
3.535642	3.1	(2.4)	19.4 ± 3.5	< 0.95	21
3.535741	11.1	(9.6)	26.9 ± 0.6	14.4 ± 1.2	22
3.644 ^j								
3.644129	3.7	(2.4)	7.49 ± 0.46	5.96 ± 0.46	1
3.646								
3.645796	5.4	(4.7)	1.98 ± 0.30	< 0.53	1
3.646023	4.2	(3.2)	2.16 ± 0.34	2.17 ± 0.47	2
3.754 ^k								
3.753072	13.3	(12.2)	7.04 ± 1.05	< 1.11	1
3.753423	3.1	(2.0)	1.63 ± 0.66	< 0.65	2
3.753721	3.4	(2.4)	11.2 ± 2.6	10.4 ± 0.9	< 0.22	3
3.753875	14.1	(13.0)	64.6 ± 3.2	19.3 ± 1.3	< 0.39	4
3.754591	12.5	(11.2)	13.5 ± 1.0	8.41 ± 1.23	< 0.28	5
3.789 ^l								
3.787666	9.6	(7.9)	3.48 ± 0.43	< 1.47	< 0.29	1
3.788329	5.0	...	0.97 ± 0.32	...	< 0.24	2
3.789123	4.1	...	0.91 ± 0.30	...	< 0.44	3
3.789385	5.6	...	0.62 ± 0.32	4
3.822								
3.822044	9.9	(8.2)	3.82 ± 0.57	< 0.66	< 0.52	1
3.826 ^m								
3.824503	24.5	(23.9)	9.64 ± 1.05	8.51 ± 1.15	< 0.71	1
3.824915	8.8	(7.4)	6.96 ± 0.91	21.8 ± 0.9	< 0.53	2
3.825114	12.7	(11.5)	15.3 ± 1.0	31.1 ± 1.1	3.41 ± 0.60	3
3.825591	10.6	(9.1)	11.8 ± 1.0	37.3 ± 1.1	< 0.74	4
3.825709	4.0	(3.2)	3.09 ± 0.81	56.9 ± 2.0	5.07 ± 0.51	8.44 ± 0.85	...	5
3.825870	6.2	(5.3)	6.72 ± 0.93	64.7 ± 1.5	9.60 ± 0.56	19.1 ± 0.9	...	6
3.826128	15.7	(14.7)	36.9 ± 1.7	97.5 ± 1.6	7
3.826409	10.6	(9.4)	8.90 ± 1.57	3.01 ± 1.17	8

Table 9—Continued

z	$b(\text{C})$ km s^{-1}	$b(\text{Si})$ km s^{-1}	$N(\text{C IV})$ 10^{12}cm^{-2}	$N(\text{Si IV})$ 10^{11}cm^{-2}	$N(\text{C II})$ 10^{12}cm^{-2}	$N(\text{Si II})$ 10^{11}cm^{-2}	$N(\text{N V})$ 10^{12}cm^{-2}	n
1	2	3	4	5	6	7	8	9
3.826625	11.3	(9.9)	15.9 ± 1.5	52.2 ± 1.3	1.48 ± 0.71	9
3.826825	6.1	(5.0)	6.65 ± 1.21	31.1 ± 1.1	< 0.60	10
3.826953	8.5	(7.0)	9.42 ± 0.99	11.6 ± 0.9	< 0.56	11
3.850 ^a								
3.848942	4.8	(3.7)	< 0.81	8.09 ± 0.83	0.74 ± 0.25	1
3.849117	4.2	(2.8)	1.80 ± 0.61	13.4 ± 0.9	6.00 ± 0.30	2
3.849404	11.8	(10.4)	7.68 ± 0.91	27.0 ± 1.3	3.03 ± 0.35	3
3.849821	8.5	(7.1)	3.06 ± 0.89	23.5 ± 1.4	1.92 ± 0.41	4
3.849939	3.7	(2.4)	< 0.71	2.51 ± 1.15	1.21 ± 0.31	5
3.851346	15.9	(14.9)	7.85 ± 1.06	6.17 ± 1.60	< 0.40	6
3.884								
3.884135	6.6	(5.3)	4.29 ± 0.59	4.20 ± 1.15	< 1.18	1
3.884284	8.4	(7.1)	12.5 ± 0.7	11.8 ± 1.3	< 1.08	2
3.884521	8.0	(7.1)	1.39 ± 0.46	5.73 ± 1.20	< 0.82	3
3.934 ^a								
3.932578	10.8	(9.4)	6.86 ± 1.59	14.0 ± 0.8	< 0.60	1
3.932836	4.8	(4.0)	7.31 ± 2.06	< 1.17	< 0.43	2
3.932936	10.2	(8.6)	6.02 ± 1.60	9.92 ± 1.14	< 0.58	3
3.933580	15.5	(14.5)	14.6 ± 1.9	4.73 ± 1.12	< 0.47	4
3.934163	12.8	(11.6)	9.08 ± 1.44	24.1 ± 1.6	< 0.52	5
3.934343	8.4	(6.9)	8.06 ± 1.20	23.0 ± 1.1	< 0.53	6
3.934664	8.2	(6.9)	7.46 ± 0.88	16.4 ± 0.8	0.44 ± 0.34	7

^aC IV $\lambda 1548$ is masked by Fe II $\lambda 1608$ at $z = 2.912$.

^bC IV $\lambda 1551$ contains very weak C II at $z = 3.754$.

^cC IV $\lambda 1551$ is blended with C II at $z = 3.826$ and is not used.

^dThis is a damped Ly α system with strong Si II $\lambda 1527$ ($\lambda 1260$ is in the forest) in components 7–10: for these, $\log N(\text{H I})$ totalling ~ 20.3 gives a reasonable fit to the damping wings. Both C IV $\lambda\lambda 1548, 1551$ are partially blended with Mg II $\lambda 2804$ in a strong, extended system at $z = 1.386$. Some b -values here relate to Si II.

^eC IV $\lambda 1551$ contains weak Si IV $\lambda 1403$ at $z = 3.789$.

^fC IV $\lambda 1551$ is blended with Si IV $\lambda 1394$ at $z = 3.850$ and is not used.

^gC IV $\lambda 1551$ is blended with strong Fe II $\lambda 1608$ at $z = 3.317$ and is not used.

^hSi IV $\lambda 1394$ is heavily contaminated and also blended with C IV $\lambda 1548$ at $z = 3.063$, and is not used.

ⁱThere is an unidentified interloper observed at $\lambda 6359.9$ in Si IV $\lambda 1403$ near component 13, but in a relatively clear region in the complex. Si II $\lambda 1260$ is in the forest; Si II $\lambda 1527$ is very weak and partially blended with much stronger Si IV $\lambda 1403$ at $z = 3.934$ and, with the exception of component 5, is not useful.

^jSi IV $\lambda 1394$ resides in a clear region of C II at $z = 3.850$.

^kIn component 1 C IV $\lambda 1551$ is contaminated and is not used. In components 1 and 5 Si IV $\lambda 1403$ is blended with Mg II $\lambda 2796$ at $z = 1.386$ and is not used. In components 1 and 2 C II is blended with weak C IV $\lambda 1551$ at $z = 3.090$ and is too uncertain to include.

^lSi IV $\lambda 1394$ is masked by very strong Mg II $\lambda 2796$ at $z = 1.386$; $\lambda 1403$ is blended with C IV $\lambda 1551$ at $z = 3.332$. In component 4 C II is close to C IV $\lambda 1551$ at $z = 3.122$ and may be contaminated.

^mC II is partially blended with C IV $\lambda 1551$ at $z = 3.154$, making components 7 and 8 too uncertain to include. Si II $\lambda 1260$ is in the forest but the two strong components 5 and 6 are in a clear region and give good values consistent with $\lambda 1527$.

ⁿSi IV $\lambda 1394$ includes weaker C IV $\lambda 1551$ at $z = 3.359$. C II contains Si IV $\lambda 1394$ at $z = 3.644$ which however is in a clear part of the complex.

^oC IV is in a rather noisy region. Si IV $\lambda 1403$ contains weak Si II $\lambda 1527$ at $z = 3.533$.

Table 10. Heavy Element Absorption Lines: Q2237-0607 $z_{em} = 4.559$

z	$b(\text{C})$ km s^{-1}	$b(\text{Si})$ km s^{-1}	$N(\text{C IV})$ 10^{12}cm^{-2}	$N(\text{Si IV})$ 10^{11}cm^{-2}	$N(\text{C II})$ 10^{12}cm^{-2}	$N(\text{Si II})$ 10^{11}cm^{-2}	$N(\text{N V})$ 10^{12}cm^{-2}	n
1	2	3	4	5	6	7	8	9
3.433								
3.432163	18.1	...	1.38 ± 0.22	1
3.432536	12.5	...	5.06 ± 0.19	2
3.432898	15.4	...	4.17 ± 0.20	3
3.433372	14.4	...	8.11 ± 0.20	4
3.433793	15.7	...	2.27 ± 0.20	5
3.434216	5.9	...	0.38 ± 0.12	6
3.448								
3.448005	6.1	...	1.78 ± 0.14	1
3.454								
3.454097	6.6	...	1.88 ± 0.15	1
3.482 ^a								
3.480748	6.1	...	5.83 ± 0.33	1
3.480927	7.2	...	1.57 ± 0.39	2
3.481177	3.7	...	0.73 ± 0.21	3
3.481822	3.2	...	0.58 ± 0.21	4
3.482839	8.4	...	2.35 ± 0.51	5
3.574								
3.573626	3.7	...	1.09 ± 0.51	1
3.591								
3.590169	9.0	...	0.98 ± 0.19	1
3.591049	14.4	...	3.81 ± 0.24	2
3.604 ^b								
3.603346	6.2	...	0.78 ± 0.25	1
3.603811	8.5	...	2.20 ± 0.21	2
3.604090	9.3	...	0.44 ± 0.18	3
3.604769	21.6	...	4.87 ± 0.25	4
3.605193	9.7	...	3.18 ± 0.22	5
3.605553	5.0	...	0.93 ± 0.16	6
3.627								
3.626914	17.7	...	7.42 ± 0.86	1
3.626999	7.8	...	5.65 ± 0.65	2
3.681								
3.681086	15.6	...	3.29 ± 0.40	1
3.681386	10.4	...	1.56 ± 0.24	2
3.681817	9.7	...	0.91 ± 0.33	3
3.748 ^c								
3.746555	9.4	...	4.92 ± 0.37	1
3.746841	8.8	...	1.41 ± 0.34	2
3.748605	10.5	...	3.14 ± 0.38	3
3.756								
3.756310	6.1	...	1.56 ± 0.31	1
3.793877	17.1	...	4.78 ± 0.32	1
3.794476	26.0	...	1.45 ± 0.40	2
3.811								
3.808382	28.0	...	4.17 ± 0.63	1
3.809209	9.4	...	1.60 ± 0.38	2

Table 10—Continued

z	$b(\text{C})$ km s^{-1}	$b(\text{Si})$ km s^{-1}	$N(\text{C IV})$ 10^{12}cm^{-2}	$N(\text{Si IV})$ 10^{11}cm^{-2}	$N(\text{C II})$ 10^{12}cm^{-2}	$N(\text{Si II})$ 10^{11}cm^{-2}	$N(\text{N V})$ 10^{12}cm^{-2}	n
1	2	3	4	5	6	7	8	9
3.810407	6.7	...	4.47 ± 0.38	3
3.810683	7.1	...	1.44 ± 0.36	4
3.810956	13.1	...	2.62 ± 0.48	5
3.811462	9.3	...	2.98 ± 0.39	6
3.811873	7.6	...	0.52 ± 0.34	7
3.812786	16.9	...	3.42 ± 0.50	8
3.813286	5.9	...	1.02 ± 0.32	9
3.825 ^d								
3.824609	8.6	(7.0)	4.08 ± 0.63	17.3 ± 0.9	1
3.824776	7.2	(4.7)	2.80 ± 0.98	1.64 ± 0.72	2
3.832 ^e								
3.829908	28.5	...	17.4 ± 2.1	1
3.830947	13.8	...	8.88 ± 1.31	2
3.831456	15.0	(13.9)	17.4 ± 1.5	42.4 ± 37.6	3
3.831962	12.8	(11.5)	41.7 ± 1.9	108 ± 33	4
3.832343	12.4	(11.1)	5.18 ± 1.28	39.9 ± 18.4	5
3.833306	8.3	...	4.51 ± 1.27	6
3.978 ^f								
3.976804	9.1	(7.3)	1.80 ± 0.52	< 0.93	1
3.977119	5.2	...	1.39 ± 0.44	2
3.977378	8.1	(6.6)	3.07 ± 0.61	4.99 ± 1.97	3
3.977620	15.9	(14.9)	3.47 ± 0.73	< 1.86	4
3.978251	18.4	(17.5)	10.2 ± 0.7	6.03 ± 1.13	5
3.978919	8.6	(6.8)	1.85 ± 0.64	6.27 ± 1.11	6
3.979116	19.4	(18.6)	5.10 ± 0.89	< 1.53	7
4.030								
4.028698	10.5	(9.1)	2.19 ± 0.42	1.23 ± 0.87	1
4.029190	25.1	(24.5)	2.45 ± 0.61	< 1.34	2
4.029616	9.4	(7.8)	4.56 ± 0.40	4.87 ± 0.79	3
4.030437	7.4	(6.6)	0.76 ± 0.35	< 0.69	4
4.031087	17.0	(16.1)	5.37 ± 0.53	< 1.03	5
4.080 ^g								
4.078098	7.8	(6.3)	1.66 ± 0.57	1.49 ± 1.01	3.10 ± 0.33	1
4.078403	3.6	(2.5)	< 1.59	< 2.01	31.2 ± 3.7	20.8 ± 11.5	...	2
4.078431	9.1	(7.2)	3.94 ± 1.86	4.75 ± 2.69	55.2 ± 6.9	90.0 ± 14.3	...	3
4.078699	9.8	(8.2)	1.03 ± 0.84	5.36 ± 1.40	109 ± 4	188 ± 8	...	4
4.078904	8.4	(6.6)	< 0.81	12.5 ± 1.3	66.1 ± 4.5	106 ± 7	...	5
4.079071	3.3	(2.2)	1.06 ± 0.51	2.88 ± 0.92	16.9 ± 2.4	27.3 ± 4.8	...	6
4.079208	4.3	(3.2)	1.39 ± 0.56	5.69 ± 1.02	39.4 ± 1.7	85.0 ± 5.8	...	7
4.079394	8.8	(7.1)	5.36 ± 0.79	17.9 ± 1.3	< 3.46	11.8 ± 4.8	...	8
4.079639	7.5	(5.9)	18.0 ± 1.7	16.0 ± 2.6	4.65 ± 1.24	13.1 ± 6.3	...	9
4.079751	9.2	(7.4)	13.4 ± 1.8	42.1 ± 2.5	2.76 ± 0.96	< 9.99	...	10
4.080009	10.6	(9.1)	9.12 ± 1.03	45.8 ± 1.8	35.6 ± 1.0	74.2 ± 7.0	...	11
4.080235	8.1	(6.5)	3.01 ± 0.80	28.9 ± 1.5	277 ± 15	537 ± 20	...	12
4.080389	3.4	(2.3)	< 0.93	24.0 ± 2.8	28.5 ± 6.8	100 ± 12	...	13
4.080492	6.6	(5.4)	3.04 ± 0.87	31.7 ± 2.6	39.3 ± 1.5	70.1 ± 6.9	...	14
4.080685	7.4	(5.8)	1.70 ± 0.63	10.9 ± 1.2	69.0 ± 1.7	127 ± 7	...	15
4.080882	4.9	(3.9)	1.35 ± 0.55	7.28 ± 1.03	281 ± 18	441 ± 22	...	16
4.081049	7.4	(6.0)	< 0.80	4.13 ± 1.22	7.26 ± 0.56	16.4 ± 5.5	...	17
4.081219	8.4	(6.9)	< 0.92	3.85 ± 1.22	2.05 ± 0.29	18
4.081539	9.7	(8.1)	3.26 ± 0.65	4.17 ± 1.12	0.34 ± 0.20	19

Table 10—Continued

z	$b(\text{C})$ km s^{-1}	$b(\text{Si})$ km s^{-1}	$N(\text{C IV})$ 10^{12}cm^{-2}	$N(\text{Si IV})$ 10^{11}cm^{-2}	$N(\text{C II})$ 10^{12}cm^{-2}	$N(\text{Si II})$ 10^{11}cm^{-2}	$N(\text{N V})$ 10^{12}cm^{-2}	n
1	2	3	4	5	6	7	8	9
4.086 ^h								
4.085675	12.1	(10.8)	3.31 ± 0.68	6.03 ± 1.26	< 0.21	1
4.089 ⁱ								
4.088930	7.8	(6.9)	6.25 ± 0.78	2.08 ± 1.31	1
4.094								
4.094002	16.0	(15.1)	6.50 ± 0.77	4.68 ± 1.42	< 0.34	1
4.200 ^j								
4.199891	9.2	(7.4)	1.38 ± 0.68	< 1.16	1
4.200533	12.9	(11.7)	11.6 ± 0.9	6.22 ± 1.53	2
4.200840	8.4	(6.8)	6.77 ± 0.87	< 1.06	3
4.231 ^k								
4.229917	8.3	(6.7)	0.79 ± 0.41	< 2.30	< 0.38	1
4.230213	5.8	(5.1)	3.16 ± 0.41	< 1.65	2
4.230466	7.9	(6.2)	15.0 ± 0.7	4.66 ± 0.78	3
4.230802	7.8	(6.1)	3.06 ± 0.45	< 0.73	4
4.231122	5.8	(4.9)	3.06 ± 0.43	< 0.68	5
4.231416	8.9	(7.2)	1.23 ± 0.47	< 0.79	6
4.231857	6.5	(5.3)	1.15 ± 0.37	< 0.86	7
4.239 ^l								
4.237106	8.4	(6.8)	3.19 ± 0.44	< 1.31	< 0.31	1
4.238126	7.2	(4.7)	1.10 ± 0.40	< 0.73	< 0.51	2
4.239212	...	(8.6)	< 0.86	18.1 ± 1.1	3
4.239714	13.5	(12.4)	2.98 ± 0.64	29.9 ± 1.4	3.61 ± 1.20	4
4.239922	4.1	(3.0)	1.38 ± 0.42	6.40 ± 0.90	< 0.52	5
4.240153	10.5	(9.0)	3.29 ± 0.54	10.2 ± 1.0	< 1.85	6
4.247 ^m								
4.245708	7.0	(5.8)	1.16 ± 0.52	3.61 ± 1.01	< 0.30	1
4.246135	3.1	(2.1)	3.38 ± 0.56	< 0.77	< 0.34	2
4.246701	...	(12.1)	< 0.91	21.3 ± 2.0	3
4.247053	29.2	(28.7)	12.2 ± 1.5	11.6 ± 3.0	< 0.96	4
4.247420	3.5	(2.3)	< 0.48	3.63 ± 1.10	0.51 ± 0.28	5
4.247838	21.2	(20.4)	9.09 ± 1.02	25.3 ± 2.1	< 0.59	6
4.286 ⁿ								
4.284758	10.1	(8.5)	1.30 ± 0.70	5.78 ± 1.58	< 0.53	1
4.285289	8.5	(7.0)	7.82 ± 0.93	18.4 ± 1.5	< 0.49	2
4.285681	10.4	(8.8)	10.3 ± 1.3	46.2 ± 2.0	< 0.81	3
4.286035	14.4	(13.3)	6.00 ± 4.07	13.6 ± 2.1	< 0.70	4
4.286236	3.9	(2.8)	5.60 ± 1.44	< 1.24	< 0.50	5
4.286443	13.4	(12.2)	5.97 ± 0.99	< 2.76	< 0.70	6
4.361 ^o								
4.359498	15.3	(14.3)	11.5 ± 0.9	55.8 ± 4.6	1.14 ± 0.58	1
4.359981	14.4	(13.3)	17.6 ± 1.7	66.1 ± 3.5	< 0.69	2
4.360176	5.8	(4.6)	8.04 ± 1.16	51.0 ± 3.9	1.38 ± 0.52	3
4.360335	4.4	(3.5)	4.30 ± 0.93	70.6 ± 5.1	3.65 ± 0.47	4
4.360528	9.5	(7.8)	28.9 ± 1.2	33.0 ± 2.3	< 0.73	5
4.360931	6.4	6.9	14.3 ± 0.7	33.1 ± 2.0	1.11 ± 0.41	6
4.361383	10.2	(8.7)	5.32 ± 1.36	< 7.27	< 0.93	7
4.361506	7.7	(5.3)	3.41 ± 1.79	65.3 ± 8.8	3.08 ± 0.78	8
4.361790	13.7	(10.2)	13.0 ± 1.1	156 ± 9	11.6 ± 0.7	12.0 ± 5.0	...	9
4.362363	9.9	(8.2)	8.71 ± 0.73	36.3 ± 2.5	2.87 ± 0.59	10
4.362621	10.4	(8.9)	12.6 ± 0.9	88.1 ± 4.1	18.6 ± 0.8	21.8 ± 5.2	...	11

Table 10—Continued

z	$b(\text{C})$ km s^{-1}	$b(\text{Si})$ km s^{-1}	$N(\text{C IV})$ 10^{12}cm^{-2}	$N(\text{Si IV})$ 10^{11}cm^{-2}	$N(\text{C II})$ 10^{12}cm^{-2}	$N(\text{Si II})$ 10^{11}cm^{-2}	$N(\text{N V})$ 10^{12}cm^{-2}	n
1	2	3	4	5	6	7	8	9
4.362835	6.9	(5.7)	2.29 ± 0.75	64.2 ± 4.9	8.43 ± 0.69	11.7 ± 4.8	...	12
4.363066	22.4	(21.7)	14.0 ± 1.0	15.1 ± 4.5	< 1.04	13
4.389 ^P								
4.388746	7.2	(5.7)	3.59 ± 0.82	...	< 0.56	0.30 ± 0.24	...	1
4.389312	3.7	(2.4)	0.90 ± 0.48	< 3.91	< 0.45	< 0.20	...	2
4.390075	6.1	(5.2)	2.78 ± 1.11	< 3.01	< 0.56	< 0.24	...	3

^aC IV $\lambda 1548$ is in a blend with Si IV $\lambda 1394$ at $z = 3.978$ and very weak C II at $z = 4.200$.

^bC IV $\lambda 1548$ is partially blended with Si IV $\lambda 1403$ at $z = 4.080$.

^cC IV $\lambda 1548$ is blended with Si IV $\lambda 1403$ at $z = 4.239$; $\lambda 1551$ is in a blend with Si IV $\lambda 1403$ at $z = 4.247$ and C IV $\lambda 1548$ at $z = 3.756$.

^dC IV $\lambda 1548$ encroaches on Si IV $\lambda 1394$ at $z = 4.361$; $\lambda 1551$ is blended with C IV $\lambda 1548$ at $z = 3.832$. Si IV $\lambda 1394$ is in the forest but $\lambda 1403$ is just clear.

^eC IV $\lambda 1548$ is in a blend with Al III $\lambda 1855$ at $z = 3.032$ and C IV $\lambda 1551$ at $z = 3.825$ and also is noisy, and is only partly used. Si IV $\lambda 1403$ is outside the forest but immersed in very strong C II at $z = 4.080$: the values given are useful despite the large errors.

^fC IV $\lambda 1551$ has some contamination from atmospheric emission. Si IV $\lambda 1394$ is blended with C IV $\lambda 1548$ at $z = 3.482$ and very weak C II at $z = 4.200$; $\lambda 1403$ partially overlaps with very weak C II at $z = 4.231$.

^gThis is a damped Lyman α system with C II, Si II and O I (in the forest) very strong in components 3–7 and 12–16, and C IV relatively weak: collectively $\log N(\text{H I}) \sim 20.3$ gives a good fit to the outer parts of the damping wings. C IV $\lambda 1551$ is blended with C IV $\lambda 1548$ at $z = 4.089$. Si IV $\lambda 1394$ contains weak C IV $\lambda 1548$ at $z = 3.574$; $\lambda 1403$ is blended with C IV $\lambda 1548$ at $z = 3.604$. C II $\lambda 1335$ contains much weaker Si IV $\lambda 1403$ at $z = 3.832$ which is approximately determined with the help of $\lambda 1036$ in the forest; in components 12 and 16 C II is saturated, making the values listed for these uncertain; there is weak associated C II* $\lambda 1336$. The Si II values are from $\lambda 1527$.

^hC IV $\lambda 1551$ is blended with C IV $\lambda 1548$ at $z = 4.094$.

ⁱC IV $\lambda 1548$ resides in C IV $\lambda 1551$ at $z = 4.080$ but is strong and well determined; $\lambda 1551$ is in a very noisy region and is not used. Si IV $\lambda 1394$ is blended with C IV $\lambda 1551$ at $z = 3.574$; $\lambda 1403$ is blended with C IV $\lambda 1551$ at $z = 3.604$. C II is somewhat contaminated by an unknown weak feature and is not included.

^jIn components 1 and 3 C IV $\lambda 1551$ is rather noisy and is not used. Si IV $\lambda 1394$ is weak and dominated by C IV $\lambda 1548$ at $z = 3.681$, and is not used. C II is masked by C IV $\lambda 1548$ at $z = 3.482$ and Si IV $\lambda 1394$ at $z = 3.978$.

^kC IV $\lambda 1551$ is blended with C IV $\lambda 1548$ at $z = 4.239$. In components 1 and 2 Si IV $\lambda 1394$ contains an unidentified strong feature. In components 2–4 C II is in a very noisy region and in 5–7 is confused with Si IV $\lambda 1403$ at $z = 3.978$.

^lC IV $\lambda 1548$ is blended with C IV $\lambda 1551$ at $z = 4.231$; $\lambda 1551$ is blended with C IV $\lambda 1548$ at $z = 4.247$. Si IV $\lambda 1403$ is blended with C IV $\lambda 1548$ at $z = 3.748$. C II is overlapped by Si II $\lambda 1304$ at $z = 4.361$ but this is very weak and only the value in component 3 is significantly affected.

^mC IV $\lambda 1548$ is blended with C IV $\lambda 1551$ at $z = 4.239$; $\lambda 1551$ is rather noisy. Si IV $\lambda 1403$ is partially blended with C IV $\lambda 1551$ at $z = 3.748$.

ⁿC IV $\lambda 1548$ contains very weak Si II $\lambda 1527$ at $z = 4.361$.

^oC IV and Si IV have some interference from atmospheric emission but the values obtained from both doublets are little affected. Si II is derived from a combination of complementary portions of $\lambda 1260$ (in the forest, but useful for the stronger components), $\lambda 1304$ (partially blended with C II $\lambda 1335$ at $z = 4.239$) and $\lambda 1527$ (partially blended with C IV $\lambda 1548$ at $z = 4.286$); errors are from $\lambda \lambda 1304, 1527$ alone.

^PC IV values are dominantly from $\lambda 1551$ as $\lambda 1548$ is heavily affected by atmospheric emission. Si IV $\lambda 1394$ is masked by strong Al III $\lambda 1863$ at $z = 3.032$; in component 1 $\lambda 1403$ is obscured by atmospheric emission.

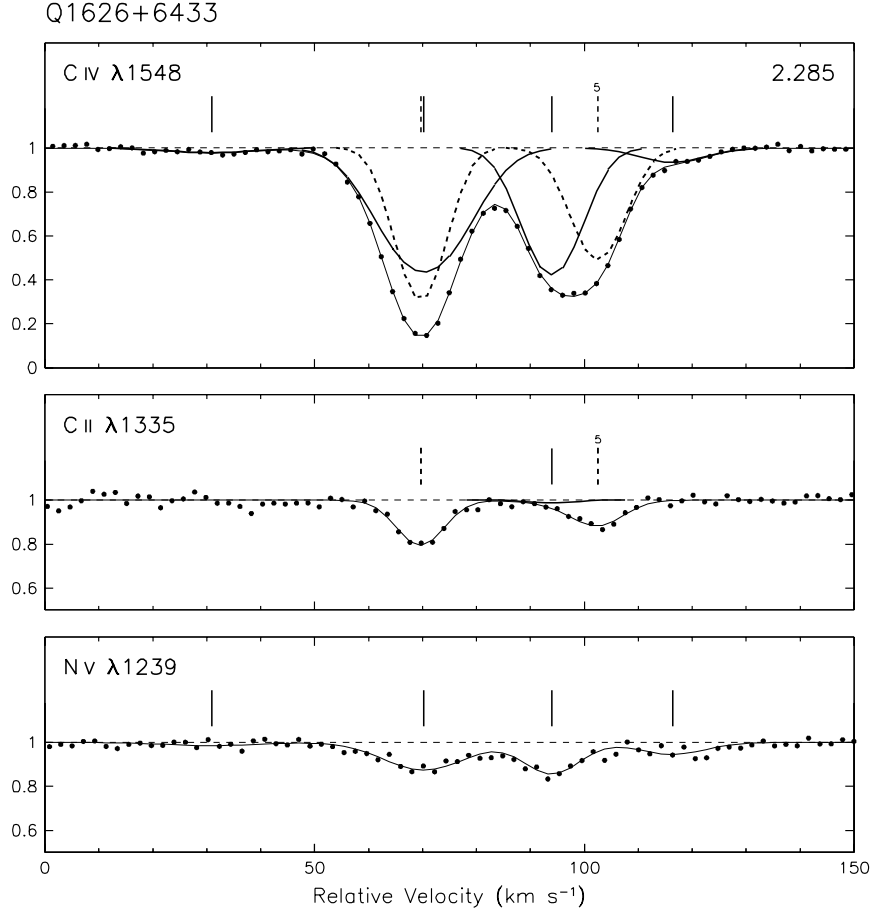


Fig. 1.— Continuum-normalized spectra demonstrating the separation of an absorption system ($z = 2.285$ in Q1626+6433) into single-phase-ionization components by means of the VPFIT analysis described in the text. For each profile the composite fit through the data points is shown by a *continuous thin line*. Component parameters and numbering (the fifth component is indicated) are given in Table 2. C IV is shown also with separate fits to the six constituent components. The different widths of the two nearly coincident components 2 and 3 and the positions of the more spaced components 4 and 5 are mirrored separately in the other two species, with the C IV components dominant in C II (low ionization) identified by *dashed lines and vertical ticks* and those dominant in N V (high ionization) by *continuous thick lines and ticks*. Ticks are shown only at the positions of detected components, not upper limits. Component 4 which is strong in N V is weakly evident in the C II profile and is also shown there separated. Note the truncation of the vertical axes in the lower two panels.

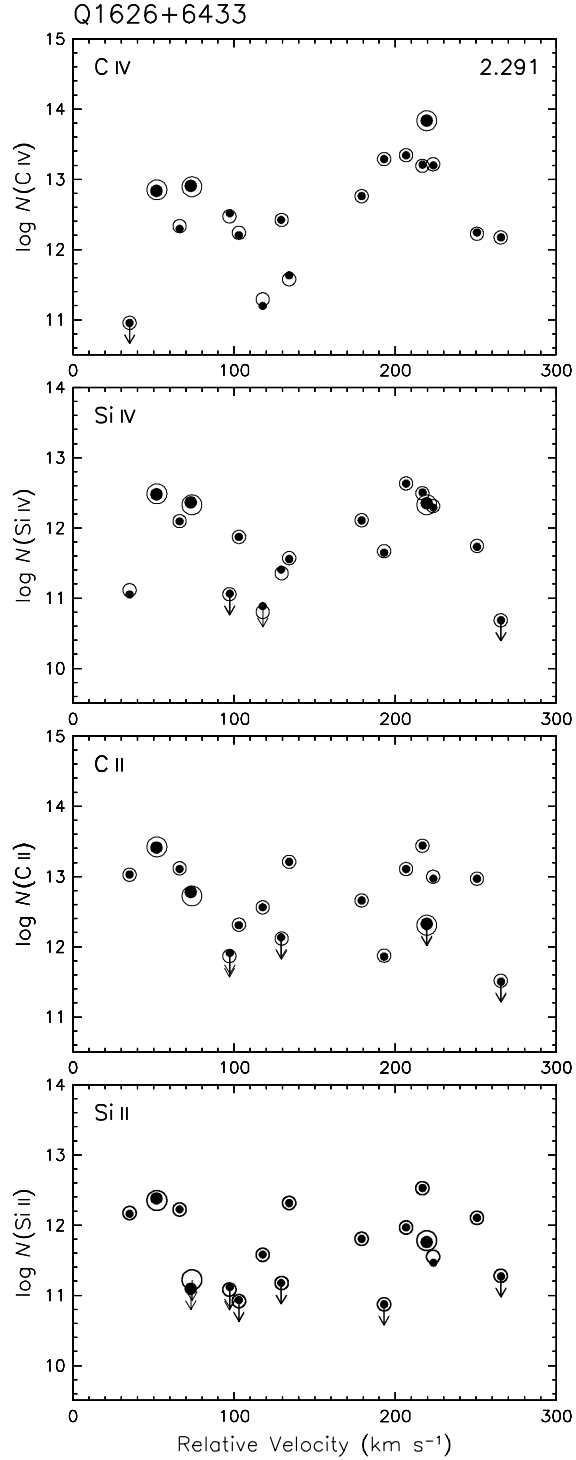


Fig. 2.— C IV, Si IV, C II and Si II component column densities N (cm⁻²) for the complex absorption system at $z = 2.291$ in Q1626+6433. Two individual runs in the VPFIT analysis show the differential effect of fixing the set of three broadest components (indicated by *enlarged symbols*—see Figure 5 and Table 2 for identification) at the two widely different temperatures 1×10^4 K and 1×10^5 K, but otherwise having the same mix of specific starting values for the remainder of the components (see text). All component values yielded in the first case are shown by *filled circles* and in the second by *open circles*.

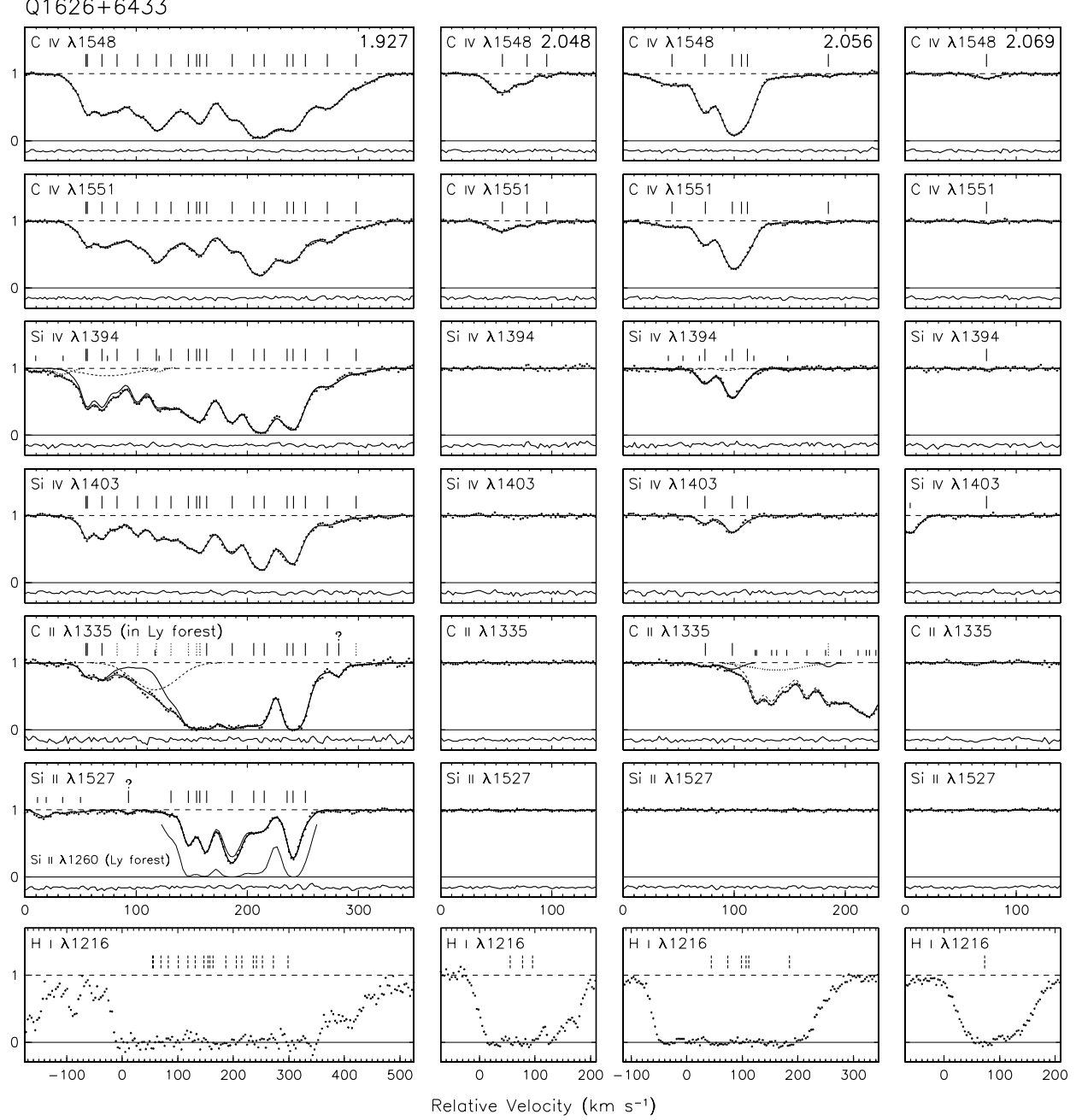


Fig. 3.— Continuum-normalized spectra for all systems detected in Q1626+6433 ($z_{em} = 2.320$) having at least C IV and Si IV outside the Lyman forest. For each system the available metal species of interest in this paper are compared on a common velocity scale. The system components identified using VPFIT are marked with *long vertical ticks*; a few questionable features are so indicated. Components yielding only upper limits are unmarked. Component parameter values and upper limits are listed in Table 2; in the few cases where components have values which are too uncertain to be included in the table they are marked with *dotted ticks*. Blended or nearby interloper species from other systems are indicated by *short ticks* and are identified in the notes to Table 2. The data values are given as points and the fits obtained to these (including the convolved instrumental profile) are shown as *continuous bold lines* when there is no blending and *continuous thin lines* when blending is present; residuals (*i.e.* [data] – [fit]) are shown on the same scale beneath the profiles. In the blended cases the deconvolved fits to the appropriate species are shown by *continuous bold lines* and fits to the interlopers by *short-dashed or dotted lines*. Si II $\lambda 1527$ at $z = 1.927$ is shown with a correction (*thin line*) accounting for mild unknown contamination deduced from related transitions; this and $\lambda 1527$ at $z = 2.110$ have superimposed fits to $\lambda 1260$ (for the same column densities) which match data in relatively clear regions of the forest. Lyman α observations, covering twice the velocity range, are shown unfitted, but with the positions of all components detected in C IV indicated by *broken ticks*.

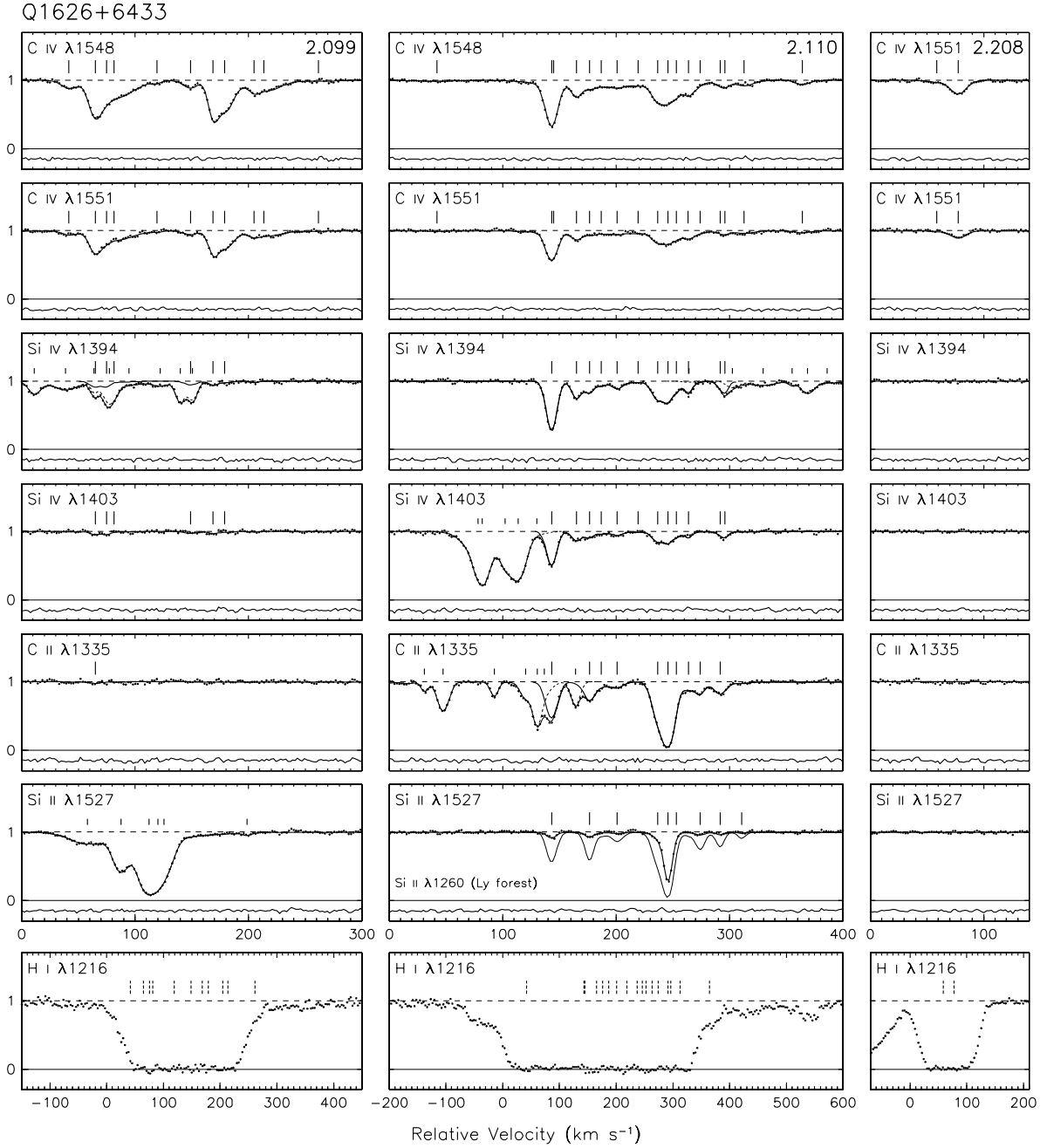


Fig. 3.— Continued.

Q1626+6433

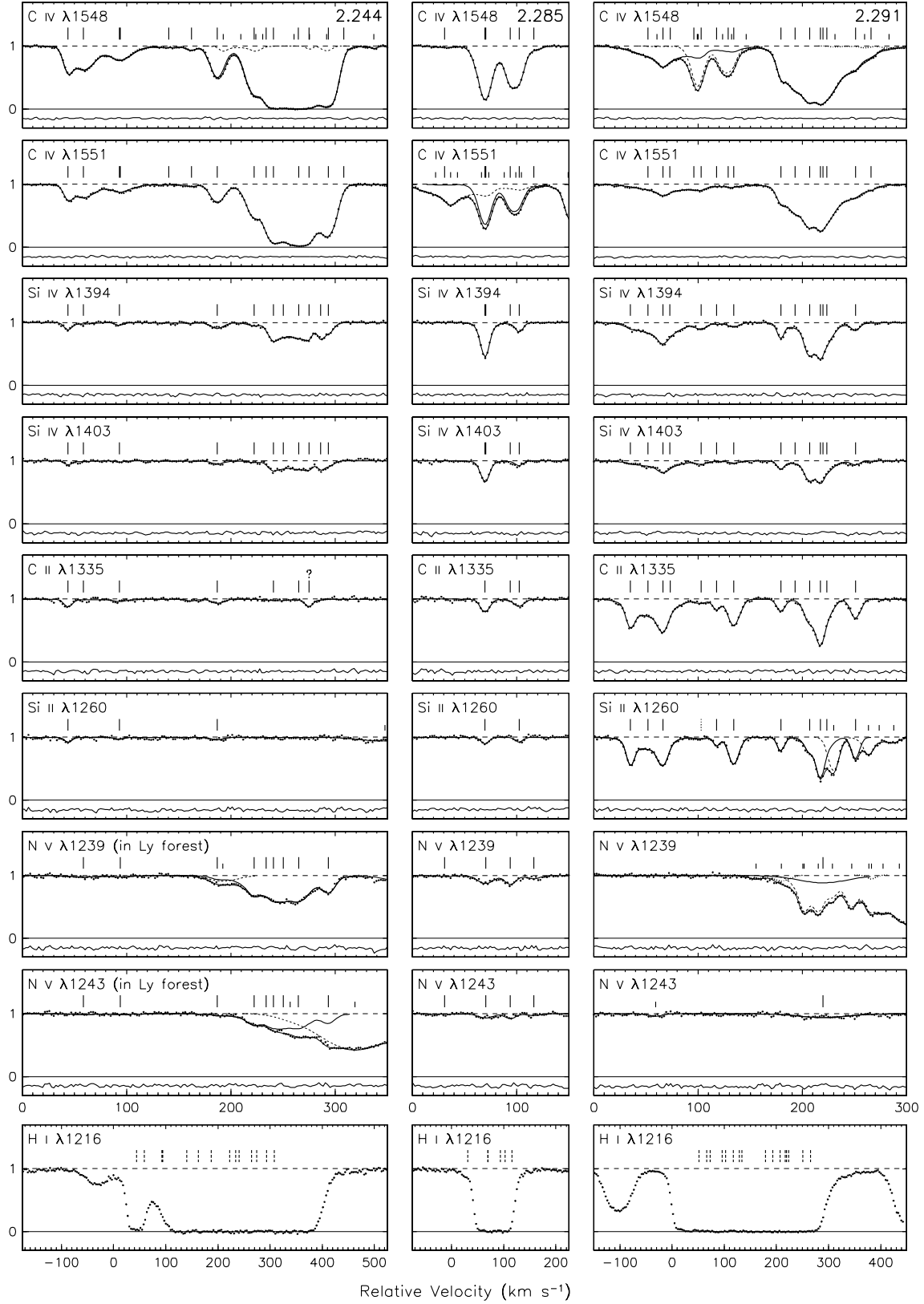


Fig. 3.— Continued.

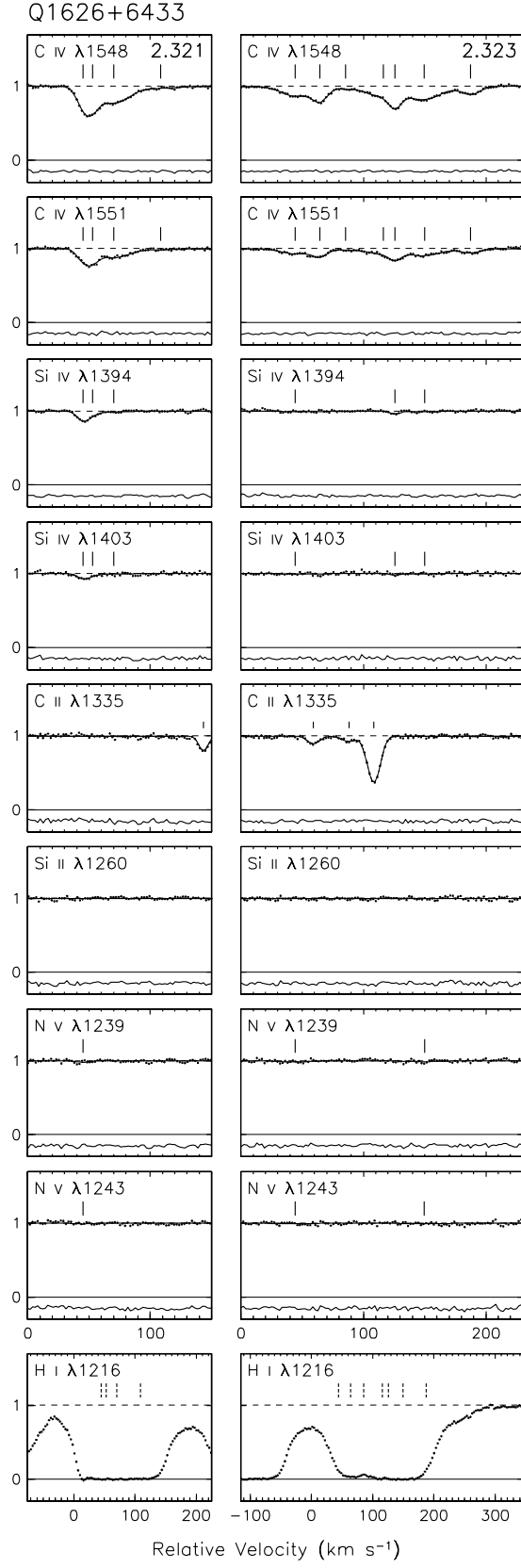


Fig. 3.— Continued.

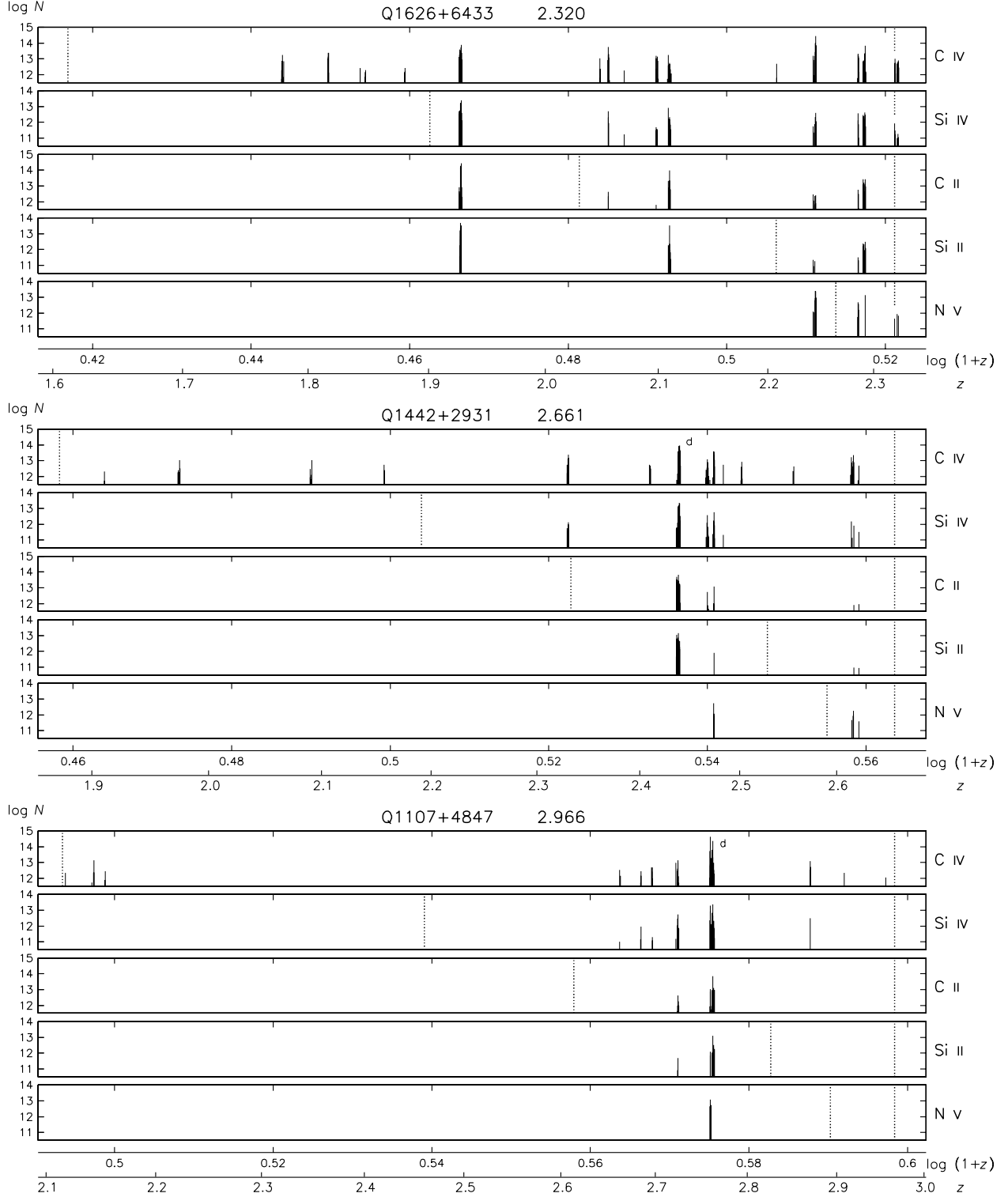


Fig. 4.— C IV, Si IV, C II, Si II and N V column densities N (cm^{-2}) plotted versus redshift z and $\log(1+z)$ for the absorber components *detected* in the nine QSOs (see Tables 2–10). Systems with significant Lyman α damping wings are marked *d*. Note the vertical scales for Si IV, Si II and N V are shifted lower by 1 dex than the others. All frames cover the same extent in $\log(1+z)$ which for C IV encompasses the region between the Lyman α and C IV emission lines with some margin. The *dotted vertical line* at the right of each frame is at the emission redshift; the similar line to the left marks the specific limit where a given ion falls in the Lyman forest (in Si II this is shown for $\lambda 1260$ only). Reliable values appear at redshifts in the forest, but for Si II most of these apparent cases actually indicate values from strong $\lambda 1527$, not from $\lambda 1260$, as clarified in the footnotes to Tables 2–10.

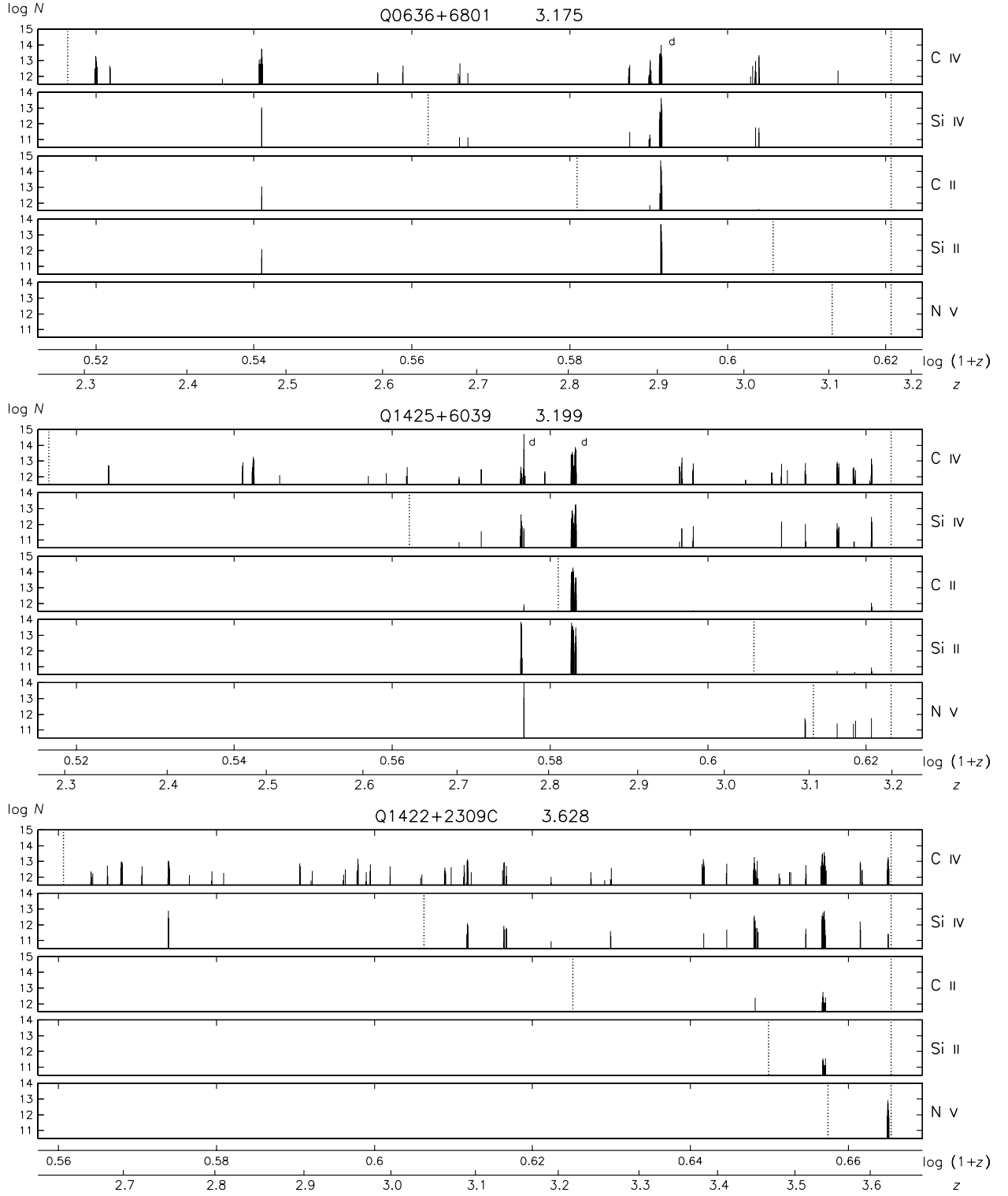


Fig. 4.— Continued.

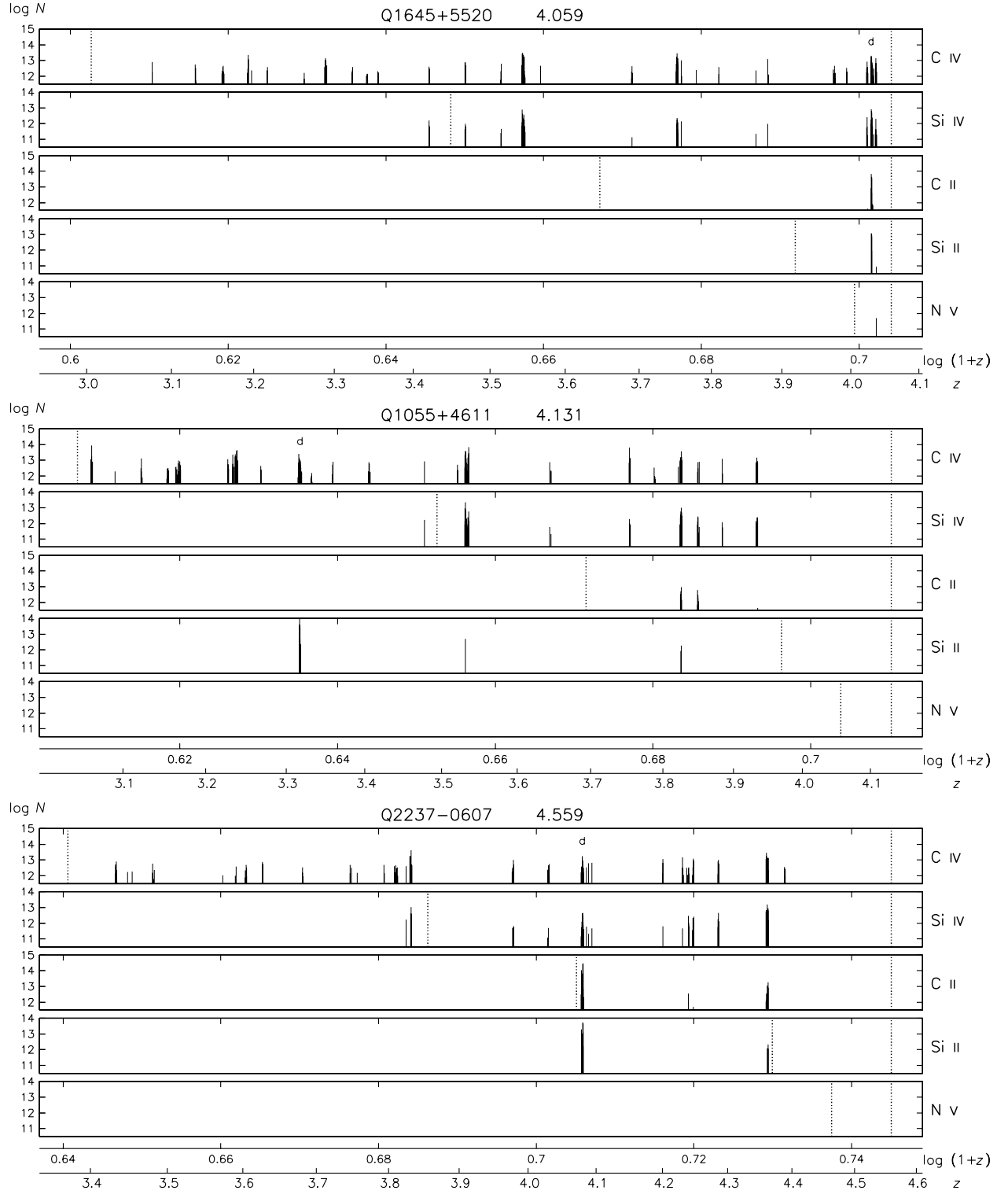


Fig. 4.— Continued.

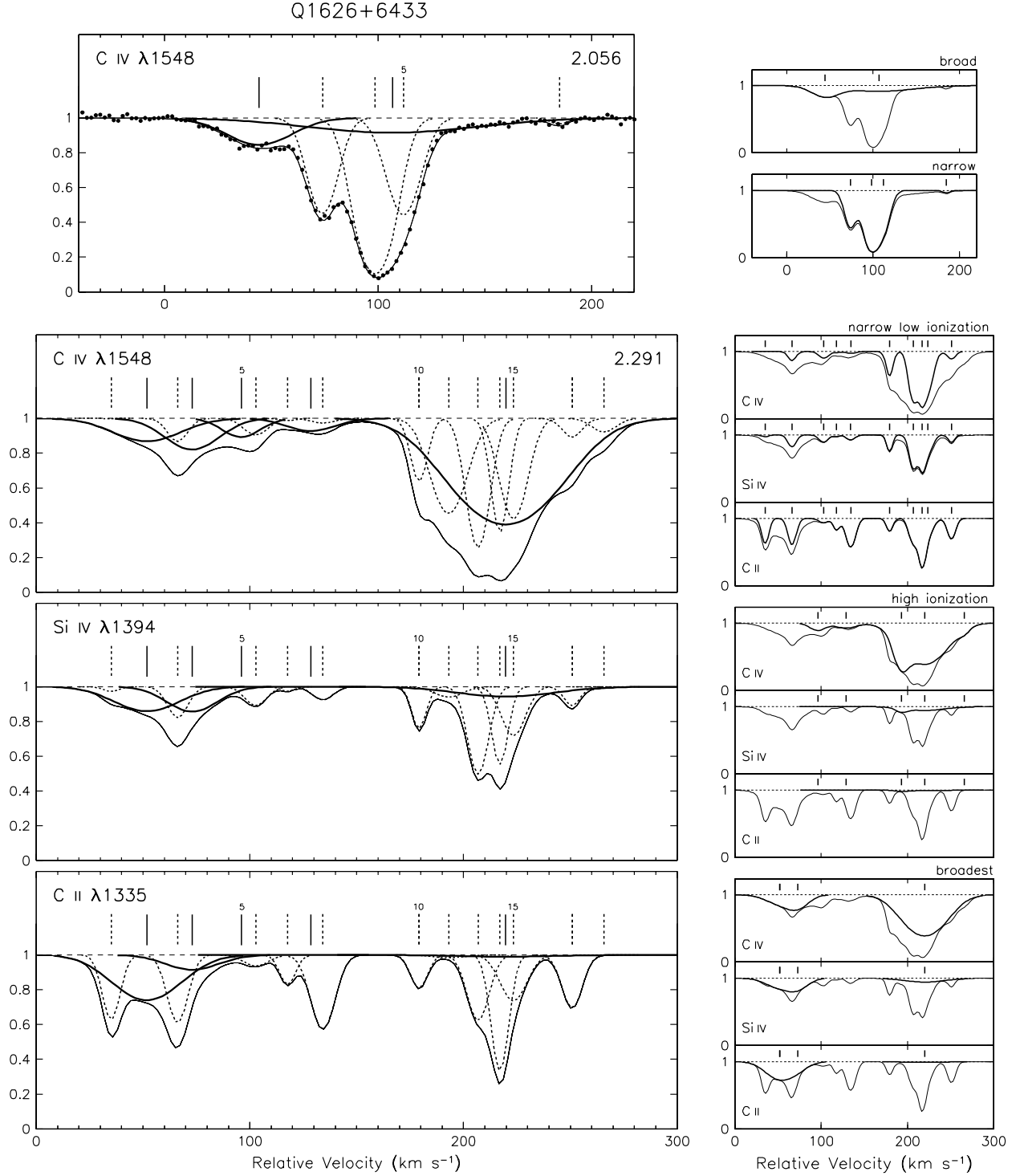


Fig. 5.— Two examples from Figure 3 showing component details of systems containing broad components (continuous thick lines and ticks) among the more numerous narrow components, $b(\text{C IV}) \lesssim 10 \text{ km s}^{-1}$ (short-dashed lines and ticks), with numbering as in Table 2. The overall composite fits to the pure system profiles (i.e. excluding any interloper species) are shown in continuous thin lines. Upper left panel: C IV profile in a simple system with exposed broad components, also showing the data points. Upper right panels: Separately highlighting the combined profiles of the broad and narrow components. Lower left panels: C IV, Si IV and C II profiles in a complex system with immersed broad components. The ticks here include positions of upper limits. Lower right panels: Highlighting the combined profiles of *top*, narrow components which are strong in C II, *middle*, all high ionization components and *bottom*, the broadest components.

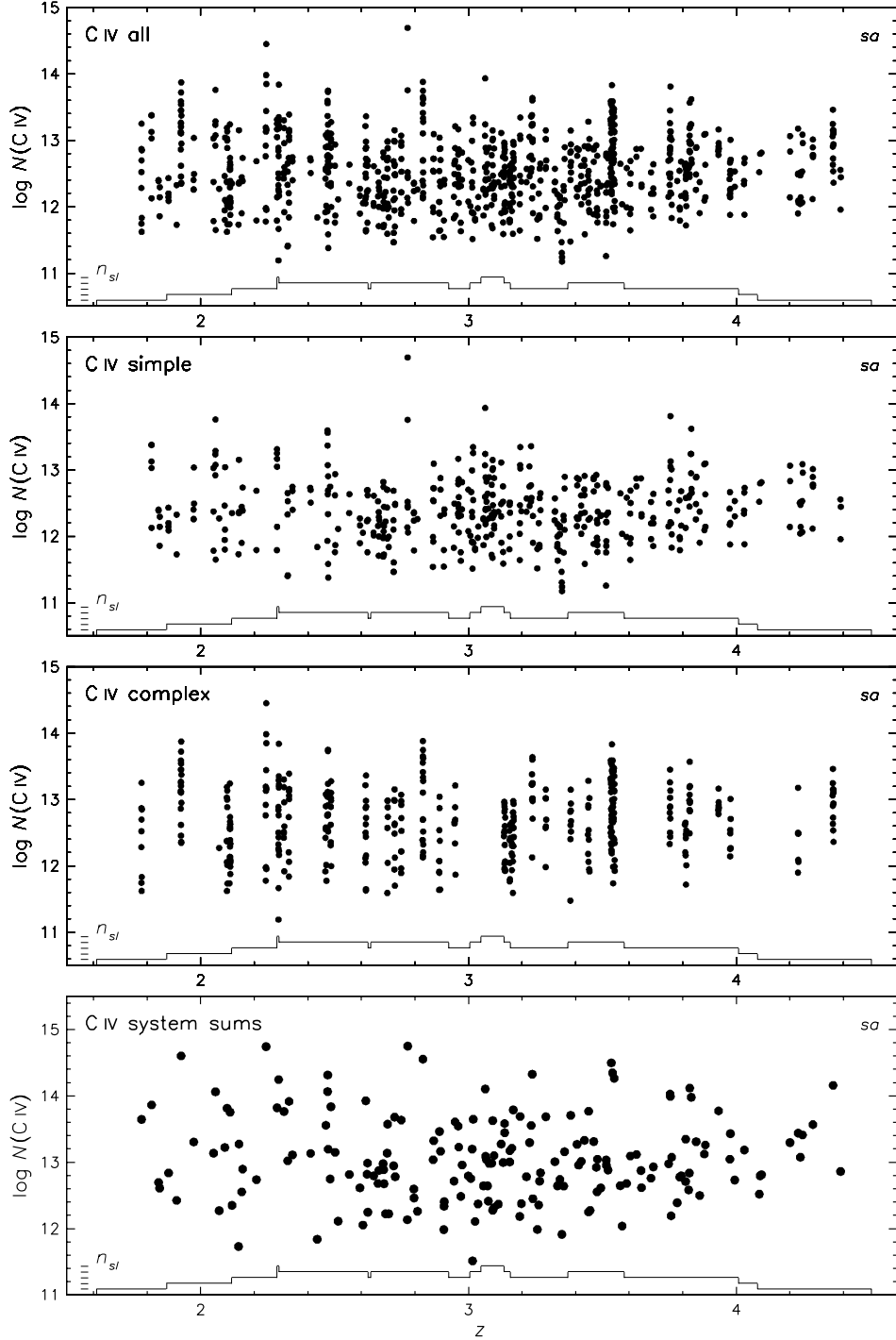


Fig. 6.— C IV column densities N (cm^{-2}) in sample *sa* plotted versus redshift z . To avoid clutter, errors (see Tables 2–10) are not shown. The thin continuous histograms display, in unit steps, the distribution of number of sightlines (n_{sl}) from the nine QSOs of the sample within the applied redshift constraints. *Upper three panels:* component values in *all* systems, *simple* systems (≤ 6 identified components) and *complex* systems (≥ 7 identified components). *Bottom panel:* *system* summed values for the same sample.

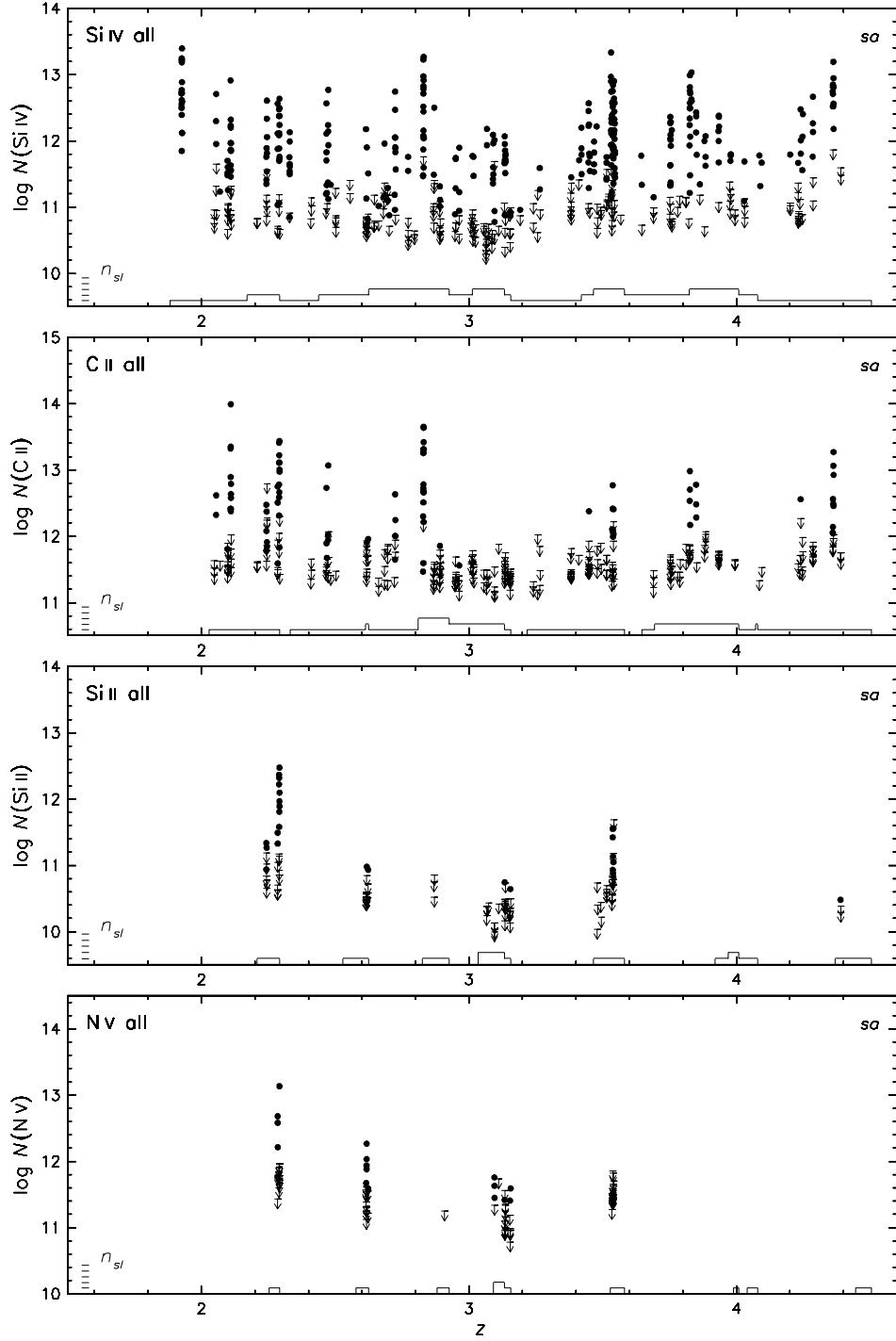


Fig. 7.— Si IV, C II, Si II and N V component column densities N (cm^{-2}) in sample *sa*, following the style of Figure 6. All components detected in C IV in the nine QSOs within the redshift intervals available to each species are represented. Upper limits are 1σ values.

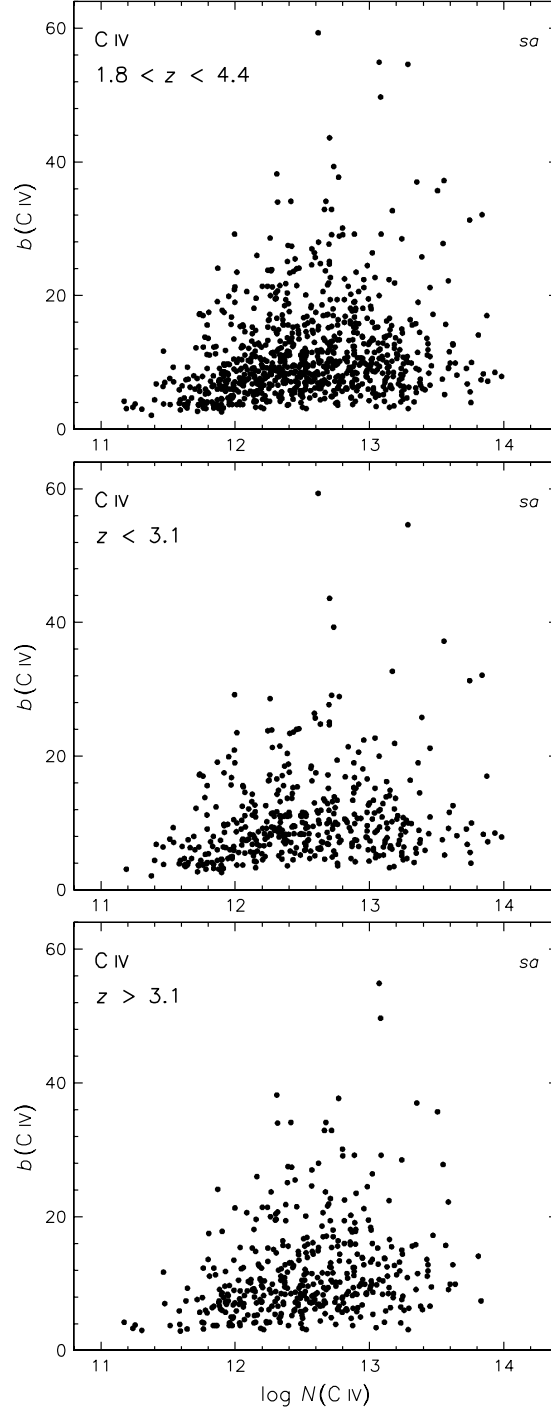


Fig. 8.— C IV Doppler parameter b (km s^{-1}) versus column density N (cm^{-2}) for all observed components of sample *sa*, also separately showing those with $z < 3.1$ and $z > 3.1$.

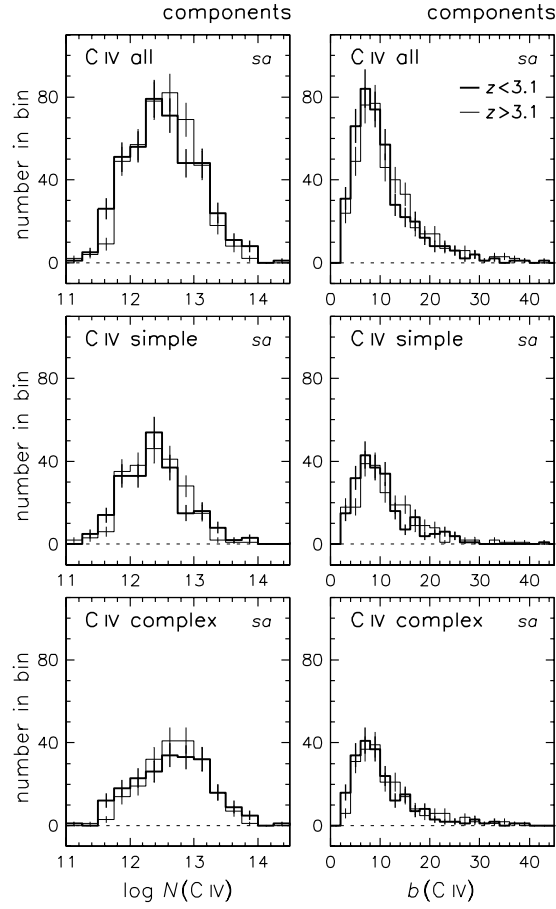


Fig. 9.— Histograms of C IV column density N (cm^{-2}) and Doppler parameter b (km s^{-1}) for all observed components of sample sa , comparing values for $z < 3.1$ (*thick lines*) and $z > 3.1$ (*thin lines*) and showing the data for *all* systems, *simple* systems (≤ 6 identified components) and *complex* systems (≥ 7 identified components).

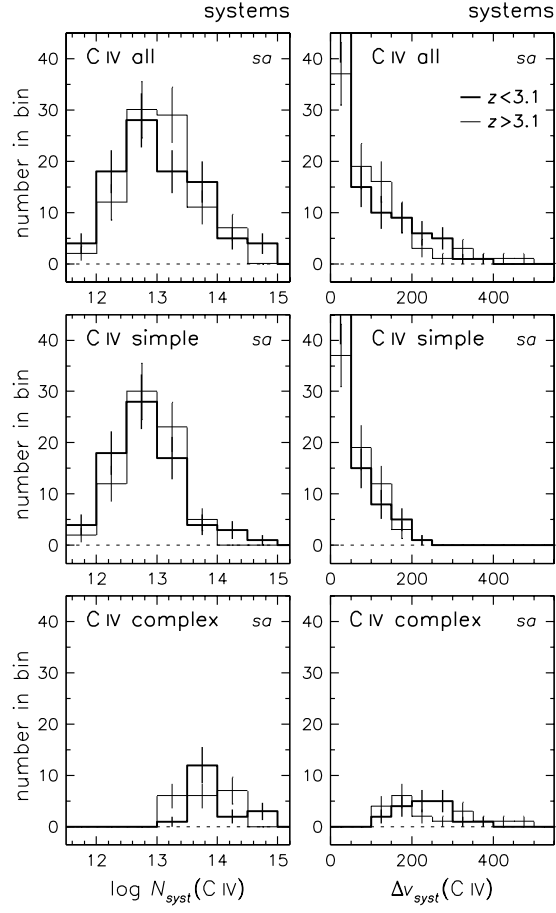


Fig. 10.— Histograms as in Figure 9, of system summed C IV column density N_{syst} (cm^{-2}) and overall velocity spread of the components within a system Δv_{syst} (km s^{-1}).

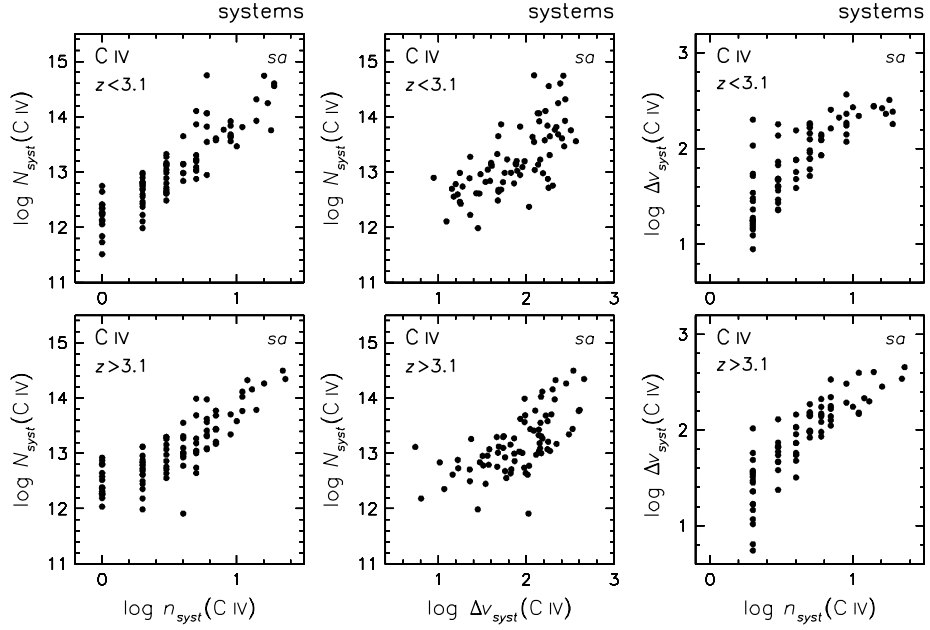


Fig. 11.— Relationships for all C IV systems of sample *sa* at redshifts $z < 3.1$ and $z > 3.1$, showing: *left panels*, system summed C IV column density N_{syst} (cm^{-2}) and number of components in the system n_{syst} ; *middle panels*, N_{syst} and overall velocity spread of system components Δv_{syst} (km s^{-1}); *right panels*, Δv_{syst} and n_{syst} .

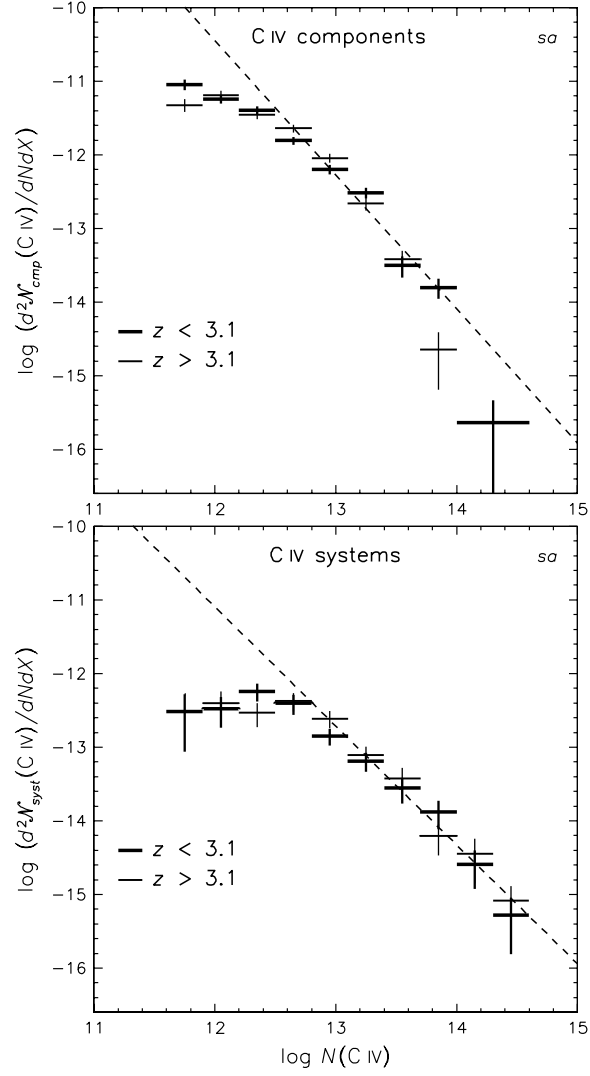


Fig. 12.— Differential column density distribution of C IV components (*upper*) and systems (*lower*) for sample *sa* at redshifts $z < 3.1$ and $z > 3.1$. The bin size (shown by horizontal bars) is $10^{0.3} N \text{ (cm}^{-2}\text{)}$ where N is the column density; errors (vertical bars) are $\pm 1\sigma$ values based on the number of absorbers \mathcal{N} in each bin. The dashed lines are approximate power-law fits as described in the text with index $\beta = 1.84$ (components) and $\beta = 1.6$ (systems).

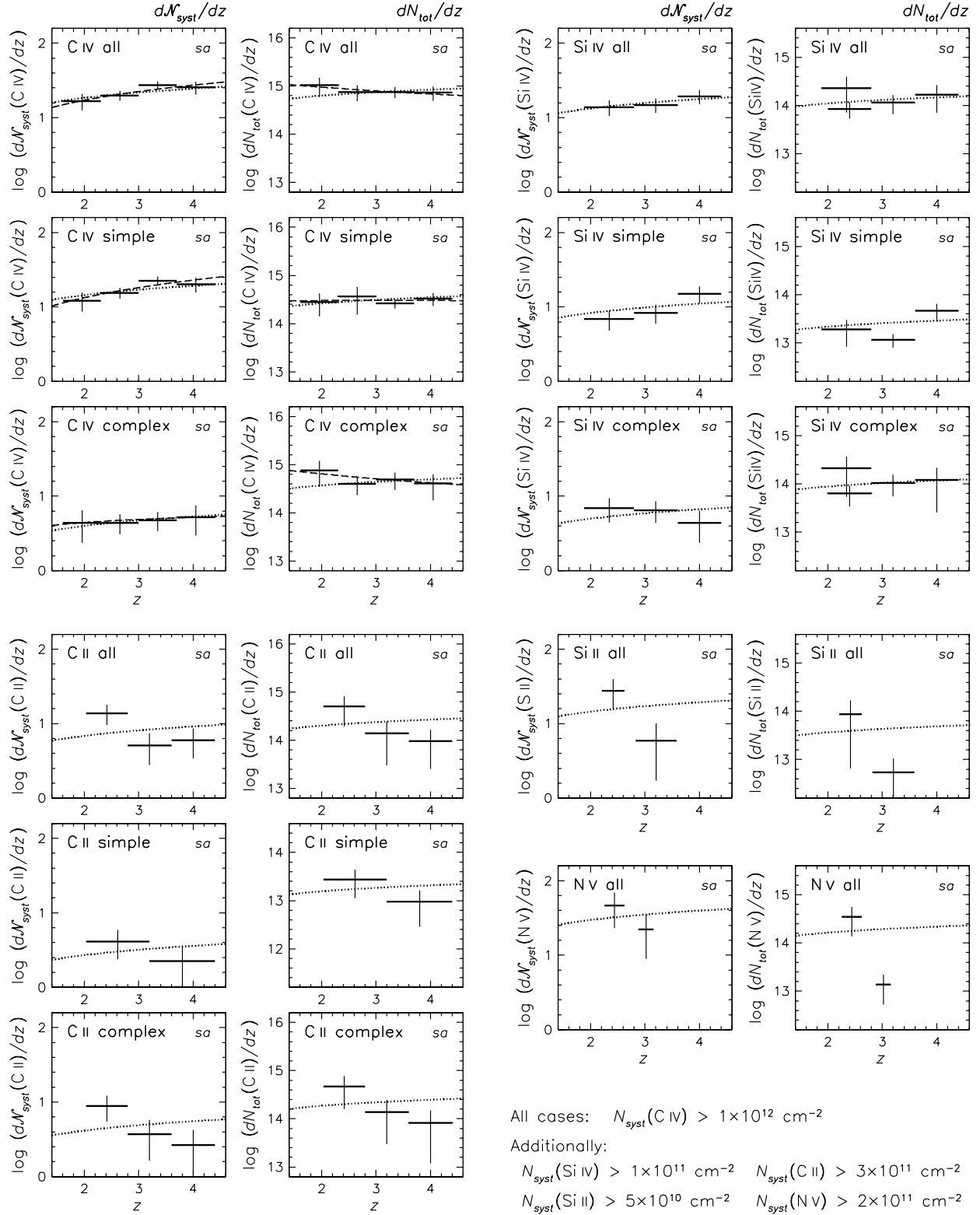


Fig. 13.— *Upper left panels:* Redshift evolution of C IV total number of systems per unit redshift interval, dN_{syst}/dz , and total column density (cm^{-2}) per unit redshift interval, dN_{tot}/dz , accounted over the redshift range shown by each bar, for systems in sample *sa* having $N_{\text{syst}}(\text{C IV}) > 1 \times 10^{12} \text{ cm}^{-2}$, showing *all* systems, *simple* systems (≤ 6 C IV components) and *complex* systems (≥ 7 C IV components); for errors see text. *Upper right and lower left panels:* Corresponding data for the same systems also having *detected* components in Si IV and C II above the indicated thresholds. *Lower right panels:* Similarly for *all* systems having *detected* components in Si II and N V. Note the various changes in vertical scale for dN_{tot}/dz . The dotted curves indicate non-evolving quantities (see text); dashed curves shown only for C IV represent fits to the data.

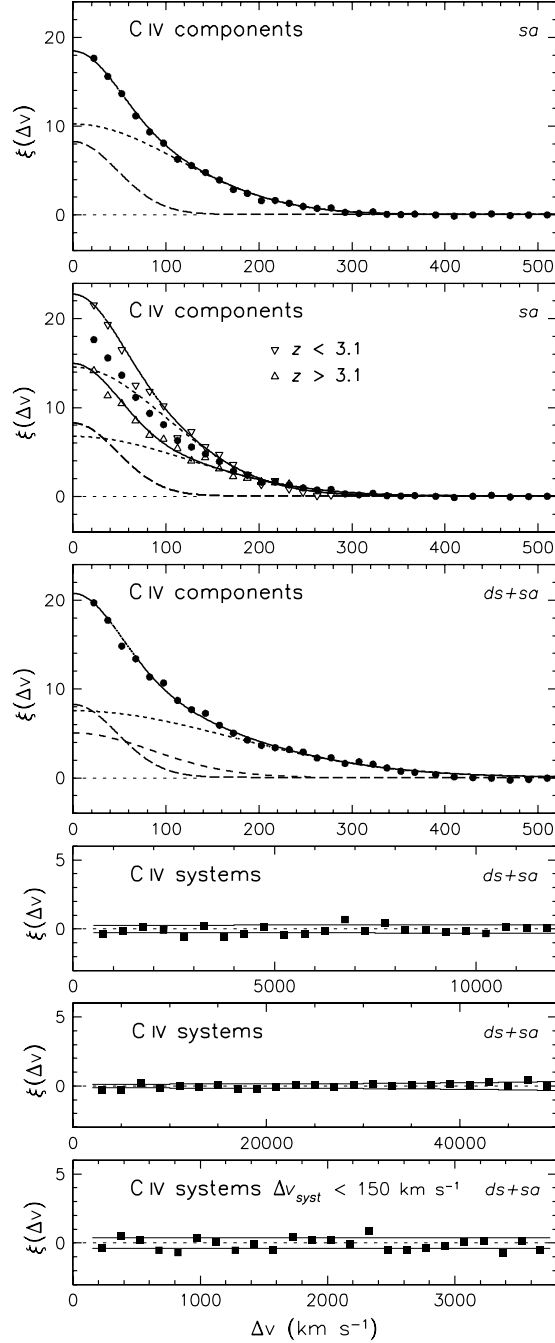


Fig. 14.— Two-point correlation functions $\xi(\Delta v)$ versus velocity separations Δv for C IV absorber redshifts spanning $1.6 \lesssim z \lesssim 4.4$. *Top panel:* Points give $\xi(\Delta v)$ for the individual components of sample *sa*, binned over 15 km s^{-1} for $\Delta v \leq 370 \text{ km s}^{-1}$ and 20 km s^{-1} for $\Delta v \geq 370$; $\pm 1\sigma$ errors in the random distribution are smaller than the symbol size. A two-component Gaussian fit and the separate components of the fit are shown with parameters as given in the text. *Second panel:* Same as *top panel*, also showing results for subsets with $z < 3.1$ and $z > 3.1$. *Third panel:* Same as *top panel*, now adding all components of the 7 systems with significant Lyman α damping wings and separated by $\gtrsim 3000 \text{ km s}^{-1}$ from the emission redshift, giving sample *ds+sa*; a three-component Gaussian fit is shown. *Fourth panel:* Result for the system redshifts of sample *ds+sa*, binned over 500 km s^{-1} and extending to $\Delta v = 12000 \text{ km s}^{-1}$; $\pm 1\sigma$ errors in the random distribution are shown by bounding thin lines. *Fifth panel:* Same as *fourth panel* but binned over 2000 km s^{-1} and extending to $\Delta v = 50000 \text{ km s}^{-1}$. *Sixth panel:* Same as *fourth panel* but including only systems of velocity spread $\Delta v_{\text{syst}} < 150 \text{ km s}^{-1}$, binned over 150 km s^{-1} and extending to $\Delta v = 3800 \text{ km s}^{-1}$.

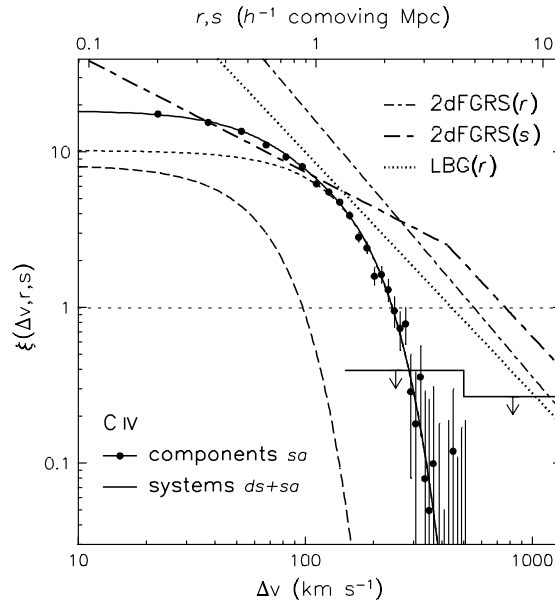


Fig. 15.— Comparison of C IV absorber and galaxy two-point correlation functions in logarithmic form. The C IV sample *sa* data for individual components are shown with the two-component Gaussian fit as in Figure 14; $\pm 1\sigma$ errors in the random distributions are given with the data points. Sample *ds+sa* data for systems as described in the text are shown here as upper limits using $+1\sigma$ errors from Figure 14. Fits to data from the 2dF Galaxy Redshift Survey in real-space (*r*) and redshift-space (*s*) and for a sample of Lyman-break galaxies (LBG), all as described in the text, use the upper axis.

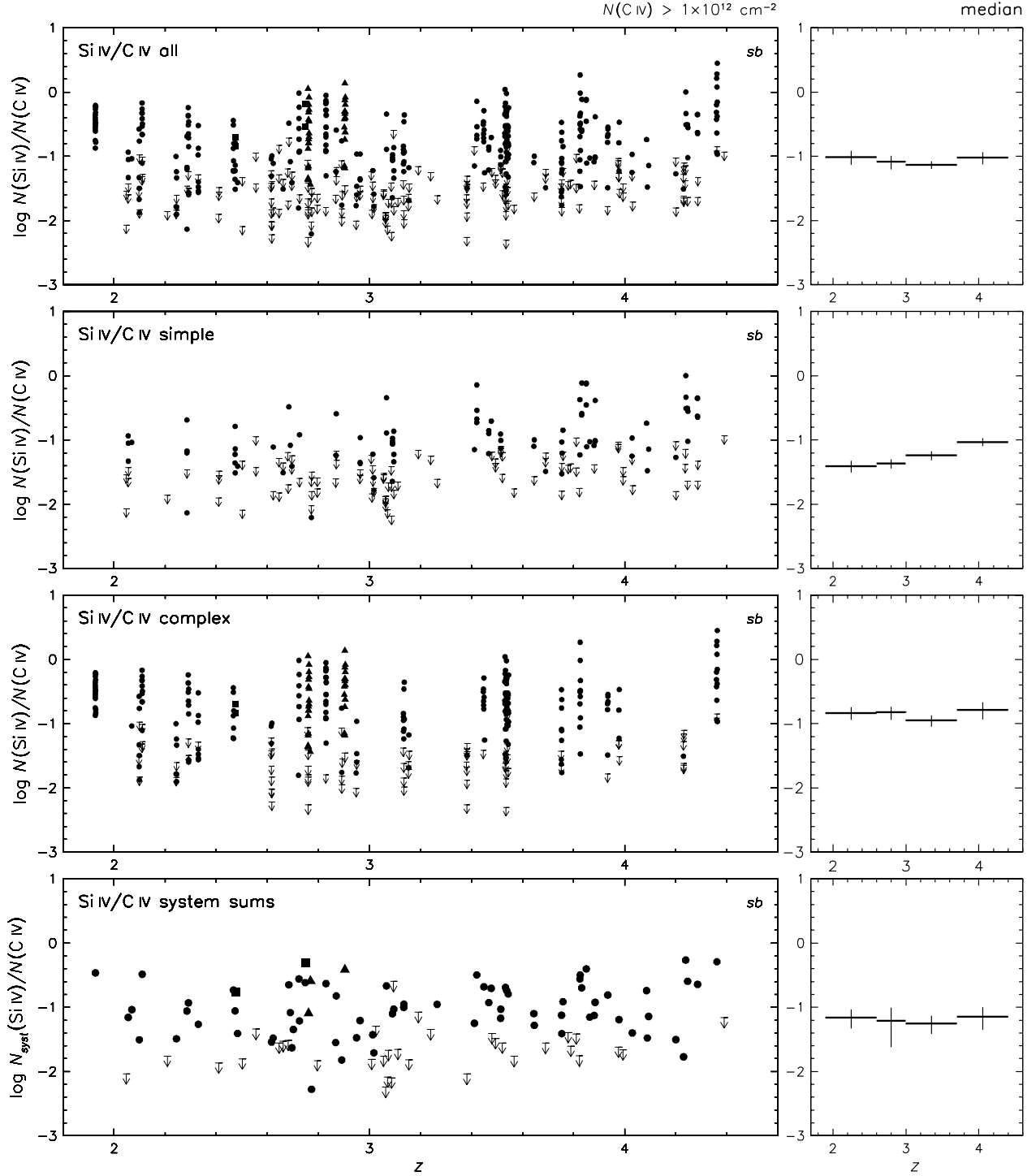


Fig. 16.— *Left panels:* Redshift evolution of Si IV/C IV column density ratios. Upper limits are 1σ values. The *upper three panels* show individual component values having $N(\text{C IV}) > 1 \times 10^{12} \text{ cm}^{-2}$ from sample *sb* for *all* systems, *simple* systems (≤ 6 C IV components) and *complex* systems (≥ 7 C IV components). *Filled circles* show values obtained outside the Lyman forest; reliable values from lines in the Lyman forest are identified by *filled squares*; selected components clear of regions of high $N(\text{H I})$ in systems containing mild Lyman α damping wings are shown by *filled triangles*. The *bottom panel* gives values obtained from *summed* column densities for all available *systems* in sample *sb* having $N_{\text{sys}}(\text{C IV}) > 1 \times 10^{12} \text{ cm}^{-2}$. *Right panels:* Redshift evolution of corresponding median values, obtained over the extent of each horizontal bar, indicated with 1σ error bars.

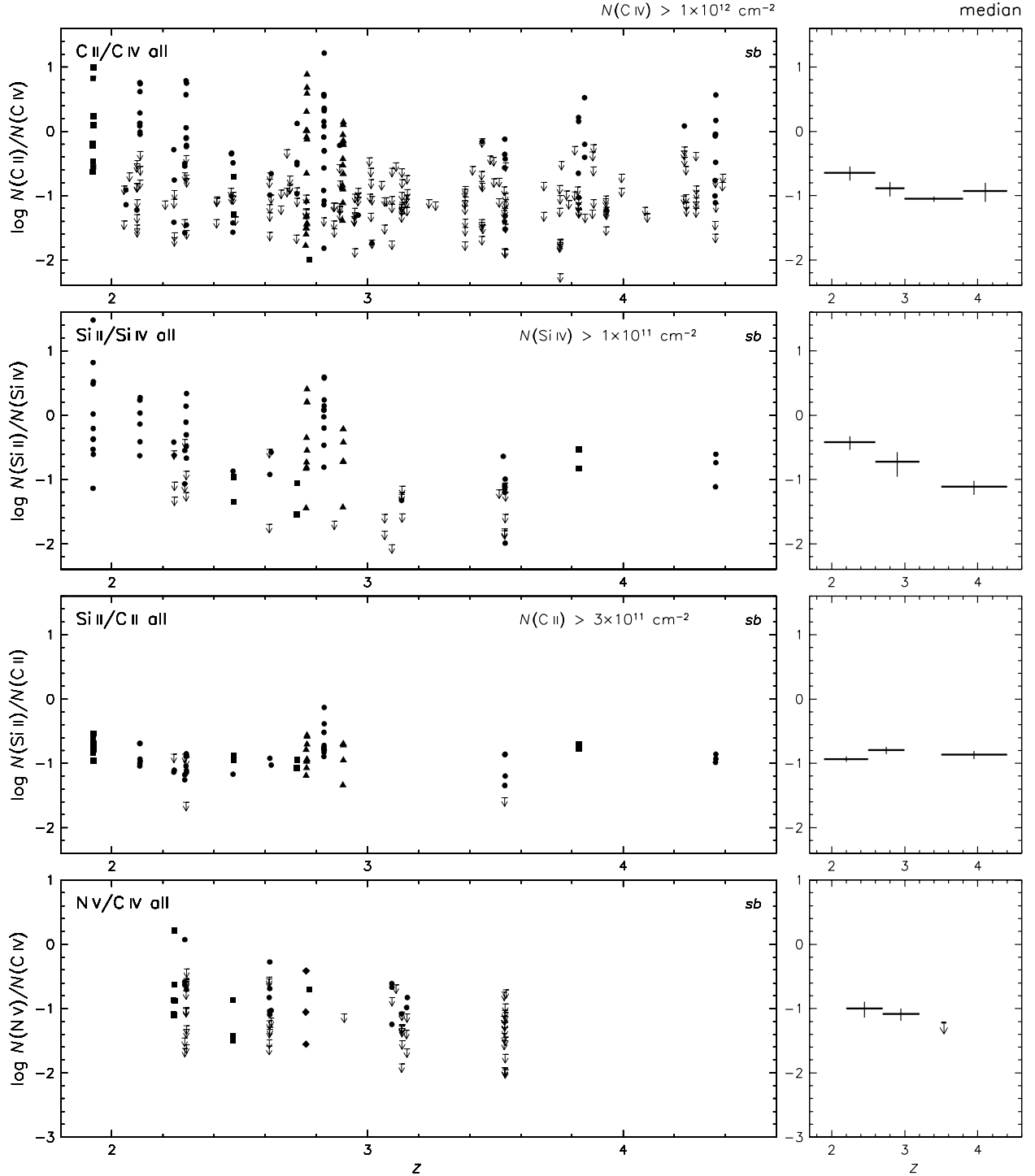


Fig. 17.— Same as for the *top* panels in Figure 16, here for the component column density ratios C II/C IV, Si II/Si IV (having *detected* Si IV with $N(\text{Si IV}) > 1 \times 10^{11} \text{ cm}^{-2}$), Si II/C II (having *detected* C II with $N(\text{C II}) > 1 \times 10^{11} \text{ cm}^{-2}$) and N V/C IV (*filled diamonds* indicate values from components that are both in the forest and selected from mildly damped systems). In all cases components have $N(\text{C IV}) > 1 \times 10^{12} \text{ cm}^{-2}$.

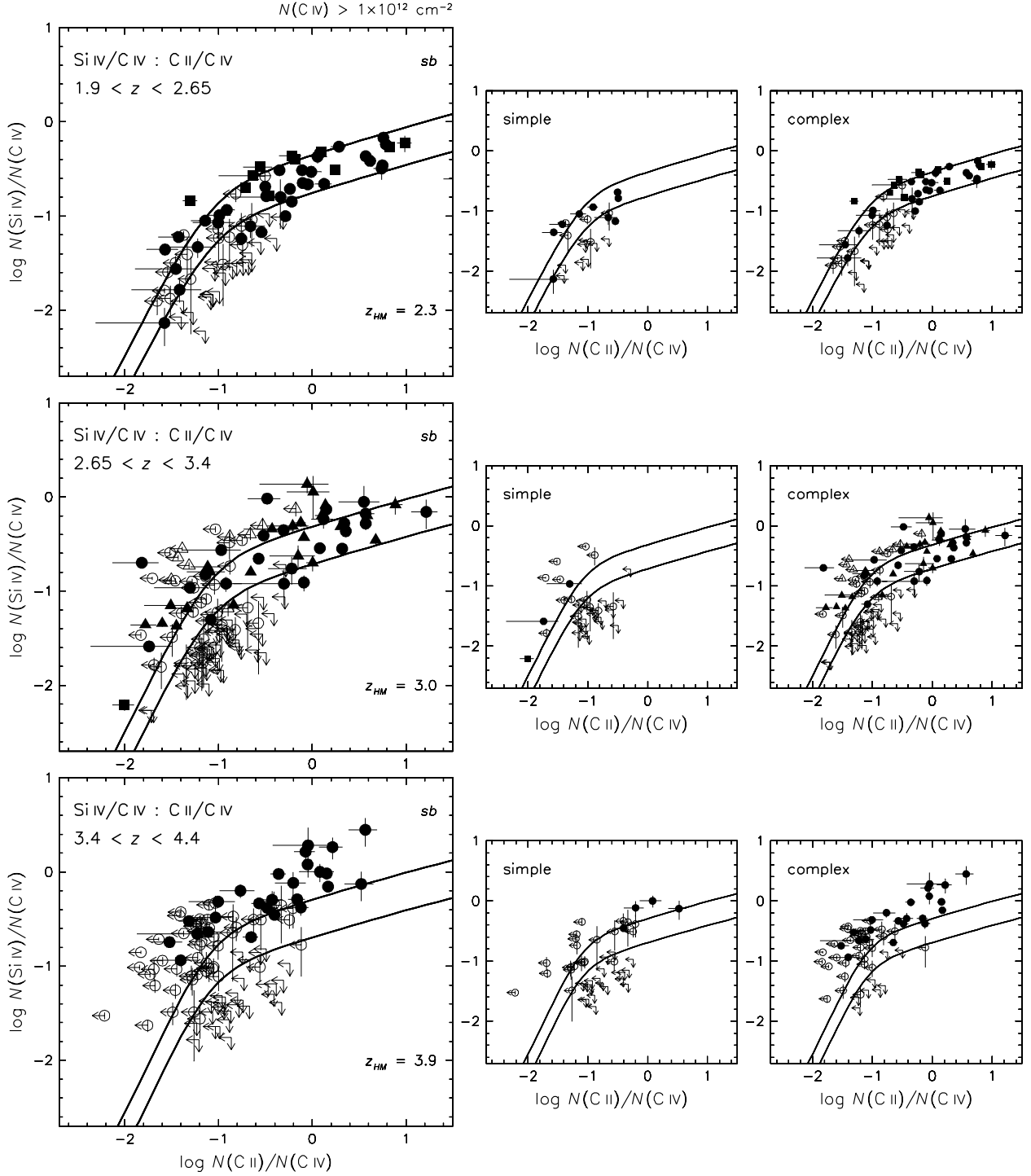


Fig. 18.— *Left panels:* Column density ratios $\text{Si IV}/\text{C IV} : \text{C II}/\text{C IV}$ in three redshift intervals for *all* components having $N(\text{C IV}) > 1 \times 10^{12} \text{ cm}^{-2}$ in sample *sb*. *Filled symbols* are defined in Figure 16. Error bars give $\pm 1\sigma$ uncertainties; upper limit arrows point from $+1\sigma$ values. Cases where one of the two ionic ratios is an upper limit are indicated by an *open* symbol. The *thick lines* give model predictions of the Cloudy code for absorbers optically thin in the H I Lyman continuum ($N(\text{H I}) = 1 \times 10^{15} \text{ cm}^{-2}$), low metallicity ($0.003 \times$ solar) and Si/C relative abundance values of solar and $2.5 \times$ solar (see text), computed at appropriate redshifts z_{HM} for Haardt & Madau latest available versions of the metagalactic ionizing radiation background with the QSO contribution alone (model Q—see text for a full description); $J_{\nu 0} = 3.5 \times 10^{-22} \text{ erg s}^{-1} \text{ cm}^{-2} \text{ Hz}^{-1} \text{ sr}^{-1}$ at $z_{\text{HM}} = 2.3$, 2.5×10^{-22} at $z_{\text{HM}} = 3.0$ and 1.6×10^{-22} at $z_{\text{HM}} = 3.9$. The cosmic microwave background is included. *Right panels:* Subsets of *simple* systems (≤ 6 C IV components) and *complex* systems (≥ 7 C IV components).

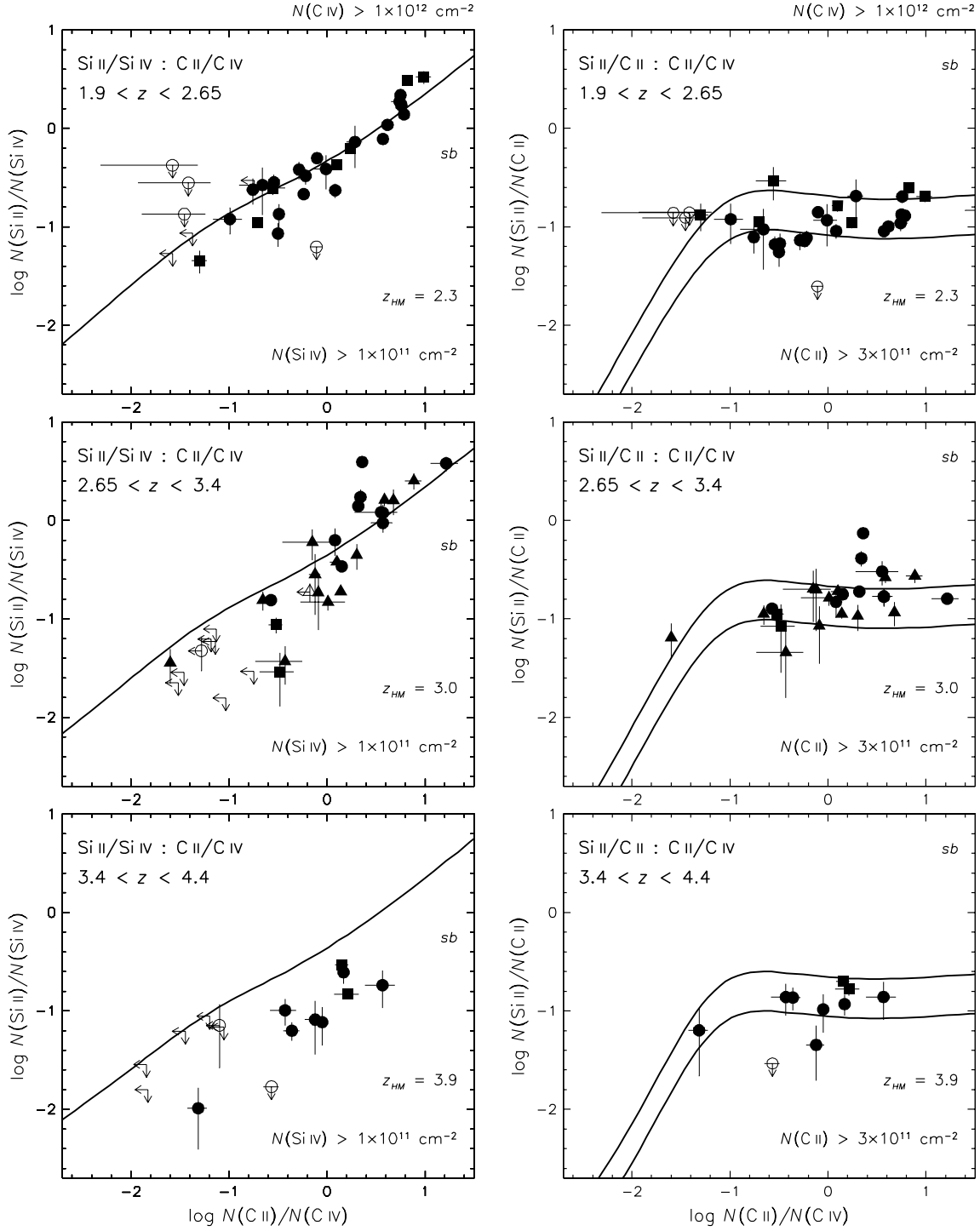


Fig. 19.— *Left panels:* Same as for *left panels* in Figure 18, here for Si II/Si IV : C II/C IV and additionally using only *detected* Si IV components having $N(\text{Si IV}) > 1 \times 10^{11} \text{ cm}^{-2}$. *Right panels:* Same for Si II/C II : C II/C IV, but using only *detected* C II components having $N(\text{C II}) > 3 \times 10^{11} \text{ cm}^{-2}$. Both Si/C relative abundance values used in Figure 18 are shown.

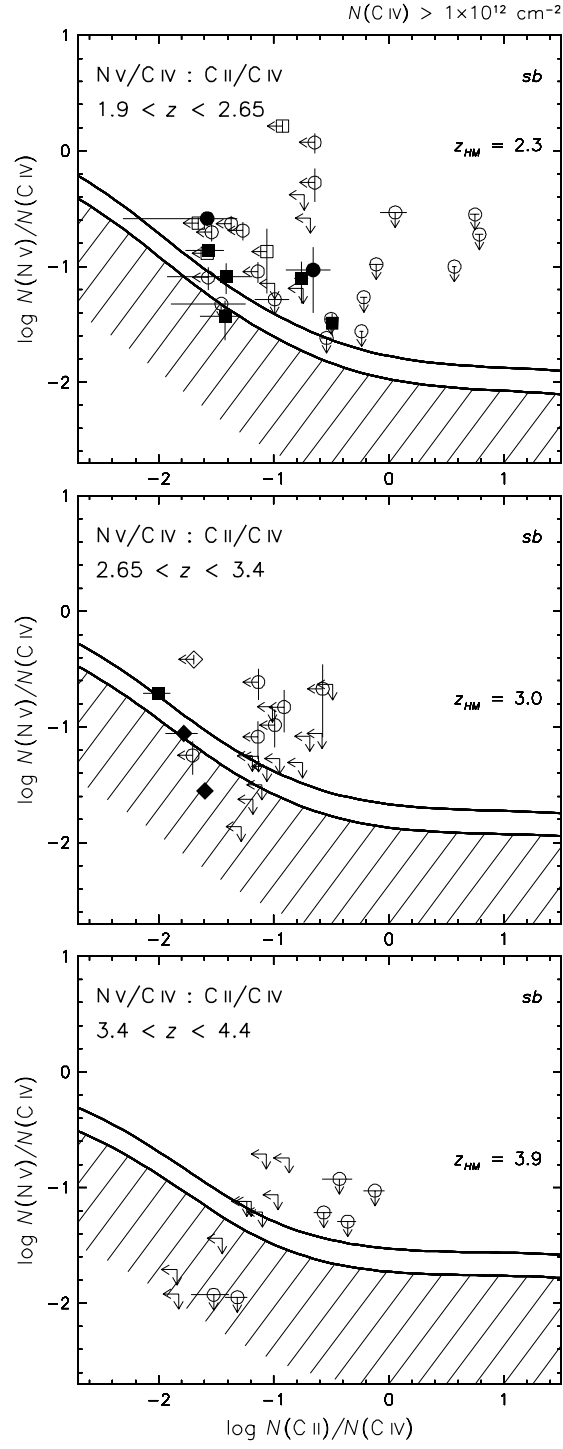


Fig. 20.— Same as *left* panels in Figure 18, here for $\text{N V/C IV} : \text{C II/C IV}$ and N/C relative abundance values of solar and $0.63 \times$ solar with shading for the latter indicating the possible range extending lower by 1 dex (see text).

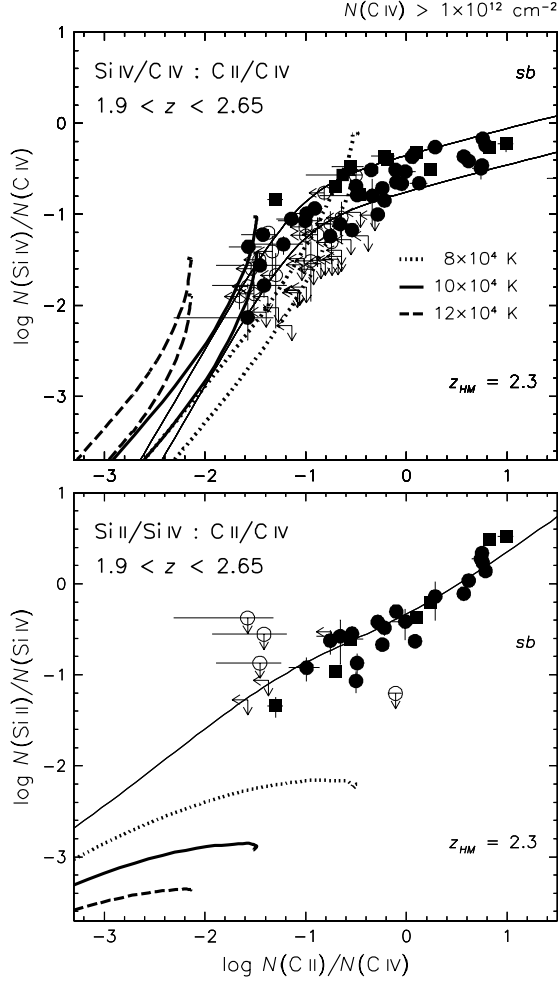


Fig. 21.— Si IV/C IV : C II/C IV and Si II/Si IV : C II/C IV as in the top panels of Figures 18 and 19, with extended axes. The curves show Cloudy models representing collisional ionization at fixed temperatures near 10^5 K (indicated in the *upper* panel) in the presence of the latest available Haardt & Madau pure QSO version of the metagalactic ionizing radiation background (model Q—see text) at $z_{HM} = 2.3$; for reference, models in photoionization equilibrium as in Figures 18 and 19 are shown here in *continuous lines*. Both values of Si/C relative abundance are included as in the previous figures. The collisional ionization curves terminate in the diagram where the process becomes independent of density.

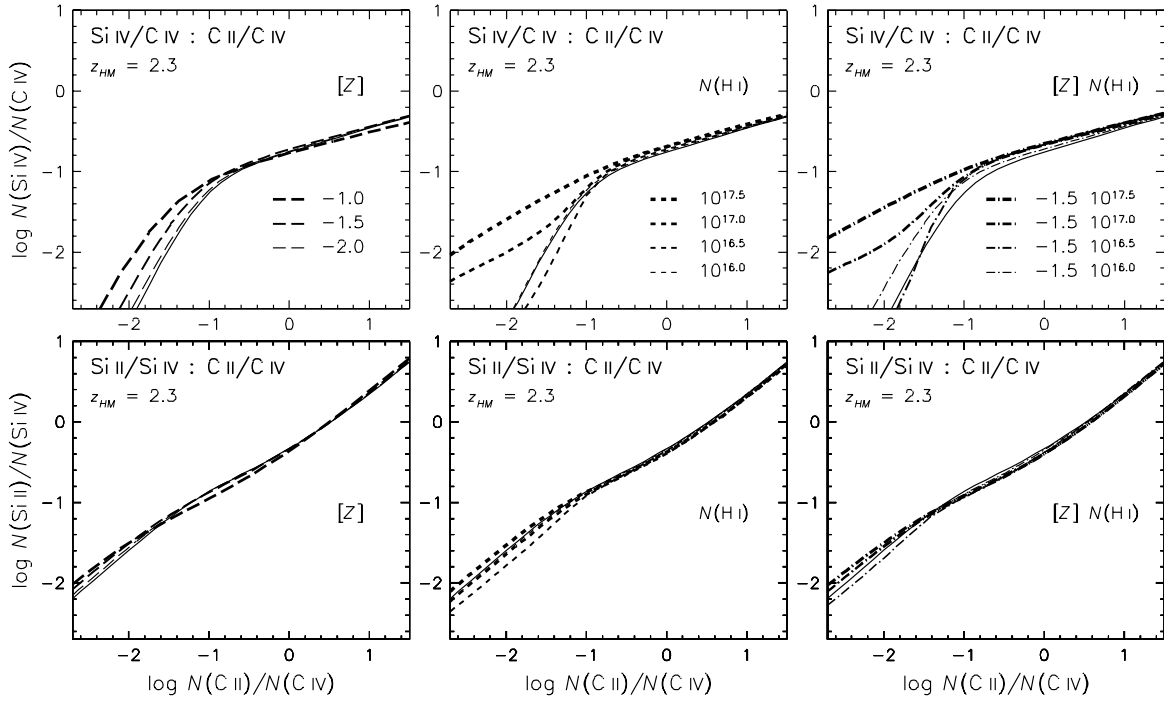


Fig. 22.— $\text{Si IV/C IV} : \text{C II/C IV}$ and $\text{Si II/Si IV} : \text{C II/C IV}$ Cloudy models in photoionization equilibrium using the latest available Haardt & Madau pure QSO version of metagalactic ionizing radiation background (model Q—see text) at $z_{\text{HM}} = 2.3$ with absorber parameters arbitrarily differing in metallicity, $[Z] = -2.0$ to -1.0 , and hydrogen column density, $N(\text{H I}) = 10^{16}$ to $10^{17.5} \text{ cm}^{-2}$, as indicated; the nominal case with $[Z] = -2.5$ and $N(\text{H I}) = 10^{15.0} \text{ cm}^{-2}$ used in Figures 18 and 19 is shown here in *continuous lines*. For clarity only the solar Si/C relative abundance value is included.

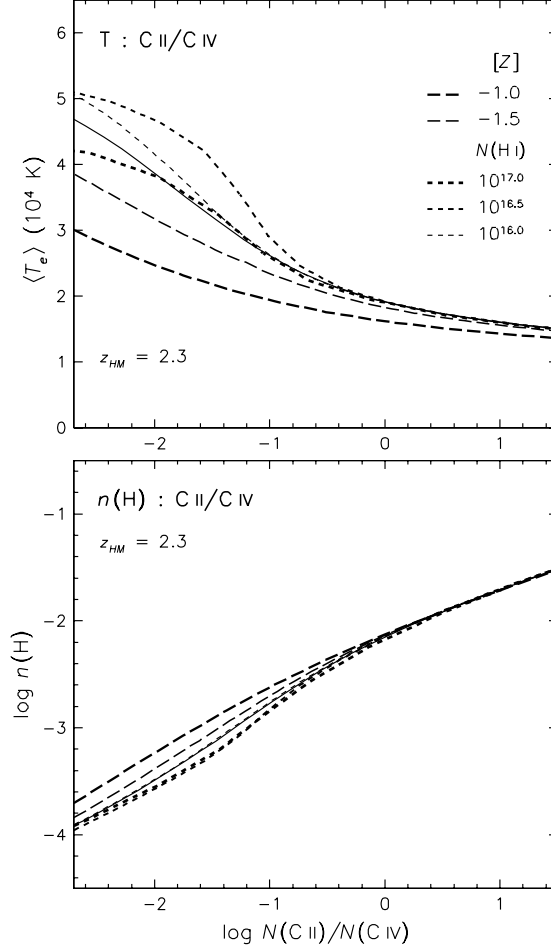


Fig. 23.— Photoionization equilibrium mean column temperature, $\langle T_e \rangle$ (K), and total hydrogen volume density, $n(\text{H})$ (cm^{-3}), versus C II/C IV, for the Cloudy-modelled case using the latest available Haardt & Madau pure QSO version of metagalactic ionizing radiation background (model Q—see text) at $z_{\text{HM}} = 2.3$ with absorber parameters arbitrarily differing in metallicity $[Z]$ and hydrogen column density $N(\text{H I})$ as indicated, compared with the nominal case with $[Z] = -2.5$ and $N(\text{H I}) = 10^{15.0} \text{ cm}^{-2}$ shown in *continuous lines*.

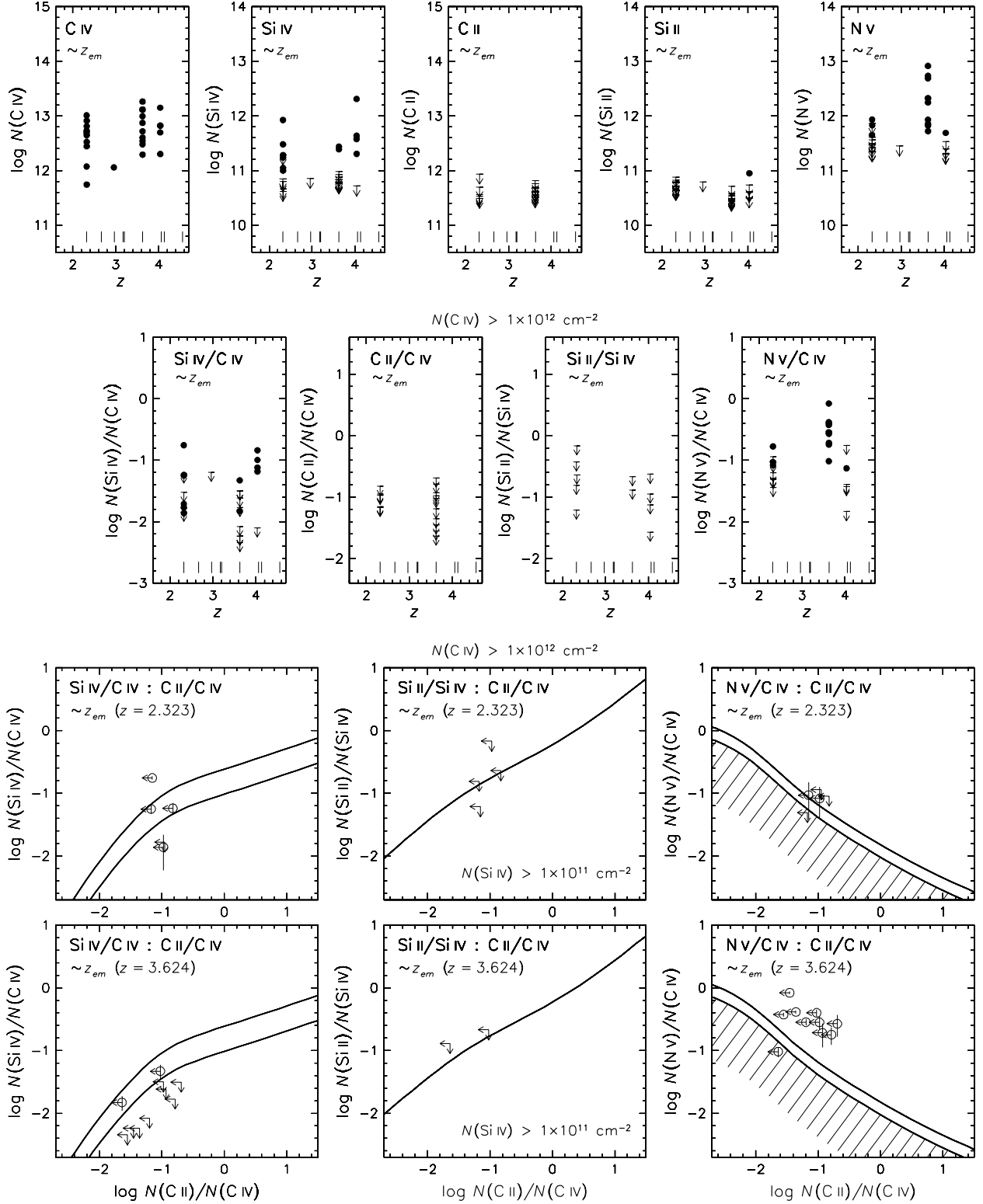


Fig. 24.— Systems with redshift close to the emission redshift z_{em} of their sightline QSO, (indicated by *vertical ticks*). *Top panels:* C IV , Si IV , C II , Si II and N V component column densities (cm^{-2}). *Middle panels:* Component ($N(\text{C IV}) > 1 \times 10^{12} \text{ cm}^{-2}$) column density ratios $\text{Si IV}/\text{C IV}$, $\text{C II}/\text{C IV}$, $\text{Si II}/\text{Si IV}$ ($N(\text{Si IV}) > 1 \times 10^{11} \text{ cm}^{-2}$) and $\text{N V}/\text{C IV}$. *Bottom set of panels:* Column density ratio combinations for components ($N(\text{C IV}) > 1 \times 10^{12} \text{ cm}^{-2}$) of the systems at $z = 2.323$ in Q1626+6433 and $z = 3.624$ in Q1422+2309C compared with Cloudy results as in Figures 18–20, but using radiation with a power-law spectrum of index -1.8 having $J_{\nu 0} = 3.5 \times 10^{-21} \text{ erg s}^{-1} \text{ cm}^{-2} \text{ Hz}^{-1} \text{ sr}^{-1}$; the cosmic microwave background is included.

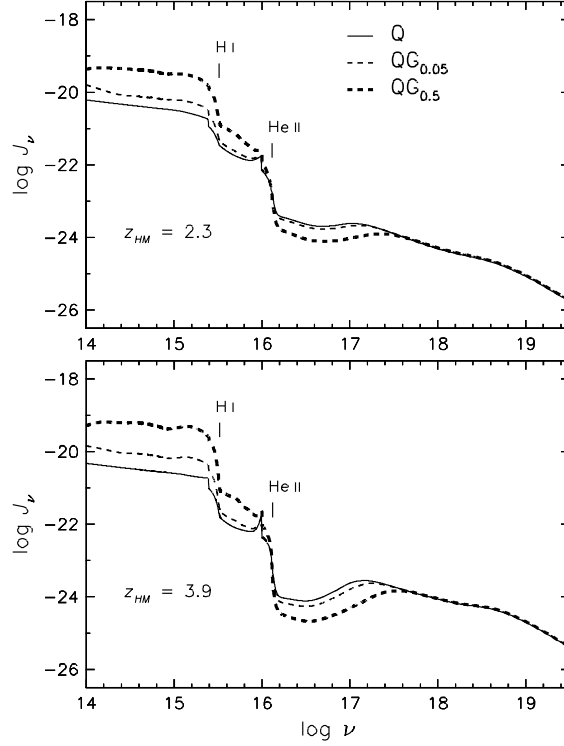


Fig. 25.— Rest spectral energy distributions plotted as mean intensity J_ν ($\text{erg cm}^{-2} \text{ s}^{-1} \text{ Hz}^{-1} \text{ sr}^{-1}$) over frequency ν (Hz), obtained from new Haardt & Madau metagalactic ionizing radiation background models having contributions both from QSOs and galaxies for the two values $f_{\text{esc}} = 0.05$ and 0.5 (see text), termed models $\text{QG}_{0.05}$ and $\text{QG}_{0.5}$, at redshifts $z_{HM} = 2.3$ and 3.9 . The pure QSO case as used in Figures 18–20, model Q, is shown for comparison. The values of J_{ν_0} in the models containing galaxy contributions are respectively: 4.3×10^{-22} and $1.2 \times 10^{-21} \text{ erg s}^{-1} \text{ cm}^{-2} \text{ Hz}^{-1} \text{ sr}^{-1}$ at $z_{HM} = 2.3$; 2.2×10^{-22} and $8.4 \times 10^{-22} \text{ erg s}^{-1} \text{ cm}^{-2} \text{ Hz}^{-1} \text{ sr}^{-1}$ at $z_{HM} = 3.9$. The positions of the ionization thresholds for H I and He II, at 1 and 4 Rydberg, are indicated.

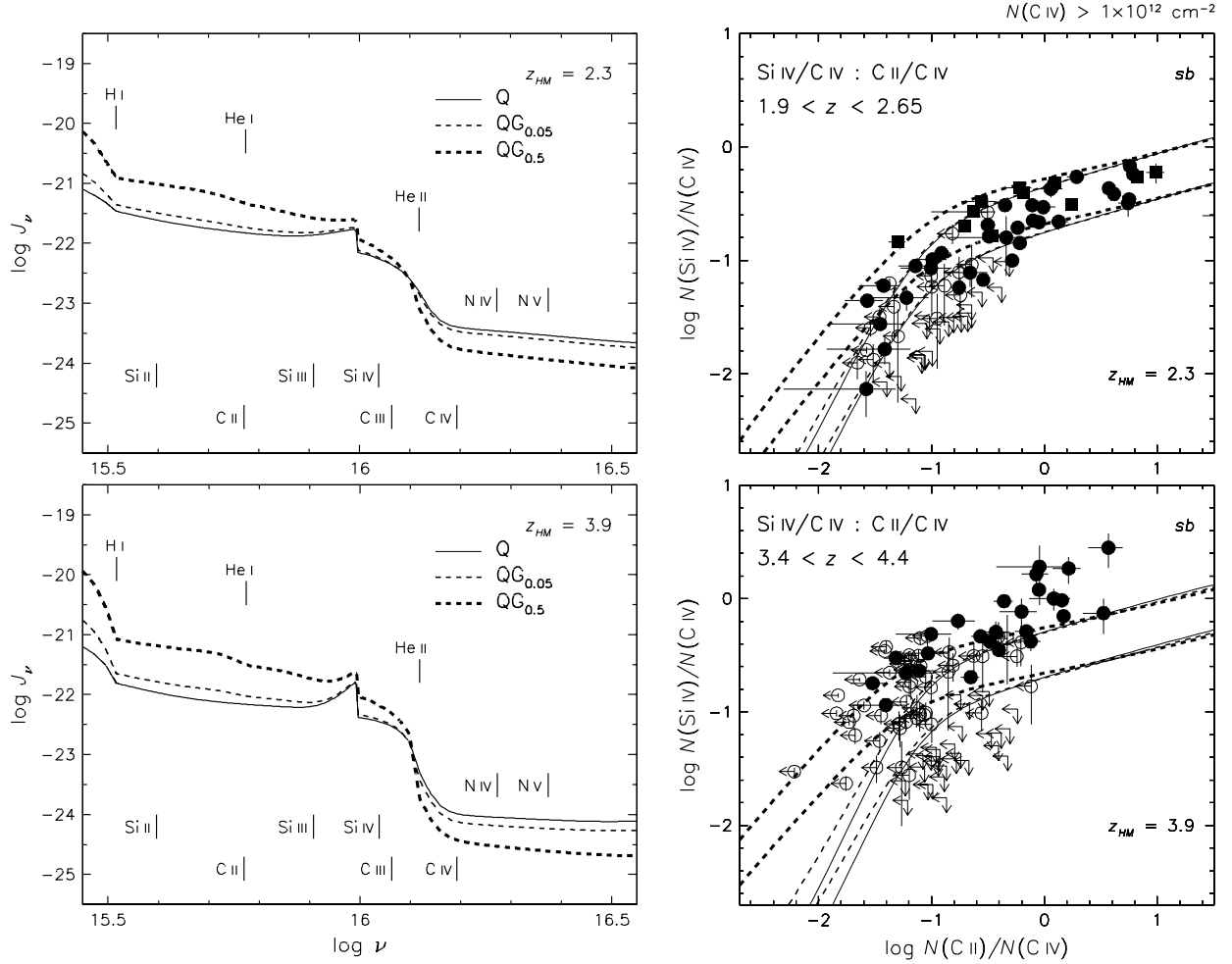


Fig. 26.— *Left panels:* Rest spectral energy distributions for the new Haardt & Madau metagalactic ionizing radiation models $QG_{0.05}$ and $QG_{0.5}$ defined in Figure 25 but here concentrating on the region containing the ionization thresholds for H, He, C, Si and N significant for this paper. *Right panels:* Observed column density ratios $\text{Si IV}/\text{C IV} : \text{C II}/\text{C IV}$ in two redshift intervals taken from Figure 18 compared with Cloudy results using models $QG_{0.05}$ and $QG_{0.5}$ (coding as indicated in the left panels) with absorber parameters as defined in Figure 18. The cosmic microwave background at the two redshifts is included to account for Compton cooling.

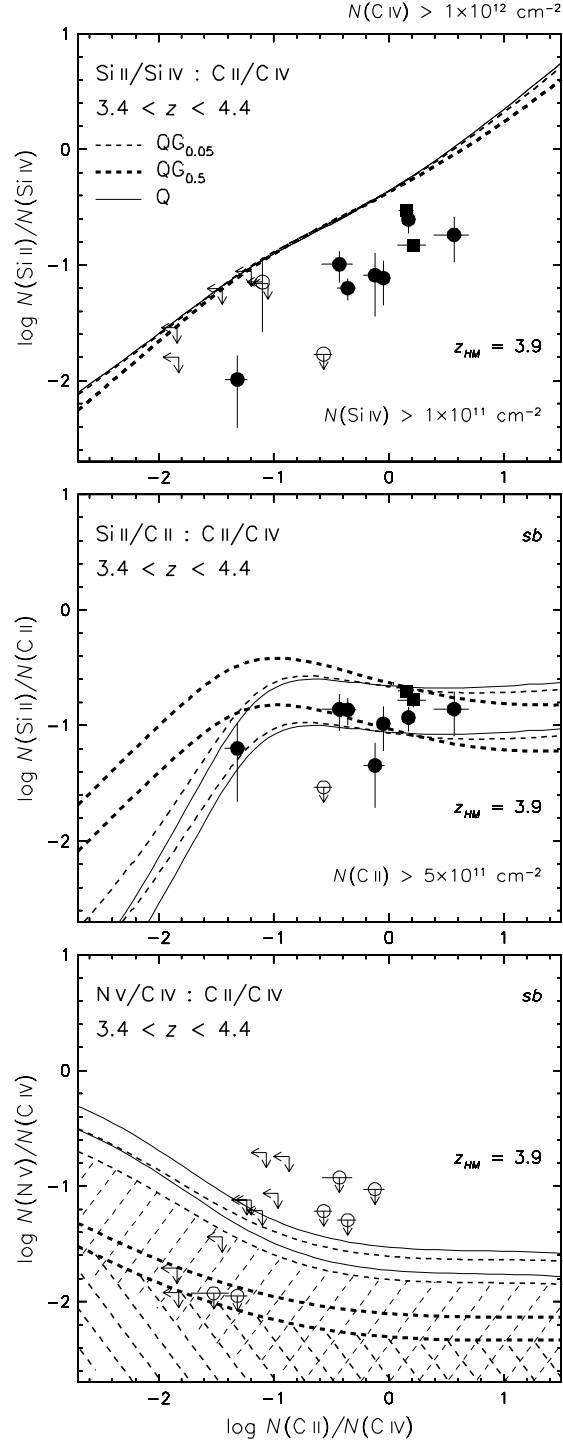


Fig. 27.— Same as for *lower right* panel in Figure 26, here for $\text{Si II/Si IV} : \text{C II/C IV}$, $\text{Si II/C II} : \text{C II/C IV}$ and $\text{N V/C IV} : \text{C II/C IV}$, with the data values taken from Figures 19 and 20. The N/C relative abundance ranges as given in Figure 20 are also shown here but to avoid confusion the shading indicating possible lower values by up to 1 dex is omitted for model Q .

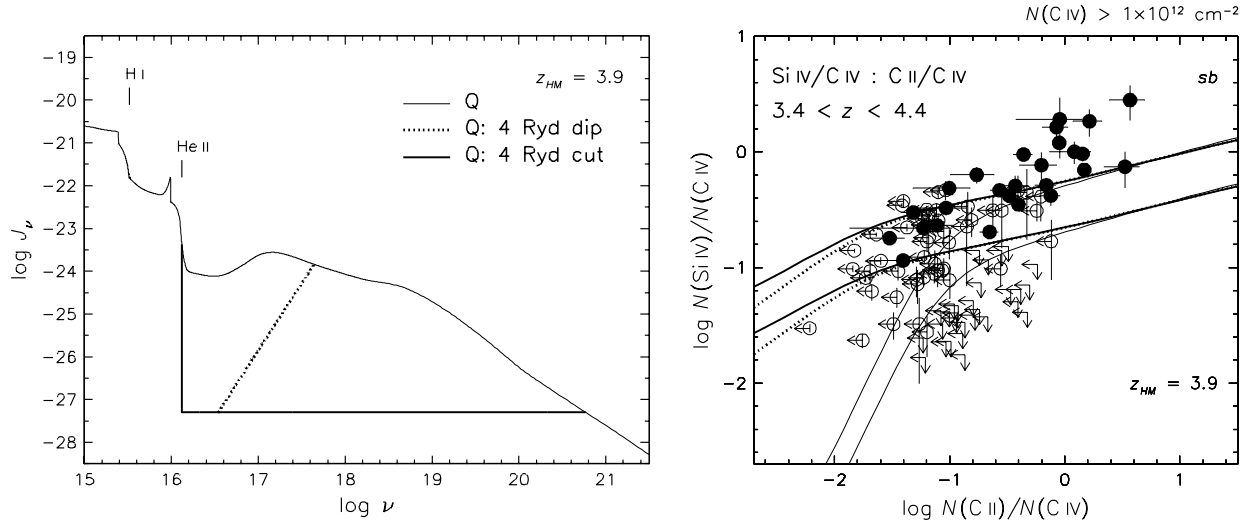


Fig. 28.— *Left panel:* Spectral energy distributions plotted similarly to those in Figure 25, for the QSO metagalactic ionizing radiation background model Q at $z_{HM} = 3.9$ with post-computation modifications in the He II continuum contrived for two cases, a horizontal cut and a deep depression, both initiated with a drop of 4 dex at the He II ionization edge. *Right panel:* Column density ratios Si IV/C IV : C II/C IV in our highest redshift interval compared with Cloudy results, presented as in Figure 18 but here using model Q with the modifications in the *left* panel and shown with the same coding; the unmodified case is shown for comparison. The cosmic microwave background is included.

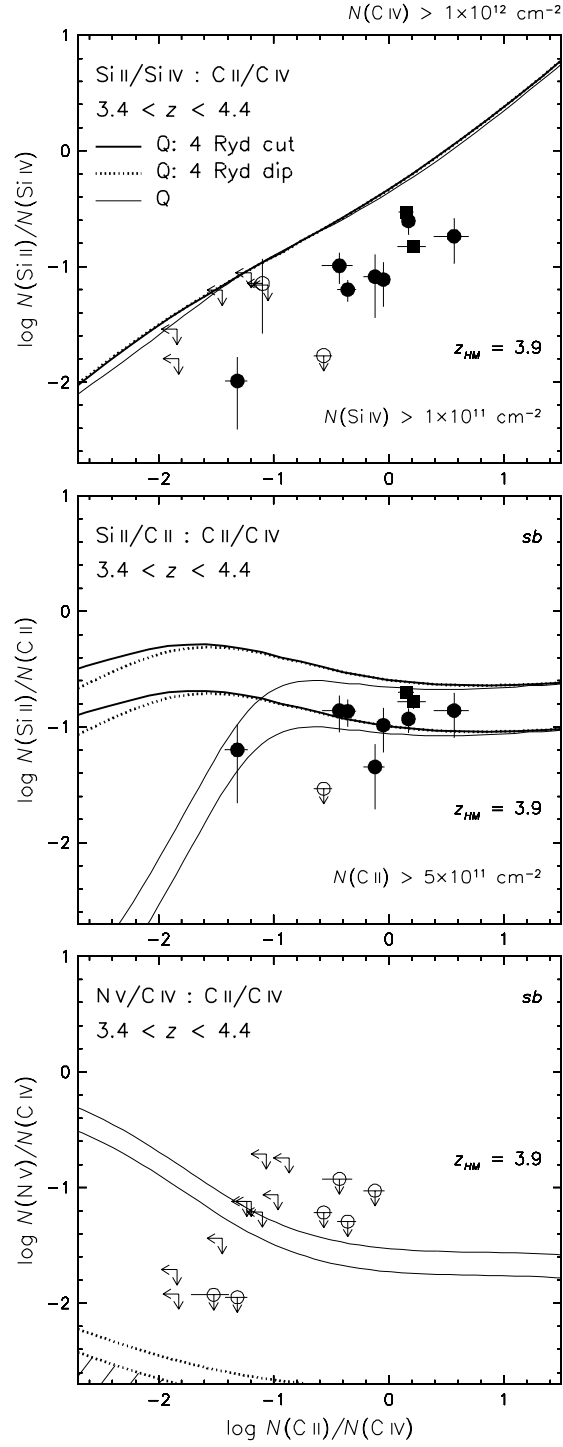


Fig. 29.— Same as for *right* panel in Figure 28, here for $\text{Si II/Si IV} : \text{C II/C IV}$, $\text{Si II/C II} : \text{C II/C IV}$ and $\text{N V/C IV} : \text{C II/C IV}$ (see comment in Figure 27 regarding N/C relative abundance, and shading), with the observed ratios taken from Figures 19 and 20.

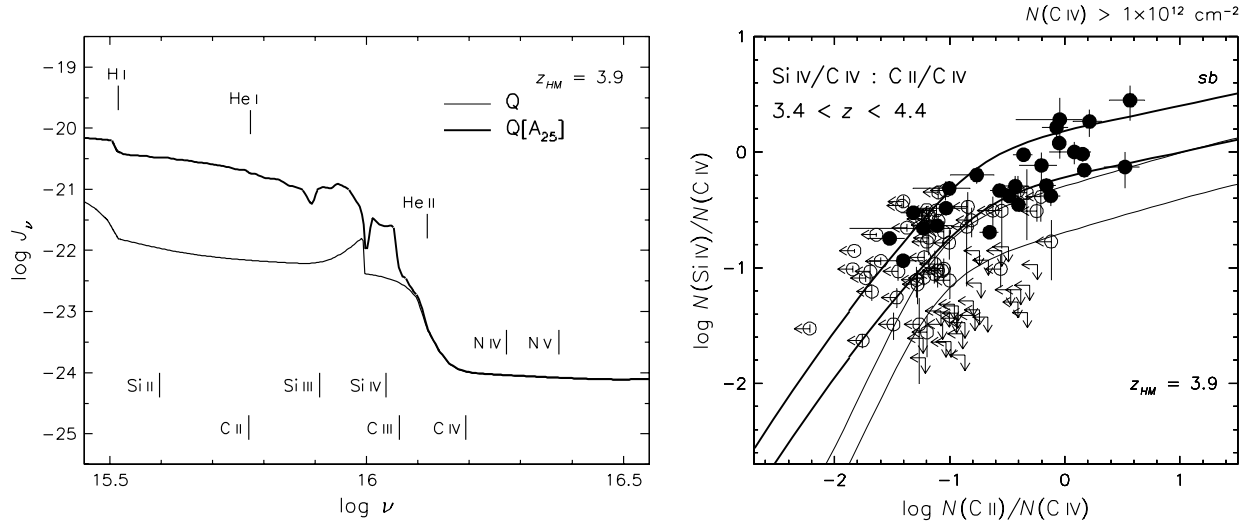


Fig. 30.— *Left panel:* Spectral energy distribution as presented in Figure 26, here using the new Haardt & Madau metagalactic ionizing radiation background model containing only QSO sources, model Q, combined with a contribution from *local* sources represented by a specific 45,000 K stellar spectral model (see text) scaled at the H I Lyman limit by $f_{\text{loc}} = 25q$ (i.e. 25 times the mean intensity of the model Q background); this model is termed Q[A₂₅]. The model Q case is shown for comparison. *Right panel:* Column density ratios Si IV/C IV : C II/C IV in our highest redshift interval compared with Cloudy results as presented in Figure 18, here using model Q[A₂₅] with model Q for comparison (coding as indicated in the *left panel*). The cosmic microwave background is included.

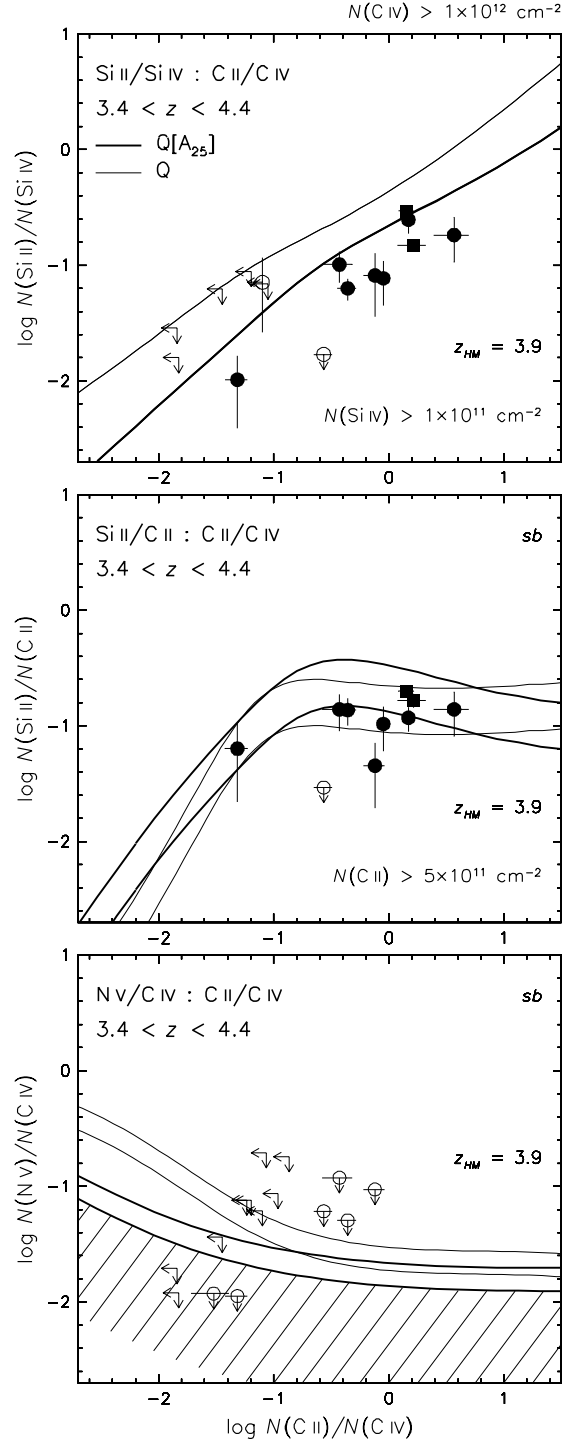


Fig. 31.— Same as for *right* panel in Figure 30, here for $\text{Si II/Si IV} : \text{C II/C IV}$, $\text{Si II/C II} : \text{C II/C IV}$ and $\text{N V/C IV} : \text{C II/C IV}$ (see comment in Figure 27 regarding N/C relative abundance, and shading), with the observed ratios taken from Figures 19 and 20.

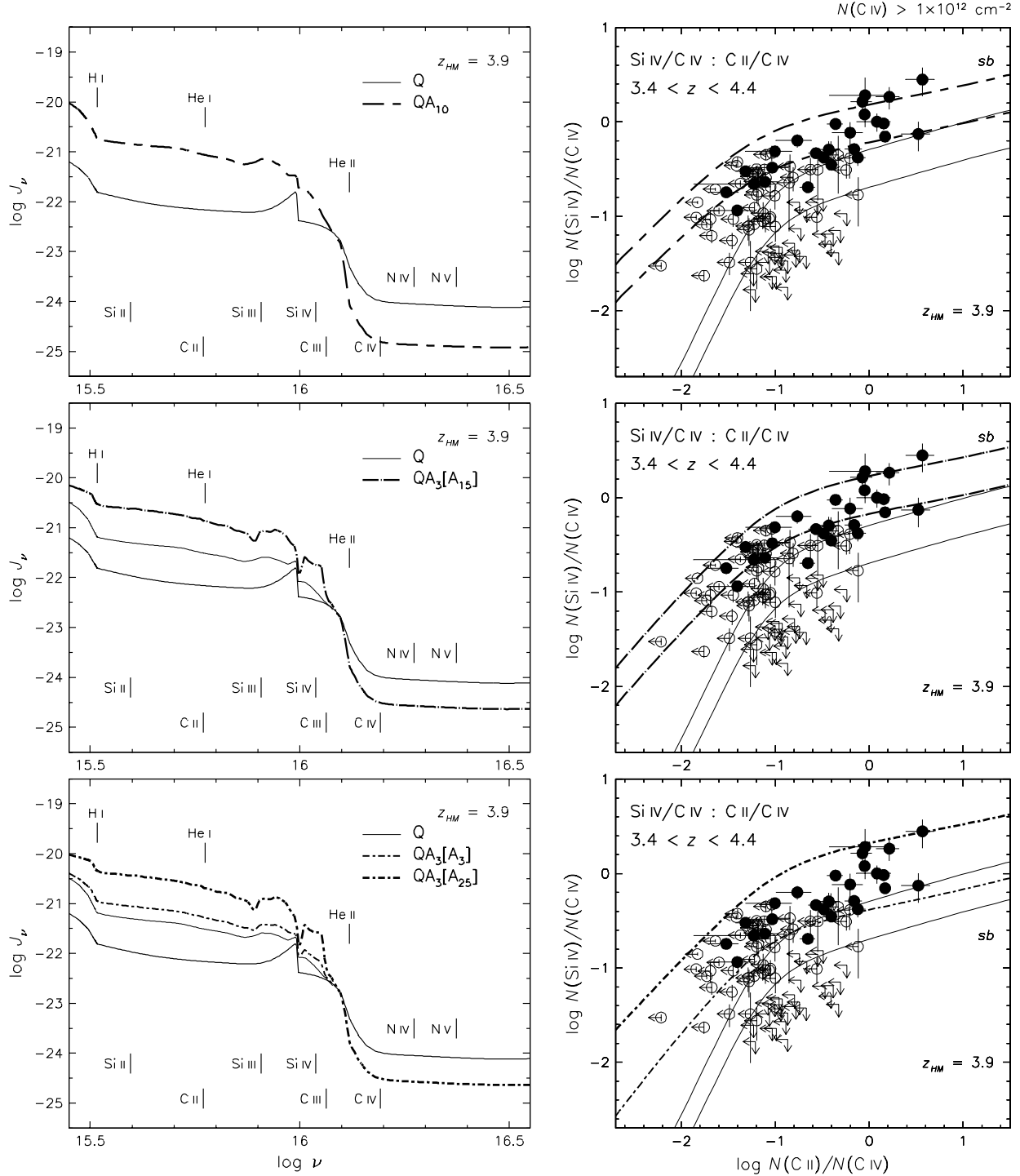


Fig. 32.— *Top left panel:* Spectral energy distribution as presented in Figure 26, here with a contrived Haardt & Madau QSO + galaxy metagalactic background using “galaxies” made up from the 45,000 K stellar spectral model employed in Figure 30 *included* in the cosmological radiative transfer computation with a scaling in volume emissivity at the H I Lyman limit relative to the QSOs by factor $f_{\text{met}} = 10$ (see text), termed model QA₁₀; $J_{\nu 0} = 1.8 \times 10^{-21} \text{ erg s}^{-1} \text{ cm}^{-2} \text{ Hz}^{-1} \text{ sr}^{-1}$. Model Q is shown for comparison. *Middle left panel:* Similar to *top* panel with $f_{\text{met}} = 3$ (shown by the thin continuous line; $J_{\nu 0} = 6.6 \times 10^{-22} \text{ erg s}^{-1} \text{ cm}^{-2} \text{ Hz}^{-1} \text{ sr}^{-1}$), combined with the 45,000 K stellar model representing *local* sources as in Figure 30 scaled by $f_{\text{loc}} = 15q$, termed model QA₃[A₁₅]; $J_{\nu 0} = 3.0 \times 10^{-21} \text{ erg s}^{-1} \text{ cm}^{-2} \text{ Hz}^{-1} \text{ sr}^{-1}$. *Bottom left panel:* Similar to *middle* panel, showing bounds representing cosmic variance in the local source contribution with $f_{\text{loc}} = 3q$ and $25q$, termed models QA₃[A₃] and QA₃[A₂₅]; $J_{\nu 0} = 1.1 \times 10^{-21}$ and $4.6 \times 10^{-21} \text{ erg s}^{-1} \text{ cm}^{-2} \text{ Hz}^{-1} \text{ sr}^{-1}$, respectively. *Right panels:* Column density ratios Si IV/C IV : C II/C IV in our highest redshift interval compared with Cloudy results as in Figure 18, obtained using the models in the *left* panels with coding as indicated; for the curves in the *bottom* panel, QA₃[A₃] is coupled with absorber Si/C solar relative abundance and QA₃[A₂₅] with $2.5 \times$ solar. The cosmic microwave background is included.

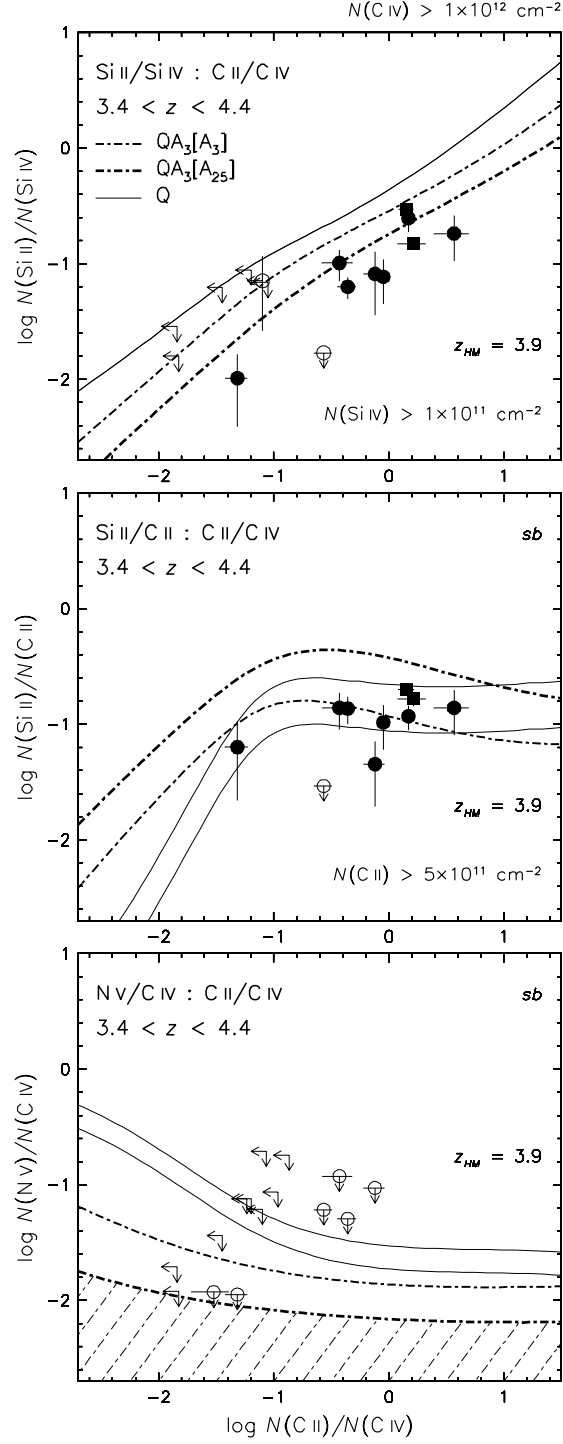


Fig. 33.— Same as for *bottom right* panel in Figure 32, for $\text{Si II/Si IV} : \text{C II/C IV}$, $\text{Si II/C II} : \text{C II/C IV}$ and $\text{N V/C IV} : \text{C II/C IV}$ (see comment in Figure 27 regarding shading), with the observed ratios taken from Figures 19 and 20. $QA_{3Q}+A_{3q}$ is coupled with absorber Si/C and N/C solar relative abundance and $QA_{3Q}+A_{25q}$ with $2.5 \times$ and $0.63 \times$ solar, respectively.

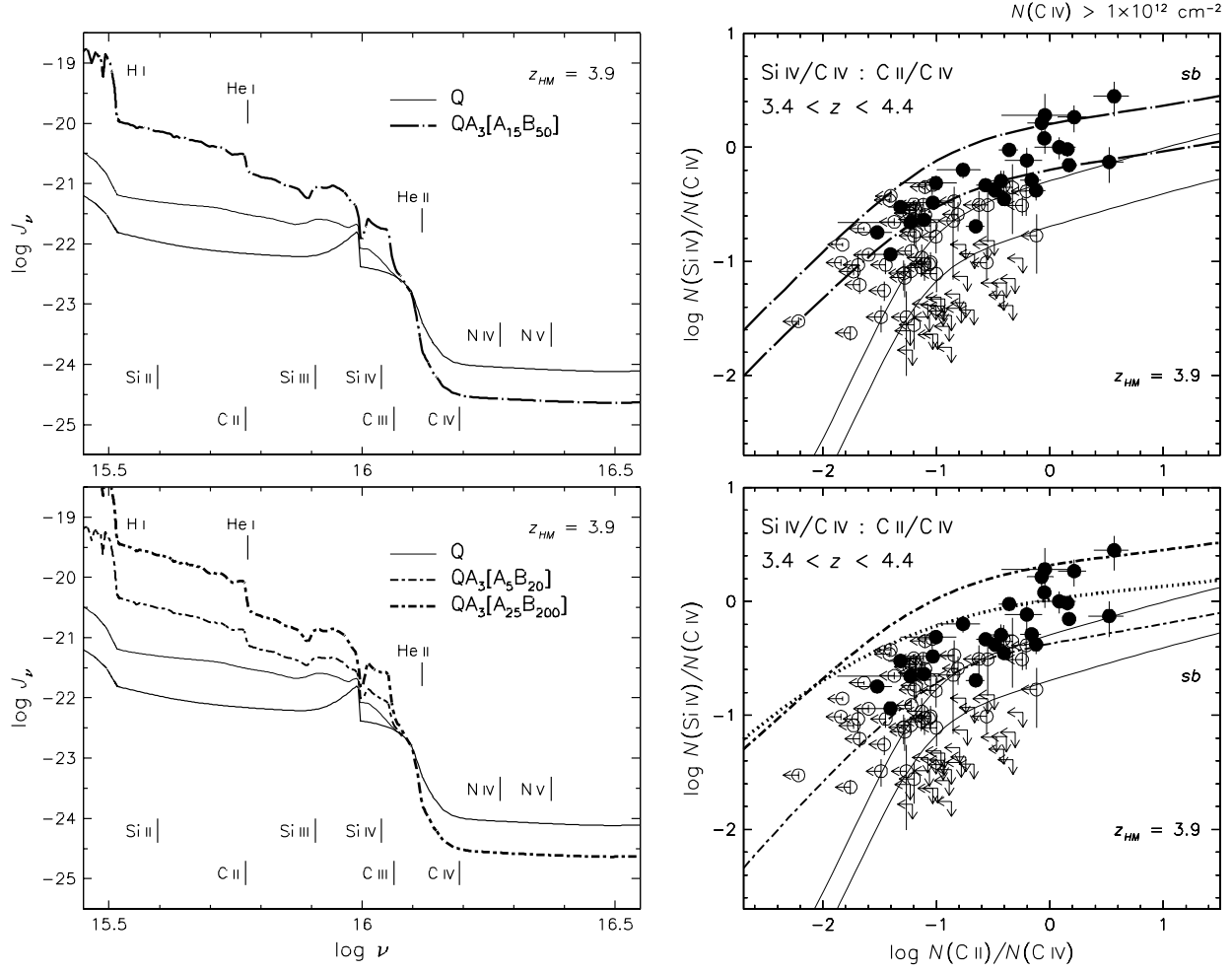


Fig. 34.— *Upper left panel:* Spectral energy distribution as presented in *middle left panel* of Figure 32, here with an added local stellar component introducing a significant He I ionization edge (see text) scaled by $f_{loc} = 50q$, termed model $QA_3[A_{15}B_{50}]$; $J_{\nu_0} = 1.1 \times 10^{-20} \text{ erg s}^{-1} \text{ cm}^{-2} \text{ Hz}^{-1} \text{ sr}^{-1}$. The faint trace is the metagalactic contribution within this case as given in Figure 32. *Lower left panel:* Similar to *upper panel*, showing bounds representing cosmic variance in the local source contributions, termed models $QA_3[A_5B_{20}]$ and $QA_3[A_{25}B_{200}]$; $J_{\nu_0} = 5.3 \times 10^{-21}$ and $3.5 \times 10^{-20} \text{ erg s}^{-1} \text{ cm}^{-2} \text{ Hz}^{-1} \text{ sr}^{-1}$, respectively. *Right panels:* Column density ratios Si IV/C IV : C II/C IV in our highest redshift interval compared with Cloudy results as in Figure 18, obtained using the models in the *left panels* with coding as indicated; for the curves in the *lower panel*, model $QA_3[A_5B_{20}]$ is coupled with absorber Si/C solar relative abundance and $QA_3[A_5B_{20}]$ with $2.5 \times$ solar. The additional heavy dotted line in the *lower panel* is a case using model $QA_3[A_{25}B_{200}]$ with absorbers of *solar* Si/C relative abundance and metallicity $[Z] = -1.5$. The cosmic microwave background is included in all computations.

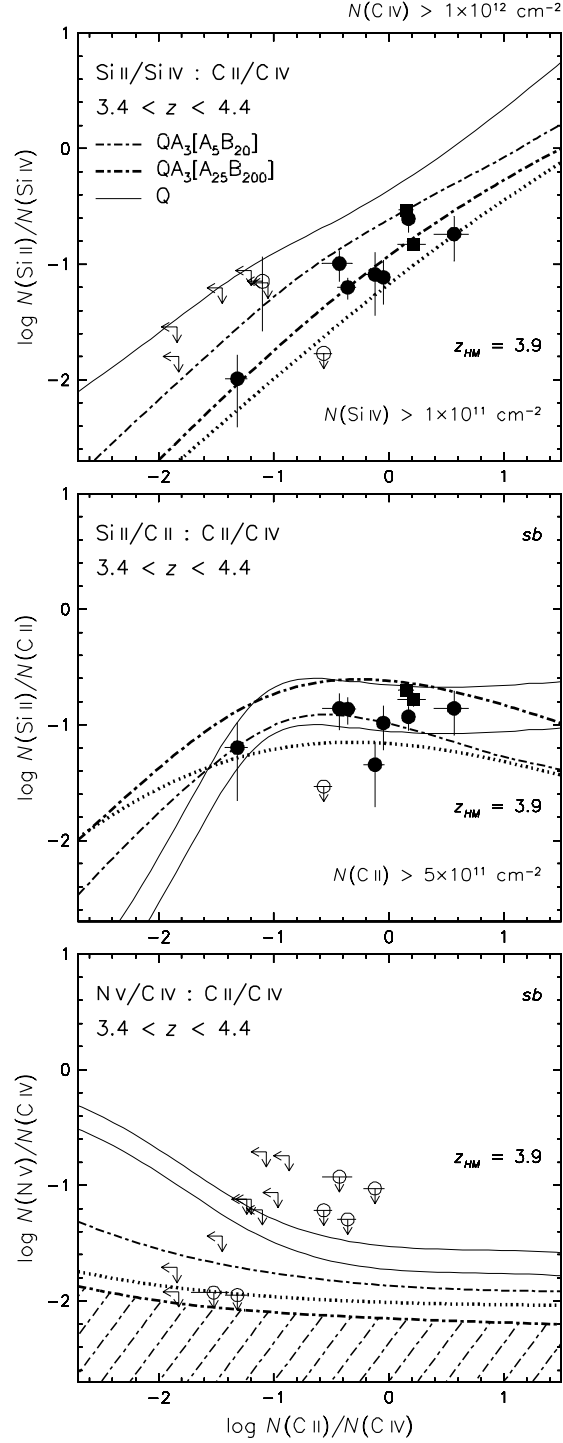


Fig. 35.— Same as for *lower right* panel in Figure 34, for Si II/Si IV : C II/C IV, Si II/C II : C II/C IV and N V/C IV : C II/C IV (see comment in Figure 27 regarding shading, applying also to the dotted line), with the observed ratios taken from Figures 19 and 20. Model QA₃[A₅B₂₀] is coupled with absorber Si/C and N/C solar relative abundance and QA₃[A₂₅B₂₀₀] with $2.5 \times$ and $0.63 \times$ solar, respectively.

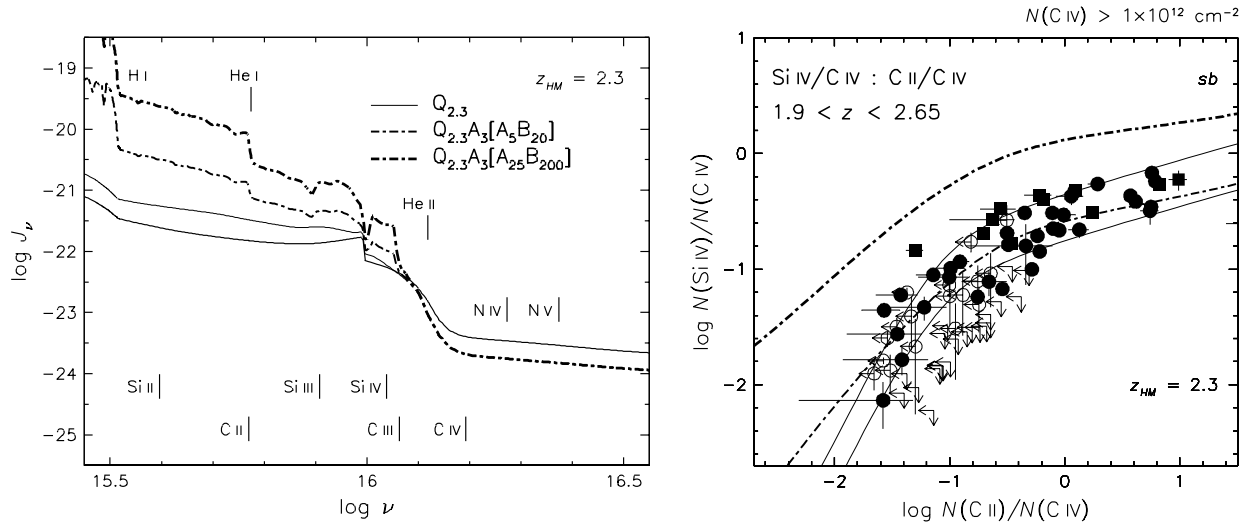


Fig. 36.— Similar to *lower* panels in Figure 34, substituting the QSO source flux at $z_{HM} = 2.3$ but otherwise using the same stellar source quantities, termed models $Q_{2.3}A_3[A_5B_{20}]$ and $Q_{2.3}A_3[A_{25}B_{200}]$, and comparing the Cloudy results with the data in our lowest redshift interval presented in Figure 18. The appropriate cosmic microwave background is included.